MINISTRY OF EDUCATION, RESEARCH, YOUTH AND SPORT

THE ANNALS OF "DUNAREA DE JOS" UNIVERSITY OF GALATI

Fascicle IX
METALLURGY AND MATERIALS SCIENCE

YEAR XXVII (XXXII),
November 2009, no. 2

ISSN 1453-083X

2009
GALATI UNIVERSITY PRESS

THE ANNALS OF "DUNAREA DE JOS" UNIVERSITY OF GALATI.
FASCICLE IX. METALLURGY AND MATERIALS SCIENCE
N^0. 2 – 2009, ISSN 1453 – 083X

Table of Content

THE ANNALS OF "DUNAREA DE JOS" UNIVERSITY OF GALATI.
FASCICLE IX. METALLURGY AND MATERIALS SCIENCE
N^0. 2 – 2009, ISSN 1453 – 083X

ESTABLISHING THE CONSTITUTIVE LAW OF A CrMo ALLOYED STEEL

N. CANANAU, P ALEXANDRU, L. GURAU, G. GURAU
"Dunărea de Jos" University of Galati
email: ncananau@ugal.ro

The paper shows the results of the researches for establishing the equation of the deformation behavior of alloyed steel with chromium and molybdenum. The behavior law is established in the experimental way, using the results of a set of torsion tests. The composed constitutive law had very good experimental verification.

KEYWORDS: constitutive equation, torsion test, stress, strain, temperature.

1. Introduction

The establishing of the equation of plastic deformation behavior is a process of transformation of the torsion moment function in the stress intensity function, respectively, the equation between the stress intensity, strain, strain rate and temperature [1]:

$$\sigma = \sigma(\varepsilon, \dot{\varepsilon}, T) \qquad (1)$$

In this equation, σ is the stress intensity, in the real deformation conditions, ε - strain intensity, $\dot{\varepsilon}$ - strain rate intensity, T – temperature.

This equation is used in the modelling and simulation process of the plastic deformation to apply the three-dimensional constitutive law according to the mono-dimensional constitutive law (1).

With this aim, the paper presents the results of researches carried out for the transformation of the torsion moment diagrams [1], in the equation of plastic deformation behavior for chromium, molybdenum alloyed steel.

The start point is the experimental data concerning the variation of the torsion moment with the strain, strain rate and temperature.

2. Establishing the viscoplastic law

Generally, we can define the function of the torsion moment under the form:

$$M = M(\varepsilon, \dot{\varepsilon}, T) \qquad (2)$$

In the differential form, the relation (2) becomes:

$$dM = \frac{\partial M}{\partial \varepsilon} d\varepsilon + \frac{\partial M}{\partial \dot{\varepsilon}} d\dot{\varepsilon} + \frac{\partial M}{\partial T} dT \qquad (3)$$

For the maximum values of the torsion moment the equation (2) may be written:

$$dM_{\max} = \frac{\partial M_{\max}}{\partial \dot{\varepsilon}} d\dot{\varepsilon} + \frac{\partial M_{\max}}{\partial T} dT$$

Thus, we can establish the function:

$$M_{\max} = M_{\max}(\dot{\varepsilon}, T) \qquad (4)$$

which describes the functional influence of the strain rate and temperature on the deformation strength.

Using the experimental results obtained for the sixteen combinations between the strain rate and temperature, [1] we have the data written in the table 1.

Table 1. *Values of the maximum torque*

Strain rate, s^{-1}	Temperature, ^{0}C			
	850	900	950	1000
0.0964	3.9642	3.2257	2.6622	2.2347
0.2849	5.1439	4.2807	3.4807	2.0342
0.8949	5.9657	5.0637	4.2325	3.6532
3.0217	6.5681	5.7102	5.0102	4.1836

In the graphical form, the data from the table 1 are rendered in figure 1.

The maximum torsion moment increases when the strain rate increases and decreases when the temperature increases.

The variation of the maximum torsion moment depends on the strain rate by a power function and on the temperature by an exponential function.

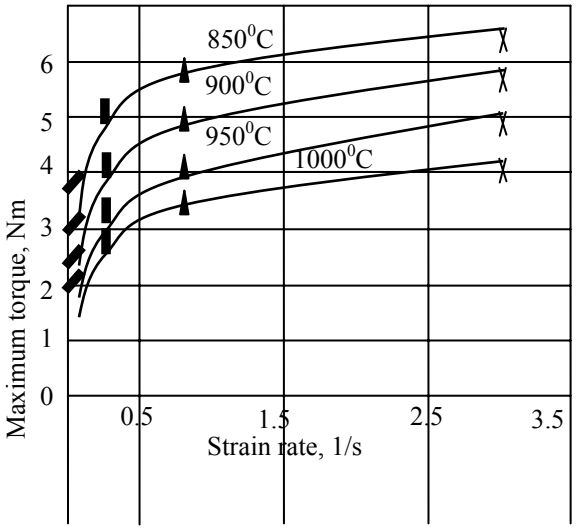

Fig. 1. *Variation of the maximum torque with strain rate and temperature*

Thus, the mathematical expressions of the dependence of the maximum torsion moment, frequently used for the characterization of the plastic deformation behavior, are the following:

$$M_{\max} = A_1 \cdot \dot{\varepsilon}^m \cdot \exp(-\alpha \cdot t) \qquad (5)$$

$$M_{\max} = A_2 \cdot \dot{\varepsilon}^m \cdot \exp\left(\frac{m \cdot Q}{RT}\right) \qquad (6)$$

$$M_{\max} = A_3 \cdot \ln\left(\frac{Z}{B}\right) \qquad (7)$$

In these expressions, *m* is the sensibility of the stress at the strain rate, α – the temperature coefficient, t, T – temperature, in ^{0}C and K, respectively, Q – activation energy, R – constant of the perfect gas, A_1, A_2, A_3, B – experimental constants, Z – Zener-Hollomon parameter.

We used DATAFIT software for statistical calculus for the evaluation of the mathematical models of the plastic deformation behavior showed above.

We obtained the following results:

-For equation (5): A_1=0.06949; m=0.168387; Q=247294 J/(kmol·K) and the Coefficient of Multiple Determination (R^2) = 0.9739782376

- For equation (7): A_2=117.06; m=0.168387; α=-0.00351 and the Coefficient of Multiple Determination (R^2) = 0.9743690499

- For equation (8): A3=0.682538; B=131757975; Q=254727 J/(kmol·K). Coefficient of Multiple Determination (R^2) = 0.9842024264.

$$M_{\max} = 0{,}694 \cdot \dot{\varepsilon}^{0{,}1683} \cdot \exp\left(\frac{5005{,}6792}{T}\right) \qquad (8)$$

$$M_{\max} = 117{,}06 \cdot \dot{\varepsilon}^{0.1683} \cdot \exp(-0{,}00351 \cdot t) \qquad (9)$$

$$M_{\max} = 0.682538 \cdot \ln\left(\frac{\dot{\varepsilon} \cdot \exp\left(\frac{254727}{8314 \cdot T}\right)}{131757975}\right) \qquad (11)$$

The three equations (5), (6) and (7) have a very good verification on the basis of the experimental results.

The tension is defined by the relation:

$$\sigma = \frac{\sqrt{3}}{2\pi r^3} \cdot \left(3M + \varepsilon \frac{\partial M}{\partial \varepsilon} + \dot{\varepsilon} \frac{\partial M}{\partial \dot{\varepsilon}} + T \frac{\partial M}{\partial T}\right) \qquad (12)$$

The tension that corresponds to the maximum torque, for the constant temperature, if we use the expression (8), is defined by the relation:

$$\sigma_m = \frac{\sqrt{3} \cdot (3+m)}{2\pi r^3} \cdot M_{\max} \qquad (13)$$

In this relation, *r* is the radius of the sample used at the torsion tests.

Considering the equation (8) for the value of the radius of 3mm, we obtain:

$$\sigma_m = 22.434 \cdot \dot{\varepsilon}^{0{,}1683} \cdot \exp\left(\frac{5005{,}6792}{T}\right) \qquad (14)$$

The variation of the maximum torsion moment with the strain must be described by a compose function. The first part must be a hardening factor described by a power or, recommended, by an exponential expression.

The second part will be defined by an exponential function that must consider the caloric effect of the plastic deformation.

In these conditions, the general expression of the plastic deformation stress may be written as below:

$$\sigma(\varepsilon, \dot{\varepsilon}, T) = \begin{cases} A_1 \cdot (1 - \exp(-n\varepsilon)) \cdot (\dot{\varepsilon})^m \cdot \exp\left(\frac{mQ}{RT}\right) & \text{for } \varepsilon \le \varepsilon_0 \\ A_2 \cdot \exp(-p(\varepsilon - \varepsilon_0)) (\dot{\varepsilon})^m \cdot \exp\left(\frac{mQ}{RT}\right) & \text{for } \varepsilon > \varepsilon_0 \end{cases} \qquad (15)$$

Table 2. *Values of the strain to maximum torque*

Strain rate, s^{-1}	Temperature, ^{0}C			
	850	900	950	1000
0.0964	0.4240	0.4337	0.4144	0.3754
0.2849	0.4558	0.5983	0.5128	0.3954
0.8949	0.2564	0.2849	0.2294	0.2279
3.0217	0.5858	0.7856	0.6268	0.2369

In this expression ε_0 is the strain according to the maximum of the torsion moment.

The values of the ε_0 are rendered in table 2 and are shown in the graphic form in figures 2 and 3.

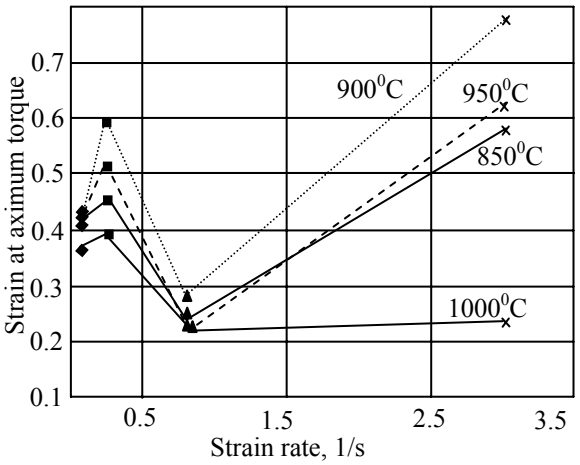

Fig. 2. *Variation of the strain at maximum torque with strain rate and temperature*

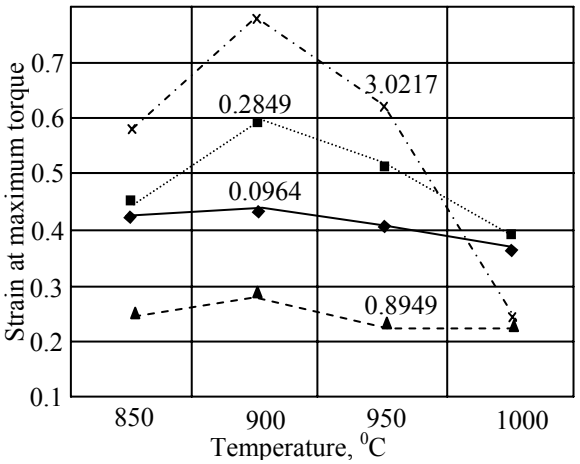

Fig. 3. *Variation of the strain at maximum torque with strain rate and temperature*

The influence of the temperature and strain rate on the strain at the maximum torque has a complex character because, in the domain of the testing temperature, the deformation process is simultaneous with the structural transformations. Thus at 850^{0}C, the transformation perlite-austenite is finished, but the process of the carbides solving is at the beginning. At 1000^{0}C, the process of increasing the austenite grains is very strongly activated and, consequently, the intensity of the deformation hardening is greater.

Very complex is the influence of the strain rate explained through the interaction of the plastic deformation hardening and the opposite process as the caloric effect of the plastic deformation. For a very small value of the strain rate, the ε_0 factor has a smaller dispersion rate. Also, for a mean value of the strain rate, the value of the ε_0 factor decreases and the dispersion is small, but at the great value of the strain rate, relatively, the dispersion of the values of the ε_0 factor is great.

This is the reason why it is necessary to extend researches for establishing the complete data for the ε_0 factor.

The constants form of the equation (15): A_1, A_2 n, p may be established on the basis of experimental researches [2].

4. Conclusions

The knowledge of the constitutive equation of the material is necessary for the modelling, simulation and optimization of the plastic deformation process. The best method for establishing the constitutive equation is the torsion testing. Applying a research program aton, the torsion testing machine in the Plastic deformation laboratory at the Faculty of Metallurgy and Materials Science from *Dunarea de Jos* University of Galati established the constitutive equation of steel for wires with a view to reinforcing concrete.

The constitutive equation shows that the influence of the strain rate is described by the power mathematical function, while the influence of the temperature is described by an exponential function.

References

[1]. Cănănău N. - *Teoria deformării plastice,* Universitatea Dunarea de Jos din Galati, 1994.

[2] Dumitrescu A.T. - *Contribuţii la modelarea laminarii in calibre*. Teza de doctorat, Institutul Politehnic Bucureşti, 1986.

[3] Corobete, G. - *Contribuţii la cercetarea procesului de laminare a sârmelor din otel cu caracteristici mecanice superioare. Teza de doctorat,* Universitatea Dunărea de Jos din Galaţi, 2006.

[4] Moussy F., Franciosi P. - *Physique et mecanique de la mise en forme des meteaux.* Presses du CNRS, Paris, 1990

[5] Cananau N., Petrea I, Corobete G. - *Modelling of the flow and deformation fields at the profiles rolling by field lines method*, The Annals of "Dunarea de Jos" University of Galati, Fascicle IX, Nov. 2005.

THE ANNALS OF "DUNAREA DE JOS" UNIVERSITY OF GALATI.
FASCICLE IX. METALLURGY AND MATERIALS SCIENCE
N^0. 2 – 2009, ISSN 1453 – 083X

THE TEMPERATURE EFFECT ON SEVERELY DEFORMED ALUMINIUM BY HIGH PRESSURE TORSION

Carmela GURAU[1], Gheorghe GURAU[1], Nicolae CANANAU[1], Florentina POTECASU[1], Victor DOGARU[1], F M Braz FERNANDES[2]
[1]Universitatea"Dunărea de Jos" din Galaţi
[2]CENIMAT Department of Material Science, FCT/UNL, Caparica, Portugal
email: gheorghe.gurau@ugal.ro

ABSTRACT

The process of deforming materials started to attract the interest of the researchers after the development of the severe plastic deformation techniques.

A number of aluminium samples were severe deformed by HPT method with different deformation degree. The researches follow to determine SPD effect on this material and temperature influence on fine aluminium structure. The paper present XRD and DSC results.

KEYWORDS: severe plastic deformation, high pressure torsion, XRD, DSC

1. Introduction

Over 20 years ago, Herbert Gleiter presented the first concepts for developing nanocrystalline materials, or ultrafine-grained materials with a grain size under 100 nm, with special properties. After his research the field of nanostrucured materials has developed rapidly in virtue of science interest for this field. He stated that because of containing an extremely large fraction of grain boundaries with special atomic structure, nanomaterials should have unusual properties., for example their mechanical properties present very high strength, toughness, fatigue life and wear resistance [1]

After severe plastic deformation, in the material can appear high internal stresses caused by high density of dislocations inside the grains and their boundaries. The presence of non-equilibrium grain boundaries containing numerous grain-boundary dislocations is an immediate consequence of severe straining, but it can be controlled by subsequent annealing or special thermomechanical treatments, or both. It is well known that grain refinement promotes mechanical strength, and thus one can expect ultrafine-grained materials to possess very high strength.

Moreover, introduction of a high density of dislocations in SPD-processed nanometals may result in even greater hardening.

However, all this normally decreases ductility. Strength and ductility are the key mechanical properties of any material, but they are typically opposing characteristics. Materials may be strong or ductile, but rarely both at once. Recent studies have shown that material nanostructuring may lead to a unique combination of exceptionally high strength and ductility (Fig. 1), but this task calls for original approaches[2].

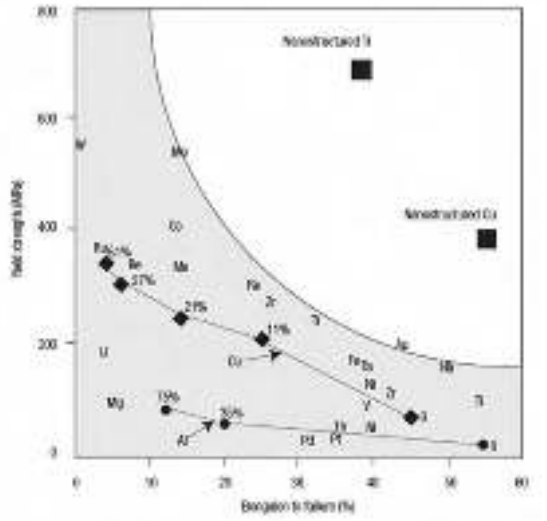

Fig. 1. *Strength and ductility of the nanostructured metals compared with coarse-grained metals [2]*

Conventional cold rolling of copper and aluminium increases their yield strength but decreases their ductility. The two lines represent this tendency for Cu and Al and the % markings indicate a percentage on rolling. In contrast, the extraordinarily

high strength and ductility of nanostructured Cu and Ti clearly set them apart from coarse grained metals[2]. Experiments have shown that in SPD produced metals, the diffusion coefficient grows considerably (by two or three orders), and this is associated with non-equilibrium grain boundaries. So perhaps grain-boundary sliding is easier in these ultrafine-grained metals and develops during straining even at lower temperatures, producing increased ductility. It is well known that enhanced sliding in nanostructured metals can lead even to superplasticity at relatively low temperatures[2]. Methods of severe plastic deformation can provide formation of nanostructures in different materials. However, an obtained grain size and a character of a nanostructure forming depend on the SPD methods applied, processing regimes, phase composition and initial microstructure of a material. Below, are examples of typical nanostructures.

2. Experimental procedures

The samples cylinder shape were severe deformed in lab using HPT constraint scheme. The rotating movement is applied on the upper punch. Also the upper punch has no vertical movement in SPD process. The necessary force is applied on the inferior punch using a hydraulic system. The samples having cylindrical shape were deformed in a number of steps (table1). The force variation is registered with an accurate Spider 8 Hottinger system.

***Table1**. SPD parameters and samples dimensions*

Sample Φ=9.4mm The starting material for Al suffered repression		**Height**		**Force**	**Rpm**	**Nr of SPD pass**	**Experiments**	
Name	**No.**	**Ho**	**H1**				**DSC**	**X-Ray**
		[mm]		[N]	[N/mm^2]			
I Al	1	6.4	5.4	2016.968	180	1		
	2.1	4.8	2.9	15604.96	180	2		
	3.2	2.9	1.9	28280.01	180	3		
	4.3	1.8	1.4	59744.71	180	4		
	5.4	*1.2*	*0.7*	*54946.45*	*180*	*5*	*X*	*X*
II Al	1	4.4	1.4	42059.09	180	1		
	2.1	1.5	1.2	39744.88	180	2		
	3.2	1.1	1.0	34628.15	180	3		
III Al	1	4.4	1.9	19023.19	180	1		
	2	4.5	1.6	19511.51	180	2		
	3	4.4	1.3	19214.27	180			

2.1. Methods of characterisation

X-ray structural analysis is a method providing important data on the defect structure of NSM (nanostructured materials). X-ray patterns of nanostructured materials processed by SPD methods differ significantly from X-ray patterns of corresponding coarse-grained materials.

These differences are revealed, first of all, in changes of integral intensity of background, changes of width and intensity of X-ray peaks and appearance of crystallographic texture. The background on X-ray patterns is a result of diffuse scattering of X-rays.

The recent results of calculations show that the integral intensities of the background on the X-ray pattern of nanostructured material exceed the corresponding value for coarse-grained material. The increase in the integral intensity of the background indicates an elevated density of crystal structure defects and a possible change in the vibrational spectrum of atoms in nanostructured copper. The XRD analyses were made in CENIMAT laboratories Portugal. The equipment currently available in the Laboratory of X-ray diffraction of CENIMAT is a system Rigaku, Dmax III-C model and a system based on a Siemens rotating anode generator.

***Fig. 2.** The XRD Lab in the CENIMAT, Portugal*

2.2. The XRD samples preparation

The Al sample was studied on X-Rays and DSC. First it was done the DSC analysis to establish the temperature cycle for the XRD analysis.

Before preparing the sample, it was taking in account what surface of the sample shell be studied, so it was chosen the surface that is more sharp than the other. After it was taking in account the geometry of the sample, and it was cut where the surface was symmetrical and parallel to the sample-holder after had been arranged in the cavity.

The preparation for the XRD analysis starts by cutting a rectangular piece from the deformated sample to mach the sample-holder's cavity (L =14mm, l =10mm, H= 0.2; 0.9).

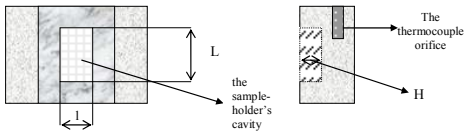

Fig.3. *The sample-holder*

It is very important to know that the deformed samples can't be polish because we risk loosing the information that will help us analyse the surface of the sample.

The NITI samples where cleaned in acid from the oxides on the surface and after their where clean with alcohol. The rectangular piece was glued (the glue that we used is Araldit rapid with a little bit of silver to make it stronger) in the cavity of the sample-holder and placed inside the cavity vertically therefore to be radiated with ka beam. After the thermocouple is introduced in a special hole inside the upper sample-holder and it will measure the temperatures that it will reach during the temperature cycle.

After is checked that the sample-holder is well introduced in the special place and the sample doesn't fall out of the cavity, the installation is prepared for the analysis by checking that the doors are well closed, setting the intensity to be 100-150 mA and the and voltage 30-35 KV, vacuuming the enclosure where the sample is staying.

The alignment of the beam and sample holder can start. For the alignment we used a limitation for the X Ray with an aperture of 1 mm and a copperplate. After the alignment the copperplate was change with a plate with a different aperture of 0.6mm it is necessary for the alignment to be done because it has to be corrected by rotation and translation the way of the beam above the surface of the sample.

After the alignment is done and the parameters are well established, the analysis can start on a different cycle of temperatures for each different sample. A full scan lasted for about 5-7 hours, for each sample. The results where saved on different files for each temperature. With the peaks that where shown in the scans there were build in Eva program 3D graph and with them it can be seen very well the movement of the peaks and the phases appearing and disappearing. The reading files for all the temperatures from each cycle were saved in different.

After, it was created an EVA file, it can be seen all the transformation at different temperatures. With EVA file we can compare all the scans at different temperatures.

The results were processed in programs like: Microsoft XLS, Origin.

3. Results and discussions

The results for the sample of Al are presented in the previous graphics.

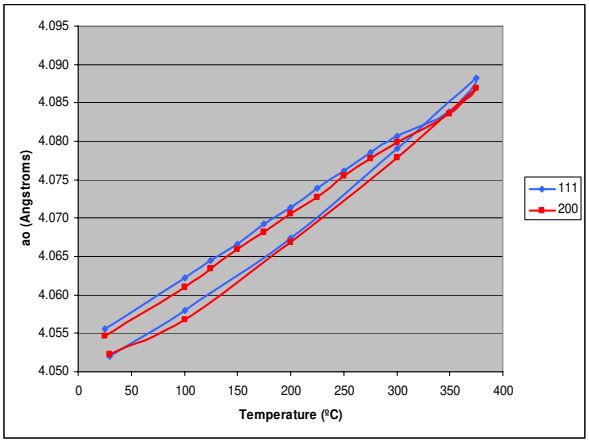

Fig.4. *The lattice parameter - Temperature*

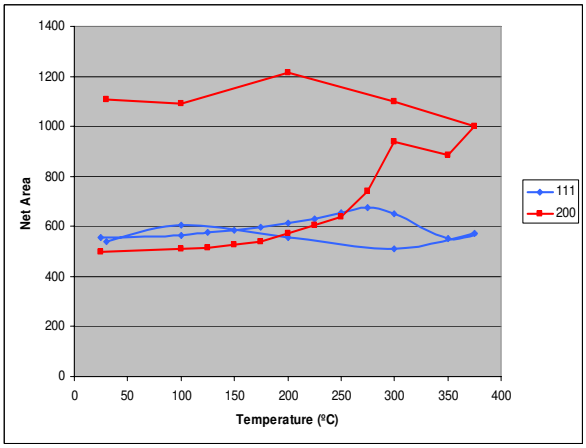

Fig.5. *Net area - Temperature*

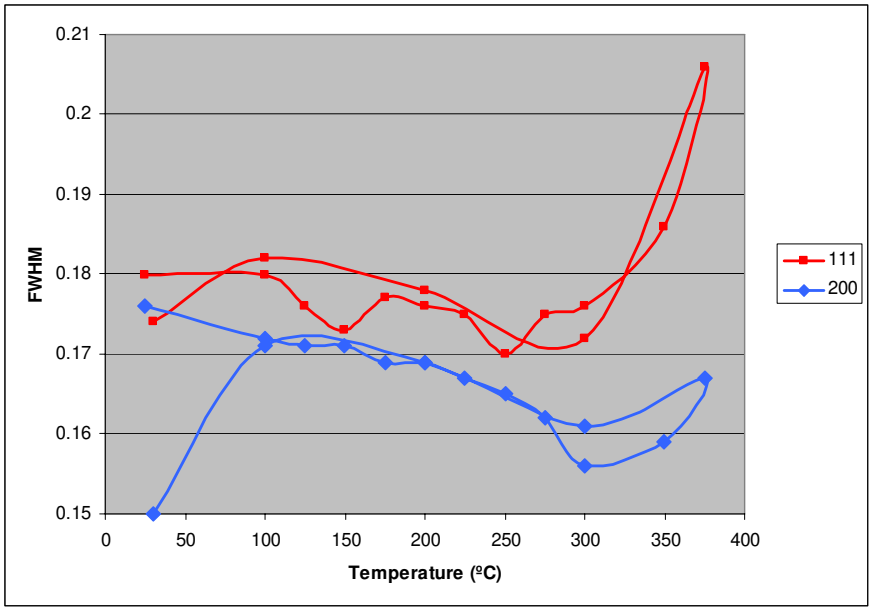

Fig.6. *FWHM (full width at half maximum)-temperature variation*

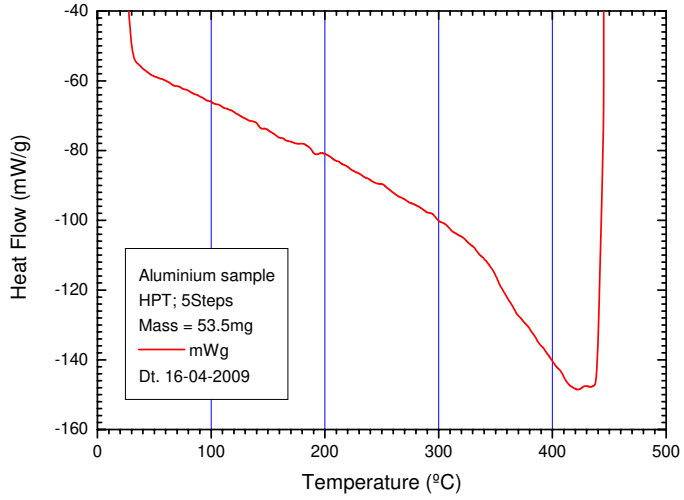

Fig.7. *Aluminium DSC variation*

Looking at the DSC graph, it results that when the sample receives heat, when it reaches the point of 400ºC, in its structure occurs the recrystalisation.

4. Conclusions

In laboratories of University *Dunarea de Jos* of Galati vas developed a SPD technique based on High Pressure Torsion method. Aluminium disk shape samples vas made at different deformations degree. The fine structure vas confirmed after lab tests which consists in X ray diffraction tests and DSC tests. The X ray diffraction tests developed at different temperatures point out behaviour fine aluminium structure.

References

[1]. Ruslan Valiev - *Nanostructuring of metals by severe plastic deformation for advanced properties, article in progress*, Institute of Physics of Advanced Materials,Ufa State Aviation Technical University,12 K.Marx str., Ufa 450000, Russia, p.511

[2]. R.Z. Valiev, R.K. Islamgaliev, I.V. Alexandrov - *Bulk nanostructured materials from severe plastic deformation* , Institute of Physics of Advanced Materials, Ufa State Aviation Technical University, 12 K. Marx Street, 450000 Ufa, Russian Federation, p.51-514

[3]. H.P. Karnthaler, T. Waitz, C. Rentenberger, B. Mingler - *TEM of nanostructured metals and alloys,* Materials Science and Engineering A 387–389, 2004, 777–782

[4]. L. Kommel, I. Hussainova, O. Volobueva - *Microstructure and properties development of copper during severe plastic deformation*, Materials and Design, 2006

[22]. E. Schafler, M.B. Kerber - *Microstructural investigation of the annealing behaviour of high-pressure torsion (HPT) deformed copper*, Materials Science and Engineering, 2006

THE ANNALS OF "DUNAREA DE JOS" UNIVERSITY OF GALATI.
FASCICLE IX. METALLURGY AND MATERIALS SCIENCE
N^0. 2 – 2009, ISSN 1453 – 083X

REDESIGNING A JAW CRUSHER USING VALUE ANALYSIS
Part II

Florin CHICHERNEA, Alexandru CHICHERNEA
"Transilvania" University of Brasov
email: chichernea.f@unitbv.ro

ABSTRACT

The paper presents a complete study of VALUE ANALYSIS applied concretely to a selected piece of equipment. The phases and ITERATIVE operation of the Value Analysis method are presented.

Value Analysis combines both ENGINEERING and ECONOMICS without, however, placing neither ENGINEERING or ECONOMICS first. They both are similarly important, as it can be concluded at the end of this paper.

KEYWORDS**:** value analysis, value, optimum variant

9. Establishing the functional - technological form of the parts in view of cost reduction

Further on, an analysis from the technical and economic viewpoint will be carried out in order to select a technically optimum variant for one of the parts: the flywheel.

Four constructive variants of flywheel will be studied and eventually the most cost effective and the most competitive one from the technical and economic viewpoints will be selected.

Prior to the actual study, a number of basic ideas of creative engineering will be shortly presented.

Figures 6 and 7 present a flywheel made from welded semi-products.

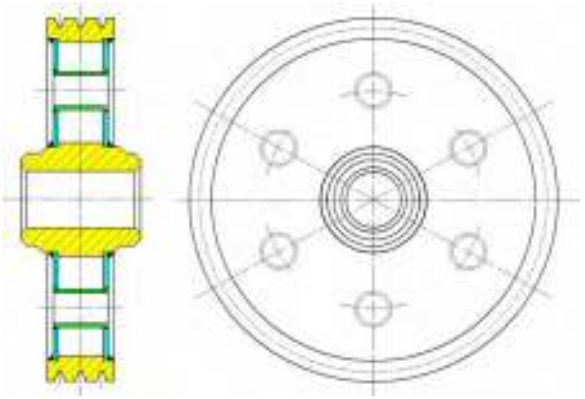

***Fig. 6**. Flywheel made from welded semi-products.*

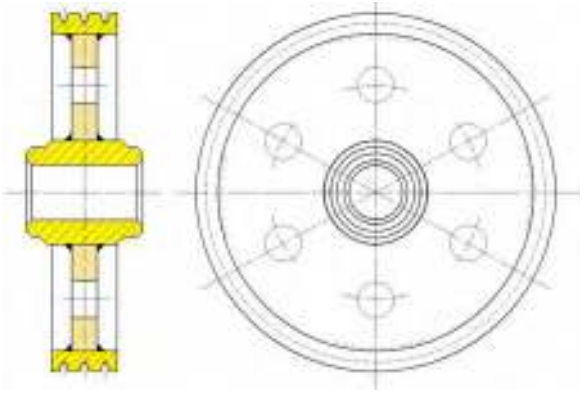

***Fig. 7**. Flywheel made from welded semi-products.*

The functional characteristics of this type of part are the following:

- maximum diameter,
- diameter of egagement,
- geometrical elements of connecting gear,
- internal diameter of wheel hub,
- concentricity between flywheel axis and diameter of egagement,
- wearing resistance,
- reconditioning method.

Figure 8 presents an assembled flywheel screw and figure 9 presents a flywheel made from a cast semi-product.

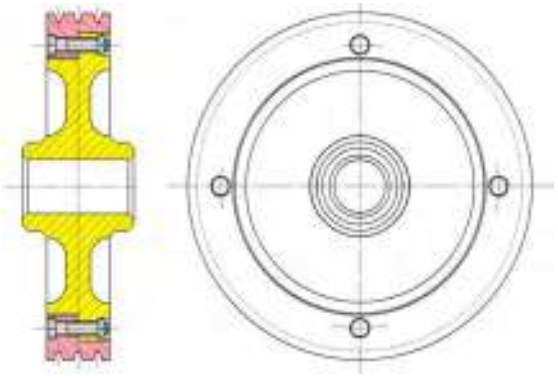

Fig. 8. *Assembled flywheel screw.*

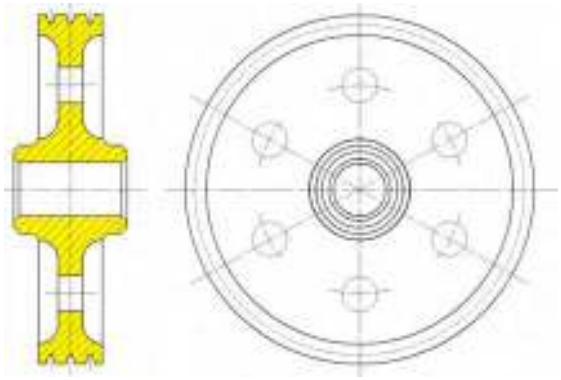

Fig. 9*. Flywheel made from a cast semi-product.*

All variants are technological and the selection of one of them depends on the level of endowment of the company. Thus the variants present the aspects enumerated below:

The analysis of the constructive variants for the flywheel of figures 6, 7, 8 and 9 is presented further on.

The example above represents an analysis on the influence of the semi-product on the constructive form and functional characteristics of the part.

By analyzing the welded variants based on the criterion UNDER WHAT CONDITIONS IS IT ACHIEVED? valid conclusions follow also for other parts made from such semi-products:

The welded semi-products are usually obtained by welding simple parts made from rolled semi-products. In order to ensure a good weldability, steels with reduced contents of carbon are used for welded constructions, like OL 37 (C = 0.15 – 0.22%); even if the additive material has an identical composition to the one of the base material, these semi-products cannot be hardened or hardened-annealed in order to achieve the imposed wear resistance, only subsequent to cementing the surfaces that require a higher hardness.

The welding seams need to be protected during cementing in order to avoid the occurrence of cracks during and after heat treatment. The solution of heat treating constructions welded from low carbon steels is not applicable due to the required large number of technological conditions.

On the other hand, any welded construction is subjected to a relaxation heat treatment in order to eliminate the welding stress and to ensure stability of form. Using for the simple welded parts rolled semi-products of hardening-annealing high carbon steels like OLC 45, 25MoC11 does not ensure a good weldability.

These steels allow for superficial hardening-annealing or hardening by high frequency currents or oxy-acetylene flame. This is not a correct solution as the mechanical strength of the part is not ensured by classical welding procedures.

Using a rolled semi-product of OLC 45 for disks and of OL 37 for the ribs does not ensure a strong joining as the steels have different carbon contents (OLC 45 has 0,45% C, and OL 37 has 0.15-0.22% C). Such solutions need to be completely avoided as cracks occur in the welding seam due to welding stress. The imposed characteristics are not ensured for the studied part. In order to avoid obtaining a fragile welding seam by rapid cooling particularly when rolled semi-products with large differences of cross-sections and different carbon contents are used, a pre-heating of the part to 200-300^{o}C is required, while the cooling needs to take place slowly, in the furnace or by wrapping the part in asbestos. The pre-heating is successfully applied in all described cases. Finally it can be argued that the „welded construction" variant is not one to ensure all imposed characteristics. Dimensional precision is obtained in any welded construction by machining the functional surfaces, but never prior to welding, as at times it is wrongly done. Prior to welding only the contour of the simple parts is machined if they have been cut with oxy-acetylene flame, as well as their joining surfaces. A series of mechanical machining operations are eliminated by mechanical cutting. From the viewpoint of achieving the assembly of the flywheel, the welded variant is technological, as the welding ribs are not positioned with a hidden welding. Further analyzing the variants by the FROM WHAT IS THE PART MADE? criterion, the following can be established:

Flywheel can be achieved only from a semi-product cast of OT 45 or OT 55. In this semi-product casting defects appear observable after machining, and can be eliminated by welding followed again by machining.

The constructive variant of figure 9 obtained from a cast semi-product ensures the best functional characteristics, if the technical conditions for heat treatment are provided. It has, however, the disadvantage that it allows only one solution for reconditioning: build-up welding and re-machining to the initial functional dimensions.

10. Comparison of the variants

Table 5 presents the denoting according to 9 assessment criteria of the analyzed constructive variants of a flywheel. The cost variant of figure 9 has obtained the highest score, and will thus be selected as the constructive solution within the assembly of the jaw crusher.

The cost of the final variant of figure 9 presented in table 6 (step 2 of the Value Analysis – VA – study) is of 1120 monetary units and has a weighting of 15.79% of the final cost as compared to the initial situation of 1320 monetary units with a weighting of 17.72%, for function F7 presented in table 3 (step 1 of the VA study).

Table 5. *Synthetic table with the analyzed constructive variants*

No.	Analysis criteria	Figures			
		6	**7**	**8**	**9**
		welded 5 modules	**welded 3 modules**	**screw assembled**	**cast**
	variant	initial			final
1	Functional characteristics	4	4	4	4
2	Semi-product	1	2	3	4
3	Mechanical machining	1	2	3	1
4	Mounting	4	4	4	4
5	Repair	4	4	4	4
6	Rigidity	3	3	2	4
7	Ergonomics	2	2	2	4
8	Aesthetics	3	3	3	4
9	Cost	1	2	3	4
	TOTAL	23	26	28	**33**

Table 6. *Cost distribution on functions (partial) (*Y coordinate, ** monetary units).*

No.	Parts	Functions							Cost/ part**
		F_1	F_2	F_3	F_4	F_5	F_6	F_7	
7	Flywheel	*300*				*20*	*250*	*550*	*1120*
...									
n		800	600	200	800	300	1600	600	4900
Total cost			1950	825	460	1600	350	2010	1350
Ratio		0.2282	0.0965	0.0538	0.1872	0.041	0.2352	0.158	1
Cost of functions %		**22.82**	**9.65**	**5.38**	**18.72**	**4.09**	**23.523**	**15.79**	**100**

The final situation – step 2 of the VA study

By introducing the new data into table 7 the four diagrams of figures 10, 11, 12 and 13 are plotted.

These diagrams will be compared to those of figures 2, 3, 4 and 5.

Table 7. *Computational elements for plotting the diagrams.* $S' = 2 * a *(X_i)^2 - 2 * X_i * Y_i$*

No.	Computational elements	Functions							Total value
		F_1	**F_2**	**F_3**	**F_4**	**F_5**	**F_6**	**F_7**	
1	X_i	**25**	**10.71**	**7.149**	**17.85**	**3.57**	**21.42**	**14.28**	100
2	Y_i	**22.82**	**9.65**	**5.38**	**18.72**	**4.09**	**23.52**	**15.79**	99.97
3	$(X_i)^2$	625	114.8	51.02	318.88	12.755	459.18	204.08	1785.7
4	$X_i * Y_i$	570.5	103.39	38.429	334.29	14.607	504	225.57	1790.8
5	$(Y_i - a*X_i)^2$	5.067	1.1984	3.1796	0.6596	0.2585	4.1232	2.1425	16.629
6	S' *	112.55	23.458	25.473	-29.01	-3.632	-87.02	-41.82	7E-13

The parameters have the following computed values: a = 1.028, α = 45.081 ^{o}, S = 16.62, S' = 0.

It can be noticed that S and S' have smaller values than in the initial variant.

Table 7 provides the necessary values for the plotting of the following types of diagrams:

1) The diagram of the value weighting of the functions (figure 10). This diagram has not changed, as the value of the system and of the functions has remained the same.

2) The Diagram of the cost weighting functions (figure 11). The diagram of figure 11 presents the functional costs of the new variant, step 2.

3) The diagram of the cost weightings of the functions, in step 1 and step 2 (figure 12). Figure 12 presents comparatively the old variant, step 1 and the new one, step 2.

4) The diagram of the comparison of value weighting (x---) and functional costs (y- - -) (figure 13).

Only the costs are represented in order not to overload the diagram and to observe the decrease of the value of cost of function F7, from 17.72 %, in the first step of VA study to 15.79 % in the second step of VA study, decrease by 10.89 %.

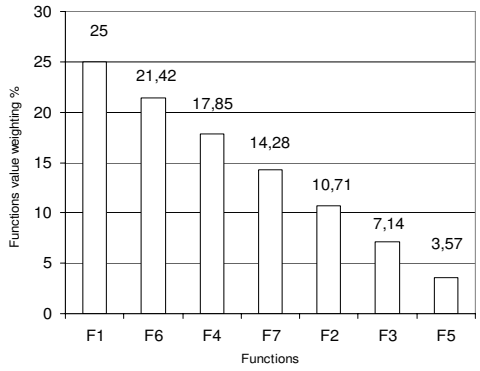

***Fig. 10**. Diagram of the value weighting of the functions.*

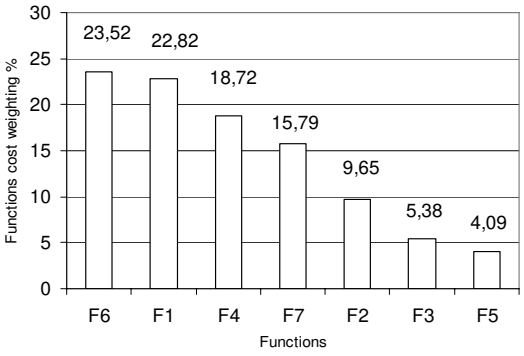

***Fig. 11**. Diagram of the cost weighting functions.*

The economic dimension or the cost of the function represents the main criterion for the critical evaluation of functions.

These evaluations aim at identifying those functions, the too costly technical solutions whose achievement affects the total manufacturing cost of the analyzed product. A correctly completed critical evaluation will directly lead to the identification of what can be called the deficient functions of the analyzed product, that is of those functions that include useless costs.

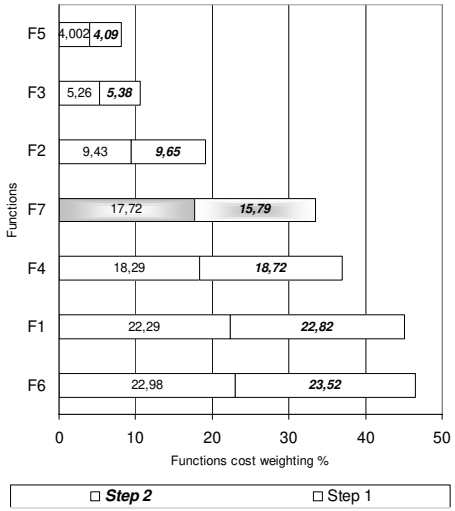

***Fig. 12.** The diagram of the cost weightings of the functions, in step 1 and step 2.*

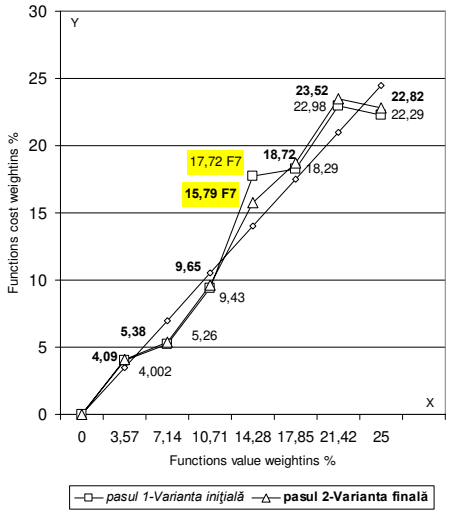

***Fig. 13**. Value and cost weightings of the functions, in step 1 and step 2.*

The deficient functions from the economic viewpoint appear as:

- very expensive functions in relation to the others,

- too expensive functions in relation to the existing technical possibilities of achievement.

Evaluation based on the criterion of economic dimension can be achieved in several ways, presented below:

1) comparison of costs per function, by means of the diagram presented in figure 12,
   This diagram allows for the comparisons of:
   - the costs of the functions and comparisons of the total cost and the cost of each function,
   - work and material costs, highlighting the very expensive costs, with the highest weighting in the total cost of the product,
   - functions whose achievement requires disproportionate costs, of either work or material,
2) comparison between the functions of other products,
   Other products refer to:
   - products of the same typo-dimensional range or family, manufactured by that company,
   - products similar to the analyzed one, manufactured by other companies,
   - products with other destinations, but having some functions similar to those of the analyzed product.
3) Theoretical evaluation of the costs of the function.

11. Conclusion

In the two steps of the Value Analysis study, one component of jaw crusher, the flywheel which contributes to the function F7 (ensures uniformity of the movement) was redesigned and optimized:

1 – from the engineering viewpoint, the variant of flywheel of figure 6 which consists of five welded modules, one complicated part (many components, mechanical machining, turning of metal parts complicated, long and very expensive, etc.) and the variant of figure 9 consists of cast semi-product (one component, mechanical machining, turning of metal parts, simple, short and less expensive than the flywheel of figure 6, etc.)

2 – from the economic viewpoint: the cost of function F7 (figure 13) decreases from 17.72 %, in the first step of the Value Analysis study to 15.79 % in the second step of the Value Analysis study (decrease by 10.89 %).

3 – in the third step of the Value Analysis study are analyzed the functions F6 above the regression straight line and their costs reduced (figure 14); the cost of function F6 (figure 14) decreases from 22.98%, in the second step of the Value Analysis study to 21.69 % in the third step of the Value Analysis study (decrease with 5.61 %).

Then the regression line is re-plotted and the functions relocated above it are noted; these functions too are analyzed with the view of reducing their costs, followed by the re-plotting of the regression line, etc.

The cost of function F7 (figure 14) increases from 15.79 %, in the second step of the Value Analysis study to 16.17 % in the third step of the Value Analysis study (increase with 2.89 %), but with the decrease in the second step results a final increase with 8%.

At the end of the Value Analysis study, the points are aligned as perfectly as possible along the straight line y = a * x, with a tilt of 45^o, this is the optimal situation, the values weighting of functions and the functions cost weighting are equal.

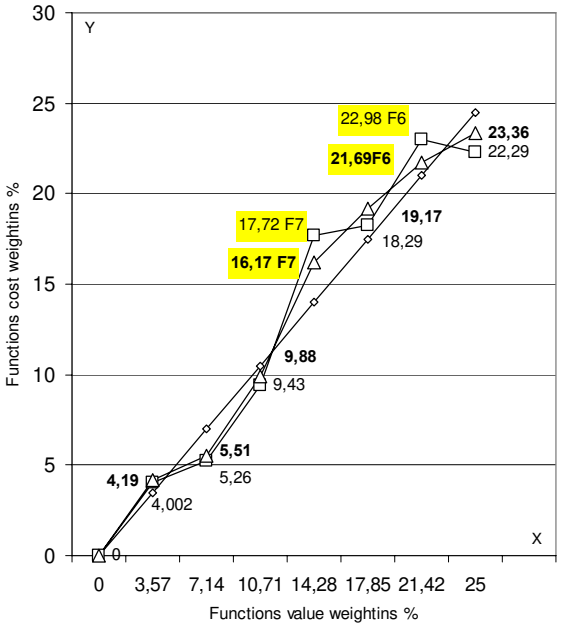

***Fig. 14**. Value and cost weightings of the functions, in step 1, step 2 and step 3.*

References

[1]. Chichernea Fl. - *Analiza Valorii*, Editura Universităţii Transilvania din Braşov, 2002

[2]. Bejan V. - *Tehnologia fabricării şi a reparării utilajelor tehnologice, vol.I şi vol.II*, Oficiul de Informare Documentară pentru Industria Construcţiilor de Maşini, Bucureşti, 1991

[3]. Chichernea Fl. - *Analiza valorii,* Editura Universităţii Transilvania Braşov, 2007

[4]. Chichernea Fl. - *Analiza valorii*, Universitatea Transilvania Braşov, sept., 2007, suport electronic CD;

[5]. Chichernea Fl. - *Analiza Valorii. Partea I*, Bramat 2007, Proceedings-International Conference on Materials Science and Engineering, Braşov, România, 22-24.feb.2007, vol.I

[6]. Chichernea Fl. - *Analiza Valorii – diagrame FAST. Partea IV*, Revista Metalurgia, nr.5, 2005, pg.30

[7]. Chichernea Fl. - *Analiza valorii în industrie*, Editura Universităţii Transilvania Braşov, 2008, CD

[8]. Chichernea Fl. - *Aplicaţiile Analiza valorii în industrie*, Editura Universităţii Transilvania Braşov, 2008

[9]. Chichernea Fl. - *Value Analysis, parth II*, Rev.Metalurgia International nr.3, 2009, pg. 5
[10]. Chichernea Fl. - Chichernea Al., *Analiza Valorii, Partea II*, Rev. Metalurgia nr.2, 2009, pg. 31
[11]. Chichernea Fl. - Chichernea Al., *Analiza Valorii, Partea III*, Rev. Metalurgia nr.3, 2009, pg. 36
[12]. Chichernea Fl. - Chichernea Al., *Managementul valorii un proces iterativ în proiectare, Partea I*, Revista de turnătorie, nr. 3 – 4 / 2009, pg.17
[13]. Chichernea Fl. - Chichernea Al., *The iterative process of value Analysis – Parth I* – The seventh international Congress in materials Science and Engineering, Iaşi, May 28 th – 31st, 2009, section 2 – Modern Technologies and Equipment in Material Science, pg.59, in Buletinul Institutului Politehnic din Iaşi, Tomul LV (LIX), fasc.2, 2009, Secţia Ştiinţa şi Ingineria Materialelor
[14]. Chichernea Fl. - Chichernea Al., *The iterative process of value Analysis – Parth II* – The seventh international Congress in materials Science and Engineering, Iaşi, May 28 th – 31st, 2009, section 2 – Modern Technologies and Equipment in Material Science, pg.67, in Buletinul Institutului Politehnic din Iaşi, Tomul LV (LIX), fasc.2, 2009, Secţia Ştiinţa şi Ingineria Materialelor.

THE ANNALS OF "DUNAREA DE JOS" UNIVERSITY OF GALATI.
FASCICLE IX. METALLURGY AND MATERIALS SCIENCE
N^0. 2 – 2009, ISSN 1453 – 083X

VARIATION OF MECHANICAL CHARACTERISTICS FOR THIN WALL TUBES PROCESSED IN ULTRASONIC FIELD

Mihai SUSAN[1], Dragoş Cristian ACHIŢEI[1], Roxana Gabriela ŞTEFANICĂ[1], Bogdan Lucian GAVRILĂ[1]
[1]Gheorghe Asachi Technical University of Iaşi, Faculty of Material Science and Engineering
[2]Institutul de Fizică Aplicată din Chişinău, Republica Moldova
email: mihaisusan@yahoo.com

ABSTRACT

The paper presents the variation of mechanical characteristics of resistance and plasticity for thin wall tubes made of stainless steel 10TiNiCr180, processed in ultrasonic field. Decrease of mechanical characteristics of resistance and increase of plasticity ones in tubes processing in ultrasonic field, with respect to classic technology, are made on account of cold hardening reduction, implicitly metal-tool contact friction. Tubes processing is made through drawing without inner guidance/to empty, using convergent conic dies made of metallic carbides.

KEYWORDS: thin walls tubes, stainless steel, ultrasonic field, cold hardening, convergent conic dies, mechanical characteristics.

1. Introduction

The paper discusses the influence of the relative drawing speed expressed as the ratio $v_{tr}/\bar{v}_v$ (v_{tr} is the drawing speed and $\bar{v}_v$ is the vibration speed of the die) on the resistance and plasticity mechanical characteristics and on the safety of drawing in processing tubes with ultrasonic vibrations applied to the auger die on drawing direction "ultrasonic vibration drawing - UVD" or UVD system [1, 3].

The experiments are made on 10TiNiCr180 / AISI321 stainless steel tubes through drawing without interior guide.

The principle scheme of the processing tubes installation in UVD system/UVD technology is presented in figure 1.

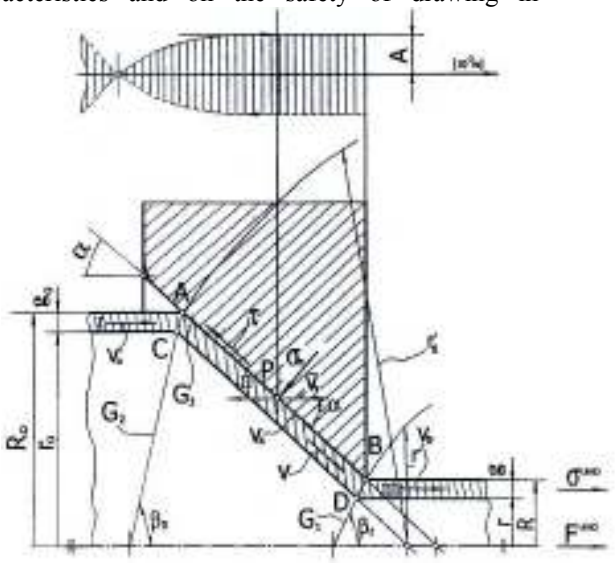

1 - semi-finished tube; 2 - die;
3 - processed tube: g_0 and g - wall thickness-semi-finished and processed tube; v_0 - speed of semi-finished tube; v_{tr} - drawing speed; v_a - slipping speed of the metal; v - speed of the semi-finished tube in deformation zone;
τ - tangential shearing stress;
σ_n - normal stress in a certain point at metal-tool contact; P - certain point at metal-tool interface; α - half angle of the die opening.

***Fig. 1.** The scheme of ultrasonic drawing of the tubes in UVD system.*

The scheme of ultrasonic drawing of the tubes in UVD system is presented in figure 1.

In UVD system processing tubes, with the die situated in the maximum of waves oscillations and activated on drawing direction, produces in the deformation focus the reduction of metal-tool contact friction, respectively cold hardening, with direct influence on mechanical characteristics and on the safety of drawing. The reduction of metal-tool contact friction, respectively cold hardening, in UVD system processing tubes is explained on the basis of "the reverse mechanism of the intermediate friction force" [1].

In order that the oscillated system should not get out of resonance in the die activation (located in the maximum of oscillation waves and activated on drawing direction) are used reflectors of ultrasonic energy.

The role of the ultrasonic energy reflectors is to permit the making of a stable system of stationary waves in the semi-finished and processed tube.

The positioning of ultrasonic energy reflectors is realized at well defined distances-resulted on the basis of the making mechanism of a stable system of stationary waves in the tube. The peculiarities of plastic deformation of the metal in UVD system of processing tube, unto CT classical technology, consist in the reduction of metal-tool contact friction determined by the mechanics of plastic deformation – fractioned deformation or in impulses at a complete oscillation period (considering Coulomb type friction).

The variation movement of waves (u), of vibration speed of the die (v_v) and drawing speed at a complete oscillation period (T) is presented in figure 2.

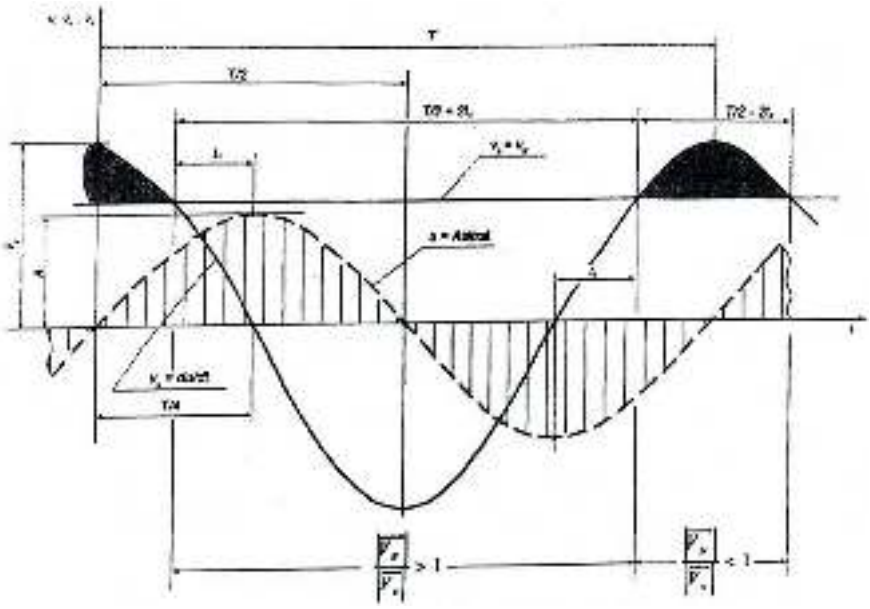

Fig. 2. *The variation movement of the waves (u), the vibration speed of the die (v_v) and drawing speed (v_{tr}) at a complete oscillation period (T.)*

2. The mechanics of plastic deformation

It is observed from figures 2 and 3 that a P point arbitrarily chosen to the metal-tool interface participates in two movements: advance on the generator of plastic deformation tool cone with v_a speed and vibration movement with v_v speed. The vector of the friction force ($\overrightarrow{F_f}$) in the case of classical technology CT opposes to movement direction of the metal ($\overrightarrow{v_a}$) and in the case of UVD technology opposes to the direction of the resultant vector – the composition between $\overrightarrow{v_v}$ and $\overrightarrow{v_a}$. Practically, in UVD system, at a complete oscillation period (T), the deformation of the metal is realized in fractions or in impulses.

Thus during T/2 + 2 t_1, when $\left|\overrightarrow{v_{tr}}/\overrightarrow{v_v}\right|>1$, is produced the proper deformation of the metal and during T/2 - 2 t_1, when $\left|\overrightarrow{v_{tr}}/\overrightarrow{v_v}\right|<1$ takes place at the most elastic deformation.

In classic technology-CT, friction coefficient (μ) is determined with the relation [5]:

$$\mu^{CT}=\frac{\tau}{\sigma_n} \qquad (1)$$

In UVD technology, friction coefficient (μ^{UVD}) is smaller than in classic technology CT with the term which includes the influence of ultrasonic activation of the die, justified by $4t_1/T$ noted with ξ.

Under these conditions, the size of the coefficient (μ^{UVD}) has the expression:

$$\mu^{UVD} = \frac{\tau}{\sigma_n} - \frac{4t_1}{T}\cdot\frac{\tau}{\sigma_n} = \mu^{CT}\left(1-\frac{4t_1}{T}\right) \quad (2)$$

Or $\mu^{UVD} = \mu^{CT}(1-\xi)$, with $0 \le \xi \le 1$.

Considering the movement of the ultrasonic waves after movement law u=Asinωt; the vibration speed is determined as the movement time derivative:

$$v_v = \frac{du}{dt} = A\omega\cos\omega t \quad (3)$$

The maximum value of vibration speed of the die ($\vec{v}_v$) gets under the condition cosωt=1 meaning:

$$\vec{v}_v = \omega \cdot A = 2\pi f \cdot A \quad (4)$$

For small angles of dies opening (α) / $\alpha \le 120^\circ$ - it can be considered $v_a \approx v_{tr}$ because cos α →1.

Equalizing the two speeds $v_{tr}=v_v$ results t_1 with the expression: $t_1 = \frac{1}{\omega}\arccos\frac{v_{tr}}{v_v}$.

Taking into consideration the determined expression for t_1 and the factor of effective influence of the ultrasonic oscillations on the metal-tool contact friction (ξ) it results the expression for μ^{UVD}:

$$\mu^{UVD} = \mu^{CT}\left(1-\frac{2}{\pi}\arccos\frac{v_{tr}}{\bar{v}_v}\right),$$

with

$$v_{tr}/\bar{v}_v \le 1{,}0 \quad (5)$$

It is noticed from the last relation that relative drawing speed or the ratio $v_{tr}/\bar{v}_v$ has direct influence on the size of friction coefficient in UVD system processing tubes (μ^{UVD}) and implicitly on the drawing force (F^{UVD}).

It can be concluded that plastic deformation in tubes drawing in UVD system is accomplished fractionatedly or in impulses: the proper plastic deformation during T/2 + 2 t_1 at a complete oscillation period (T), and without plastic deformation-at the most elastic deformation during T/2 - 2 t_1.

3. Experiments and obtained results

The experiments are made on tube samples of stainless steel 10TiNiCr180 / AISI 321 having the dimensions: D_0=4,85 mm, g_0=0,70 mm, the length is 1500 mm with one polished end and solution heat treated. It is used a classical drawing machine – drawn from coil in coil which develops a drawing force of $15\cdot10^4$ [N].

The scheme of the oscillated system used in experiments is presented in figure 4.

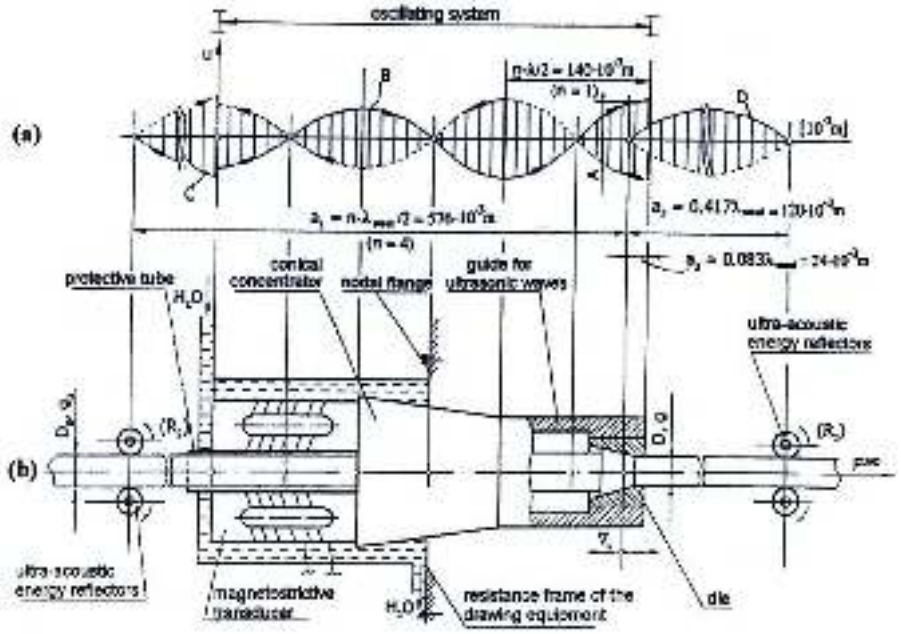

Fig. 3. *The scheme of the oscillated system used in experiments: a) the oscillation of the waves; b) the proper scheme: — progressive wave, ----regressive wave.*

It is used for experiments the ultrasounds generator GUS P-1000 with magnetostriction transducer, with actual output of 1000 W and resonance frequency of 17500 Hz, [3]. In order to

succeed in processing the tubes in UVD system are used ultrasonic power reflectors/ presser rolls (R_1) and (R_2) located at the distances a_2 respectively a_1 resulted on the basis of the making mechanism in the processed and semi-finished tube of a stable system of stationary waves (λ is wave length: λ=c/f, where c is the propagation speed of ultrasounds and f is resonance frequency). For processing the tubes are used conical convergent dies with WCr core, with the angle $\alpha=8^0$, the opening of the die. The experiments are made with constant drawing speed (v_{tr} = 0,33 m/s) and five values of the oscillation amplitudes of the die, A = 5, 10, 15, 20, 25 μm, meaning (based on relation (4) different values of the vibration speed ($\vec{v_v}$): 0.55; 1.09; 1.65; 2,20 and 2.74 m/s. The section reduction of the processed tube r, %=ct, is 23% (D = 4.32 mm and g = 0.65 mm).

The processing of tube samples, UVD and CT technologies, is realized through singular drawing on five sets of samples A, B, C, D and E, selected according on the value of the relative drawing speed ($v_{tr}/\bar{v}_v$).

Drawing force F^{CT} and F^{UVD}, the mean of five determinations, corresponding to sample sets A…E, is determined experimentally with the help of force pick-ups (DT106000) using the tensometer bridge type N2314. Also, experimentally, it is measured the drawing speed (v_{tr}) and the amplitude of the oscillation (A). In order to evaluate the resistance and plasticity mechanical characteristics, in accordance with SR-EN 10002-1/95 norms, is used the tension test machine type MTS 81024. The recorded results, through traction test, for Rm, $Rp_{0,2}$ and A5 also represent the average of the five determinations. The safety coefficient of the drawing is determined with relation: C = 100[(S·Rm/F)], % - where S is the plan area for the processed tube, Rm – the average fracture strength and F – drawing force (F^{CT} respectively F^{UVD}). The obtained experimental results are synthetically presented in table 1.

Table 1. *Obtained experimental results*

Samples	Technological parameters			Safety coefficient		Mechanical characteristics					
	$\frac{V_{tr}}{-}$ / V_v	F^{CT}	F^{UVD}	C^{CT}	C^{UVD}	CT	CT	CT	UVD	UVD	UVD
						$Rp_{0,2}$	Rm	A_5	$Rp_{0,2}$	Rm	A_5
		[N]		[%]		[MPa]					
A	0.6	812	676	4.89	5.62	352	532	32.2	349	509	33.2
B	0.3	812	637	4.89	5.83	352	532	32.2	348	498	33.6
C	0.2	812	597	4.89	6.10	352	532	32.2	343	488	34.0
D	0.15	812	574	4.89	6.22	352	532	32.2	335	478	34.5
E	0.12	812	545	4.89	6.29	352	532	32.2	328	459	35.4

The percentage relative reductions ΔF, ΔC, $\Delta Rp_{0,2}$, ΔR_m and ΔA_5 are calculated with the next relations [1]: $\Delta F = \frac{F^{CT} - F^{UVD}}{F^{CT}} \cdot 100[\%]$

$$\Delta C = \frac{C^{UVD} - C^{CT}}{C^{UVD}} \cdot 100[\%]$$

$$\Delta Rp_{0,2} = \frac{Rp_{0,2}{}^{CT} - Rp_{0,2}{}^{UVD}}{Rp_{0,2}{}^{CT}} \cdot 100[\%]$$

$$\Delta Rm = \frac{Rm^{CT} - Rm^{UVD}}{Rm^{CT}} \cdot 100[\%]$$

$$\Delta A_5 = \frac{A_5{}^{UVD} - A_5{}^{CT}}{A_5{}^{UVD}} \cdot 100[\%] \quad (6)$$

The calculated relative reductions are synthetically presented in table 2.

Table 2*. The calculated relative reductions.*

Samples	v_{tr}/v_v	ΔF	ΔC	$\Delta Rp_{0,2}$	ΔR_m	ΔA_5
		[%]				
A	0.60	16.74	12.98	0.85	4.32	3.01
B	0.30	21.55	16.12	1.13	6.39	4.16
C	0.20	26.47	19.83	2.55	8.27	5.29
D	0.15	29.31	21.38	4.83	10.15	6.66
E	0.12	32.88	22.25	6.81	13.72	9.03

In figure 4 is presented the variation of percentage relative reductions ΔF, ΔC, $\Delta Rp_{0,2}$, ΔR_m and ΔA_5 which represent, in fact, the efficiency of the new technology, the drawing of the tubes in UVD tubes with respect to classic technology CT.

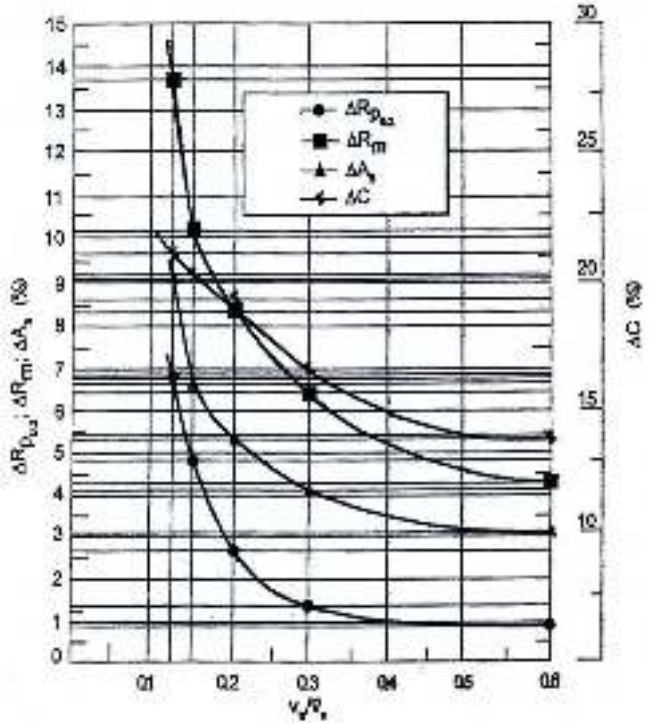

Fig.4. *Variation of the relative reductions of the field stress ($\Delta R_{p0.2}$), tensile strength (ΔR_m) and the ultimate strain (ΔA_5) and relative increase of the safety coefficient of drawing (ΔC) as a function of the drawing rate (v_{tr}/v_v) at 10TiNiCr180 (AISI 321) austenitic stainless steel tubes processing.*

It is noticed a decrease of resistance mechanical characteristics by keeping a plasticity reserve for smaller values of relative drawing speed ($v_{tr}/\bar{v}_v$) by increasing the safety of drawing. These direct influences of the relative drawing speed on the resistance and plasticity mechanical characteristics and on the safety drawing coefficient are determined by the reduction of metal-tool contact friction, respectively cold hardening, due to the fractioned or in impulses deformation of the metal. The size of the reduction of metal-tool contact friction can be the value of friction coefficient (μ^{UVD}) which can be calculated with relation (5). The new technology of processing the tubes in UVD system presents practical interest when $v_{tr}/\bar{v}_v$ <<1,0. The $v_{tr}/\bar{v}_v$ ratio also presents practical importance because v_{tr} defines the technological productivity and v_v permits the election of the process installation and transfer of ultrasonic power in the basis of relation (4).

4. Conclusions

The paper emphasizes the influence of relative drawing speed or $v_{tr}/\bar{v}_v$ ratio in processing the tubes without interior guide with direct influence on the resistance (R_m and $R_{p0,2}$) and plasticity (A_5) mechanical characteristics and on the safety of drawing (C).

The experiments are made on tube samples of 10TiNiCr180 / AISI 321 stainless steel.

References

[1]. Susan, M., *Tragerea metalelor cu vibratii ultrasonice*. Editura CERMI, Iasi, 2007.
[2]. Cazimirovici, E., s.a., *Teoria si tehnologia deformarii prin tragere*, Editura Tehnica, Bucuresti, 1990.
[3]. Contract CEEX 293/2006.

THE ANNALS OF "DUNAREA DE JOS" UNIVERSITY OF GALATI.
FASCICLE IX. METALLURGY AND MATERIALS SCIENCE
N^0. 2 – 2009, ISSN 1453 – 083X

THE MECHANISM OF PHASE TRANSFORMATION TO OBTAIN ZINC-IRON COATINGS

Tamara RADU, Simion BALINT, Olga MITOŞERIU
"Dunărea de Jos" University of Galaţi, Romania
email: tradu@ugal.ro

ABSTRACT

Important changes in the ratio of constitutive phases take place during heating of galvanized parts due to Zn coating layer changed into Zn-Fe alloy. The work deals with a mathematical correlation between diffusion phenomena occurring in layer, depending on temperature and time of heat treatment, and iron content of coating. Both terms define a certain structure.

KEYWORDS: coating layer, interphase surface, heat treatment.

1. Introduction

Various coating procedures, based on zinc, oriented to physico - chemical and mechanical characteristics improvement, have emerged lately.

Zn-Fe alloy protective coatings are considered among favorites due to their high weldability, resistance to corrosion, excellent varnishability, lower specific weight of layer, and thus of the whole product, resulting in zinc saving. Zinc alloying with iron is put into operation using diffusion procedures during heating of galvanized products.

2. Experimental conditions

Galvanized steel samples, with chemical composition: 0.05 % C, 0.26 % Mn; 0.02 % Si; 0.012 % P; 0.015 %S; 0.039 % Al and zinc layer specific weight of 108 g/m^2 were heated for 1÷30 minutes at 500÷650 ^{o}C. Heat treated samples were metallographically examined and X - ray diffraction tested with a view to establish structural and chemical composition change due to heat treatment [1].

3. Results and conclusions

As a result of microscopic examination (fig.1) and X-ray diffraction testing (fig. 2) in coating layer were detected phase ratio changes, according to heat treatment parameters. Considering that the physico-chemical and mechanical properties differ for the two phases and phase ratio, the properties of the product are to be decided; these structural changes are of great importance in practice. The desirable coating would be a Zn-Fe coating with 8÷10 % Fe (according to some authors, up to 12% Fe [2]), with a structure consisting mainly of δ_1 phase and a small quantity of Γ phase. Therefore it is necessary an accurate mathematical correlation between layer phenomena, depending on heat treatment parameters and iron content of coating, both defining a certain structure. It was found that structural changes, due to rise temperature occur in three distinct stages:

a). η phase disappearance and ξ phase growth (500-530 ^{0}C)

b). ξ phase gradual disappearance and δ_1 phase growth (530 - 600 ^{0}C).

c). the rapid growths Γ phase (600 – 650 ^{0}C).

The formula and Fe content (wt %) of these Zn-Fe intermetallic phases are given in Table 1.

***Table 1**. Characteristics of Zn-Fe intermetallic phases*

Phase	Formula	Fe content (wt %)
η	Zn	0.003 (c_6)
ζ	FeZn13	6.2-6.0 (c_4-c_5)
δ	FeZn10; Fe_3Zn_7	11.5-7.0 (c_2-c_3)
Γ	Fe5Zn21;Fe3Zn10	20.5-28.0 (c_0-c_1)

These changes include transformations characteristic to a reactive diffusion process. In this type of diffusion, the rate depends on reaction constant ratio, resulting three possible processes [3].

In the case specified (at stage a), under 550 ^{0}C, when the diffusion of iron atoms is negligible, the process is considered as diffusion process.

Stage b) at 550÷600 ^{0}C, when the mobility of iron atoms is rising is considered as intermediate

process. Stage c) at 600÷650^{o}C is considered a kinetic process, emphasized by the rapid growth of Γ phase.

The transformations occurring in the stage a) may be considered as reactions at interphase surface level.

Let: x_1, x_2, x_3 – instantaneous points of Γ/δ, δ/ξ, ξ/η interfaces able to change their position with v_1, v_2, v_3 rates and J_I – the iron quantity related to the moving interface and representing the iron given by i phase to i+1 phase (where i =1; 2; 3). Phase growing ratio is calculated using the relations:

$$\frac{d\Gamma}{dt} = v_1; \quad (1)$$

$$\frac{d\delta}{dt} = v_2 - v_1; \quad (2)$$

$$\frac{d\xi}{dt} = v_3 - v_2; \quad (3)$$

The content of iron at interface boundaries (c_0 to c_6 in table 1) was considered according to the Fe-Zn equilibrium diagram [4], showing its constant maintaining up to 550^{o}C.

Considering J_0 as the total quantity of iron related to the interfaces in the underlayers of coating (fig.3), the law of iron conservation [5] results in the following:

$$J_0 - J_1 = \frac{d\Gamma}{dt} \cdot \frac{c_0 + c_1}{2} = 0.242\frac{d\Gamma}{dt}; \quad (4)$$

$$J_1 - J_2 = \frac{d\delta}{dt} \cdot \frac{c_2 + c_3}{2} = 0.092\frac{d\delta}{dt}; \quad (5)$$

$$J_2 - J_3 = \frac{d\xi}{dt} \cdot \frac{c_4 + c_5}{2} = 0.061\frac{d\xi}{dt}; \quad (6)$$

Total input quantity of iron is in balance with the size of phase growth (local diffusion of iron atoms is moving at the same rate as interface 3), therefore:

$$J_0 = 0.242\frac{d\Gamma}{dt} + 0.092\frac{d\delta}{dt} + 0.061\frac{d\xi}{dt}; \quad (7)$$

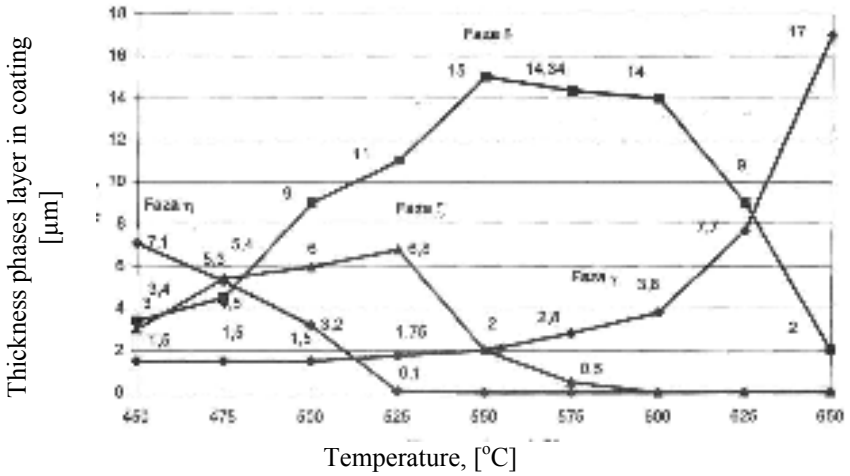

Fig. 1. *Dimensions of the phase layers depending on the heat treatment temperature*

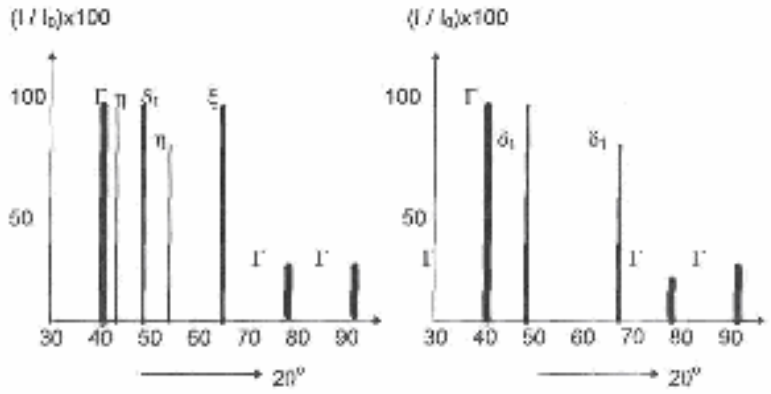

a) 500^{0}C – 4.23% Fe b) 550^{0}C – 8.10% Fe

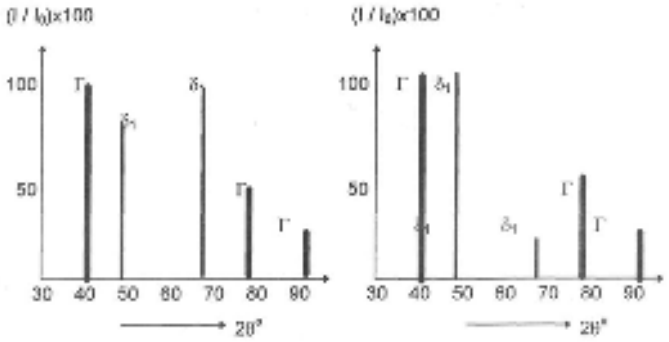

a) 600^{0}C – 13.98% Fe b) 650^{0}C – 18.21% Fe

***Fig. 2**. Results of the diffractometric analysis on samples treated at various temperatures*

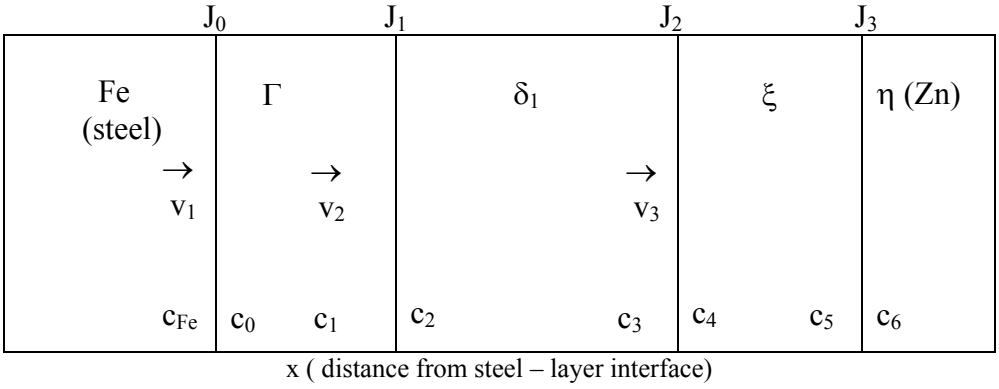

***Fig. 3.** Coating layer diagram in kinetic process modeling.*

The quantity of iron on various interfaces is related to the difference of chemical potential of iron through the chemical constant K_i (i=0; 1; 2; 3)

$$J_i = K_i(\mu^a_{Fe} - \mu^b_{Fe}); \quad (8)$$

where: $K_{i(T)} = K_i e^{\frac{-Q_{ai}}{RT}}$;

where μ^a_{Fe} = chemical potential of iron at interface left side; μ^b_{Fe} = chemical potential of iron at interface right side; Q_{ai} = interface activating energy.

The chemical potential of iron can be approximated with its concentration, resulting J_0, J_1, J_2, J_3 using relation (8)

$J_0 = K_0(c_{Fe}-c_0) = 0.72K_0$ (9)
$J_1 = K_1(c_1-c_2) = 0.09K_1$ (10)
$J_2 = K_2(c_3-c_4) = 0.01K_2$ (11)
$J_3 = K_3(c_5-c_6) = 0.06K_3$ (12)

Replacing these values in relations (4),(5),(6) are obtained:

$$\left(\frac{d\Gamma}{dt}\right)_a = 2{,}975K_0 - 0{,}372K_1; \quad (13)$$

$$\left(\frac{d\delta}{dt}\right)_a = 0.978K_1 - 0.109K_2; \quad (14)$$

$$\left(\frac{d\xi}{dt}\right)_a = 0.164K_2 - 0{,}984K_3; \quad (15)$$

Considering the relations (1), (2), (3) are obtained:

$v_1 = 2.975K_0$-$0.372K_1$ (16)
$v_2 = 2.975K_0$-$0.606K_1$-$0.109K_2$ (17)
$v_3 = 2.975K_{0+}0.606K_1$=$0.055K_2$-$0.98K_3$ (18)

In stage b) $\left(\frac{d\Gamma}{dt}\right)_a = \left(\frac{d\Gamma}{dt}\right)_b$, ξ phase is rapidly eliminated in favor of δ_1 phase, as a consequence of its showing at the surface, and with no effect concerning Γ phase growth. Thus, ξ phase plays the role previously by η phase. It cannot dissolve more iron than the equilibrium amount and it changes into δ_1 phase ($J_2 = 0$). In stage c), temperature rising over 600^{o}C leads to an increasement of iron diffusion coefficient and Γ phase is rapidly growing until complete disappearance of δ phase ($J_1 = 0$) and:

$$\left(\frac{d\Gamma}{dt}\right)_c = -\left(\frac{d\delta}{dt}\right)_b; \quad (19)$$

Computation of the experimental data concerning heat treatment influence on iron content of layer results in various relations reflecting diffusion

process operation. At 550^{o}C (fig.4), the diffusion process is carried out as intermediate process – stage b, respectively.

The function is:

$$y = a\left(1 - e^{-bx}\right); \quad (20)$$

where: r = 0.989185
y = % Fe
x = heat treatment period (s)

a = 8.3322985
b = 0.42589374

At 600 ^{0}C (fig.5), the process is carried out as kinetic process – stage c, respectively. The function is:

$$y = \frac{ax}{b + x}; \quad (21)$$

where: r = 0.9568720
y = %Fe
x = heat treatment period (s)
a = 15·110744
b = 0.23708356

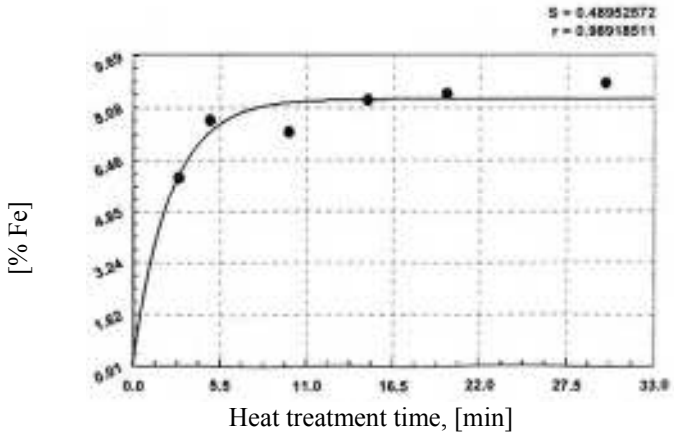

Fig. 4. *Diagram of iron content variation as function of heat treatment time at 550 ^{0}C.*

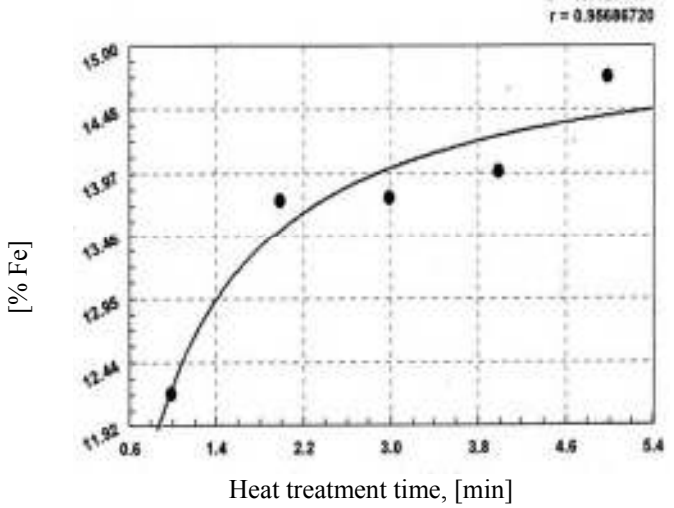

Fig.5*. Diagram of iron content as function of heat treatment time at 600 ^{0}C.*

References

[1]. T, Radu, A Ciocan, L. Balint, O. Mitoseriu - *"Surface protection of the Steel Sheet with Zn-Fe Alloys*", Materials 2009 Lisabona

[2]. A. R. Marder - *Progress in Materials Science,* 45, 191-271, 2000.

[3]. F.Oprea - "*Teoria proceselor metalurgice*", Ed. Didactică şi pedagogică, Bucureşti, 1978, p. 33-55

[4]. Bo Zhang - "*Development of corrosion resistant galvanising alloys"*, Metallurgy and Materials School of Engineering, The University of Birmingham, July 2005, p.5.

THE ANNALS OF "DUNAREA DE JOS" UNIVERSITY OF GALATI.
FASCICLE IX. METALLURGY AND MATERIALS SCIENCE
N^0. 2 – 2009, ISSN 1453 – 083X

X-RAY DIFFRACTION ANALYSIS AT ULTRASONIC WELDING

Constantin DUMITRACHE[1], Mihaela BĂRHĂLESCU[1], Adrian SABĂU[1], Corneliu COMANDAR[2]
[1]Maritime University Constanţa
[2]Technical University „Ghe. Asachi" Iaşi
email: ldumitr@yahoo.com

ABSTRACT

In the article [2] the author present experimental investigations regarding of residual stress distribution in weld bead vicinity of submerged arc welded naval plates. In this way, residual stresses from vicinity of weld bead acts like compressive stress. The ultrasonic welding is acting in order to compress the weld bead and the heat affected zone. In this paper is presented X-ray analysis to obtain information about mosaic block dimensions, micro stresses fields and density of dislocations.

KEYWORDS: density of dislocations, residual stresses, X-ray analysis

1. Introduction

The welding process of polycrystalline carbon steel produces essential structure changes in heat affected zone (HAZ). The HAZ grains structure differs from the other zones and this is a subject of thermal stress action.

After welding, these strains will result in the retention of elastic stresses in the welded joint referred to as residual stresses.

If the strain is different from point to point within the crystallites it is the micro stress (second order stress), whereas stress existing over large distances is macro stress (first order stress) [1].

The effect of strain can be seen in the diffraction peaks. Uniform strain will make the peak shift to one side or the other of ideal Bragg peak, while non uniform stress will broaden the peak as some parts of aggregate will shift the peak to one side and other parts will shift it to the other side.

In figure 1 the shift of position X-ray diffraction line appeared at big diffraction angle is shown.

The amount of first order stress σ_I that leads to a normal deformation on the superficial layer can be calculated with relation:

$$\sigma_I = -\frac{E}{\upsilon}\left(ctg\,\theta\right)\cdot\Delta\theta \qquad (1)$$

where $\Delta\theta$ is the shift o diffraction line, $E=2.1\cdot10^5$ [MPa]-Young Module, υ=0,3-Poisson Coefficient.

This all happens because the strain changes the distances between diffracting planes.

In figure 2 a schema concerning unstressed and stressed crystalline lattice that implied the existence of second order stress is shown.

In figure 3 the influence of second order stress on the shape of the diffraction line appeared at big diffraction angle is displayed.

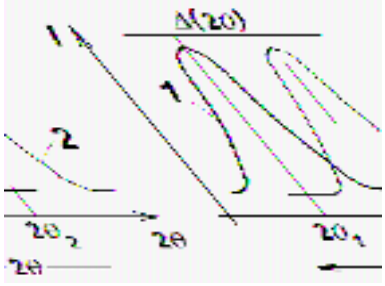

Fig. 1. *Shift of (nh nk nl) diffraction line due to σ_I [3]*

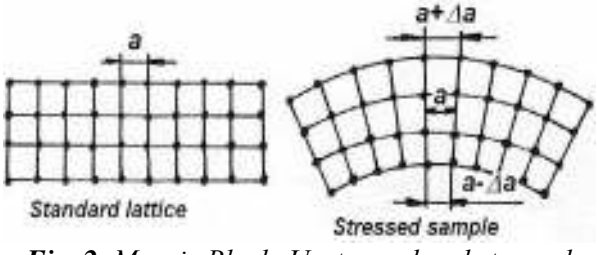

Fig. 2*. Mosaic Block. Unstressed and stressed crystalline lattice [4]*

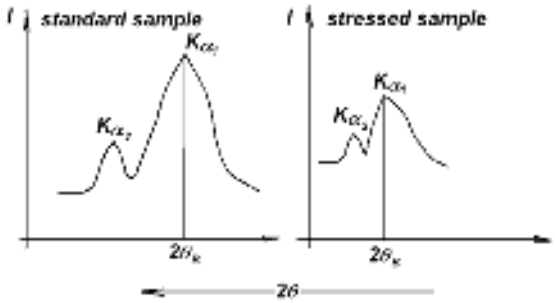

***Fig. 3**. Influence of σ_{II} on shape of diffraction line [3]*

The amount of second order stress σ_{II} was evaluated using the physical width of the diffraction line (220), β_{220}, knowing that:

$$\sigma_{II} = \frac{E}{\upsilon} \cdot \eta_{220} \qquad (2)$$

where η_{220} is a measure of the interplanar distance non-homogeneity given by relation [4]:

$$\eta_{220} = \left(\frac{\Delta a}{a}\right)_{220} = \frac{\beta_{220}}{4 tg\,\theta_{220}} \qquad (3)$$

with

$$\beta_{220} = \sqrt{(\beta_{220})_S^2 - (\beta_{220})_{ST}^2} \qquad (4)$$

where $(\beta_{220})_S$ is a width of diffraction line (220) from stressed sample, while $(\beta_{220})_{ST}$ is the same parameter from standard sample.

The level of dislocation density, ρ, in the crystalline lattice was estimated with:

$$\rho \approx \left(\frac{I_{\min}}{I_{\max}}\right)_{220} \qquad (5)$$

where I_{min} is the intensity of the background diffraction line (220), I_{max} is the maximum intensity of the same line.

2. X-ray diffractograms. Experimental research

For determining the diffractograms were used CoK_α radiation with wave length of $K\alpha_1$ $K\alpha_2$ components:

$\lambda_{K\alpha} = 1{,}79019\,\mathring{A}$; $\lambda_{K\alpha 1} = 1{,}78897\,\mathring{A}$; $\lambda_{K\alpha 2} = 1{,}79279\,\mathring{A}$

The (110) diffraction line is $2\theta = 52^\circ$ and for (220) diffraction line is $2\theta = 123{,}8^\circ$.

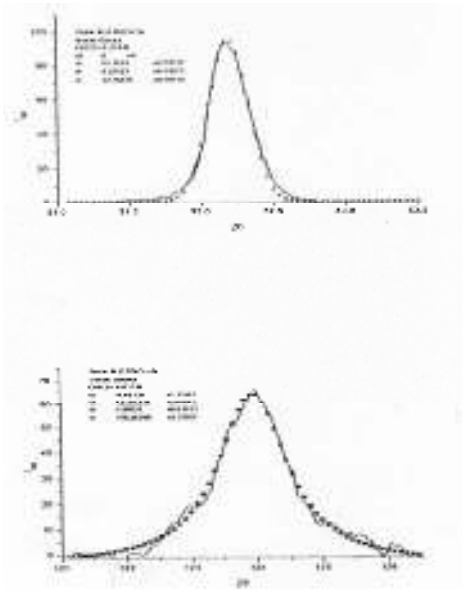

***Fig. 4**. Aspects of diffraction line (110) and (220) for normal welded plates-NWP[1]*

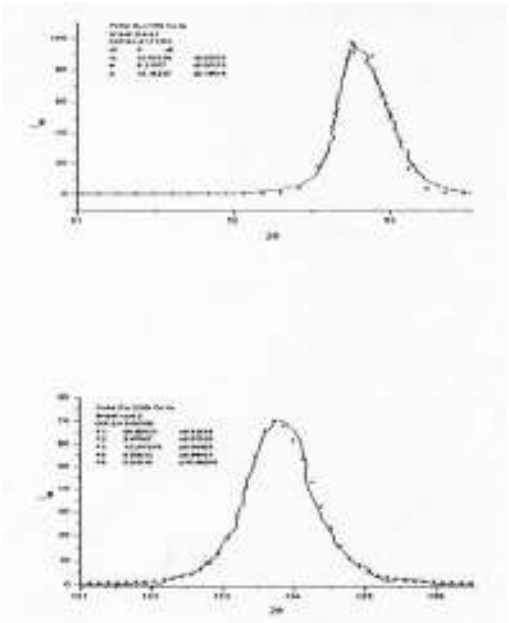

***Fig. 5.** Aspects of diffraction line (110) and (220) for ultrasonic welded plates-UWP [1]*

Table 1. *Dimensions of mosaic blocks, interplanar distance, density of dislocations*

Samples	The average dimensions of mosaic blocks D(μm)	Interplanar distance non-homogeneity η_{220}	Density of dislocations ρ
NWP	>2 μm	$2.154x10^{-3}$	$2.65x10^{-3}$
UWP	>2 μm	$1.41x10^{-3}$	$1.13x10^{-3}$

Table 2. *Normal and parallel strain*

Samples	$\varepsilon_{\perp}=\sigma_{\perp}/E$	$\varepsilon_{\phi}=((1+\nu)/E)\,\sigma_{\Phi}$
NWP	$1.53x10^{-3}$	-0.060
UWP	$2.22x10^{-5}$	0.00816

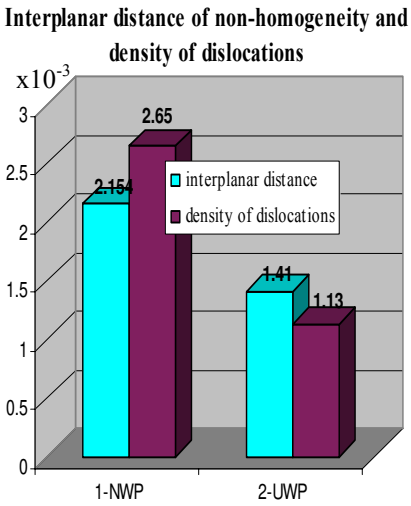

Fig. 6. *Interplanar distance η_{220} and density ρ [1]*

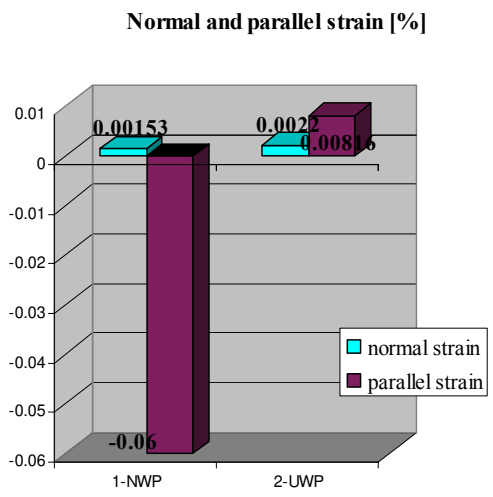

Fig. 7. *The normal strain $\varepsilon_{\perp}=\sigma_{\perp}/E$ and parallel strain $\varepsilon_{\phi}=((1+\nu)/E)\,\sigma_{\Phi}$ at surface layer(220) [1]*

Welding it was performed under both normal conditions (classical welding-NW) and ultrasonic activation of electrode wire (UW) with amplitude in welding zone A=$10x10^{-6}$m.

During ultrasonic welding, both micro and macro residual stresses are reduced, but the strength and hardness of welded joint remain high.

All experimental data were performed on the submerged welded plates in the proximity of welded beads which corresponding with heat affected zones (HAZ).

4. Conclusions

Ultrasonic welding in condition of submerged arc improves mechanical resistance characteristics because it is supposed that ultrasonic energy transmitted by an electrode wire into metal liquid bath at resonance, breaks primary crystals forming into the weld and reduces grains' size.

The interplanar distance non-homogeneity η, and density of dislocations ρ, depends of ultrasonic welding process and decrease with 34 (η) and 57 (ρ) percents. This reduction depends with amplitude of electrode wire.

First order strains (normal and parallel) give information about the signs of residual stresses in surface layers.

The normal strain is increasing in UWP plates with 31 percents because of ultrasonic field influence in surface layers. Normally, at the thin welded plates with low stiffness, parallel strain at the right angle on weld bead determine the compressive stress which is changing rapidly in tensile stress during ultrasonic welding.

References

[1]. Dumitrache C. - *Cercetări privind influenţa ultrasunetelor asupra elementelor de substructură şi tensiuni ale construcţiilor sudate*, Teză de doctorat, Iaşi, 2000;

[2]. Dumitrache C., Comandar C., Barsanescu P. - *Residual Stresses Measurements in Welded Naval Steel using the Hole-Drilling Strain-Gage Method*, pg. 145-151, 21-24 may 2000, Third International Congress in Materials Science and Enginneering, Iasi, ISSN 1453-1690;

[3]. Gheorghieş C. - ***Analysis of the surface layer by X-rays diffraction method*** National Tribology Conference **ROTRIB '03**, 24-26 sept. 2003, Galaţi, The Annals of University "Dunărea de jos", Fascicle VIII, pag. 302-311, Tribology, ISSN 1221-4590;

[4]. Gheorghieş C - *Controlul structurii fine a metalelor cu radiaţii X,* Ed. Tehnică, Bucureşti, 1990.

THE ANNALS OF "DUNAREA DE JOS" UNIVERSITY OF GALATI.
FASCICLE IX. METALLURGY AND MATERIALS SCIENCE
N^0. 2 – 2009, ISSN 1453 – 083X

MORPHOLOGICAL ASPECTS AND CORROSION BEHAVIOUR OF PHENOL FORMALDEHYDE/Zn COMPOSITE COATINGS

Alina – Crina CIUBOTARIU[1,2], Lidia BENEA[1,2], Olga MITOŞERIU[1], Pierre PONTHIAUX[3], François WENGER[3]

[1,2]Dunarea de Jos, University of Galati,
[1]Competences Center Interfaces –Tribocorrosion and Electrochemical Systems;
[2]Metallurgy and Materials Science Faculty,
[3]Ecole Centrale Paris, Laboratoire Génie de Procédées Matériaux, Chatenay Malabry, France
email: Alina.Ciubotariu@ugal.ro

ABSTRACT

The present work has the purpose of studying morphological aspects and corrosion behaviour of pure zinc and composite coatings having zinc as metal matrix and phenol – formaldehyde resin type Novolac (RESITAL 6358/1) as dispersed phase obtained during the electrodeposition process of zinc. The phenol – formaldehyde resin/Zn composite coatings were electrodeposited from a suspension of phenol – formaldehyde resin particles in aqueous zinc sulphate electrolyte by adding 10g/L and 25g/L of phenol – formaldehyde resin particles in the electrolyte solution. The dimensions of resin particles were 0.1 - 5μm. The morphological aspects of the coatings were investigated by scanning electron microscopy method. While the pure zinc coatings have a rather regular surface, the composite coatings surfaces have finer grains and different morphologies. The electrochemical behaviour of the coatings in the corrosive solution was investigated by potentiodynamic polarization and electrochemical impedance spectroscopy methods. As electrochemical test solution, 0.5M NaCl was used in a three electrode open cell. The polarization resistances of phenol – formaldehyde resin/Zn composite coatings are bigger than that of pure zinc coatings obtained under the same condition for electrodeposition.

KEYWORDS: PF resin/Zn composite coatings, electrodeposition, scanning electron microscopy, polarization resistance

1. Introduction

Composite materials are material systems that consist of a discrete constituent (the reinforcement) distributed in a continuous phase (the matrix) and that derive their distinguishing characteristics from the properties and behavior of their constituents, from the geometry and arrangement of the constituents, and from the properties of the boundaries (interfaces) between the constituents.

Composites are classified either on the basis of the nature of the continuous (matrix) phase (polymer-matrix, metal-matrix, ceramic-matrix, and intermetallic-matrix composites), or on the basis of the nature of the reinforcing phase (particle reinforced, fiber reinforced, dispersion strengthened, laminated, etc.). The properties of the composite can be tailored, and new combinations of properties can be achieved [1]. Metal matrix composites offer a number of advantages compared to their base metals, such as higher specific strengths and moduli, higher elevated temperature resistance, lower coefficients of thermal expansion, and, in some cases, better wear resistance. From this potential, metal matrix composites fulfil all the desired conceptions of the designer [2 – 5].

Composite coatings on zinc are finding increased interest in surface technology and corrosion protection. Potential fields of application are improved corrosion and wear resistance of zinc composite layers with extended lifetime [6].

Electrochemical deposition of composite coatings can bring many advantages as compared to other methods. Electrodeposition of zinc on steel is carried out to protect steel from corrosion. The reason for the pre-eminence of zinc in the world of electrodeposition can be attributed to its relative

readiness of deposition and better corrosion resistance [7 – 9].

The application of potentiodynamic polarization and electrochemical impedance spectroscopy (EIS) methods to coated metals has resulted in provisions of new information concerning their degradation in corrosive environments [10, 11]. EIS has been shown to be a useful technique in the study of the corrosion performance of surface coated metals in recent years [12–21].

The present work has the purpose of studying the morphological aspects and corrosion behaviour of pure zinc and composite coatings having zinc matrix and phenol – formaldehyde (PF) resin type Novolac with commercial name RESITAL 6358/1 synthesized by Hüttenes – Albertus Group (Germany) as dispersed phase obtained during electrodeposition process of zinc.

2. Experimental

For electrodeposition it was used zinc sulphate plating bath [22]. The pH of the solution was 3.8. Zinc plate of 99.9% purity was used as anode. As cathode we used carbon steel type DC04. Before deposition, the samples were degreased with alkaline solution at 80 – 90^{0}C during 10min. After decreasing, the surfaces were etched with 15% HCl for 1 – 2min and washing with distilled water.

The PF resin/Zn composite coatings were electrodeposited from a suspension of PF resin particles in aqueous zinc sulphate electrolyte by adding 10g/L and 25g/L PF resin dispersed particles with dimensions 0.1 – 5μm.

PF resin is a highly cross linked thermosetting material that is produced by the poly-condensation of phenol and formaldehyde in the presence of either acidic or basic catalyst. An acid catalyst is usually used in preparing Novolac type resin (see Fig. 1).

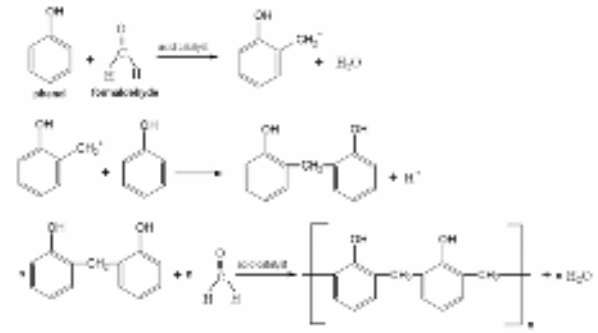

Fig. 1. *The schematic formation of the Novolac type structures*

The term novolac refers to the early use of phenolic to replace expensive shellac-based coatings. Novolacs are now those resins made at formaldehyde to- phenol molar ratios of less than one-to-one [23, 24].

The pure zinc and composite coatings were obtained at current density of 5A/dm^2, time for electrodeposition 60min, a stirring rate of 1000 rpm and an electrolyte temperature of 25^{0}C. Polished, degreased and cleaned cathodes of 2.5cm^2 exposed areas were used.

Before electrochemical corrosion investigations, the morphologies of deposits were examined by Scanning Electron Microscope type JEOL, JSM-T220A.

For electrochemical corrosion measurements were used a Solartron 1286 Electrochemical Interface coupled with a 2895 Solartron Frequency Response Analyser and the Z-Plot / Z-View SOFTWARE. A three - electrode open cell with pure zinc and PF resin/Zn composite coatings layers as working electrode (W.E.), a platinum gauze as counter electrode (C.E.) and mercury – mercurous sulphate electrode Hg/Hg_2SO_4/ saturated K_2SO_4 as reference electrode (R.E.; E = + 658mV/NHE). As test solution, 0.5M NaCl were used at room temperature (20±1^{0}C).

EIS measurements used initial frequency (I. F.) 65000Hz, final frequency (F. F.) 0.001Hz, AC sine wave amplitude of 10mV, frequency per decade: 10Hz, delay before integration 1s. The electrochemical impedance spectroscopy diagrams were recorded after 30min of immersion. All the recorded impedance spectra were analyzed as Nyquist Diagrams.

For potentiodynamic polarization measurements were used initial potential (I. P.) – 1900mV (Hg/Hg_2SO_4), final potential (F. P.) – 1200mV (Hg/Hg_2SO_4) and a scan rate of 1.66mV/s. The polarization potentiodynamic curves were recorded after 30min of immersion. The corrosion current density (i_{corr}) for the particular specimens was determined by extrapolating the anode and cathode Tafel curves.

3. Results and discussions

The thicknesses of pure zinc and composite coatings obtained by electrodeposition at 5A/dm^2 current density, 60min deposition time and 1000rpm are shown in Fig. 2.

From Fig.2 it can be observed that by adding PF resin particles the thickness of the coatings is a little beat smaller. Decreases of the thickness could be possible because the resin particles determined smoother and fine structure of PF resin /Zn composite coatings than pure zinc electrodeposited.

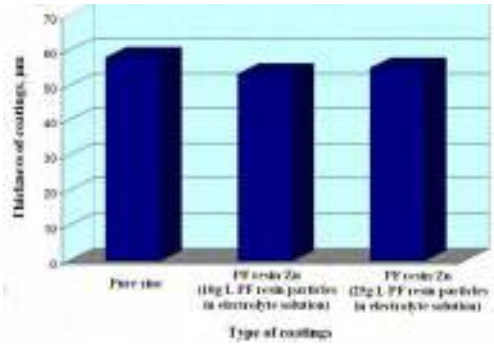

Fig. 2. *The thickness of pure zinc and composite coatings obtained by electrodeposition at 5A/dm^2 current density, time 60min, 1000rpm*

Figs. 3 – 5 compares morphological aspects of pure zinc coating and PF resin/Zn composite coatings by scanning electron microscopy method.

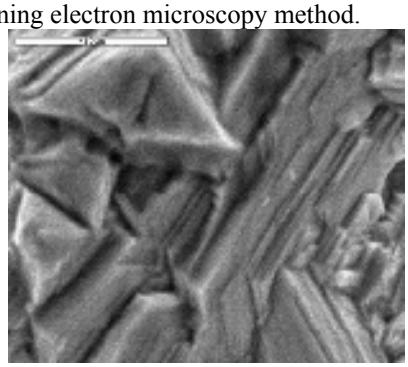

Fig. 3. *SEM surface morphology of pure zinc electroplating (x 5000)*

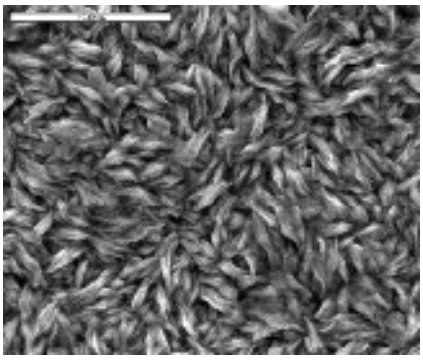

Fig. 4. *SEM surface morphology of PF resin/Zn composite coatings (10g/L PF resin particles in electrolyte solution) (x 5000)*

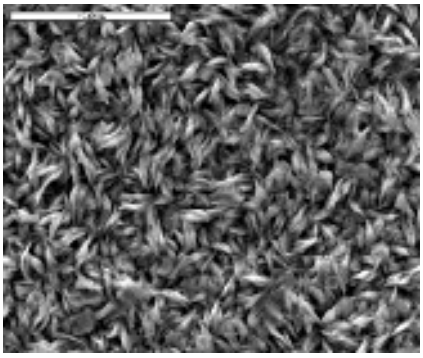

Fig. 5. *SEM surface morphology of PF resin/Zn composite coatings (25g/L PF resin particles in electrolyte solution) (x 5000)*

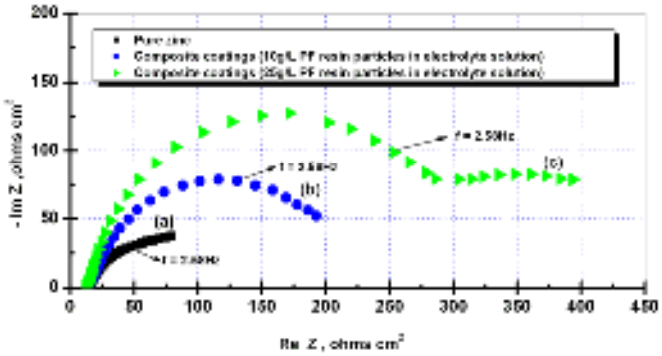

Fig. 6. *Nyquist diagrams of impedance spectrum for pure zinc and PF resin/Zn composite coatings in 0.5M NaCl after 30 min from immersion:*
(a) – pure Zn, (b) – PF resin/Zn composite coatings (10g/L PF resin particles in electrolyte solution), (c) - PF resin/Zn composite coatings (25g/L PF resin particles in electrolyte solution)

The surface of zinc is made up of regular crystals. The PF resin particles codeposit with zinc radically change the structure of the metal: disorder the regular crystal structure and the structure of the zinc matrix becomes finely crystalline. The pure zinc coatings have a rather regular surface, whereas the composite coating surfaces have finer grains structure with particles of PF resin uniform distributed on the surfaces. The electrochemical investigation of each sample began with monitoring the open circuit potential (OCP). OCP changes immediately after the immersion into the testing solutions till reaching

relatively stable stationary values. The Nyquist plot representation of impedance spectra performed in 0.5M NaCl for pure zinc and PF resin/Zn composite coatings after 30min of immersion it is shown in Fig. 6. Two equivalent electrical circuits were proposed to fit the experimental impedance data [25 – 26]. In most cases, these circuits, represented in Fig. 7 (a and b) allows to obtain an excellent agreement between experimental and simulated impedance plots. The experimental data of our work was simulated with these equivalent circuits where: R_e – electrolyte resistance between the reference electrode and the working electrode; CPE1 – the double layer capacitance of pure zinc coatings depending on frequency in parallel with the polarization resistance R_p. R_r could represent the resistance of resin dispersed particles, C_c the coating capacitance due to resin particles and CPE2 the double layer capacitance of composite coatings depending on frequency.

CPE are a constant phase elements, accounting for the fact that the centres of the capacitive arcs of the circle are under the axis of real part. This feature of capacitive arcs is encountered in all electrochemical impedance studies performed on inhomogeneous surfaces and has given rise to extensive studies. CPE are not pure capacitors, but components depending on frequency.

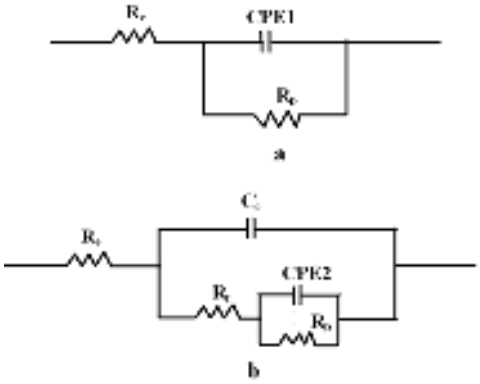

***Fig. 7**. Equivalent circuits to calculate the polarization resistance from impedance data*

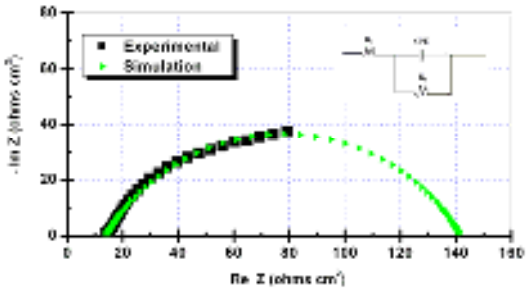

***Fig. 8.** Nyquist diagrams of impedance spectrum of experimental data (square points) and fitting curve (triangle points) for pure zinc coatings in 0.5M NaCl solution after 30min of immersion*

On the Figs. 8 and 9 were represented the experimental diagrams together with the simulation curves described by the equivalent circuits from fig. 7. It could be observed that the experimental impedance data fit very well with the equivalent circuit proposed.

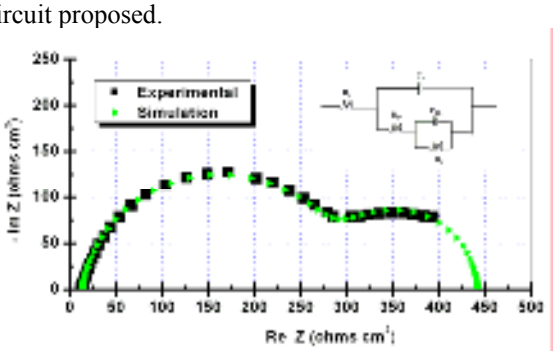

***Fig. 9.** Nyquist diagrams of impedance spectrum of experimental data (square points) and fitting curve (triangle points) for PF resin/Zn composite coatings in 0.5M NaCl solution after 30min of immersion*

The corresponding calculated polarization resistance values from impedance diagrams for pure zinc and PF resin/Zn composite coatings in 0.5M NaCl solution using the equivalent circuits from Fig. 7 are presented in the Fig. 10.

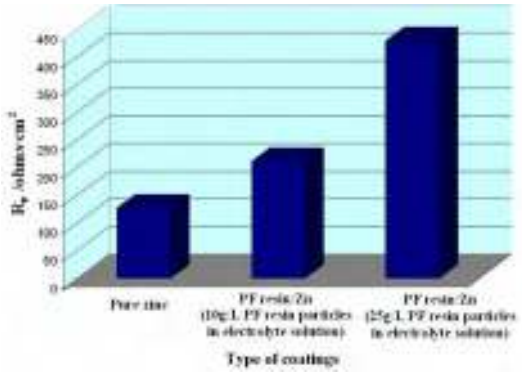

***Fig. 10**. Variation of polarization resistance for pure zinc and PF resin/Zn composite coatings in 0.5M NaCl after 30min from immersion*

For pure zinc coatings the polarization resistance was 127.37Ω·cm^2.

For PF resin/Zn composite coatings layers obtained by adding 10g/L PF resin particles in electrolyte solution the polarization resistance was 211.38Ω·cm^2 and with increasing the concentration of the particles in electrolyte solution to 25g/L the polarization resistance increase to the value of 428.69Ω·cm^2.

It was observed that o good polarization resistance was found for PF resin/Zn composite

coatings with 25g/L PF resin particles in electrolyte solution. The value of polarization resistance for this type of coatings is about four times bigger than polarization resistance of pure zinc coating obtained at the same electrodeposition conditions.

The performed potentiodynamic diagrams for pure zinc and PF resin/Zn composite coatings in 0.5M NaCl after 30min of immersion are presented in Fig. 11.

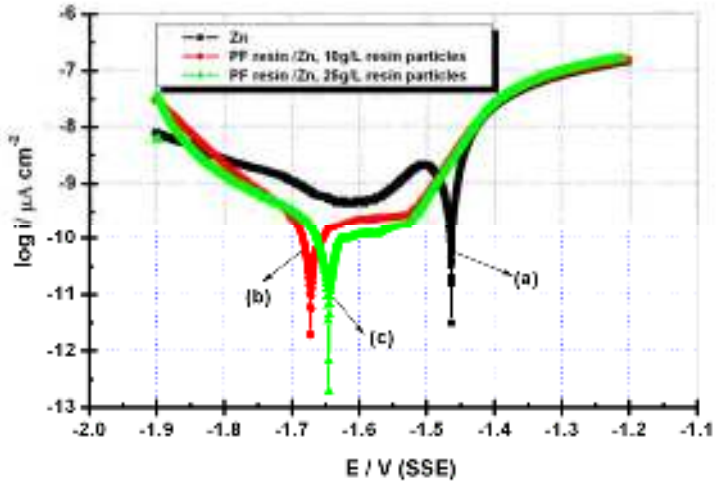

Fig. 11. *Comparative polarization potentiodynamic curves for pure zinc and PF resin/ Zn composite coatings in 0.5M NaCl solution obtained after 30minutes from immersion time (log scale): (a) – pure Zn, (b) – PF resin/Zn composite coatings (10g/L PF resin particles in electrolyte solution), (c) - PF resin/Zn composite coatings (25g/L PF resin particles in electrolyte solution)*

In corrosion, quantitative information on corrosion currents and corrosion potentials can be extracted from the slope of the curves, using the Stern-Geary equation, as follows [27]:

$$i_{corr} = \frac{1}{2.303 R_p}\left(\frac{\beta_a \cdot \beta_c}{\beta_a + \beta_c}\right) \qquad (1)$$

- i_{corr} is the corrosion current density in Amps/cm^2;
- R_p is the corrosion resistance in ohms cm^2;
- β_a is the anodic Tafel slope in Volts/decade or mV/decade of current density;
- β_c is the cathodic Tafel slope in Volts/decade or mV/decade of current density;
- the quantity, $(\beta_a \cdot \beta_c)/(\beta_a + \beta_c)$, is referred to as the Tafel constant.

The corrosion potential (E_{corr}), corrosion current density (i_{corr}) and polarisation resistance (R_p), which were obtained from the potentiodynamic polarisation curves are summarized in Table 1.

Table 1*. Polarization resistances values of pure zinc and PF resin/Zn composite coatings calculated from polarization potentiodynamic curves obtained after 30min from immersion in 0.5M NaCl solution*

Type of coatings	**E_{cor}, V** Hg/Hg_2SO_4	**β_a** mV/decade	**β_c** mV/decade	**i_{cor},** µA/cm^2	**R_p** Ω·cm^2
Pure zinc	-1.47	53.95	21.26	52.00	127.34
PF resin/Zn composite coatings with 10g/L PF resin particles in electrolyte solution	-1.67	37.94	33.21	35.98	213.66
PF resin/Zn composite coatings with 25g/L PF resin particles in electrolyte solution	-1.64	26.31	26.93	13.43	430.19

The corrosion potential is shifted to more negative values for PF resin/Zn composite coatings (-1.67V for coatings obtained with 10g/L resin in electrolyte solution, respectively - 1.64V for coatings obtained with 25g/L resin in electrolyte solution) than pure zinc coatings (-1.47V).

From potentiodynamic polarization curves the polarization resistance for pure zinc coatings was 127.34Ω·cm^2. For PF resin/Zn composite coatings layers obtained by adding 10g/L PF resin particles in electrolyte solution the polarization resistance was 213.66Ω·cm^2 and with increasing the concentration of the particles in electrolyte solution to 25g/L the polarization resistance increase to the value of 430.19Ω·cm^2.

The polarisation resistance values calculated with Stern-Geary formula from potentiodynamic diagrams was in a good agreement with those obtained from impedance measurements.

From experimental data it was observed that corrosion current density (corrosion rate) has a big value for pure zinc coatings (52.00μA/cm^2) and small value for PF resin/Zn composite coatings (35.98μA/cm^2 for PF resin/Zn composite coatings layers obtained by adding 10g/L PF resin particles in electrolyte solution), respectively 13.43μA/cm^2 for PF resin/Zn composite coatings layers obtained by adding 25g/L PF resin particles in electrolyte solution).

It was observed that by adding PF resin particles in zinc electrolyte for electrodeposition it was obtained PF resin/Zn composite coatings most resistant at corrosive attack at 0.5M NaCl solution than pure zinc obtained from electrodeposition in same conditions.

This improvement of corrosion resistance could be due to the fine surface structure of composite coating compared with pure zinc coating as well as to the incorporation of PF resin particles into composite coatings.

3. Conclusions

It has been demonstrated that PF resin particles type Novolac with commercial name RESITAL 6358/1 could be codeposited with zinc to obtain composite coatings.

The surface morphology to PF resin/Zn composite layers is different compared with pure zinc coatings: the regular crystal structure characteristic of electroplated zinc coatings was disturbed. The PF resin particles embedded in the zinc matrix perturb the zinc crystals growth during electrodeposition.

By increasing the PF resin concentration in the zinc electrolyte the surface structure of composite coating is changed more to finer crystallites. The PF resin acts as reducing the crystals size of electrodeposited zinc during co-deposition.

Electrochemical impedance spectroscopy and polarisation potentiodynamic methods are powerful techniques to investigate the corrosion protection of pure zinc and PF resin/Zn composite coatings. The polarization resistance values obtained from both methods are in good agreement.

The corrosion potential is shifted to more negative values for composite coatings (-1.67V and -1.64V) than those of pure zinc coatings (-1.47V) obtained in the same conditions of electrodeposition.

For composite coatings, the polarization resistance is bigger than for pure zinc coatings obtained under the same condition for electrodeposition. It was observed that a good polarization resistance was found for PF resin/Zn composite coatings with 25g/L PF resin particles in electrolyte solution. The value of polarization resistance for this type of coating is about four times bigger than polarization resistance of pure zinc coatings.

From experimental data it was observed that corrosion current density (corrosion rate) is higher for pure zinc coatings and smaller for PF resin/Zn composite coatings.

The better corrosion resistance of PF resin/Zn composite coatings could be due to the fine surface structure of composite coating compared with pure zinc coating as well as to the incorporation of PF resin particles into composite coatings could have an inhibition effect of zinc crystals growth and a catalytic effect in increasing nucleation sites.

References

[1]. Asthana R., Kumar A., Dahotre N. B. - *Materials Processing and Manufacturing Science*, ISBN-13: 978075A67765, Edited by Butterworth-Heinemann, London, 2006.

[2]. Campbell F. C. - *Manufacturing Technology for Aerospace Structural Materials,* ISBN-13: 9781856174954, Edited by Blsevier, London, 2006.

[3]. Chawla K. K. - *Composite Materials: Science and Engineering*, 2 ed., Springer - Verlag, New York, 1998.

[4]. Kaczmar J. W., Pietrzak K., WlosinskiW. - *The Production and Application of Metal Matrix Composites*, Journal of Materials Processing Technology, Vol. 106, (l) ,2000, p.58 - 67.

[5]. Lindroos V. K., Talvitie M. J. - *Recent Advances in Metal Matrix Composites*, Journal of Materials Processing Technology, Vol. 53. (1 - 2), 1995, p. 273-284.

[6]. Azizi M., Schneider W. and Plieth W. - *Electrolytic co-deposition of silicate and mica particles with zinc*, Journal of Solid State Electrochemistry, Vol. 9, (6), 2005, p. 429 - 437.

[7]. Flinn R. A. and Trojan P. K. - *Engineering Materials and Their Applications*, 4th ed., Houghton Mitfflin Co., Boston. 1990.

[8]. Kim B. S., Sung R. J., Sekino T., Nakayama T., Kusunose T., Niihara K., *Aqueous Suspicion Process of Multi - Dimensional Alumina/Nickel Nanocomposites*, Advanced in Technology of Materials and Materials Processing Journal, Vol. 6, (2), 2004, p.200 -205.

[9]. Naik A. and Venkatesha T.V. - *A new condensation product for zinc plating from non-cyanide alkaline bath*, Bulletin of Materials Science, Vol.28, (5), 2005, p. 495 - 501.

[10]. **Deflorian F., Fedrizzi L., Bonora P. L**. - *EIS study of organic coating on zinc surface pretreated with environmentally*

friendly products, Progress in Organic Coatings, Vol.52, (4), 2005, p. 271-279.
[11]. Chung S.C., Cheng J.R., Chiou S.D., Shih H. C. - *EIS behavior of anodized zinc in chloride environments*, Corrosion Science, Vol. 42, (7), 2000,p.1249 - 1268.
[12]. Monetta T., Belluci F., Nicodemo L. - *Protective properties of epoxy-based organic coatings on mild steel*, Progress in Organic Coatings, Vol. 21, (4), 1993, p. 353 - 369.
[13]. Sekine I. - *Recent Evaluation of Corrosion Protective Paint Films by Electrochemical Methods*, Progress in Organic Coatings, Vol. 31, (1), 1997, p. 73 - 80.
[14]. Miskovic V. B., Stanic M. R., Drazic D. M. - *Corrosion protection of aluminium by a cataphoretic epoxy coatings*, Progress in Organic Coatings, Vol. 36, (1), 1999, p. 53 - 63.
[15]. Nie T., Ooij W. J., Gorecki G. - *Comparative EIS study of pretreatment performance in coated metals*, Progress in Organic Coatings, Vol.30, (4), 1997, p. 255-263.
[16]. Miskovic Stankovic V. B., Maksimovic M. D., Kacarevic Popovic Z., Zotovic J. B. - *The sorption characteristics and thermal stability of epoxy coatings electrodeposited on steel and steel electrochemically modified by Fe-P alloys*, Progress in Organic Coatings. Vol. 33, (1), 1998, p. 68 - 75.
[17]. Deflorian F., Fedrizzi L., Bonora P. L. - *Organic coating capacitance measurements by EIS: ideal and actual trends*, Electrochimica Acta, Vol. 44, (24), 1999, p. 4243 - 4249.
[18]. Deflorian F., Miskovic V. B., Bonora P. L., Fedrizzi L. - *Degradation of epoxy coatings on phosphatized zinc electroplated steel,* Corrosion, Vol. 50, (6), 1994, p. 438 - 446.
[19]. Sabata A., Ooij W. J. and Koch R. J. - *The Interphase in Painted Metals Pretreated by Functional Silanes*, Journal of Adhesion science and Technology, Vol. 7, (11), 1993, p. 1153 – 1170.
[20]. Amirudin A., Thierry D. - *Application of electrochemical impedance spectroscopy to study efficiency of anticorrosive pigments in epoxy-polyamide resin*, British Corrosion Journal, Vol. 30, (2), 1995, p. 128-134.
[21]. Kendig M., Scully J. - *Basic Aspects of Electrochemical Impedance Application for the Life Prediction of Organic Coatings on Metals,* Corrosion, Vol. 46, 1990, p. 22 -29.
[22]. Ciubotariu A. C., Benea L., Mitoşeriu O., Ponthiaux P., Wenger F. - *Influence of particles size on the morphology and corrosion behaviour of phenol –formaldehyde/Zn composite coatings obtained by electrodeposition*, Journal of Optoelectronics and Advanced Materials. Vol. 11, (6), 2009, p. 892 - 897.
[23]. Detlefsen W. D., *Phenolic resins: some chemistry: technology and history*, Edited by M. Chaudhury, A .V. Pocius, 2002.
[24]. Wei W., Hu H., You L., Chen G., *Preparation of carbon molecular sieve membrane from phenol-formaldehyde Novolac resin*, Carbon Vol. 40, (3), 2002, p. 465 – 467.
[25]. Ciubotariu A. C., Benea L., Lakatos - Varsanyi M., Drăgan V. - *Electrochemical Impedance Spectroscopy and Corrosion Behaviour of Al_2O_3 - Ni Nano Composite Coatings*, Electrochimica Acta, Vol. 53, (13), 2008, p. 4557 - 4563.
[26]. Souza M. E. P., Ballester M., Freire C. M. A. - *EIS characterization of Ti anodic oxide porous films formed using modulated potential*, Surface and Coatings Technology, Vol. 20l, (18), 2007, p. 7775 - 7780.
[27]. Stern M., Geary A. - Journal of the Electrochemical Society, Vol. 105, 1958, p. 638 - 647.

THE ANNALS OF "DUNAREA DE JOS" UNIVERSITY OF GALATI.
FASCICLE IX. METALLURGY AND MATERIALS SCIENCE
N^0. 2 – 2009, ISSN 1453 – 083X

ON THE CORROSION BEHAVIOR OF ORGANIC NANOCOMPOSITE COATINGS

Constantin GHEORGHIEŞ, Livia GHEORGHIEŞ, Constantin OANCEA, Petrica HAGIOGLU, Valeriu Onuţ ATANASIU
"Dunărea de Jos" University of Galaţi
email: cgheorg@ugal.ro

ABSTRACT

Recently, researches on composite coatings of organic nature with the addition of metallic oxide nanopowders have shown an increasing corrosion resistance of metallic materials. Carbon steel shows an improved behavior in corrosive environments when it is covered with an organic layer that includes nanoparticles of titania. This was shown by several measurements of electrochemical corrosion in aqueous solution of 3% NaCl, such as polarization resistance, corrosion potential, corrosion current and electrochemical impedance. The explanation of the improved behavior of carbon steel samples starts from the assumption that the presence of titania leads to a decrease of gas permeability through the composite organic coatings and an improvement of the adherence between the cover and the sample surface.

KEYWORD**:** steel, corrosion, organic coating, titania, EIS

1. Introduction

There are several methods and techniques for protecting the surface of metallic materials against aggressive action of environment. One of them refers to surface modification of metallic substrates by covering with non-organic, organic coatings. In this way, certain surface properties of metallic materials such as resistance at corrosion, oxidation and wear processes become enhanced.

The deposited coating can be considered as an effective barrier between the metal and its environment. For example, an enrichment of metallic surface by a compound containing chromium leads to a superior behavior into corroding medium. However, due to the health and environmental concerns, this kind of material is recommended to be substituted by an alternative material without ecological or biological impacts. Lately, the researches in field have been focused a using organic coatings, being mostly a good anticorrosive agent.

In the domain of organic coatings having protective character, there can be mentioned polymers including polyurethanes [1], epoxy resins [2], polyesters [3]. These coatings have a protective function being a physical barrier against aggressive species such as ions of hydrogen or molecules of oxygen. Other type of organic coatings such as polypyrrole [4], polythiophene [5] or polyaniline [6] have also a protective character due to their redox catalytic properties they lead to formation of metal oxide layer on metallic substrate having a passivation role. All these assumptions are accepted only when the organic coatings are without intrinsic defects.

In numerous cases, it was found that even neat organic coatings are not permanently impenetrable because small defects can appear and they can be considered as attack zones of various corrosive species. Therefore in such areas a localized corrosion will occur. One of method for removal of this inconvenient consists in introducting into coating of certain impurity of the type Me_xO_y having the role to increase the length of diffusion pathway for oxygen and water decreasing the permeability of the coating [7-9]. In this way, the adherence of composite coating to metallic substrate becomes stronger due to apparition of a further bond between coating and metallic surface, being of the type Fe-O-Me.

In this paper are reported some results concerning the behavior into corrosive environment of carbon steel samples covered with a coating obtained by hydrothermal method. For this aim, amino-titania nanoparticles were introduced into hybrid of fluorinated polyimide-titania followed by a conventional thermal polymerization reaction that occurs during hydrothermal deposition, as it is

presented in many papers [10-12]. It is reported that the F- ions protect the metal from corrosion, at lower temperature, but at higher concentration or at higher temperature, fluoride accelerates the attack on the metal. The main goal of this paper is to present the corrosion protection performance of fluorinated polyimide-titania hybrid sol-gel coating deposited on carbon steel sample. To achieve this objective, Voltalab 40 and Voltalab 21 instruments were used and the following studies were performed: polarization resistance, corrosion potential, corrosion current, corrosion rate and electrochemical impedance spectroscopy (EIS).

2. Experimental research

Electrochemical measurements of polarization resistance, corrosion potential, corrosion current, corrosion rate and electrochemical impedance spectroscopy of uncoated and coated carbon steel samples were performed by using standard instruments. The electrochemical corrosion cell consists of stainless steel rod counter electrode, reference electrode and working electrode that is uncoated or coated carbon steel sample having dimension of 10x10mm. The thickness of prepared coatings ranged around 20µm and the corrosion solution consists of aqueous solution of 3% NaCl.

The polarization resistance, $R_p\left(k\Omega/cm^2\right)$, was determined by sweeping the applied potential from 20 mV below to 20 mV and above the E_{corr} at a scan rate of 500mV/min and the corresponding current change was recorded. The value of the polarization resistance was obtained from the slope of the potential-current plot, as in fig1.

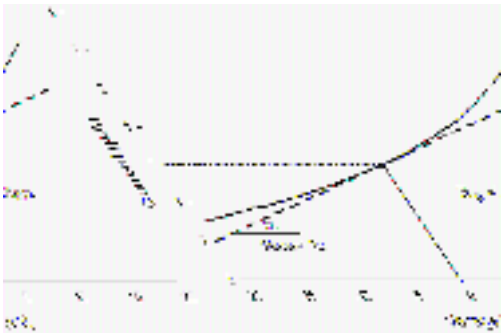

Fig.1. *How to calculate the polarization resistance*

Tafel curves were plotted by scanning the potential from 250 mV below to 250 mV above the E_{corr} at a scan rate of 500mV/min and allowed to determine the corrosion current (i_{corr}). Corrosion current has been determined by drawing a straight line along the linear portion of the cathodic or anodic curve and by extrapolating it through E_{corr}. Corrosion rate (R_{corr}, in millimeter per year) was calculated from the following equation :

$$R_{corr}\left(mm/y\right)=\frac{0.051\cdot I_{corr}\cdot(e.w.)}{A\cdot\rho} \qquad (1)$$

where e.w. is the equivalent weight (in g/eq.), A is the area (in cm^2) and ρ is the density (in g/cm^3).

By using the Stearn-Geary equation can be determined the polarization resistance, R_p, namely

$$R_p=\frac{b_a b_b}{2.303\cdot\left(b_a+b_b\right)\cdot I_{corr}} \qquad (2)$$

where b_a and b_b are the Tafel slopes $\Delta E/\Delta\log I$ for positive and negative domains of Tafel curve as presented in fig. 2.

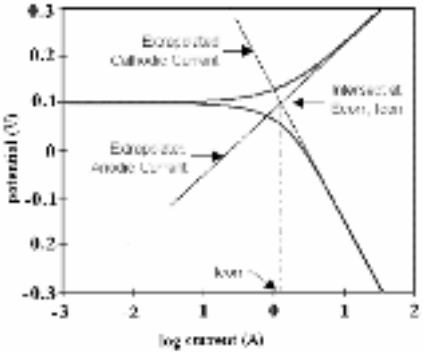

Fig. 2. *Analysis of Tafel curve*

The value of the protection efficiency, $P_{ef}(\%)$, can be used to measure the corrosion protective effect of prepared coatings. For this aim it is recommended [13] to use the relation

$$P_{ef}(\%)=\frac{R_p(c)-R_p(unc)}{R_p(c)}\cdot 100\% \qquad (3)$$

where $R_p(c)$ and $R_p(unc)$ are, the values of polarization resistance for coated and uncoated sample, respectively.

3. Results and discussion

The corrosion protection effect of prepared coatings was studied at both neat polymeric coatings and hybrid coatings. Electrochemical corrosion parameters such as corrosion potential, corrosion current, polarization resistance and protection efficiency were determined for each kind of coating allowing for its anticorrosive characteristics. The anticorrosion properties of prepared coatings resulted from the analysis of Tafel curves which are presented in fig.3. By analyzing the curves 1 and 2, results the corrosion protecting effect of the coated sample with flourinate polyimide.

3.1. Tafel curves

As shown in fig.3, the corrosion potential in case of coated sample (flourinate polyimide) is 634.3 mV, that is more positive than that for uncoated sample being of 688.7 mV. Moreover, the corrosion current is 1.62 $\mu A/cm^2$ in case of uncoated sample and the same size is 1.08 $\mu A/cm^2$ for coated sample (flourinate polyimide). These data show that the coating with flourinate polyimide has a real protection effect. In addition, the distribution of the Tafel remaining curves in relation to the first two discussed demonstrate the superiority of using coatings containing titania nanoparticle in corrosion protection.

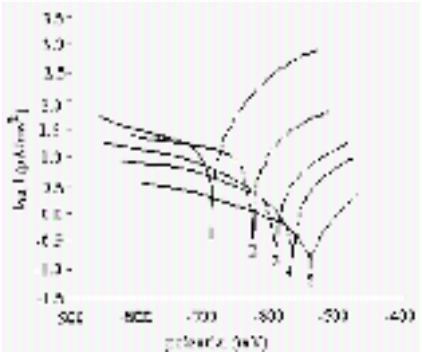

Fig.3. *Tafel curves for prepared coatings: 1- uncoated sample, 2- coated sample (flourinate polyimide), 3- coated sample (flourinate polyimide + titania 5%), 4- coated sample (flourinate polyimide +5% titania nanoparticle), 5- coated sample (flourinate polyimide +10% titania nanoparticle), 6 –coated sample (flourinate polyimide +15% titania nanoparticle).*

3.2. Polarization resistance

The polarization resistance, R_p, is are other important size in order to characterize the performance of anticorrosive properties of coatings. This was estimated from Tafel plots, according to the Stearn-Geary equation.

The values of this size are increasing from sample 1 up to sample 5 being, respectively, $R_p = 2.68\left(k\Omega \cdot cm^2\right)$, $2.98\left(k\Omega \cdot cm^2\right)$, $3.22\left(k\Omega \cdot cm^2\right)$, $5.62\left(k\Omega \cdot cm^2\right)$, $8.88\left(k\Omega \cdot cm^2\right)$, $10.12\left(k\Omega \cdot cm^2\right)$ showing that by increasing of titania nanoparticles content, the anticorrosive properties of coating get bigger.

3.3. Protection efficiency

The protection efficiency, $P_{ef}(\%)$, was calculated for uncoated sample and for all coated samples. The obtained values are increasing with increase of the content of titania nanoparticle concentration. The obtained value are $P_{ef} = 0\%$, 16.77%, 52.31%, 70.15%, 73.81%. These data show that the efficiency of prepared coatings at corrosion starts to become increasingly larger with the increase of nanoparticles concentration.

3.4. Corrosion rate

The corrosion rate was calculated for each sample taking into account the value of I_{corr} obtained from Tafel curve by superimposing a straight line along region of the negative or positive curve and extrapolating it through E_{corr}. The obtained values are, respectively $R_{corr} = 43.37\left(mm/y\right)$ $6.12\left(mm/y\right)$, $4.22\ \left(mm/y\right)$, $3.12\ \left(mm/y\right)$, $2.89\ \left(mm/y\right)$. Increasing the concentration of titania nanoparticles in coating leads the significantly decreasing of corrosion rate.

3.5. Electrochemical impedance spectroscopy

Electrochemical impedance spectroscopy can be used in order to evaluate the corrosion activity variation of all coated samples, noted from 1 to 5. Any electrochemical bath together with its electrodes introduced into AC circuit having a frequency (ω) is characterized by the following sizes: an impedance (Z) that depends on the charge transfer resistance (*R*ct), a solution resistance (*R*s), a capacitance (C_{dl}) of the electrical double layer [14-16] by relation

$$Z = \frac{R_s + R_{ct}}{1+\left(R_{ct}C\omega\right)^2} + j\frac{R_{ct}^2 C_{dl}\omega}{1+\left(R_{ct}C\omega\right)^2} \qquad (4)$$

Figs. 4 and 5 display the Nyquist and Bode plots, respectively, for samples immersed in aqueous solution of NaCl (3%) having a temperature of 25^{o}C.

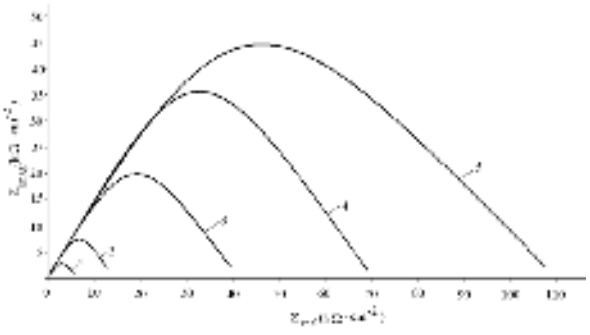

Fig. 4*. Nyquist curve for studied samples*

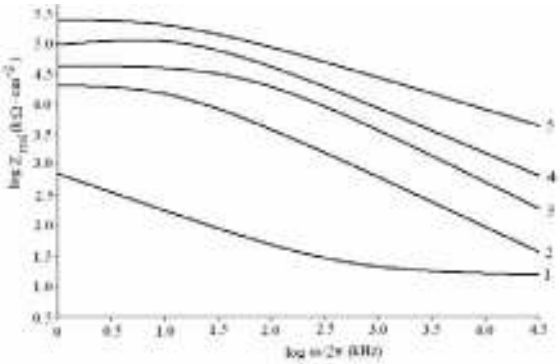

Fig. 5. *Bode curves for studied samples*

The charge transfer resistances of samples were determined by subtracting the intersection of the high-frequency end from the low-frequency end of the semi-circle arc with the real axis (1) - (5) such as $6.21\,k\Omega\cdot cm^{-2}$, $13.08\,k\Omega\cdot cm^{-2}$, $40.07\,k\Omega\cdot cm^{-2}$, $70.03\,k\Omega\cdot cm^{-2}$, and $109.38\,k\Omega\cdot cm^{-2}$, respectively. Moreover that, the larger the semicircle diameter correspond to the lower the corrosion rate and the Bode plots depend on impedance versus frequency of samples (1)-(5). These plots show that the 5 coated samples exhibit a better corrosion protection.

4. Conclusions

In this paper, preliminary investigations for the corrosion protection effect of certain organic composite coatings onto carbon steel electrode were presented. For this aim, a series of electrochemical corrosion measurements such as polarization resistance, corrosion potential, corrosion current, corrosion rate and EIS in corroding media have been performed. The obtained data show that by increasing the titania nanoparticles concentration in organometalic composite coatings through the sol-gel process, an improved behavior of covered carbon sample into corroding environment consisting of an aqueous solution of 3% NaCl. This can be explained by a decreasing in gas permeability of organic composite coatings and improvement of adhesion between the interface of coatings and surface of metallic sample. This research will continue and it aims at confirming the EIS results by microscopic studies.

References

[1]. Moijca J, García E, Rodriguez F. J, Genescá J., Prog. Org. Coat., 42 (2001) 218-225.
[2]. MacQueen R.C, Granata R.D, Prog. Org. Coat. 28 (1996) 97-112.
[3]. Deflorian F, Fedrizzi L, Bonora P.L, Corrosion Sci., 38 (1996) 1697-1708.
[4]. Iroh J.O, Su W, Electrochim. Acta 46 (2000) 15-24.
[5]. Kousik G, Pitchumani S, Renganathan N.G, Prog. Org. Coat. 43 (2001), 286-291.
[6]. Wessling B, Posdorfer J, Electrochim. Acta 44 (1999) 2139-2147.
[7]. Yeh J. M, Liou S.J, Lai C.Y, Wu P.C, Tsai T.Y, Chem. Mater. 13 (2001) 1131-1136.
[8]. Lee Y. K, Murarka S. P, Mat. Res. Bull, 34, 6, (1999) 869-876.
[9]. Gheorghies C., Stasi I. V, Lalau C. C, Journal of Optoelectonics and Advanced Materials, Vol. 11, No. 2, February (2009) 146 – 154.
[10]. Pomogailo A. D, Kestelman V. N, Metallopolymer Nanocomposite, Springer, vol. 81, part III, pp. (2006) 273-320.
[11]. Joly C, Goizet S, Schrotter J.C, Sanchez J, Escoubes M, J. Membrane Sci. 130 (1997) 63-74.
[12]. Cornelius C.J, Marand E, Polymer 43 (2002) 2385-2400.
[13]. Bockris J, Reddy K.N, *Modern Electrochemistry*, Plenum: New York, 1973.
[14]. Lemaitre L, Moors M, Van Peteghem A. P, Journal of Applied Electrochemistry, Vol. 13, Number 6 / November (1983) 803-806.
[15]. Benea L, Lakatos-Varsanyi M, Maurin G, The Annals of "Dunarea de Jos" University of Galati, Fascicle IX Metallurgy and Materials Science 1453 – 083X NR. II (2003) 10-17.
[16]. Musat, V, Fortunato E, Stefan D, Iticescu C, Rev. Roum. de Chimie 52, 7, (2007) 671-676.

THE ANNALS OF "DUNAREA DE JOS" UNIVERSITY OF GALATI.
FASCICLE IX. METALLURGY AND MATERIALS SCIENCE
N^0. 2 – 2009, ISSN 1453 – 083X

RESEARCHES ON THE CORROSION BEHAVIOR FOR A DRAWING STEEL THAT WENT THROUGH NATURAL AGEING

Florentina POTECAŞU, Octavian POTECAŞU, Elena IONIŢĂ, Alina CIUBOTARIU
Dunărea de Jos University of Galaţi
email: fpotec@ugal.ro

ABSTRACT

The paper presents the results of a study on the corrosion behaviour of the sheets of drawing steel with 0,04% C gone through natural ageing and run for a period of 112 days from the moment of drawing. The researches highlighted the fact that the phenomenon of natural ageing speeds up the corrosion process. As a result the durability of the products realized from sheet and straps of steel depend also on the protection of their surfaces through different coating procedures.

KEYWORDS: corrosion behaviour, drawing steel, natural ageing, structure

1. Introduction

By drawing there is executed a wide range of marks, very varied as shape and dimensions that are a component of the resistance structure, as well as in elements of car bodies. This drawn marks, simple or complex, require that the used semiproducts to satisfy certain conditions referring to the physical and mechanical characteristics, durability, accessibility, low price, good workability, etc. The usage of steels in the car industry is conditioned to accessibility, low price, good workability besides the mechanical and physical characteristics.

The running conditions often make the environment be a factor that determines an increase to corrosion and a decrease of the lifetime of the marks obtained through the plastic deformation of the steel sheets.

The chemical composition and the main mechanical characteristics of the chosen steel for the study of the corrosion behaviour are presented in table 1 according to STAS SR EN10030.

Table 1. *The chemical composition of the steel*

Steel	C	Mn	Si	P	S	Al	Cu	Cr	Ni	V	Mo	Ti
	[%]											
DC04-A	0.040	0.3000	0.025	0.015	0.010	0.068	0.020	0.010	0.020	0.004	0.003	0.005

Table 2. *The mechanical characteristics of the steel*

The breaking strength, Rm	The yield point, Rp0.2	The elongation strength, An	The Erichsen parameter, IE	The anisotropy coefficient, r_{90}	The cold-hardening coefficient, n
[N/mm^2]		[%]	[mm]		
270-370	max 210	min 30	min 8.90	min 1.6	min 0.18

The corrosion resistance, or the chemical stability, is the metallic materials' property to oppose to the destructive action of the atmospheric and chemical agents, called corrosion.

When the corrosive environment is an electrolyte (environment with dissociated ions capable to get metal ions), the corrosion is an electrochemical process. The corrosion is manifested by the loss of weight, the structure change, the

chemical composition, the dimensions, the surface colours and the physical, mechanical and technological properties of the metallic materials.

In fact, all the metallic materials in the presence of oxygen get oxidized, but their resistance to oxidation and corrosion depend on the oxide film quality formed at the surface. When the oxide film is compact, thin and adherent to the metal, this isolates the metal from the corrosive agent, and the corrosion resistance of this one is high (the case of platinum, iridium, gold, copper, silver, wolfram, zinc, lead, nickel, crom, molibden, titanium, etc., that normally do not corrodate). The phenomenon is called metal passivisation. When the oxide film is spongy and nonadherent to the material, this allows permanent contact between the material and the chemical agent, and the corrosion phenomenon continues up to the complete elimination, as it is the case for iron and its common alloys with Carbon – steels and pig irons.

The degradation after the interaction with the environment can be the result of a general corrosion or by pitting corrosion [1, 2].

One can notice that the pitting corrosion is one of the major mechanisms that affect the integrity of the marine structures. As a rule, the pitting corrosion is initiated due to some physical and chemical heterogeneousness [3] on the metal's surface, determined by inclusions, secondary phases, flaws, mechanical degradation.

It is known that the pitting corrosion has a special effect on the fatigue resistance. The fatigue flaws are usually initiated from the zones with pitting degradations [4]. As a result of the interaction between the cyclic stress and the corrosive environment, the cyclic stress favours the pitting process, and the pitting corrosion, as a form of some geometrical discontinuity, leads to the nucleation and later on to the spread of flaws [5].

The concomitant action of mechanical stresses and aggressive environment lead to the degradation of the element areas made of steel or other metallic materials, a process called corrosion under tension and in case of variable stresses - corrosion fatigue, which have different causes and effects as compared to the degradation under the single action of either mechanical stresses or corrosive environment.

The evolution rate of the corrosion under stress and the fatigue process in corrosive environment (fatigue corrosion) is much higher than the two processes considered separately and their effect is not additive (simple overlapping of individual effects), but much more complex.

The complex interaction of the mechanical and chemical factors is highlighted by the fact that the phenomenon of corrosion under stress and the fatigue corrosion can occur in weakly corrosive chemical environments and the mechanical stress producing the process is of low levels, below the material yielding point, in some cases representing only a fraction of its value.

According to the electrochemical theory [11], the occurrence of cracks in the metal under the concomitant action of the corrosive environment and the mechanical stresses is a predominantly electrochemical process and is related to the localization of the corrosion process in various areas of the deformed metal. These areas are considered of high sensitivity for the production of anodic dissolution processes. They are usually located on the border of the crystalline grains and facilitate destruction by intercrystalline corrosion [12]. Thus, the large group of carbon steels and alloys based on aluminium can be destroyed through such a mechanism [13]. However, the sensitivity of these alloys to intercrystaline corrosion is not a sufficient condition for destruction by corrosion under stress. There are such cases when the destruction takes place due to intercrystalline corrosion. This phenomenon is related to the fine structure of the deformed metal. In metals, due to mechanical stresses, the dislocation movement is based on their plane accumulation; they tend to decay by trans-crystalline corrosion, while those with the cell structure dislocations are mainly destroyed by inter-crystalline corrosion.

In metals where there are no local areas favouring dissolution, dislocation migration occurs due to mechanical stresses. In these metals process localization takes place because of the rupture of the protective oxide films [14], which will lead to the formation of new anodic areas, the other areas forming the cathode.

Research [15, 16] has shown that flaws may occur on metal surfaces in those places where the slip bands exit which further result in formation of small pits.

2. Determinations and experimental results

2.1. The evaluation of the corrosion resistance of the steel sheets

In figure 2 it is presented the microstructure of the blank assay before going through corrosion.

Fig. 1. *The surface aspect of the blank assay x200 (before the corrosion)*

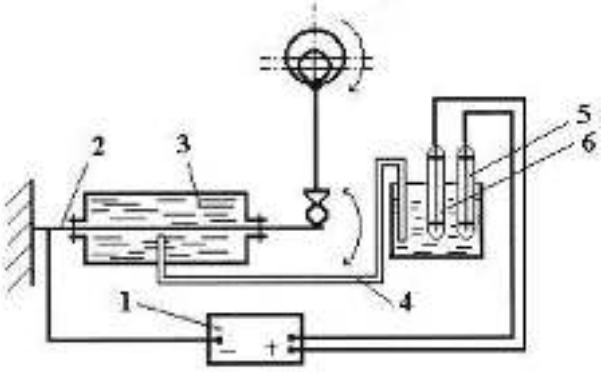

Fig. 2. *Potentiometer device:1 – PGP 201 Potentiostat; 2 – working electrod (WE); 3 – the sollution of 3.5% NaCl; 4 – bridges of salt; 5 – auxiliary electrod (CE); 6 – refernce electrod (RE)*

By means of a potentiometers device (fig. 3) consisting of a PGZ100 All-in-one Potentiostat (1), a saturated calomel electrode as reference electrode (6), a platinum electrode as auxiliary electrode (5) and a sample as working electrode (2), was recorded in situ, the evolution of the electrode potential after the cold plastic deformation and after the natural ageing run for a period of 5 months.

The system was connected to a computer with data analysis software. The samples to be analysed (the working electrode) were isolated at one end before the immersion in the testing solution 0,5N NaCl. The corrosion tests of each sample began with monitoring the corrosion potential (open circuit potential – OCP) after the sample immersion in the testing solution until this **reached the stationary values.**

Seven determinations were made in ≈ 30 minutes and the following results from the table 3 graphically represented in fig. 3 were obtained:

Table 3. *The evaluation of the corrosion resistance of the steel sheets*

	Sample surface	**Rp**	**Calculated Rp t**	**The corrosion speed**	**The calculated corrosion speed**
	[cm^2]	[Ωxcm^2]		[μm/an]	
1	1.8	292.1	525.78	486.3	875.34
2	1.8	321.4	578.52	441.9	795.42
3	1.8	308.2	554.76	460.9	829.62
4	1.8	344.3	619.74	412.6	742.68
5	1.8	333.2	599.76	426.3	767.34
6	1.8	317.5	571.5	447.4	805.32
7	1.8	203.0	365.4	699.6	1259.28

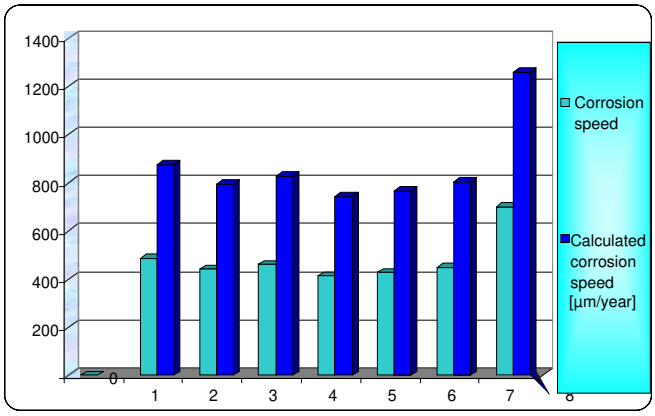

Fig. 3. *The corrosion speed of the steel sheets before the natural ageing*

In figure 4 are presented macrostructural aspects from the surface of the steel samples after three weeks of natural ageing after having been exposed to corrosion.

Figure 4 *The macrostructural aspects of the surface of the steel samples after three weeks of natural ageing, exposed to corrosion; x 100*

After 112 days other determinations of speed corrosion were made in order to observe the differences owed to the process of natural ageing. The corrosion tests began by monitoring the corrosion potential (open circuit potential – OCP) after the sample immersion in the testing solution until it reached the stationary value. In table 4 and fig. 5 are presented the obtained results.

Table 4. *The evaluation of the corrosion resistance of the steel sheets (after112 days)*

	The sample surface	**Rp**	**Calculated Rp**
	[cm^2]	[Ωxcm^2]	
1	1.2	519.663	623.596
2	1.2	539.075	646.890
3	1.2	525.210	630.252
4	1.2	466.697	560.036
5	1.2	476.953	572.344
6	1.2	494.408	593.290
7	1.2	415.654	498.785

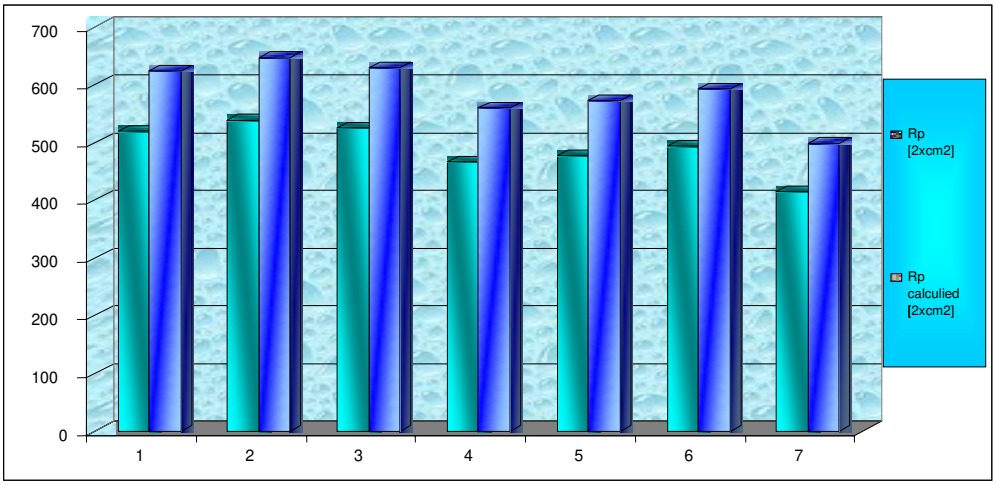

Fig. 5. *The polarization resistance of the steel sheets exposed to natural ageing for 112 days.*

In figure 6 it is presented the evolution of the electrode potential for the two situations – before and after the natural ageing of the steel sheets. As one can notice, the phenomenon of natural ageing leads to moving the potential of electrode towards the more electronegative anodic zone.

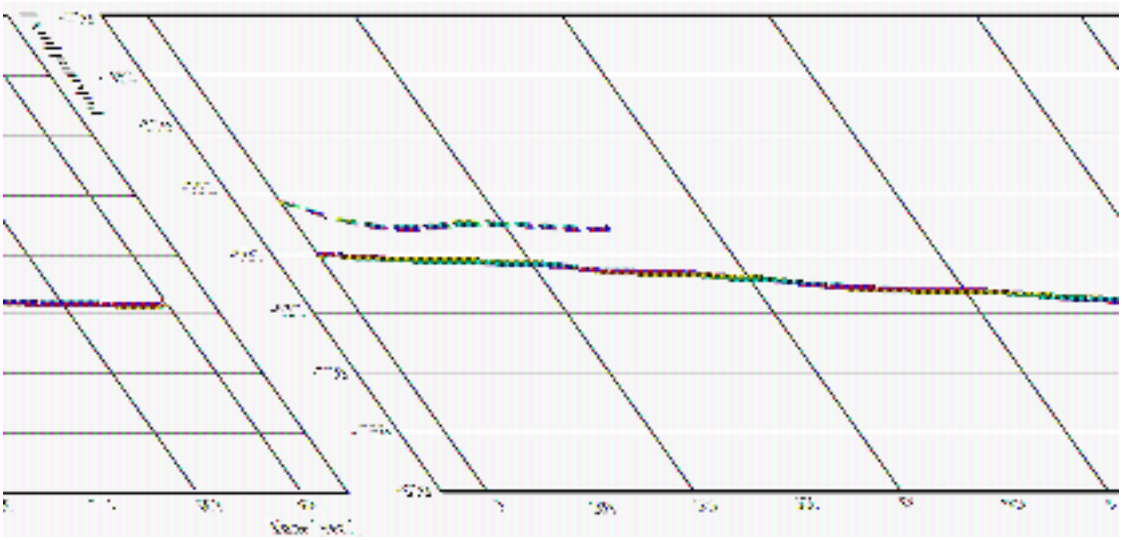

Fig. 6. *The evolution of the electrode potential [mv] in time [seconds] for the steel sheet before (- - -) and after corrosion (——)*

In fig. 7 it is presented the macrostructural aspect of the samples exposed to corrosion after 112 days of natural ageing.

One can notice a noticeable evolution of the corrosion mechanisms.

The corrosion is realized mainly by pitting and in other zones it developed a local corrosion on surfaces identified through the red colour, due to the elimination of a brown-red powder of iron oxide (Fe_2O_3 hard and Fe_3O_4).

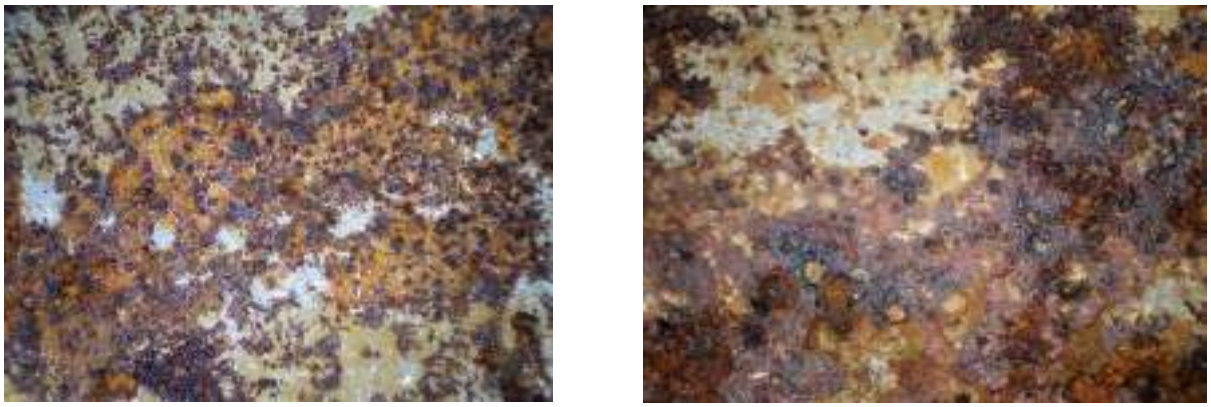

***Fig. 7** .The macrostructural aspects of the steel sample surface exposed to corrosion, after 112 days of natural ageing, x 100*

3. Conclusions

- The research made on the corrosion behaviour of the steel intended for drawing, showed that the phenomenon of natural ageing speeds up the corrosion process.
- Thus, it was highlighted the correlation between the polarization resistance and the corrosion speed. The higher the polarization resistance, the lower the corrosion speed. The samples naturally aged for a period of 112 days presented a much lower polarization speed as compared to the behaviour between the ageing; the polarization resistance is 1,7 times lower and the speed corrosion is much increased by 2,5 times, which requires a very strict control of the coating for the table protection with the objective of increasing the product's lifetime.
- In the tests of accelerated corrosion, we noticed that the main mechanisms of corrosion are the pitting and the local corrosion on zones identified by the red colour due to the elimination of a brown-red powder of iron oxide (Fe_2O_3 hard and Fe_3O_4).
- When exploiting it is necessary to use the covered sheets (with compact films, adherent, without flaws) for increasing the corrosion resistance and the exploiting durability.

References

[1]. Melchers, R. - *The effect of corrosion on the structural reliability of steel offshore structures.* Corrosion Science, 47, 2005, pp. 2391–2410

[2]. Vasudevan, A.K., Sadananda, K. - *Classification of environmentally assisted fatigue crack growth behaviour*. International Journal of Fatigue, doi: 10.1016/j. ijfatigue.2009.03.019.

[3]. Pidaparti, R.M., Rao, A.S. - *Analysis of pits induced stress due to metal corrosion*. Corrosion Science, 50, 2008, pp. 1932-1938

[4]. Rokhlin, Kim, J.Y., Nagy, H., Zoofman, B. - *Effect of pitting corrosion on fatigue crack initiation and fatigue life*. Engineering Fracture Mechanics 2, 1999, pp. 425-444

[5]. Pidaparti, R.M., Potel, R.R. - *Correlation between corrosion pits and stresses in Al alloys,* Material Letters, 67, 2008, pp. 4497-4499

[6]. Hoeppner, **D.W**. - *Fatigue mechanisms*. STP, vol.67, American Society for Testing and Materials, Philadelphia, PA, 1979, pp.841

[7]. Goswami, K., Hoeppner, D.W. - *Pitting corrosion fatigue of structural materials*. Structural integrity in aging aircraft. New York: ASME, 1995, pp. 129-139

[8]. Bastidas-Arteaga, E., Bressolette, P., Chateauneuf, A., Sanchez-Silva, M. - *Probabilistic lifetime assessment of RC structures under coupled corrosion-fatigue deterioration processes*. Structural Safety, 31, 2009, pp.84-96

[9]. Sivaprasad, S., Tarafader, S., Ranganeth, V.R., Tarafader, M, Ray, K.K. - *Corrosion fatigue crack grawth behaviour of naval steels*. Corrosion Science, 48, 2006, 1996 – 2013

[10]. Poursace, A., Hansson, C.M. - *Potential pit falls in assessing chloride-induced corrosion of steel in concrete***.** Cement and Concrete Researche, doi:10.1016/j.cemconres.2009.01.015.

[11]. Hoar, T.P., Hines, J.G. - In: Jour. Iron Steel Inst.vol.5, 1956, p.124,

[12]. Arafin, M.A., Spunzar, J.A. - *A new understanding of intergranular stress corrosion cracking resistence of pipeline steel through grain boundary character and krystallographie texture studies*. Corrosion Science, 51, 2009, pp. 119-128.

[13]. Olache, O.B., Zaro, S.A., Okafor, E.G. - *Analytical correlation between varying corrosion parameters and corrosion rate of Al-4.5Cu/10%$ZrSiO_4$ composite in hydrochloric acid by rate rare earth chloride*. Journal of Alloys and Compounds, 2009, 472, pp. 178-185.

[14]. Hall Jr, M.M. - *Film rupture model for aqueous stress corrosion cracking under constant and variable stress intensity factor,* Corrosion Science, doi: 10.1016/j.cor.sci.2008.08.052.

[15]. Nielson, N.A. - *Nature of initial corrosion of stressed austenitic steel by chloride ions*. In: Corrosion, vol.20, No.4, 1964, pp.104-112.

[16]. Jones, R.L. - *Potential and chloride effects in the stress corrosion cracking of type 304 stainless steel in 290^{o}C water*. In: Corrosion, vol.31, No.12, 1975, pp. 424-431.

THE ANNALS OF "DUNAREA DE JOS" UNIVERSITY OF GALATI.
FASCICLE IX. METALLURGY AND MATERIALS SCIENCE
N^0. 2 – 2009, ISSN 1453 – 083X

STUDY OF ZrO_2/Co-DEPOSITION WITH COBALT FROM CHLORIDE ELECTROLYTE

Lidia BENEA[1] Florentina Simona SORCARU[1]
Pierre PONTHIAUX[2], Francois WENGER[2]
[1]Dunarea de Jos University of Galati, Competences Center: Interfaces - Tribocorrosion and Electrochemical Systems (CC - ITES), Romania.
[2]Ecole Centrale Paris. Laboratoire Génie des Procédées Matériaux (LGPM). France.
email: Lidia.Benea@ugal.ro

ABSTRACT

The metal-matrix composites are materials in which the properties of a metallic host material are modified with addition of a second phase (ceramics) by electrodeposition process. The second phase can be hard oxides or carbides particles or diamond, or solid lubricants or even liquid containing microcapsules. Most composite coatings contain micron-sized particles. The major challenges with the codeposition of second phase particles are the achievement of a high level of codeposition and avoiding the agglomeration of particles suspended in the electrolytes. The poorly homogeneous distribution of second phase particles in the metallic matrix can be detrimental to the mechanical properties. This work shows the most recent results regarding the influence of ZrO_2 bioceramic dispersed in the cobalt matrix during electroplating process from a chloride cobalt electrolyte. The ZrO_2/Co composite coatings were electrodeposited from a suspension of ZrO_2 particles (mean diameter 10μm) in aqueous cobalt chloride electrolyte. Suspension was prepared by adding 20 g/L ZrO_2 particles into solution. Co-deposition of dispersed micro sized particles with cobalt during electroplating process influences the structure and surface morphology of composite coatings obtained. The pure cobalt coating has a rather regular surface, whereas the composite coatings surface has fine different disturbed structure. The composite coating thickness increases with increasing the current density, whereas the content of ZrO_2 particles inside the cobalt matrix decreases with current density.

KEYWORDS: ZrO_2 particles, electrodeposition, composite coatings, cobalt.

1. Introduction

Metal composite materials have found application in many areas of daily life for quite some time. These materials are produced in situ from the conventional production and processing of metals. These innovative materials open up unlimited possibilities for modern material science and development, the characteristics of MMC can be designed into the material, custom-made, dependent on the application.

The advantages of the composite materials are only realized when there is a reasonable cost-performance relationship in the component production. The use of a composite material is obligatory if a special property profile can only be achieved by application of these materials [1-8].

Biomaterial applications make use of all classes of material, metals, ceramics, polymers and composites, divided roughly into three user types. These are:

(i) inert or relatively inert with minimal host response,

(ii) bioactive which actually stimulate bonding to the surrounding tissue and

(iii) biodegradable which resorb in the body over a period of time.

Metals are generally chosen for their inert qualities whereas ceramics and polymers may offer bioactivity or resorption. Composites could combine the properties of metals with ceramics or metals with polymers. The metal-matrix composite coatings are materials in which the properties of metallic host material are modified with addition of a second phase (ceramics, polymers, etc.) by electrodeposition

process [9-15]. Cobalt favors wear resistance at high temperature as it increases the amount of cobalt, the temperature increases and the use of the material. Property due to cobalt crystallographic structure: cobalt crystallizes in cubic structure with girls under 417^{o}C and centered in a hexagonal structure over 417^{o}C [3].

Cobalt is the most widely material for protection of steel against corrosion. Cobalt is more corrosion resistant than steel in most natural atmospheres, the exceptions being ventilated indoor atmospheres where the corrosion of both steel and cobalt is extremely low and certain highly corrosive industrial atmospheres. Electrodeposition offers rigid control of film thickness, uniformity and deposition rate and is especially attractive owing to its low equipment cost. Due to the use of an electric field, electrodeposition is particularly suited for the formation of uniform films on substrates of complicated shape, impregnation of porous substrates and deposition on selected areas of the substrates [4].

Good deposition depends mainly on the nature of bath constituents. Generally, a plating bath contains conducting salts, buffering agents, complexing agents and metal ions. The action of these complexing agents is specific and depends on pH, nature of anion, temperature and other ingredients of the medium. Too many ingredients cause difficulties in maintaining the operating parameters of the bath solution during the plating process. There are many studies on zirconium oxide devoted to extensive research on corrosion resistance [13].

Zirconium oxide, ZrO_2, is considered nowadays one of the most important ceramic materials in modern technology. It has a wide range of industrial applications because of the excellent combination of high flexural strength (~1 GPa) and good fracture toughness, together with its stability at high temperature and its optimal dielectric constant of around 20. It is used for metal coatings, as a refractory material in insulation, abrasives, enamels and glazes, as support material for catalysis and, due to its ion conductivity, it is also applied in gas sensors, oxygen pumps for partial pressure regulation and high temperature fuel cells. Further, ZrO_2 is one of the most radiation-resistant ceramics currently known and therefore has a particular importance in the nuclear industry [14]. In the present work, efforts have been made to the synthesis and characterization of surface modified cobalt with ZrO_2 ceramic particles, in order to obtain a biocompatible material presenting at the same time good corrosion and wear performances. The composite materials were obtained by using dispersed micro sized ZrO_2 particles (mean diameter 10 μm) and cobalt plating electrolyte based on cobalt chloride. The major challenges with the co-deposition of second phase particles are the achievement of a high level of codeposition and avoiding the agglomeration of particles suspended in the electrolytes. However, in the literature, there are very limited studies in the dispersion of inert particles in the cobalt matrix and its influence on the overall properties.

It was used a bath solution without additive because it could give reactions with zirconium oxide (ZrO_2) particles and the results could not have been interpreted properly. It is necessary to note that by involving the particles of zirconium oxide in a cobalt matrix we can obtain materials with properties differing from those of the individual materials.

2. Experimental Set-Up

For electrodeposition we used a cell shown in Fig 1. Cobalt plate of 99.9% purity was used as anode.

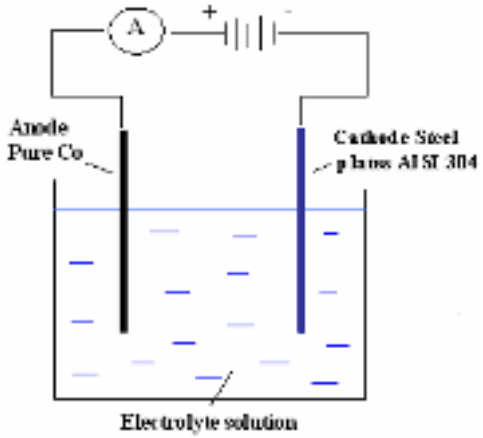

***Fig 1**. Schematic electrochemical cell for electrodeposition*

As cathode we used 304L stainless steel plates whose chemical composition and mechanical properties are presented in Table 1. They degreased with alkaline solution, after being etched with HCl 10% for 1-2 min and washed with distilled water.

***Table 1.** Chemical composition and mechanical properties for 304L stainless steel*

Steel	Chemical composition (%)									Yield strength N mm^{-2}	Max tensile strength N mm^{-2}	Min % total elongation 80 GL mm
	Cr	Mn	Si	P	S	Ni	Cu	Mo	Ti			
304	19,79	1,74	0,17	0,028	0,005	10,02	0,86	0,74	0,15	210-250	520-720	45

The ZrO_2/Co composite coatings were obtained from a suspension of ZrO_2 particles in aqueous cobalt chloride electrolyte having the composition presented in Table 2.

Table 2. *Composition and operating conditions for electrodepositing Co*

$CoSO_4$ x 7 H_2O	20 g/L
$CoCl_2$ x 6 H_2O	300 g/L
H_3BO_3	30 g/L
Temperature	25^{o}C
pH	3.5 – 4
Current density	45.7 – 5.7 mA/cm^2
U	2 V
Time	30 min
Stirred	500 rpm

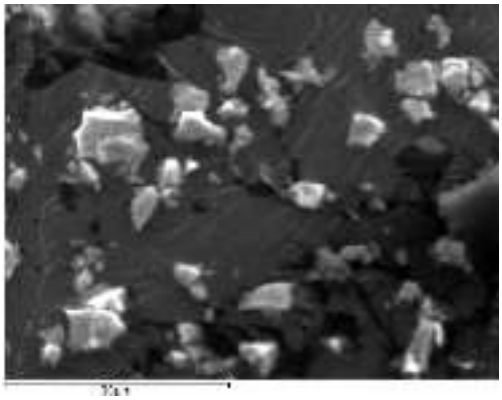

Fig. 2. *SEM image of ZrO_2 particles*

In the second phase dispersed of ZrO_2 were added to electrolyte at 20 g/L and stirred at 500 rpm 24 hours before electroplating. The shape and dimension of ZrO_2 particles are presented in Fig. 2 (SEM image). Cobalt chloride increases the conductibility and ability of uniform deposition and boric acid was used like buffering agent who stabilized the acidity of electrolyte.
The morphology of deposits was examined by scanning electron microscopy SEM coupled with energy dispersive X-Ray analysis (EDX) on surface and cross section of samples. The coating thickness was examined by optical microscopy in cross section of samples as well as by weighting the cathode before and after deposition.

3. Results and discussions

Scanning electron microscopy micrographs of the deposits obtained at two current densities of 45.7 mA/cm^2 and 28.57 mA/cm^2 respectively are shown in Figs. 3-4.

The ZrO_2 particles appear sufficiently well distributed, compact and continuous. Nevertheless, the ZrO_2/Co composite coatings obtained at same current densities as pure cobalt coatings have different shape and grain size than the pure cobalt.

Figure **3** compares a pure cobalt coating and ZrO_2/Co composite coating obtained at 45.7mA/cm^2 current density, 30min deposition time and a stirring rate of 500 rpm (5000x magnification).

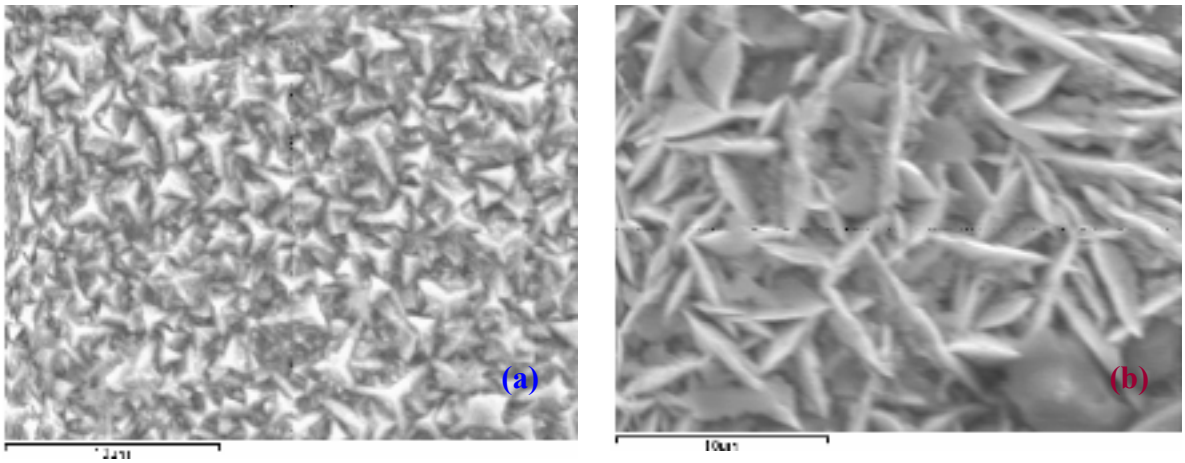

Fig. 3. *SEM surface morphology of (a) pure cobalt and (b) ZrO_2/Co composite coatings obtained at 45,7 mA/cm^2 (5000x)*

Figures 4 compares ZrO_2/Co composite coating obtained at 28.57 mA/cm^2 with pure cobalt coating at same current density, (5000x magnification).

The surface morphology of composite layers is different compared with pure cobalt coating. The pure cobalt coating has a rather regular surface, whereas the composite coatings surface has disturbed surface structure.

By increasing the zirconium oxide particles concentration in the cobalt electrolyte the surface

structure of composite coating is changed more to finer crystallites. The zirconium oxide acts as disturbing the crystals size of electrodeposited cobalt during co-deposition. The zirconium oxide could have an inhibition effect of cobalt crystals growth and a catalytic effect in increasing nucleation sites.

Studying the zirconium oxide distribution in the cobalt matrix on cross sections of coatings, Figure 5 (a, b) by SEM image and EDX element distribution (Zr) shows a good dispersion phase inside cobalt and a good adhesion and uniformity for ZrO_2/Co composite coatings on stainless steel support. The SEM -EDX images of Co and ZrO_2/Co composite coatings, on stainless steel, show the presence of dispersed phase in the cobalt matrix, which is uniformly distributed. Also SEM shows the modification of surface morphologies of cobalt matrix by adding the ZrO_2 dispersed particles.

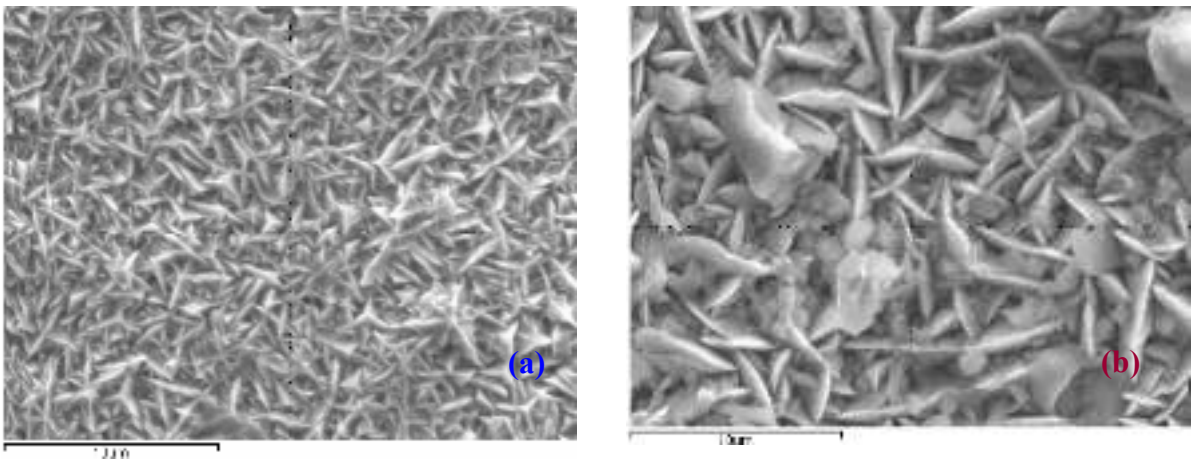

Fig. 4. *SEM surface morphology of (a) pure cobalt and (b) ZrO_2/Co composite coatings obtained at 28,57 mA/cm^2 (5000x)*

The layers thickness of pure cobalt and ZrO_2/Co composite coating calculated by weighting the deposits are presented in the Figure 6. It shows an increasing of coating thickness with increasing of current density for both types of coatings. However the increasing of thickness of ZrO_2/Co composite is a little bit higher compared with pure cobalt at the same current density. This could be explained by increasing the current efficiency of electroplating process in the presence of ZrO_2 dispersed particles in chloride cobalt electrolyte.

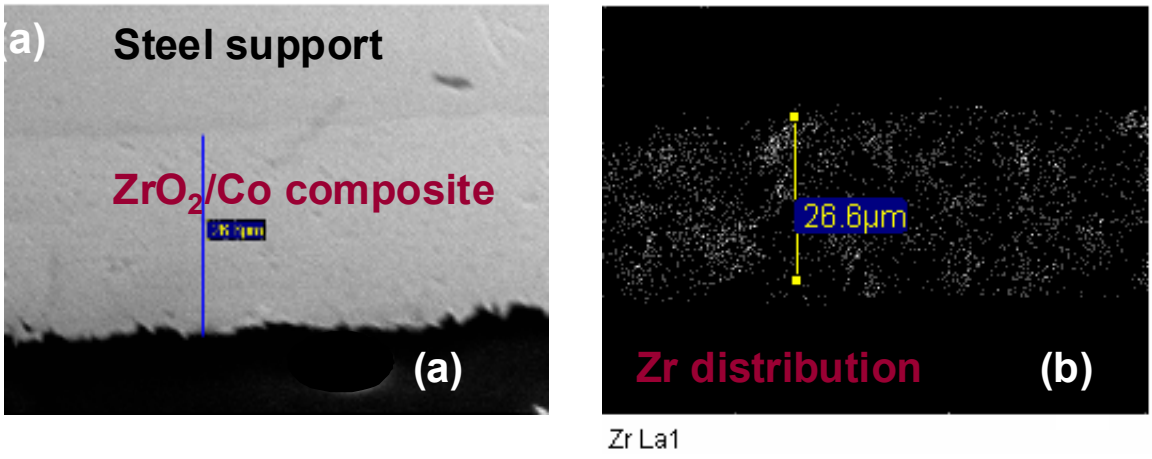

Fig. 5. *SEM image of ZrO_2/Co composite coatings in cross section showing the: (a) coating thickness and (b) uniform distribution of the zirconium oxide inside the cobalt matrix by EDX signal of zirconium in mapping mode*

The coating thickness could be determined more accurately by optical microscopy in cross section, Figure 7. By studying the cross sections of ZrO_2/Co composite coatings it was observed also the good

adhesion and uniformity. The amount of ZrO2 dispersed phase inside the cobalt matrix for ZrO_2/Co composite coatings was determined by zirconium analysis and transformed in zirconium oxide. By increasing the current densities of co-deposition process, the amount of ZrO_2 particles decreases in the composite coatings as it is shown in the Figure 8.

The highest amount of ZrO_2 particles in the composite deposit was found at smallest current density of 5.7 mA/cm^2, respectively. The smallest amount of second phase was co-deposited with cobalt at highest current density of 45.7 mA/cm^2.

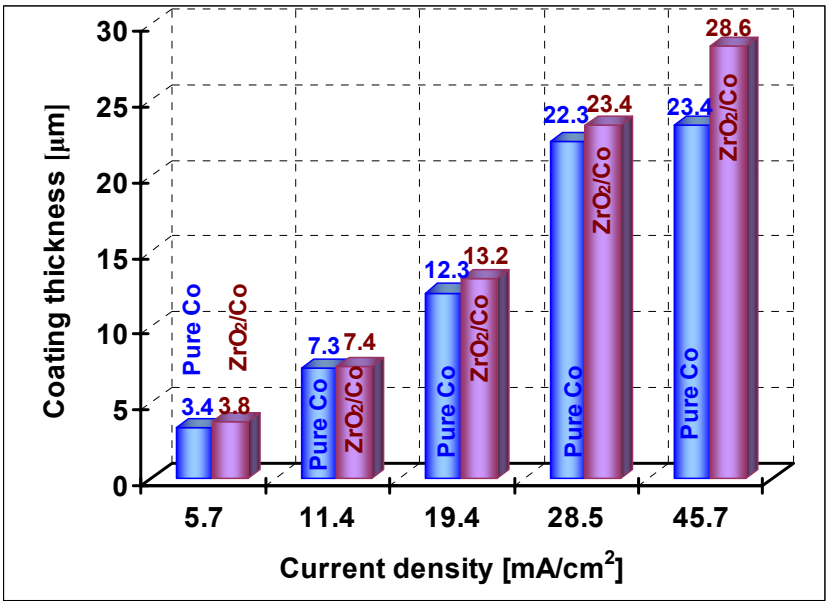

Fig.6. *(■) Pure Co coatings thickness and (■) Co+ ZrO_2/Co (20g/L ZrO_2 in the electrolyte) composite coating thickness versus current density at deposition time of 30 min.*

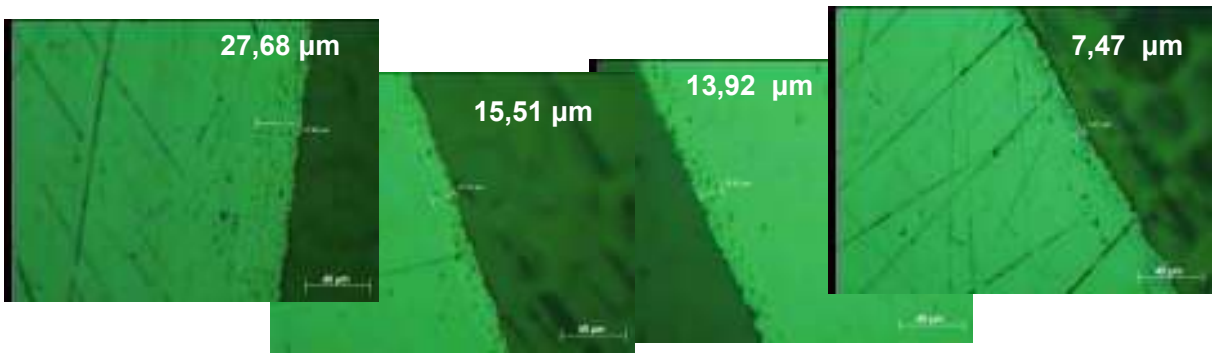

Fig.7. *Coating thickness of ZrO_2/Co composite coatings measured in cross section by optical microscopy, the coatings were obtained at current density from 45,7 mA/cm^2 at 5,7 mA/cm^2 at constant time of electrodeposition*

The data presented in Figs. 6 and 8 suggest that ZrO_2/Co films can only be deposited at low current densities (< 11 mA/cm^2) in order to have the highest amount of ZrO_2 codeposited under the deposition conditions applied in the present study.

The dependence of composition on applied current density is illustrated in Fig. 8. ZrO_2 content in the film decreases from about 9 to 3 wt.% when the current density is increased from 5.7 to 45.7 mA/cm^2.

The easy occurrence of preferred orientation in electrodeposited cobalt has stimulated number of investigations, without however, achieving the stage of a comprehensive view [16]. Cobalt electrocrystallisation has been far less studied compared to Ni. Electrolytic Co crystallizes with both hexagonal closed packed (hcp, α-Co) the stable allotropic modification at temperature below 417^{0}C and face centered cubic (fcc, β-Co) lattice structure,

as first reported by Hull [16]. β-Co is favored by low temperature, high current density and low pH. With the increase of pH the structure becomes complete of the α-phase and deposits texture depends mainly on solution pH and, to a minor extent, on temperature and current density. Our results regarding Co and ZrO_2/Co composite electrodeposition from chloride electrolyte seem to have a two-phase composition and need more inside investigation in order to explain the changes in surface morphology of composite coatings as compared with pure cobalt layers obtained in the same electroplating conditions.

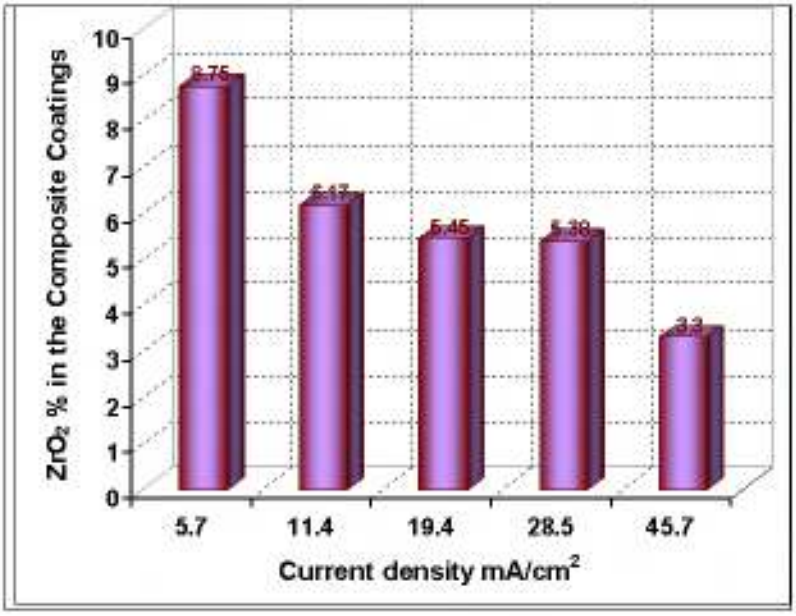

Fig.8. *Content of the ZrO_2 dispersed phase inside the ZrO_2/Co composite coatings versus current density*

Advances in the comprehension of the factors and mechanism participating in Co electro crystallization are expected to contribute to a systematic understanding of the structure-properties correlation of cobalt and matrix cobalt composites.

4. Conclusions

It is feasible to prepare ZrO_2/Co composite coating by properly incorporating the ZrO_2 microparticulates to be co-deposited in the Co plating bath from a chloride cobalt solution.

Coatings thickness increases with increasing current density; the composite layer is almost equal or a little bit higher to that of the cobalt matrix at same current density.

Moreover, the incorporation of the ZrO_2 micro-particulates in the plating bath leads to changes in the morphology of the composite coatings as compared to the pure Co coatings evidenced by SEM studies.

The surface morphology of composite coatings layers is different compared with pure cobalt coated. The regular crystal structure characteristic of electroplated cobalt coatings was distributed by ZrO_2 particles in cobalt electrolyte for electrodeposition. We obtained a very good distribution of ZrO_2 particles on cobalt surface.

The amount of zirconium oxide embedded in the cobalt matrix decreases with the increasing of the current densities of electroplating process.

The adhesion and uniformity of ZrO_2/Co composite coatings were analyzed by SEM and optical microscopy showing good results.

The future work will be done on the following directions: modelling the mechanism of co-deposition and electroplating parameters; correlation of coating thickness with electrodeposition parameters. The mechanical behavior of the modified materials is still investigated by scratch and pin-on-disc wear tests; Electrochemical Corrosion in Simulating Body Fluids (SBF); tribocorrosion studies in SBF; biocompatibility tests; bacteria attachment and biofilm growth.

Acknowledgments

The authors gratefully acknowledge the International Cooperation Project Bilateral Romania-France Programme Humbert Curien (PHC) – Brancusi: ***Etude de dépôts composites nanostructurées pour surfaces fonctionnelles***, number 19603 PC.

References

[1]. Karl U. Kainer - *Metal matrix composite*, Publisher Wiley**,** 2006

[2]. T.W.Clyne, P.J.Withers - *An Introduction to Metal Matrix Composites,* Cambridge University Press, Cambridge, 1993

[3]. L.Benea, P.L.Bonora, A.Borello and S.Martelli - Wear **249** (2002), pp 994-1003

[4]. L.Benea, P.L.Bonora, A.Borello and S.Martelli - Materials and Corrosion, 53 (2002), pp.23-29

[5]. T.L. Yau - *Stress-corrosion cracking of zirconium alloys*, in: R.H. Jones (Ed.), Stress-Corrosion Cracking: Materials Performance and Evaluation, ASM International, Materials Park, OH, 1992

[6]. **A. Heuer, L.W. Hobbs (Eds.) -** Science and Technology of Zirconia, Advances in Ceramics, vol. 3, American Ceramic Society, Westerville, OH, 1981; Science and Technology of Zirconia II, Advances inn Ceramics, vol. 12, American Ceramic Society, Westerville, OH, 1984.

[**7**]. **S. Somiya, N. Yamamoto, H. Yanagina (Eds.)** - *Advances in Ceramics,* vols. 24A and 24B, American Ceramic Society, Westerville, OH, 1988.

[8]. X. Zhao, D. Vanderbilt - Phys. Rev. B 65 (2002) 075105.

[9]. E.J. Walter, S.P. Lewis, A.M. Rappe, Surf. Sci. 495 (2001) 44.

[10]. A. Meldrum, L.A. Boatner, R.C. Ewing - Phys. Rev. Lett. 88 (2002).

[11]. C. Morant, J.M. Sanz, L. Gal´an - Phys. Rev. B 45 (1992).

[12]. V. Fiorentini, G. Gulleri, Phys. Rev. Lett. 89 (2002).

[13]. R. Punthenkovilakam, E.A. Carter, J.P. Chang - Phys. Rev. B 69 (2004)

[14]. D. Hudson, A.Cerezo,G.D.W.Smith, Ultramicroscopy (2008)

[15]. F. Bratu, L. Benea, J.P. Jean-Pierre Celis Surf Coat. Technol 201(16-17), 2007, pp. 6940.

[16]. A. Vicenzo, P.L. Cavallotti; Electrochim. Acta 49 (2004) 4079-4089.

THE ANNALS OF "DUNAREA DE JOS" UNIVERSITY OF GALATI.
FASCICLE IX. METALLURGY AND MATERIALS SCIENCE
N^0. 2 – 2009, ISSN 1453 – 083X

OBTAINING AND CHARACTERISATION OF THERMORESISTIVE PIGMENTS

Andrei Victor SANDU[1], Violeta VASILACHE[2], Ion SANDU[1,3], Mihaela SAVIUC[4], Ioan Gabriel SANDU[4], Ioan Marcel POPA[4]

[1]Romanian Inventors Forum, Iaşi
[2] „Stefan cel Mare" University of Suceava
[3] „Al. I. Cuza" University, Arheoinvest Platform, Iaşi
[4] "Gheorghe Asachi" Technical University of Iaşi
e-mail: sav@afir.org.ro

ABSTRACT

The paper describes the obtaining and chemical and physico-structural characterisation of a green thermoresistive pigment. The pigment is made of ZnO dopped with Sb, Bi, Cr, Co and Fe oxides and it is used at mosaics and stained glass. The procedure is based on a sequential coprecipitation "layer on layer" process in aqueous solution, followed by drying and calcinations at controlled temperature conditions, then grinding in a colloidal mill and mixed with glass powder forming the "frit pigment". This by vitrification and frosting colours superficial the glass.

The powder was analysed by SEM-EDX and DSC.

KEYWORD: chemical doped zinc oxide, thermoresistive pigment, mosaic, stained glass, SEM-EDX, TG/DTA.

1. Introduction

Zinc oxide based pigments are mainly white or grey. They have the disadvantage that is thermoluminiscent and they are degradated under the influence of light radiation.

The obtaining of different colours with high melting temperatures and photo-chemical resistant, from dopped zinc oxide is made on two ways: physical dopation in coloidal mills or chemical dopation by precipitation in aqueous or organic solutions [1-4] The sequential coprecipitation processes are new and allows the obtaining of powder hard fusible and photoresistant. By mixing with glass powder are obtained the frit pigments, which can be applied on the glass surface by vitrification or frosting [5]. In the paper is presented the obtaining procedure and the characterisation of the pigments by SEM-EDX and TG/DTA, for the evaluation of the structure, chemical composition and thermal stability.

2. Experimental Part

2.1. Obtaining of the pigment

The obtaining technology of pale green is based on three coprecipitation processes, as micro-eterogen system, hard soluble, based on oxyhydroxides of Zn, Bi or Sb and different cations of transitional metals, which after filtration, purification and washing are dried and calcinated.

For obtaining the pigment it is used distiled water mixed with $ZnCl_2$, $MnCl_2 \cdot 4H_2O$, $CoCl_2 \cdot 6H_2O$ şi $CrCl_3 \cdot 6H_2O$. After the total solubilisation the dispersion is filtered and mixed with a solution of NH_4OH 10N, till pH of 8.0...8.5. The system obtained is stabilised for 20...30 mins at 50°C, in order for the crystals to grow. After that is mixed with a solution of $SbCl_3$ and $BiCl_3$ with a few drops of HCl. The pH shouldn't be lower than 7.5. The pH can be adjusted with a solution of NH_4OH 10%.

2.2. SEM-EDX

The researches have been carried out with a SEM VEGA II LSH scanning electronic microscope manufactured by the TESCAN Co., the Czech Republic, coupled with an EDX QUANTAX QX2 detector manufactured by the BRUKER / ROENTEC Co., Germany.

2.3. TG/DTA

In the thermal, it analysis was used a Thermobalance Linseis STA PT1600, which allows

fast heating and cooling rates as well as a highly precise temperature control.

The temperature range was from 20 to 1000°C. The device is fully controlled by computer.

3. Results and discussions

In the figure 1 are presented the SEM images of the pigment at 1000X with secondary electrons detector (SE) and back scattered electrons detector (BSE).

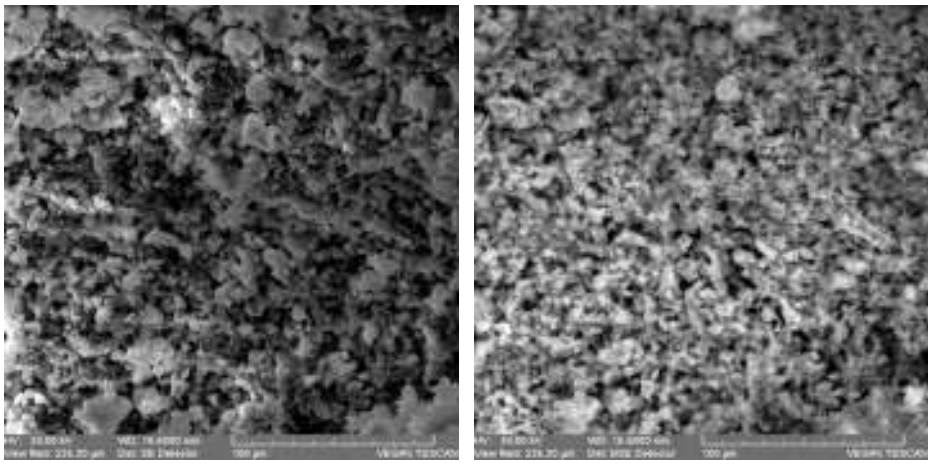

a *b*

Fig.1. *SEM image of the pigment: a – 1000X SE, b – 1000X BSE*

As it can be seen on Fig 1. the grains are uniform distributed with vitroceramic morphology, with the internal phase – grains of doped ZnO and external phase (dispersive medium) – Sb and Bi oxides. The figure 2 represents the EDX spectra of the pigment, followed by the table 1 with the elemental composition.

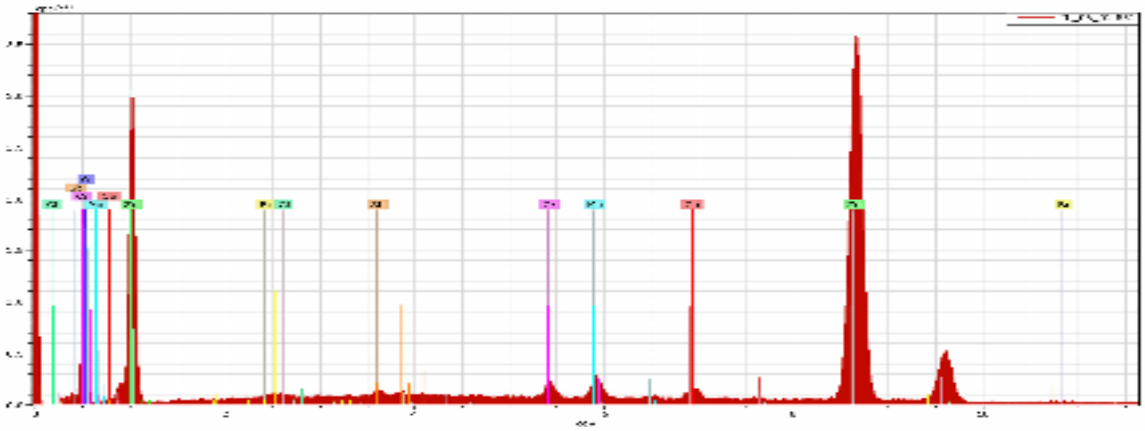

Fig. 2. *EDX Spectra of the pigment*

Table 1. *The Composition of the pigment according to the EDX Spectra from Fig. 2*

Element	Weight, %	Atoms, %	Error, %
Zinc	64.58572	37.09885	1.849272
Manganese	1.11221	0.760413	0.079453
Chromium	1.415505	1.022532	0.091944
Cobalt	1.201922	0.76604	0.068493
Antimony	1.396885	0.430925	0.084291
Bismuth	5.004422	0.899464	0.212932
Chlorine	0.259606	0.275043	0.043605
Oxygen	25.02373	58.74673	7.219001

The elemental composition determined by Xray dispersion proves the presence of the elements used in synthesis at the suggested concentration for obtaining a vitro-ceramic material. Figures 3, 4 and 5, according to the thermal analysis, presents the TG, DTG and respectively DTA curves of the pigment.

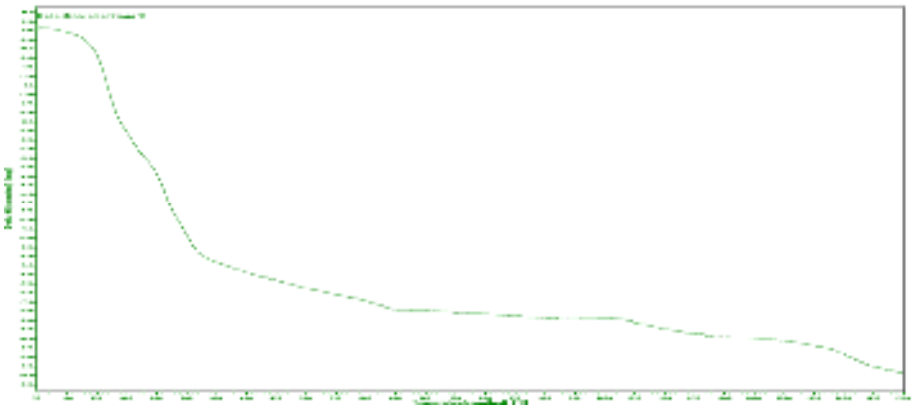

Fig. 3. *TG courve of the pigment*

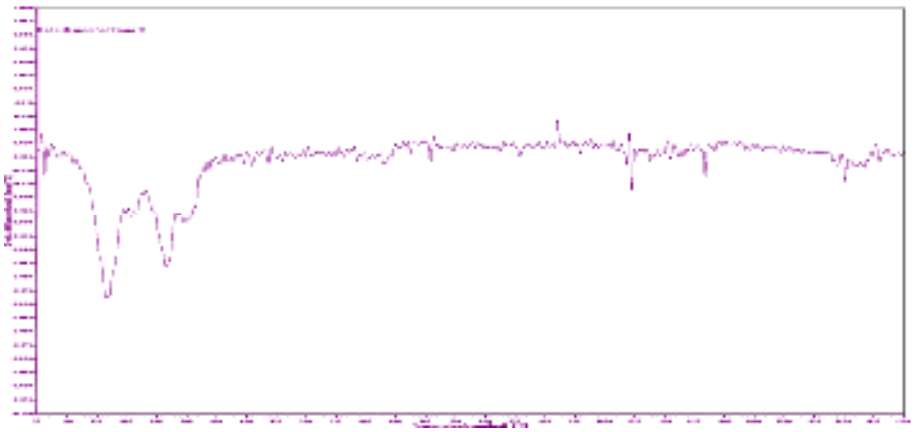

Fig. 4. *DTG courve of the pigment*

Fig. 5. *DTA courve of the pigment*

The thermal analysis data evidentiates the temperature level for the water and volatile compounds removal, followed by structural reformation and the last the vitrification processes at more than 1400°C. The structural re-formation processes are well seen at 250°C, 400°C and 670°C.

4. Conclusions

The SEM-EDX analyses evidentiates that the coprecipitation procedure obtains a phase distribution at higher temperatures.

The particle morphology is vitro-ceramic type with the two different phases, internal (doped ZnO grains) and external one (dispersive medium of Sb, Bi oxydes).

The pigment has a uniform granulometry, high coloration and covering power, chemical and thermal resistance.

The thermogravimetric data confirms that the pigment is resistent in time and at high temperatures.

The obtained pigments can be used for mosaics and stained glass.

References

[1]. Orban, N.- *Pigmenţi anorganici şi organici pentru lacuri şi vopsele*, Centrul de documentare, M.I.Ch., Bucureşti, 1978
[2]. Orban, N.- *Pigmenţi anorganici*, Ed. Tehnică, Bucureşti, 1974, p. 113
[3]. Smocot, R.- *Pigmenţi speciali*, Ed. Inst. Pol. „Gh. Asachi" Iaşi, 1986, p. 64
[4]. Beavis, C.M. - *Pigment,* Dyestufss and Laches, Ed. Chapmann and Halll, London, 1966
[5]. Sandu I., Bounegru T., Sandu I.G., Alexandru A., Sandu I.C.A., Diaconescu F., Sandu A.V.- „*Process for obtaining a green, opaque, photo- and thermoresistant pigment*", Brevet MD3296/30.04.2007

THE ANNALS OF "DUNAREA DE JOS" UNIVERSITY OF GALATI.
FASCICLE IX. METALLURGY AND MATERIALS SCIENCE
N^0. 2 – 2009, ISSN 1453 – 083X

DEVELOPMENT OF BLADE DESIGN FOR SMALL HAWT ADAPTED FOR LOWER VALUES OF WIND SPEED

Nicolae BADEA[1], Nelu CAZACU[2]
[1]Dept.of Electrical Engineering, Dunarea de Jos University of Galati
[2]Dept.of Metallurgy and Materials Science, Dunarea de Jos University of Galati
email: Nicolae.Badea@ugal.ro, Nelu.Cazacu@ugal.ro

ABSTRACT

The paper aims at studing, theoretically and experimentally, the influence of turbines blade profile on output power, in order to decrease effective domain to smaller wind speed, specific to Galati area. Studies have been made using a type of turbine with variable blade profile and another type using a blade with enlarged surface and variable angle of attack. The blade shape was designed for a torque maximization at lower wind speed values. A scale experimental model of blades and of AIR-X horizontal axis wind turbine featuring the optimized blade design was constructed and tested in the low speed wind tunnel. Research results confirm the possibility that using these two methods, the effective increasing performances of the domain of AIR-X wind turbine and increasing energy to be transferred without modifications to the electric generator.

KEYWORDS: wind energy, HAWT

1. Introduction

The extraction of energy from wind energy is the purpose of all wind turbines [1]. The wind energy is in concordance with increasing the renewable energy usage and DER concept [4, 5]. To solving engineering problems for energy caption maximization, a multi criteria design and selection of materials are necessary. Each component of the wind turbine system has to be optimized for that goal.

The paper is based by the theoretic and experimental over the small unit AIR-X wind turbine is used for generation of electricity in residential and commercial locations. Getting electricity from wind conversion intermediate of energy in mechanic work is strongly influenced by the rotation speed of the turbine shaft.

Electric generators work on a specific area of speeds for which feature are useful electricity. Because of that wind turbines are select features according to local wind [1]. The wind turbine theory is based on active disk model (Betz model - 1926). This model was developed by similarity with plane propeller based on principles of mass conservation, energy and momentum [3].

The power coefficient is defined:

$$C_p = \frac{p}{\frac{1}{2}\rho S_p V_\infty^3} \qquad (1)$$

where P – in power, W; ρ – air density, kg/m^3; S_p – surface reference turbine disk.

The induction coefficient is:

$$a = 1 - V/V_\infty$$

A maximum efficiency is obtaining for a=1/3 and Cp=0,593 (Betz coefficient).

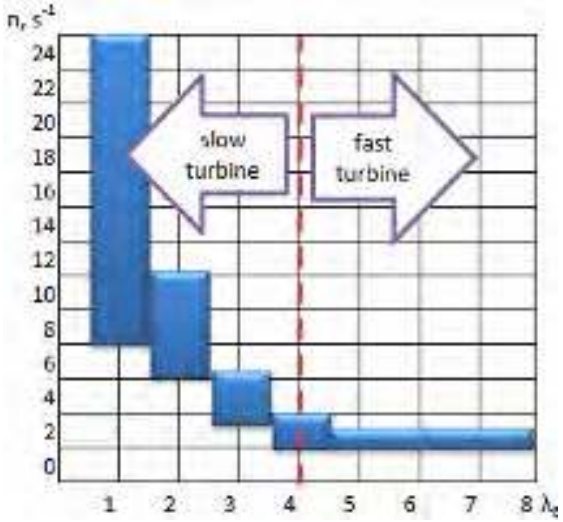

Fig. 1. *Classification of wind turbines based the number of blades and λ_E*

The rotation speed of wind turbine has variability and is dependent on wind speed. Rotation

speed and rotation momentum are actually the most important factors for wind turbine selection.

Specific speed λ_E is defined by:

$$\lambda_E = \frac{\Omega R}{V_\infty}$$

where: λ_E - = specific speed; Ω – rotation speed, s^{-1}; R – maximum length of blade, m; V_∞ - wind speed.

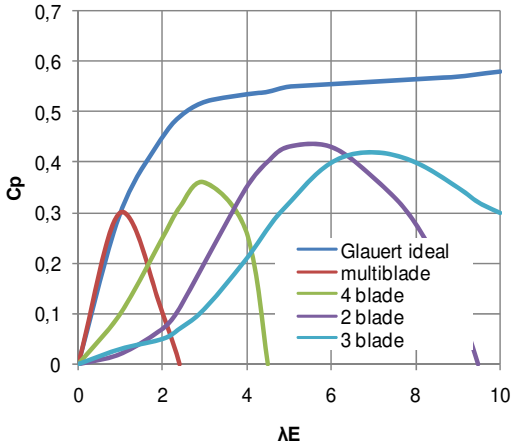

Fig. 2. *The influence of the number of blade over the power coefficient*

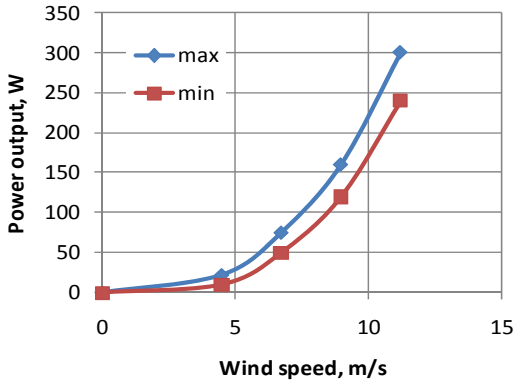

Fig. 3. *Instantaneous wind speed influence over power output for AirX small HAWT*

Increased sensitivity to low wind speeds is achieved by increasing the surface of the blades in plan disk (solidity number σ) or by increasing the number of blades) [1]. High starting torque is obtained by subtracting the increase σ and λ_E.

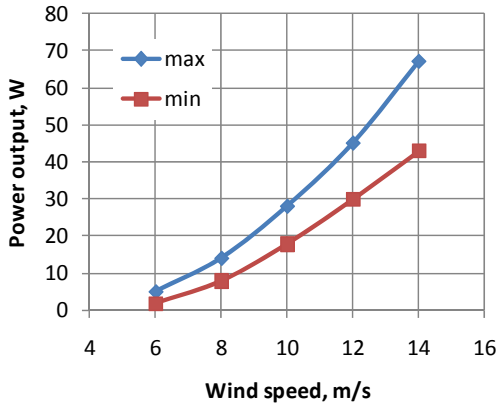

Fig. 4. *Annual average wind speed influence over power output for AirX small HAWT*

The number of blades is chosen in figure 1: λ_E = 1 (8 ... 24 blades), λ_E = 2 (6 ... 12 blades), λ_E = 3 (2 ... 4 blades), λ_E = 4 (2 ... 4 blades) 5 ≥ λ_E (2 ... 3 Performances of wind turbine AIR-X (max. 400W) are dependent on wind speed and are reached at a speed value of approximately 12,5m/s (figure 3). The rotation of electric generator is limited without 170...260 rot/min (which maintaining charging level for 12V battery). The band-width of the AIR-X HAWT is smaller for conditions of Galati city and the wind speed is lower for an efficient exploitation (figure 4).

The approach taken by this work was to improve the efficiency of the AIR-X (400W) wind turbine by modifying the blades. Studies have been made using a type of turbine with variable blade profile and another type using a blade with enlarged surface and fixed angle of attack. Increasing the total blade surface is necessary to increase sensibility of wind turbine for lower wind speed.

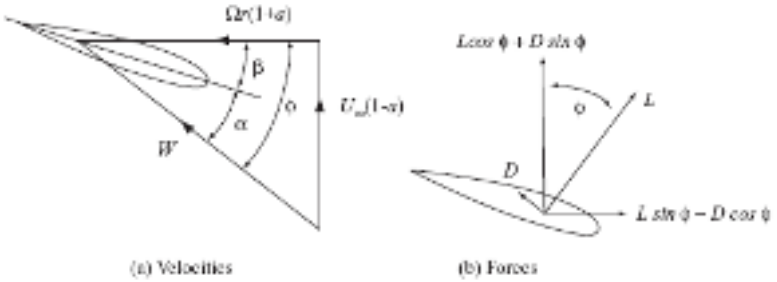

Fig 5. *Blade element velocities and forces*

Blade design is influenced by the mode of operation of the turbine that is, fixed rotational speed or variable rotational speed. Blade element velocities and forces are shown in figure 5. For AirX HAWT a

fixed rotational speed is accepted without modifying the electrical conversion systems. The blades for AirX small HAWT wind turbines must satisfy a wide range of objectives [0]: maximize annual energy yield for specific wind speed distribution, maximum power limitation, resist to extreme conditions, avoid resonance, avoid resonance, minimizing weight and cost, restrictions for up-wind conditions and collisions. The aerodynamic design for geometry (Flex PDE software simulations) was made for experimental blade aerofoil (variable chord based by NACA 4412). Hand built wind turbines blade is easy because the bottom (high pressure) side of the profile is almost flat (Reynolds number of about 5…3 10^5), the maximum lift/drag ratio occurs at a lift coefficient of about 0.7 and an attack angle of 10...20º.

The measurable component of lift force of blade has a normal position on the wind direction and that values will conduce to rotation moment and main energy.

2. Experimental conditions

For behaviour of experimental variable blade for smaller |HAWT, a wind tunnel for small dimensions was assembled. A variable speed of air lamellar flow was obtained by variable speed of a three phase motor fan using a frequency converter. Experiments were made on an original blade and experimental blade with variable profile. Blade was mounted in horizontal position and a compensation weight was necessary. A measure system in correlation with a real working system, with two perpendicular axes was fixed for lift and drag forces. Measurements were made by compensations and dynamometrically. The attack angle of original AirX blade is variable according to the blade length.

Fig. 6. *Experimental wind tunnel and system for variable wind speed*

Original surface (figure 7) are fixed to approx. 0,021 m^2. Experimental blade having a constant attack angle and was fixed at 90, 85 and 80° and a variable surfaces (S1=0.029m^2; S1=0.032m^2; S1=0.034m^2). Increasing the blade surface is necessary to increasing wind turbine sensibility to lower values of wind. Wind speed was measured by LCA 6000 (AIRFLOW Ltd.) anemometer.

Fig. 7. *Experimental variable surface blade and original AirX blade*

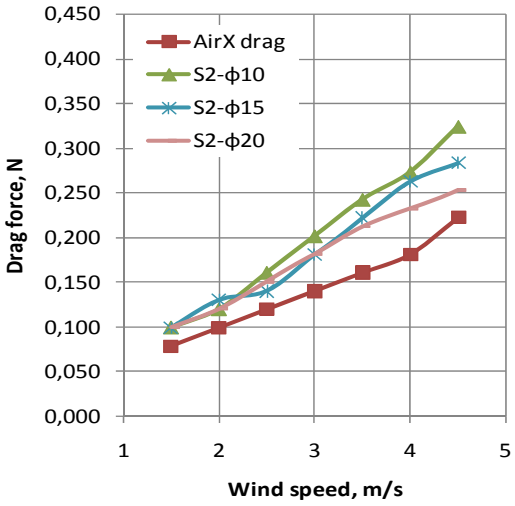

Fig. 8. *Wind speed influence over the drag force for S1*

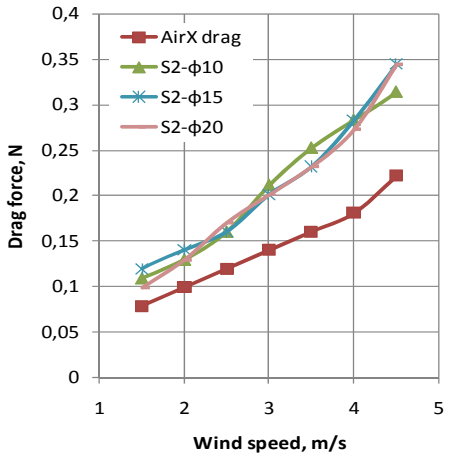

Fig. 9*. Wind speed influence over the drag force for S2*

Some important characteristics of wind tunnel (figure 6) were:

- wind speed range: 0...4.5m/s
- section (1190mm x 500mm)
- total linear length: 3750
- ¼ cylindrical blades for flow deflection (two sets) two mesh (75% transparency) transversal sections in ejector section.

Experimental procedure classical required a "full factorial" array with three factors (attack angle, wind speed and blade surface) and three levels for each factor.

3. Results and discussion

Experimental data were plotted for graphical interpretations. Original AirX blade was a constant reference for experiments.

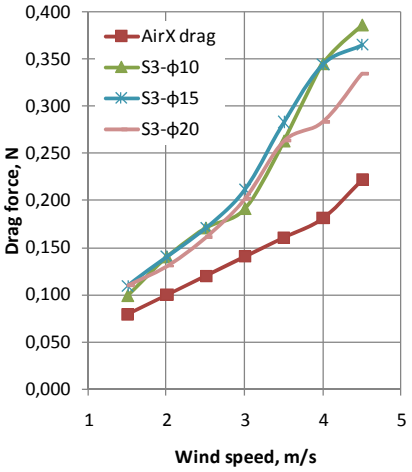

Fig. 10. *Wind speed influence over the drag force for S3*

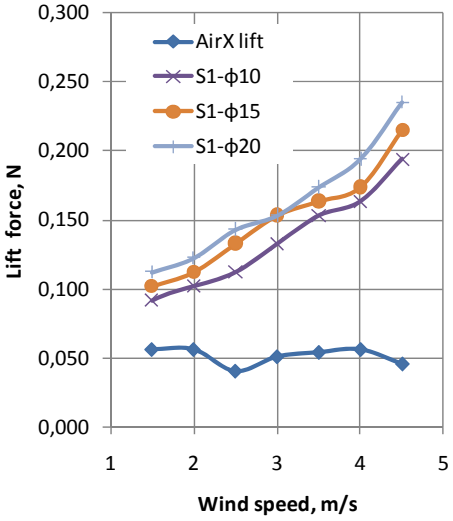

Fig. 11. *Wind speed influence over the lift force for S1*

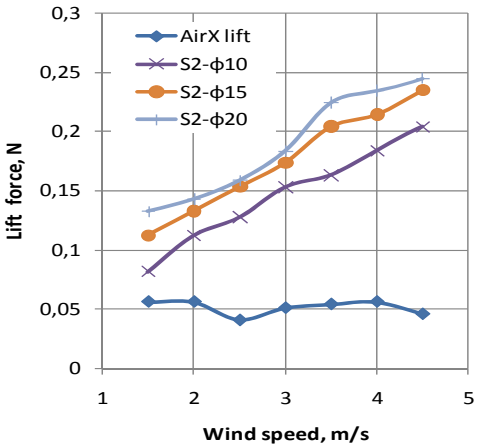

Fig. 12. *Wind speed influence over the lift force for S2*

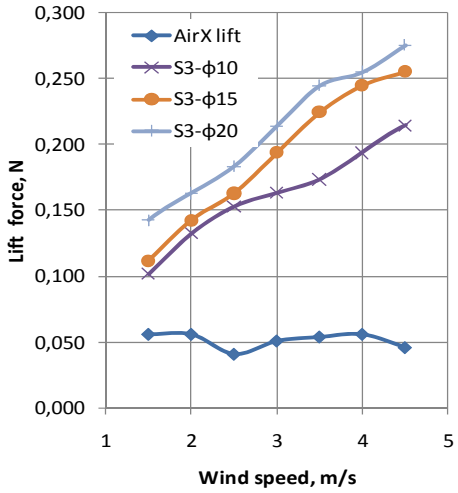

Fig. 13. *Wind speed influence over the lift force for S3*

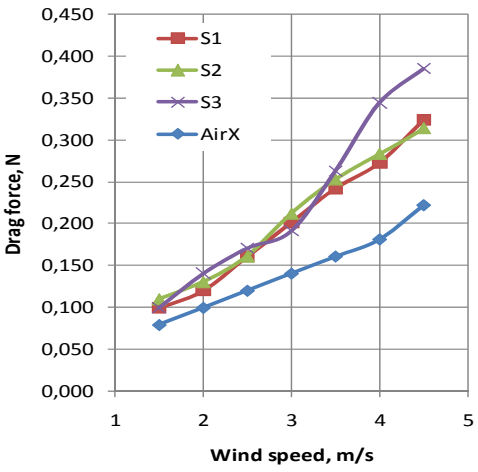

Fig. 14. *Wind speed influence over the drag force for different blade surface and 10° attack angle*

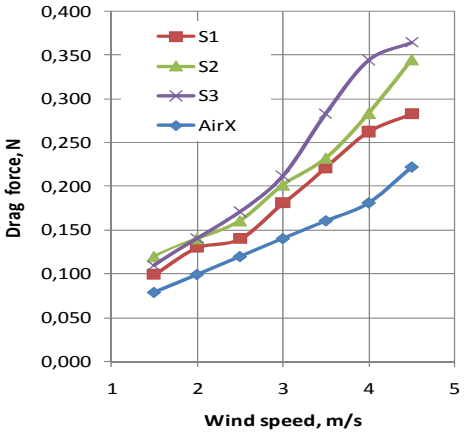

Fig. 15. *Wind speed influence over the drag force for different blade surface and 15° attack angle*

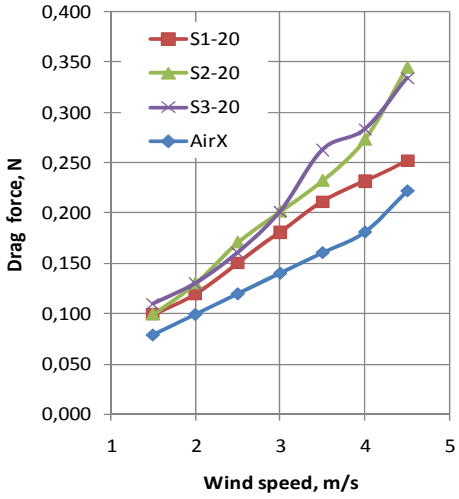

Fig. 16. *Wind speed influence over the drag force for different experimental blade surface and 20° attack angle*

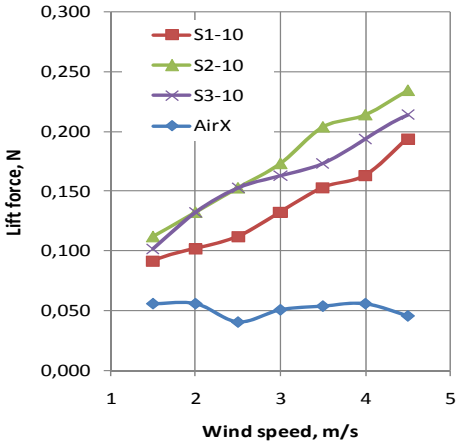

Fig. 17. *Wind speed influence over the lift force for different experimental blade surface and 10° attack angle*

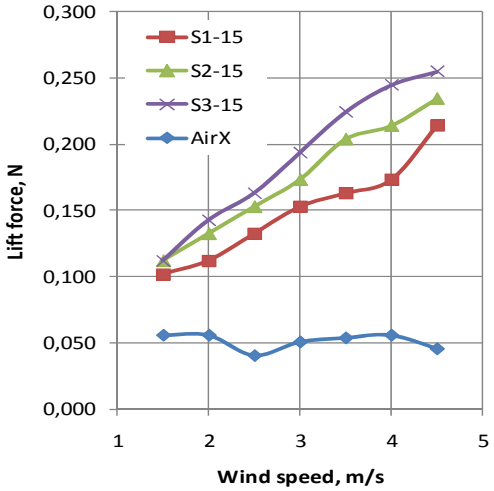

Fig. 18. *Wind speed influence over the lift force for different experimental blade surface and 15° attack angle*

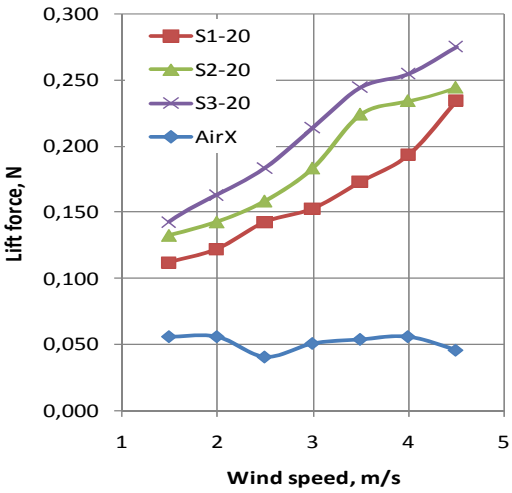

Fig. 19. *Wind speed influence over the lift force for different experimental blade surface and 20° attack angle*

Wind speed influence over drag force for S1, S2 and S3 are shows in Figure 8...10 and influence over lift force are shows in Figure 11...13, all plotted for different attack angle values. At the same attack angle the influence of the wind speed and the surface of experimental blade over drag force and lift force are shown in figure 14...16, respectively figure 17..19.

4. Conclusions

For all experimental conditions (maximum wind speed 4.5m/s) a reciprocal increasing of lift force and drag force are present. Sensibility of experimental blade for lower values of wind speed is in direct dependence of a surface blade and attack angle.

For all experiments, the increasing of attack angle made the lift force. Increasing the maximum lift

force was obtaining for maximum surface of experimental blade (0.28N for 4.5m/s). For original AirX blade the lift force was constant for wind speed 1.5…4.5m/s at value 0.05N. The drag force had a linear increasing from 0.08N at 1.5m/s to 0.22N at 4.5m/s. In these conditions, the original AirX blade are unusable for speed wind at values lower than 5m/s, which are specified in catalog data for the smaller wind turbine.

Decreasing lift forces al lower specified wind speed will determine lower values of output power (figure 1). Output of AirX wind turbine is in direct influence of the annual average wind speed (figure 2).

References

[1]. AirX - *The new 400 watt wind turbine*, Southwest Windpower, 2002

[2]. Burton T, Sharpe D, Jenkins N, Bossanyi - W*ind Energy Handbook*, John Wiley& Sons, Ltd. 2001

[3]. Dumitrecu H s.a. - *Calcului elicei*, Editura Academiei Romane, 1990

[4]. Borbely A, Kreider J. - *Distributed Generation - Power Paradigm for the New Millennium*, CRC Press, 2001

[5]. Berta G.L, Prato A.P, Garbarino L. - *Design criteria for distributed cogeneration plants,* Science direct, Elsevier, Energy 31 (2006) 1403–1416.

THE ANNALS OF "DUNAREA DE JOS" UNIVERSITY OF GALATI.
FASCICLE IX. METALLURGY AND MATERIALS SCIENCE
N^0. 2 – 2009, ISSN 1453 – 083X

OPTIMISATION OF REFRACTORY COMPONENTS OF SLIDING GATE MECHANISM FOR CONTINUOUS CASTING

Viorel MUNTEANU
"Dunărea de Jos" University of Galaţi
e-mail: Viorel.Munteanu@ugal.ro

ABSTRACT

New design techniques have been developed to optimize refractory components of sliding gate mechanism for continuous casting of steel. The overall objective is to increase CC productivity as well as steel quality by using optimized refractory from ladle to tundish. These techniques allow the prediction of steel and refractory chemical interactions and, thus, steel chemistry evolution as well as build up and corrosion occurrence. The recent developments resulted in optimized refractories for sliding gate plates that meet the various continuous casting conditions. Furthermore, fracture mechanical measurements were established as a useful tool in the selection and development of slide gate refractories. The mechanical FEA evaluations take into account specific mechanical behavior of refractory components as well as high temperature evolution of their properties.

KEYWORDS: continuous casting, refractory interactions, plate refractory properties, corrosion, thermal shock resistance

1. Introduction

The development of the continuous casting process resulted in a longer residence time of the molten steel in the steel casting ladle. The ladle stopper could no longer survive in this severe environment; an alternative device had to be implemented.

The ladle sliding gate resolved this problem and allowed longer and more sophisticate ladle secondary metallurgy to be utilized, resulting in better steel quality.

The refractory plates were exchanged after one heat in a similar manner as with stoppers, people quickly realized the potential to achieve multiple heats and to improve the reliability and workability of the systems.

The initial sliding gates were labour intensive and required a lot of care because the refractory plates were assembled with mortar into the mechanism attached to the ladle bottom. Precise torque wrench adjustment of the locking and pressure nut was essential. These rigid systems provided poor thermal expansion compensation.

The refractory materials available were not capable of resisting to the combined effects of high temperature, thermal shock, mechanical stress and corrosion.

Some system suppliers resolved the problems by designing exchangeable cassettes assembled with the refractory components in a separate workshop. Others preferred to manufacture ready-to-use canned refractories installed in "door type" mechanisms at the ladle preparation area.

Although the linear sliding gates with hydraulic actuator became the most popular, some rotary gates with electric drive showed particular merits.

Different kinds of refractory materials were progressively developed to obtain better technical and economical performances and also to improve workers' health environment.

The traditional approach of refractory component development based on empirical evaluation is now showing clear limitations in most demanding fields like steel continuous casting. To improve the performances of steel flow control there were developed new approaches in order to better understand the high temperature behavior of refractory components. One of the main objectives was to precisely evaluate steel refractory interaction to determine corrosion mechanisms. This has been achieved by coupling specific experimentation and thermodynamic evaluation. A second objective has been to determine high temperature mechanical behavior of refractory components, which are composite products. The implementation of specific

properties allows improved design of components and evaluation of material characteristic influences [1].

Finally the development of dedicated fluido-dynamic codes allows the prediction of physical and chemical phenomena occurring during steel continuous casting [2].

2. Steel inclusions and refractory interface

Using thermodynamic modeling, steel inclusion volume and type are calculated based on the total steel composition as shown on the right side of Figure 1. The newly formed oxides at the interface from steel dissolved components (like Al, Mn, Si, Ti) is determined by SEM/EDS observation [3].

The example below corresponds to a Si-killed structural steel with a total amount of 27 ppm of liquid calcium-aluminum silicate inclusions at tundish temperature (1520 °C).

New oxide precipitation at the interface is depending on steel composition and new species coming from the refractory. The new interface formed is reducing the reaction rate mentioned above. A glassy interface will progressively stop the gas transfer to the steel and thus halt the carbon dissolution.

2.1 Corrosion and build up mechanism

A new local equilibrium is subsequently established between new precipitates and existing inclusions in the steel flow [4]. Depending on refractory reactivity and inclusion modification at the interface, one can establish the stability of the steel refractory interface based on the following principles:

2.1.1 Corrosion

When the newly established local equilibrium at the refractory interface is leading to an increased liquid phase, compared to the initial content in steel oxide inclusions, the refractory interface is eroding.

Considering the inclusions in the silicon-killed steel of the previous example, if they come into contact with an alumina-based refractory, those inclusions will dissolve the refractory generating more liquid than the initial inclusion volume.

As can be seen in the model result below, the initial 27 ppm of inclusions only become saturated in alumina and the erosion stops after dissolving 30 g of refractory. In other words, the casting of 1000 T of steel like in the example from Figure 2, has an erosion potential of 30 kg of Alumina, which is in the range of the total amount of flow control refractory in a slab caster.

In Figure 2 at left is the inclusion evolution path from its original composition until the alumina saturation that is detailed semi-quantitatively and qualitatively at the right. The 27 ppm of inclusion in the steel of the example will not attack uniformly the whole refractory. The erosion will be concentrated on the flow regulation control point.

2.1.2 Build up mechanism

When the solid content of the interface is increasing compared to the solid fraction of steel inclusions, an agglomeration or build-up situation occurs at the refractory interface [5, 6]. An example of observed alumina build is shown in Figure 3.

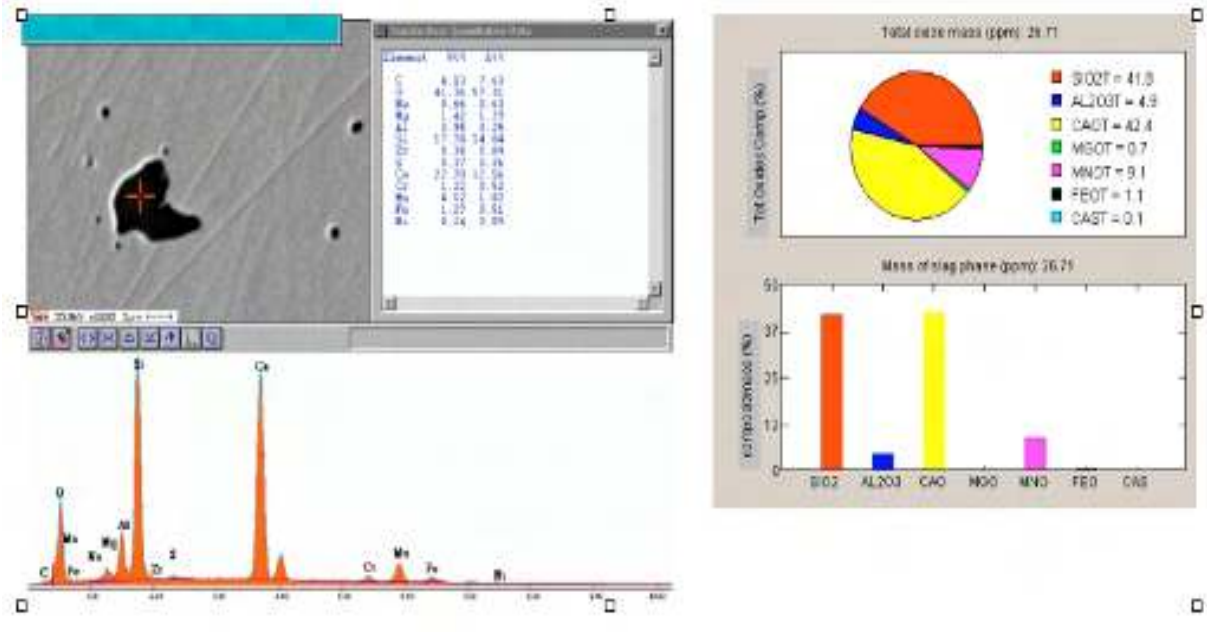

Fig. 1. *Steel inclusion determination*

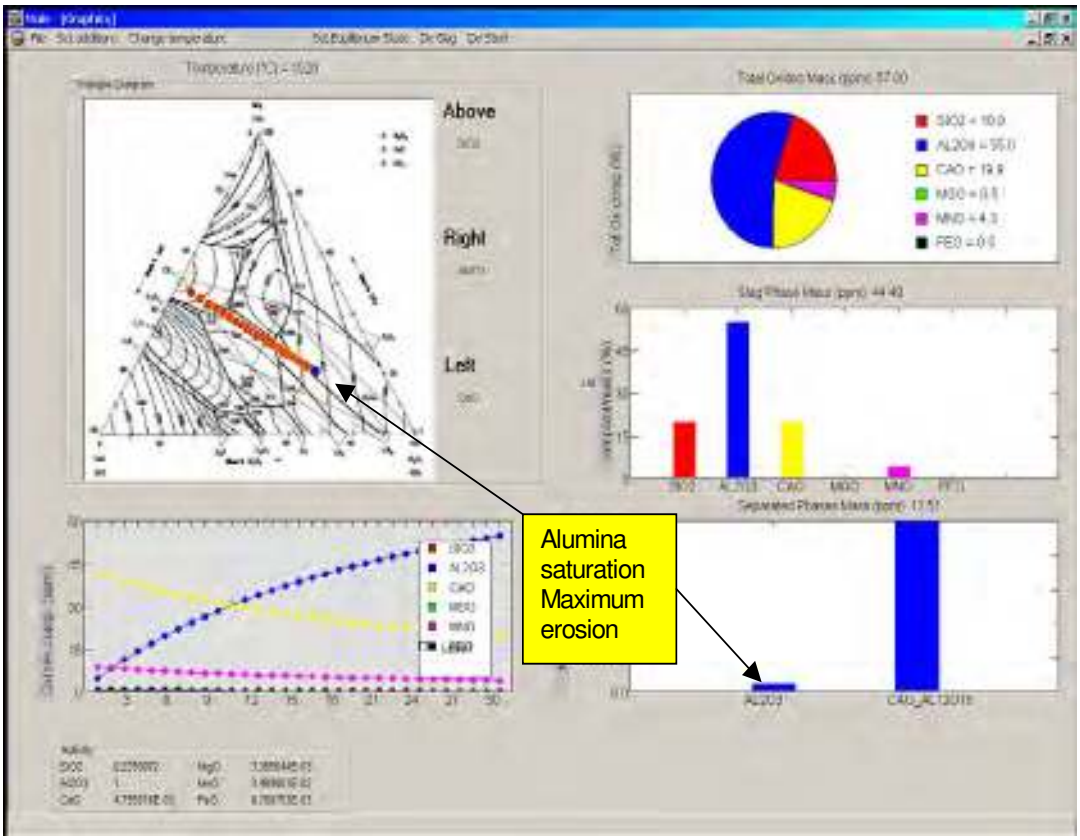

Fig. 2. *Computer modeling of Alumina dissolution in the inclusions.*

The consequences of corrosion and build-up are, for both, a reduction of casting time [7]. So the optimization of the refractory is to obtain a stable interface for a given steel quality.

The thermochemical models developed to simulate refractory interactions and the evaluation of inclusion status depending on steel quality allow a rational refractory choice.

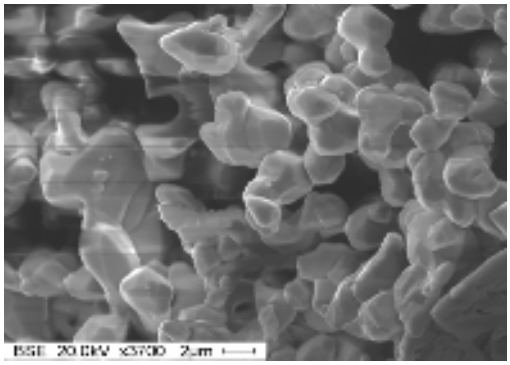

Fig. 3. *Alumina inclusions agglomerated inside a continuous casting alumina/graphite nozzle.*

3. Refractory Properties and Selection

The refractory parts of a slide gate system include the well block, the upper nozzle, the fixed and slider plate, and the lower nozzle. All these parts are subjected to specific in service stresses and must be carefully designed and developed from the specific refractory grades. Typically, the service life of the refractory components is determined by the slide gate plates. These become worn by a combination of affects, including corrosive attack and infiltration by the steel melt, thermal cycling due to multiple rounds of heating up and cooling down, oxidation by oxygen from the air, and abrasion and mechanical stress due to plate movement and clamping of the system [8].

Depending on the casting conditions and the steel grades produced at a specific steel plant, one of the aforementioned wear mechanisms predominates and limits the refractories' service life. Furthermore, the type and size of the slide gate system primarily dictate the type and grade of plate refractory selected.

When examining the plate refractory properties there is a number of major factors to consider. Clearly, the chemical composition is very important. For example, magnesia material is far more corrosion resistant than all other refractories but has limiting mechanical properties, including high thermal

expansion and low grain hardness. There is a clear and well established correlation between high density (low porosity) and high mechanical strength and abrasion resistance [9]. The typical methods to measure these properties are the modulus of rupture (MOR) and abrasion resistance by sandblasting.

These particular properties are very high in both fired and carbon-bonded alumina grades. Thermal shock resistance is difficult to measure for carbon-containing material; therefore, the modulus of elasticity and the MOR are used as criteria for selection. All these techniques are used in slide gate development; however, they are not always sufficient to select the optimum material, particularly in relation to the fracture behavior. Therefore, fracture mechanical methods have been adapted and applied to slide plate material characterization.

4. Fracture Mechanics – a tool for refractory development

Currently, there are two principal test types to analyze fracture mechanics: (1) - determination of the minimum shock to initiate cracking, and (2) - determination of the amount of damage sustained by a fixed shock, or series of shocks [10]. The following parameters have been proposed to predict the results of such tests: a thermal-stress-resistance parameter and a thermal-shock-damage-resistance parameter [11]. The latter, which relates to minimizing the extent of the crack propagation, is considered to be more significant for coarse ceramic slide gate refractories. This relates to the fact that a coarse ceramic structure always contains numerous flaws and that in slide gates cracking due to thermal stress caused by rapid heating by molten steel is unavoidable because of the temperature difference between the casting start-up at 100-200 °C and the flowing molten steel at 1500-1600 °C. The magnitude and nature of the thermal stresses are strongly dependent on various parameters, including the plate shape, the plate fixation method, and possible steel banding. However, the resulting in service crack patterns and crack opening has to be controlled by the refractories' properties [12, 13].

Until recently, the modulus of elasticity and MOR has been employed to estimate the thermal shock resistance of these materials prior to practical tests. However, these relate to crack initiation rather than propagation and do not encompass important factors including thermal expansion.

To estimate thermal shock resistance various thermal stress resistance parameters have been developed. For example, the R_{st} value, which is proportional to the minimum temperature difference required to initiate the propagation of large cracks under thermal shock conditions, is calculated using the following formula:

$$R_{st} = \left(\frac{G_f}{E \cdot \alpha^2} \right)^{\frac{1}{2}} \quad (1)$$

Where R_{st} is the thermal stress resistance parameter ($K.m^{1/2}$), G_f is the work of fracture (J/m^2), E is the elastic modulus (GPa), and α is the thermal expansion coefficient (1/K).

The calculation of R_{st} and other parameters related to crack propagation requires G_f to be determined for the approximate in service temperature in the bore vicinity during casting.

One method to determine G_f in coarse-grained materials is based on a wedge splitting test that enables stable crack propagation in sufficiently large specimens [14]. The principle of the wedge splitting test is illustrated in Figure 4.

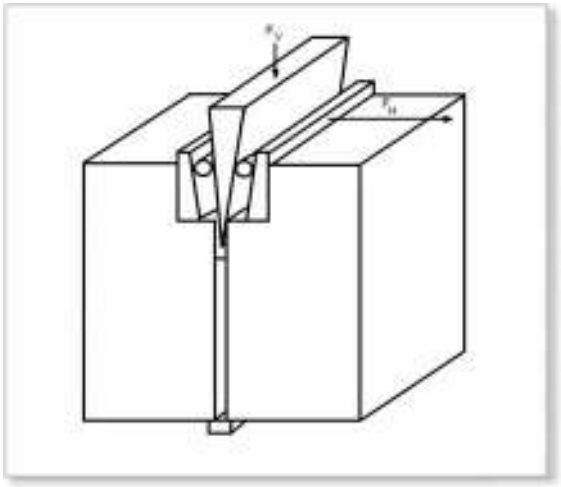

Fig. 4. *The principle of the wedge splitting test. The arrows indicate the vertical force (FV) and horizontal force (FH)*

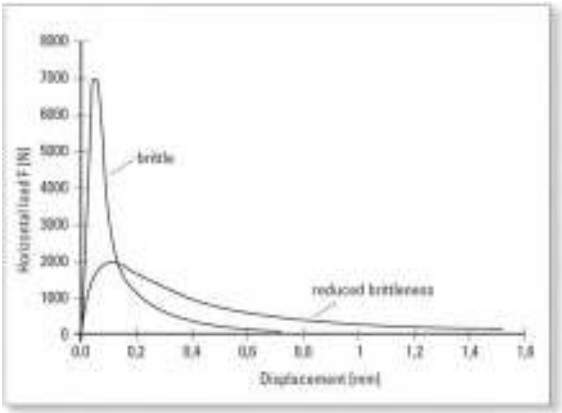

Fig. 5*. Typical load versus displacement graph*

A loading device composed of the wedge, two rolls, and two load transferring pieces is positioned in a specimen groove. Furthermore, the specimen has a starter notch and two side notches. The load of the testing machine is applied vertically to the wedge and both the load and displacement are recorded. A typical load versus displacement graph is depicted in Figure 5. The work of fracture corresponds to the area under the curve. This method has been extensively employed at both room temperature, and at elevated temperatures in an oxidizing atmosphere for refractories with ceramic bonding.

5. Conclusion

Increasing demands for steel quality and continuous casting productivity require new approaches in terms of refractory component development. Advanced refractory design is achieved by coupling dedicated thermochemical and thermomechanical models. When appropriate material behavior at operating temperatures is experimentally demonstrated and validated, model results provide innovative solutions for refractory component optimization. These new approaches, combined with empirical field experience, are necessary to improve current and future steel continuous casting process. In this paper the properties and underlying design principles of the newly developed slide gate generation have been described. Currently, the in service results from the steel plants indicate a significant increase in performance compared to conventional slide gates. Furthermore, the introduction of an adapted wedge splitting test has resulted in a fracture mechanical method for effective slide gate plate refractory selection. The superior in service performance of slide gates can only be achieved by the concurrent development and design of both the slide gate system mechanisms and the appropriate refractories.

References

[1]. Munteanu, V. - *Steel and refractory chemical interactions and mechanical behavior of plates for sliding gate during steel continuous casting* – The annals of "Dunărea de Jos" University of Galati, Fascicle IX. Metallurgy and materials science, No. 2 – 2008

[2]. Munteanu, V. - *Steel flow control of continuous casted slabs using submerged entry nozzle exchange system for tundish* – The annals of "Dunărea de Jos" University of Galati, Fascicle IX. Metallurgy and materials science, fascicle IX, No. 1-2007

[3]. Vermeulen, Y., Simoes, J., Guillo, P., Di Dionato, A. - *Advanced design of refractory components for continuous casting,* Vesuvius International.

[4]. Bennenberg, N. - *Wechselwirkungen Zwischen Feuerfestmaterial und Stahl und deren Einfluß auf den Reinheitsgrad des Stahls*, Stahl und Eisen, 1995, Vol. 115, No. 10, 75-82.

[5]. Singh, S.N. - *Mechanism of Alumina Build-up in Tundish Nozzles during continuous Casting of Al-killed Steels*, Met. Trans., 1974, Vol. 5, 2165-2178.

[6]. Duderstadt, G.C., Iyengar, R.K., Matesa, J.M. - *Tundish Nozzle Blockage in Continuous Casting*, Journal Of Metals, 1968, Vol. 20, No. 4, 89-94.

[7]. Vermeulen Y., Blanpain B., Wollants P. - *Clogging Of Submerged Entry Nozzles*, Steel Research, 2000, Vol. 71, No 10, 391-395.

[8]. Wiesel, M., Mira-Annika Mueller, M.A., Sherriff, R. - *Refractories for Innovative Ladle Slide Gate Systems.*

[9]. Höller, W., Lührsen, E., Wiesel, M. - *Refractory Components for Control and Shrouding of Steel Flow*, CN-Refractories, 1999, 3, 64-71.

[10]. Hasselman, D.P.H. - *Unified Theory of Thermal Shock Fracture Initiation and Crack Propagation in Brittle Ceramics.* Journal of the American Society, 1969, 52, 600–604.

[11]. Hasselman, D.P.H. - *Thermal stress resistance parameters for brittle refractory ceramics: A compendium.* Ceramic Bulletin, 1970, 49.

[12]. Chaudhuri, J., Mitra, S.K., Ghosh, B.N., Kamath, C.D., Swaminathan, K.S. - *Thermal Stress behaviour of Magnesite slide Gate Plates*, Presented Unified International Technical Conference on Refractories, New Orleans, U.S.A.1997, III, pp 1471–1481.

[13]. Glandus, J.C., Boch, P. -*Main methods for thermal shock,* Interceram.1984, 33, 33–37.

[14]. Krobath, M., Harmuth, H. - *Bestimmung der Brucharbeit grobkeramischer feuerfester Werkstoffe bei hohen Temperaturen*. *KeramischeZeitschrift*, 1994, 46.

THE ANNALS OF "DUNAREA DE JOS" UNIVERSITY OF GALATI.
FASCICLE IX. METALLURGY AND MATERIALS SCIENCE
N^0. 2 – 2009, ISSN 1453 – 083X

MATHEMATICAL MODEL COOLING AGGLOMERATION FERROUS IN LAYER

Adrian VASILIU
"Dunărea de Jos" University of Galati
email: avasiliu@ugal.ro

ABSTRACT

Mathematical model is based on discretization agglomeration areas layer deposited on very small. The τ Δ cooling time and the elements of space and elements xi time relationship is discretization as volume control. Based on the mathematical model was presented a program for simulation agglomerates ferrous cooling. The developed program provides the possibilities for the calculation of parameters of air cooler agglomeration.

KEYWORDS: agglomeration, cooling, mathematical model

1. Introduction

Mathematical modeling of physical processes and technology aims to simulate these processes on the computer, and to rich final optimization processes.

Cooling processes accompanied by phase transformations generating tensions between phases frequently met in the process of cooling the ferrous agglomeration. It is therefore necessary to develop three dimensional image applications using simulation calculations and computer graphics, with which endangered areas can be diagnosed.

Cooling agglomeration is a thermo-physical process based on the laws of heat transmission between elements of the cooler. The first step is always a thermal calculation, in which data on the conditions of cooling and other elements of the primary cooling. Results of the calculations give a precise allocation of fixed temperatures cooled material.

In general, this method depending on how to solve the differential equations of complex heat transmission, uses finite differences or finite elements method.

It is based on finite element models that are calculated expansions and tensions arising piece agglomeration. In this way can be localized critical areas in terms of cracks and cooling can be improved.

It is proposed to deal with themes from the heat of a mathematical modeling process of cooling linear agglomeration on which method to use finite differences.

2. Assumptions on the basis of thermal modeling preparation

2.1. Fundamentals of modeling

Material deposited on the whole linear cooling is considered as consisting of a number of variables "z" parallel zones which make up the height of layer deposited on cooling. Each area corresponds to an element of the total material deposited on the cooler being discredited $N_{sj}(j=1…z)$ layer thickness x_j, chosen by the user program.

2.2. Simplifying assumptions

Mathematical model takes into account the following assumptions:

- layer is considered homogeneous, with an equivalent thermal conductivity and a temperature equal to the entire initial mass;
- discretization contact between the layers deposited throughout the cooling process of cooling is fine.
- transmission of heat within the layer takes place primarily by forced convection, heat transfer by conduction in granular materials taking into account a coefficient of conductivity substitution.
- it neglects processes of oxidation, combustion of coke left, or loss of heat and mass training of fine dust particles in the atmosphere;
- it takes account of specific heat changes and thermal conductivity with temperature.

3. Mathematical model equations

Mathematical model is based discretization agglomeration areas layer deposited on cooling time and the elements of space x_i and elements time $\tau\Delta$ very small. The relationship is discretization as volume control. It is used for congested characteristic diagram enthalpy - temperature, because during the calculation to deduct novel temperatures of enthalpy. Thus we can calculate the enthalpy of temperature data fields.

Accuracy depends on the reliability of the thermo-physical quantities introduced as initial data. The accuracy of calculation and simulation is, the greater the discretization space and time is fine. As a result is obtained, the temperature fields and the position represented graphically points inside the layer the temperature has reached a predetermined value.

Mathematical model based on heat transfer between the layers and layer discretization combined depending on the temperatures and thermo-physical characteristics of the layers at the end of the previous time. By thermal analysis processes to determine agglomeration cooling temperatures according to primary and secondary cooling. Calculation of temperature fields is closely related to the geometry of the interior stages. The exchange of heat between layers agglomeration is described by the relationship of heat transport (conduction):

$$\frac{1}{a}\cdot\frac{\partial T}{\partial \tau}=\nabla^2\cdot T+\frac{q_v}{\lambda} \qquad (1)$$

or:

$$\rho_i^k\cdot\left(\frac{\partial H}{\partial \tau_k}+v_r\frac{\partial H}{\partial z}\right)=\mathrm{div}\left(\lambda\cdot\mathrm{grad}\cdot T_i^k\right) \qquad (1.1)$$

Exchange of heat between the air cooling and buried layers is described by the relationship:

$$\alpha_{ai}^k=C\frac{\lambda}{d_p^{1-n}}\left(\frac{w_{ar}}{\nu_a}\right)^n \qquad (2)$$

where:

- v_c - cooling average speed of the z direction;
- z - coordinates the direction of advancement of cooling agglomeration,
- w_r - relative speed of movement through the air layer, [m/s];
- ν - kinematics viscosity of air, [m^2/s];
- d_p - average diameter pieces agglomeration;
- C, n - constant coefficients determined experimentally.

Relationship (1.1) comes from an energy balance applied to an element volume and describes exactly the three-dimensional heat transfer, if data on the materials are known to be sufficiently accurate.

This should be complemented by the conditions in marginal areas agglomeration.

The degree of confidence of using a calculation model is determined, inter alia by the accuracy with which may be represented by the cooling conditions. Where appropriate, the transfer relationship can be simplified by neglecting certain terms.

Average density of layer "i" at a τ_k time is calculated by the relationship:

$$\rho_i^k=\rho_0\frac{T_0}{T_i^k} \qquad (3)$$

Coefficient of low thermal conductivity layers and valid when they are partially cooled to calculate what the relationship:

$$\lambda_i^k=\lambda_0\cdot\frac{T_i^k}{T_0} \qquad (4)$$

The coefficient of heat exchange between two adjacent layers is given by the relationship (for i = 1 at i = N+1):

$$\alpha_{i,i+1}^k=\frac{1}{\frac{x_i}{2\lambda_i^k}+\frac{x_{i+1}}{2\lambda_{i+1}^k}}, \qquad (5)$$

Values $\alpha_{0,1}^k$ and $\alpha_{N,N+1}^k$ are introduced as the initial data provided by the user as a function of temperature:

$$\alpha_{0,1}^k=f_{a,o}\left(T_0^k,T_1^k\right);\ \alpha_{N,N+1}^k=f_{a,N}\left(T_N^k,T_{N+1}^k\right) \qquad (6)$$

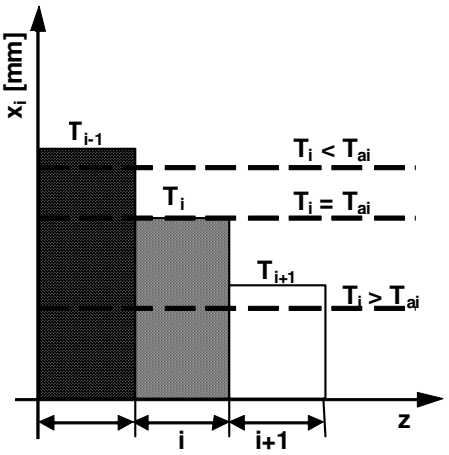

Fig 1. *Air temperature insufflates the layer.*

The three positions differ in position momentary temperature T_i at the layer "i" examined in relation to temperature cooling currently T_{ai}

Assuming that at the time τ_k agglomeration fraction is cooled ξ_1^k, depending $\Delta\tau$ fraction is cooled and the end of time ξ_1^{k+1} on the initial balance equation is:

$$\Delta Q_i^k=\left[\alpha_{i-1,j}^k\left(T_i^k-T_{i-1}^k\right)+\alpha_{i,j+1}^k\left(T_1^k-T_{j+1}^k\right)\right]\Delta\tau-\\-\alpha_{ai}^k\left(T_i^k-T_{ai}\right) \qquad (7)$$

Material granular fraction (agglomeration) when cooled at the time τ_k layer i is given by the relationship:

$$\xi_i^k = \frac{[\alpha_{i-1,i}^k(T_i^k - T_{i-1}^k) + \alpha_{i,i+1}^k(T_i^k - T_{i+1})]\Delta\tau - \alpha_{ai}^k(T_i^k - T_{ai})}{x_i \cdot c_i^k \cdot \rho_i^k} \quad (8)$$

so:

$$\xi_i^{k+1} = \frac{[\alpha_{i-1,i}^k(T_i^k - T_{i-1}^k) + \alpha_{i,i+1}^k(T_i^k - T_{i+1}^k)]\Delta\tau}{x_i \cdot c_i^k \rho_i^k} + \xi_i^k \quad (9)$$

If ξ_i^{k+1} is not converged in the range [0, 1], then the calculated temperature final layer "i" is reviewed with the following relationship:

$$T_i^{k+1} = T_i^k - \frac{\Delta Q_i^k}{x_i \rho_i^k c_i^k} = T_i^k - \\ - \frac{[\alpha_{i-1,i}^k(T_i^k - T_{i-1}^k) + \alpha_{i,i+1}^k(T_i^k - T_{i+1}^k)]\Delta\tau - \alpha_{ai}^k(T_i^k - T_{ai})}{x_i \rho_i^k c_i^k} \quad (10)$$

In case of fig.2b using the relationship:

$$T_i^{k+1} = T_i^k - \frac{[\alpha_{i-1,i}^k(T_i^k - T_{i-1}^k) + \alpha_{i,i+1}^k(T_i^k - T_{i+1}^k)]\Delta\tau}{x_i \rho_i^k c_i^k} + \\ + \frac{\alpha_{ai}^k(T_i^k - T_{ai})}{c_i^k} \quad (11)$$

4. Application model

Based on the mathematical model presented was a computer program for simulation study agglomeration ferrous cooling. The program developed provides the following possibilities:
- it can study and plot the time variation of temperature in any layer (format) on the height of material deposited on cooling;
- may be set during the cooling of noise at any point from the cooler agglomeration;
- can determine the position of points inside the layer when the temperature has reached a predetermined value;
- can study and plot the temperature distribution width cooler at a time;

It can track a crowded crossing in the cooling time or the equivalent, in the direction of travel.

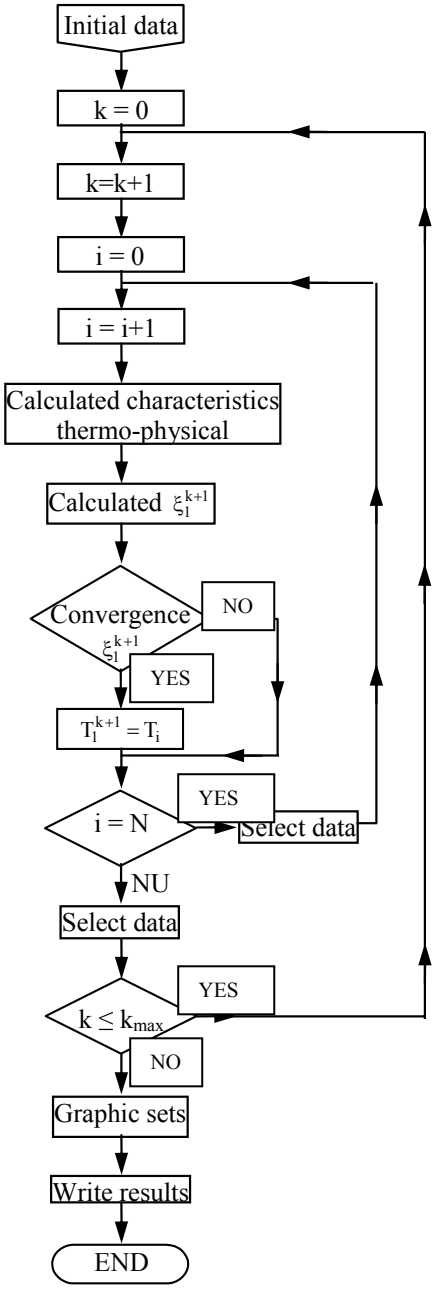

Fig. 2. *Logic diagram of the cooling agglomerate*

5. Results obtained

Based on the mathematical model presented it was created a computer simulation program for studying agglomeration ferrous cooling.

With this, the density of heat flow exhaust unit is expressed in terms of feature blowing air, as follows:

$$q = \alpha_{ai}^k \cdot (T_i^k - T_{0a}) \quad (12)$$

Other conditions have been marginal compared to other parts of the surface noise. To describe the heat discharge into the atmosphere has established empirical relationships. Evacuation to heat carts often modeled with an index of transmission of heat having the shape of the relationship (12) is usable on a length of contact.

Calculations were carried out with a large enough number of data fields. To decrease the duration of the calculations is usually accepted the hypothesis that the transport of heat conductivity in the direction "z" (in the horizontal direction in the sense of movement cooling) is negligible compared to the transport of heat by convection and conduction in the direction perpendicular to the layer (output air) and that the process is in stationary state. Under these assumptions, to an agglomeration position on the direction of the exit time τ and z are linked by the relationship $z = v_r \cdot \Delta\tau$. It can track an agglomeration crossing in the cooling time or the equivalent, in the direction of travel.

Mathematical program is complemented with a graphical program that allows tracing of the temperature curves of the type: $T^k = f(x_i)$ or $T_i = f(\tau_k)$. Cooling curves for a total crowded with $T_{initial}$ = 800 ^{0}C and T_{final} = 86 ^{0}C are shown in figure 3. Results graphic process cooling agglomeration (depending on overall height a end length).

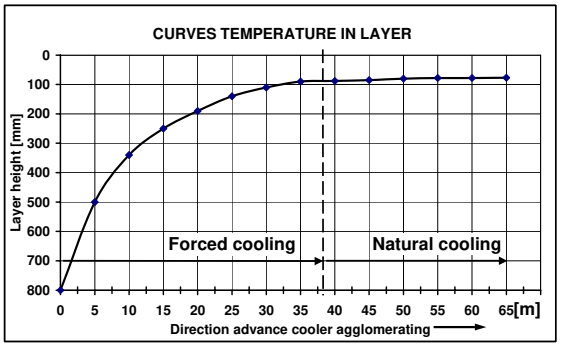

Fig. 3 *Curves of temperature distribution*

6. Conclusions

- The installation of cooling agglomeration is a whole in which various operations and processes are grouped into subsystems which can establish a relation based on the flow technology; they are equipped with peripheral devices for measurement and control.
- The heat from the cooling agglomeration, takes place in a system with many components and a small time interval, the noise temperature decreases rapidly from 800 - 900^{0}C to temperatures of 85 - 90^{0}C.
- Cooling is achieved by injection of cold air down through the top layer of material, with fans. The speed of cooling is critical to obtain agglomeration quality flow; the blow through cooling can be adjusted depending on the parameters of real operating cooler.
- To review the operation of the cooling of the agglomeration and establish the parameters that characterize the preparation process it is suggested to balance the heat.
- Knowledge of heating elements allows the required balance of flow of cooling air, the characteristics of thermal plants and cooling the quantity of heat entering and leaving the outlines of cooler balance. Based on these, we may act to reduce losses and improve thermal efficiency
- Mathematical model is based discretization agglomeration areas layer deposited on cooling time and the elements of space x_i and elements time $\Delta\tau$ very small. The relationship is discretization as volume control.

The program developed provides the following possibilities for the calculation of parameters of the agglomeration cooler:

- It can study and plot the time variation of temperature in any layer on the height of material deposited on cooling;
- It can study and plot the temperature distribution width cooling at a time;
- It may be set during the cooling of noise at any point from the cooler;
- It can study the influence of technological parameters on the process of cooling from the cooler.

References

[1] Gupta, S.S., ş.a. -*"Mathematical model of air flow during iron ore sintering process",* Iron and Steelmaker, pp.35-41 2000.
[2] Taloi D, ş.a -"*Optimizarea proceselor metalurgice*", Editura Didactică şi Pedagogică, Bucureşti, 1998.
[3] Vasiliu A. - „*Modelarea matematică a proceselor din instalaţiile de aglomerare a minereurilor de fier în vederea conducerii complexe a acestora*", Teză de doctorat U. P. Bucureşti, 1998.

THE ANNALS OF "DUNAREA DE JOS" UNIVERSITY OF GALATI.
FASCICLE IX. METALLURGY AND MATERIALS SCIENCE
N^0. 2 – 2009, ISSN 1453 – 083X

ALUMINA POWDER PROPERTIES OBTAINED BY NEUTRALIZATION PROCESS OF SODIUM ALUMINATE

Mitar PERUŠIC[1],Vladan MIĆIĆ[1],Zoran OBRENOVIĆ[2], Radislav FILIPOVIĆ[2]
[1]Faculty of Technology, University of Eastern Sarajevo, Karakaj bb, Zvornik, Bosnia and Herzegovina
[2]Factory of Alumina "Birac" Zvornik , Bosnia and Herzegovina
e-mail adress: Vlado21micic@ptt.yu

ABSTRACT

Today, the most production of alumina is used for aluminum production [1, 2] (metallurgy alumina), minor production of alumina is used for special purpose, as fire-resistant materials, electro porcelain and etc., and because this alumina are called special alumina. For production some types of special alumina, as activated alumina (alumina with good adsorption properties) Bayer process is not optimal. Aluminum-hydroxide (gibbsite) obtained with this procedure have small specific area, approximately ~10 m^2/g, and it was thermal treatment on 400-500°C given γ-Al_2O_3 with up specific area around 250 m^2/g. Some physical-chemistry properties (adsorption's properties) of obtained alumina under these conditions are unsatisfactory for requirement in last time. High specific area, and also good adsorption properties of activated alumina, can be reached by using different procedures of synthesis starting aluminum–hydroxide with adjusting synthesis conditions and later thermal treatment. The aim of this paper is research powder properties of aluminum hydroxide obtained by neutralization process of sodium aluminates.

KEYWORDS: Alumina, Bayer process, Specific area.

1. Introduction

For production some types of special alumina, like as activated alumina (alumina by good adsorption properties), Bayer process is not optimal method. Aluminum-hydroxide (gibbsite) obtained by this procedure has little specific area, approximately ~10 m^2/g, and it is thermal treatment on 400-500°C give γ-Al_2O_3 with up specific area 250 m^2/g [3]. Some physical-chemical properties (adsorption's properties) obtained alumina under these conditions is unsatisfactory for requirement in last time. A typical physical–chemistry characteristic of activated alumina was given in table 1.

High specific area and good adsorption properties of activated alumina can be reached by using different synthesis procedures of starting aluminum hydroxide with adjusting synthesis conditions and supplementary thermal treatment.

The broadest application for production of aluminum-hydroxide as starting raw material for obtaining activated alumina two procedures was found:

- Deposition from acid solutions salts of aluminum (sulfate, nitrate) with basic solution, as NH_3,
- Deposition from basic solution (aluminates) with acids as H_2SO_4, HNO_3, HCl.

Table 1. *Typical physical–chemistry characteristics of activated alumina*

Properties	Values
Specific area, (m^2/g)	~350
Middle diameter of pore, (A)	max. 100
Specific volume of pore, (cm^3/g)	around 0.5
XRD-phase of alumina	amorphous, γ
Statistic adsorption, (%) -at pH 60 - at pH 100	 22 43
Contents of Al_2O_3, (%)	93
Loss by heating, (250-1200°C)	6.5

In this paper for obtained aluminum hydroxide as starting raw material for obtained activated alumina, was used neutralization of sodium-aluminates solution with sulfuric acid. This process consists of two phase:

- First phase, neutralization free NaOH,
- Second phase, hydrolysis of sodium-aluminates, when we have deposition solid phase of aluminum - hydroxide.

Thermal activation this obtained aluminum–hydroxide is made activated alumina. In function from pH aluminates solution, in neutralization process of sodium-aluminates can be obtained three crystal phases [4-6]: boehmite, bayerite and gibbsite. In Bayer process are made gibbsite only. In this paper we have one aim, and it is to show how phases structure, size of primary and secondary particles influence to specific area of aluminum-hydroxide powder.

2. Experimental part

Sodium–aluminates with small and high caustic module and sulfuric acid with defined concentration were used for experimental research and results were presented in this paper. Sodium–aluminates solution with small and high caustic model was made in Factory "Birac" Zvornik (caustic module of aluminates solution are defined as mole ration caustic basic Na_2O_k and Al_2O_3 in alumina solution) have been used in these research. Starting aluminates solution had concentration 150-155 grams of $Na_2O_к$/l, and then dilution to concentrate of 30 and 85 grams of $Na_2O_к$/l. The temperature of neutralization aluminates solution has been 30 and 70°C, and dripping time sulfuric acid in aluminates solution were 30, 60 and 180 minute. Samples of synthesis powder were marked: A,H^{T}c - Sт и A,M ^{T}c- Sт where is:

A- Marked sample of aluminum – hydroxide powder,

M, H- marked small and high caustic model of aluminates solution,

C- Marked concentration of aluminates solution, [g $Na_2O_к$/l],

T – Marked temperature neutralization of aluminates solution, [°C],

S- Marked neutralization of aluminates solution with sulfuric acid

τ -marked dripping time sulfuric acid, [min.].

Qualitative sample identification was performed on x-ray powder (XRD) type PHILIPS PW1729.

Estimation phase's structure in synthesis sample was performed using equation (1)

$$Fi = \frac{Ii \cdot Bi}{I_B \cdot B_B + I_{BAY} \cdot B_{BAY} + I_G \cdot B_G} \qquad (1)$$

Where are:

Fi –part of observed phase,

I_i- the highest intensity of peak,

B_i-broad on half of highest peak,

Roentgen analyze was used for calculating size of primary particle using Sheerer formula:

$$d = \frac{0{,}9 \cdot \lambda}{B \cdot \cos\theta} \qquad (2)$$

Where are:

d - size of primary particle [nm],

λ - wave length of X-ray (λ =0,154 nm),

B - broad highest peak on half, [rad]

Θ - half angle diffraction on highest peak, [°].

Calculation middle diameter size performed on apparatus COULTER COUNTER T A-II. Calculation specific area performed with BET method on apparatus type "FLOWSORB".

3. Results and discussion

In process neutralization aluminates solution by sulfuric acid can appear three crystal phases:

- Boehmite (marked B),
- Bayerite (marked with Bay),
- Gibbsite (marked with G).

In dependence (function) from neutralization condition can appear samples which consist all three crystal phases (fig. 2.), samples which consist only bayerite and gibbsite (fig. 3.), and sample which consist only boehmite phase (fig. 4).

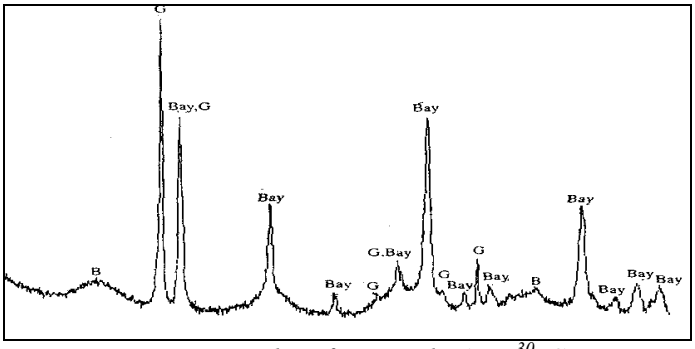

Fig. 2. *X-ray data for sample $AM_{30}^{30}\_S_{180}$*

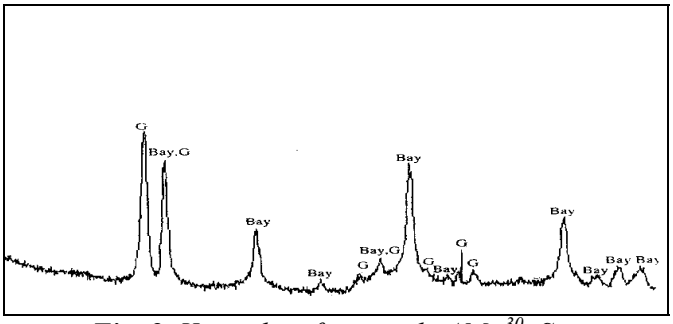

Fig. 3. *X-ray data for sample $AM_{85}^{30}\_S_{180}$*

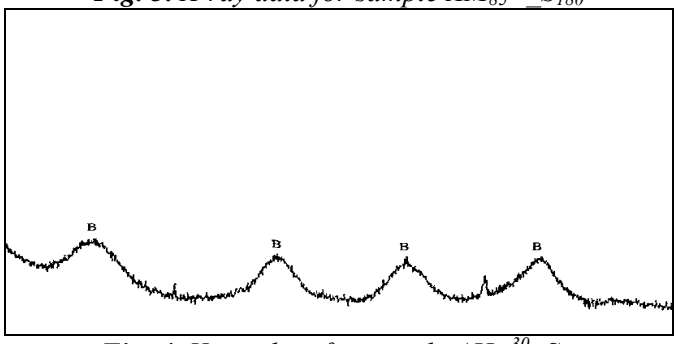

Fig. 4. *X-ray data for sample $AH_{30}^{30}\_S_{30}$*

Selected samples of aluminum–hydroxide powder are characteristic toward phase structure, size primary particle, size secondary particle and specific area. These results are given in Annex 1, and they describe the influence of phase's structure, size of primary particle and size of secondary particle on specific area of synthesis powder. From table 2 we can see that phase structure, size primary particle of bayerite and gibbsite and size secondary particle have important (significant) influence to specific area synthesis aluminum–hydroxide powder. Increasing portion in sample synthesis aluminum–hydroxide powder significantly increasing specific area of sample, because that primary particle boehmite (2-3 nm) are rapidly less then primary particle of bayerite and gibbsite (10-50 nm).

Also, decreasing size primary particle bayerite and gibbsite bring about to increasing specific area samples of synthesis powder. Further, samples of synthesis powder less secondary particle have higher specific area, and this fact can be explanation with less area contact between primary size(crystallite), and this provoke increasing specific area of synthesis powder samples.

4. Conclusion

Obtained results from performed experiments which refer to process neutralization aluminates solution by sulfuric acid given next conclusion:

- Neutralization aluminates solution with sulfuric acid can appear three crystal phase: boehmite, bayerite и gibbsite, but with Bayer procedure appear only gibbsite;
- Powder obtained by neutralization aluminates solution can have specific area to up 300 m^2/g, but aluminum–hydroxide powder (gibbsite) obtained with Bayer process have specific area less from 10 m^2/g;
- Specific area of synthesis alumina powder is in function of phase's structure, size primary particle (crystallite) and size of secondary particle, and with increasing portion of boehmite decreasing size crystallite bayerite and gibbsite, and decreasing size secondary particle bring about forming samples with high specific area. High specific area of synthesis powder are result higher portion of boehmite with primary particle 2-3 nm;

With changing processing condition neutralization of aluminates solution as: caustic model of aluminates solution, concentration of aluminates solution, temperature of neutralization, and time dripping sulfuric acid influence to characteristic of synthesis powder which are: phase structure, size of primary particle and size of secondary size.

References

[1]. Vračar R., Živković Ž. - *Ekstraktivna metalurgija aluminijuma*, Naučna knjiga, Beograd, 1993.
[2]. Baes C.F., Mesmer R.E. - *The Hydrolysis of Cations,* Wiley&Sons, New York, 1976.
[3]. Perusic M., Lazic D., Gligoric M., Zivkovic Z. - *Influence of fluorides on change of alumina specific area during calcinations process*, Travaux ICSOBA, Budapest, Vol.29.33 (2002) 143.
[4]. Heegen H. - *Mechanical activation of precursors for nanocrystaline materials*, Crystal Research Technology, 38, 2003
[5]. Wilson S. J., Me Connell G. D., *J Solid State Chem*., 34 (1980), 315.
[6]. Dorre E., Hubner A., *Alumina,* Springer-Verlag, Berlin, 1984.

Annex 1. *Specific area synthesis alumina powder in function phase structure, size primary and secondary size*

Sample	Phase structure [%] and size primary particle [nm]						Size of secondary particle	Specific area
	Boehmite		Bayerite		Gibbsite			
	Portion	ds	Portion	ds	Portion	ds		
	[%]	[nm]	[%]	[nm]	[%]	[nm]	[μm]	[m^2/g]
$AM_{30}^{30}-S_{30}$	88	(2.8)	4.5	(24.7)	7.5	(23.5)	13.5	219.1
$AM_{30}^{30}-S_{60}$	-	-	-	-	-	-	15.3	166.7
$AM_{30}^{30}-S_{180}$	19.5	(2.5)	30.0	(29.6)	50.5	(31.3)	47.0	79.4
$AM_{30}^{70}-S_{30}$	19.0	(2.6)	34.0	(24.6)	46.0	(25.6)	12.5	56.5
$AM_{30}^{70}-S_{60}$	-	-	-	-	-	-	16.0	55.2
$AM_{30}^{70}-S_{180}$	16.0	(2.9)	20	(27.0)	64.0	(28.2)	37.0	34.1
$AM_{85}^{70}-S_{30}$	67.0	(2.8)	17.5	(22.8)	15.5	(28.1)	8.2	164.0
$AM_{85}^{30}-S_{60}$	-	-	-	-	-	-	10.5	33.1
$AM_{85}^{30}-S_{180}$	-	-	49.0	(21.2)	51.0	(25.6)	43.0	30.1
$AM_{85}^{70}-S_{30}$	23.0	(3.7)	58.0	(29.7)	19.0	(28.0)	13.5	58.2
$AM_{85}^{70}-S_{60}$	-	-	-	-	-	-	19.0	55.3
$AM_{85}^{70}-S_{180}$	-	-	14.0	(40.2)	86.0	(40.2)	39.0	16.8
$AH_{30}^{30}-S_{30}$	100	(2.2)	-	-	-	-	7.9	277.7
$AH_{30}^{30}-S_{60}$	-	-	-	-	-	-	8.2	274.8
$AH_{30}^{30}-S_{180}$	100	(2.4)	-	-	-	-	10.5	226.0
$AH_{30}^{70}-S_{30}$	89.0	(2.6)	5.5	(19.8)	5.5	(18.8)	12.0	284.0
$AH_{30}^{70}-S_{60}$	-	-	-	-	-	-	12.5	213.9
$AH_{30}^{70}-S_{180}$	15.0	(2.5)	35.0	(16.5)	50	(23.5)	13.5	79.1
$AH_{85}^{30}-S_{30}$	59.0	(3.0)	11.0	(14.8)	30.0	(11.3)	9.7	295.5
$AH_{85}^{30}-S_{60}$	-	-	-	-	-	-	10.7	245.4
$AH_{85}^{30}-S_{180}$	56.0	(2.8)	14.0	(16.5)	30.0	(12.8)	12.0	218.6
$AH_{85}^{70}-S_{30}$	42	(2.4)	29.0	(17.4)	29.0	(23.5)	10.0	212.5
$AH_{85}^{70}-S_{60}$	-	-	-	-	-	-	12.0	160.6
$AH_{85}^{70}-S_{180}$	28.0	(2.6)	41.0	(29.7)	31.0	(28.2)	13.0	98.7

THE ANNALS OF "DUNAREA DE JOS" UNIVERSITY OF GALATI.
FASCICLE IX. METALLURGY AND MATERIALS SCIENCE
N^0. 2 – 2009, ISSN 1453 – 083X

RESEARCHES REGARDING THE ELEMENTS LOSS THROUGH VAPORIZATION DURING THE ELABORATION PROCESS IN LD CONVERTER

Alexandru IVANESCU, Ana DONIGA,
Elisabeta VASILESCU, Lilica IVANESCU
"Dunărea de Jos" University of Galati

ABSTRACT

The paper presents a series of researches regarding the vaporization of the component elements of the metallic bath and slag during refining in LD converter. Also, the main factors which influence the vaporization process during steel making in LD converter are studied: the converter atmosphere; the carbon content of the metallic bath; the speed of the oxygen jet; the temperature of the metallic bath; the blowing diagram. Based on these researches we sought to obtain a technology of steel making in LD converter so that the percentage of losses by vaporization is minimum.

KEYWORDS: *oxygen converter, vaporization, sludge, slag, oxygen jet speed, critical carbon content.*

1. Introduction

During steelmaking in oxygen converters, in the impact zone of oxygen jet with the metallic bath, a local temperature of 3000^{0}C is created. As a result, the boiling points of the metallic bath components are exceeded, so that a part (0.6-1.2%) of the metallic charge is volatilized as a red smoke made of fine particles having a size of approximately 1μm [1-3].

1.1. Vaporisation of the elements from the metallic bath

In Fig. 1 is presented the temperature dependence of the vapor pressure for some metals.

The greater is the temperature of the metallic bath in the impact zone of the jet, the greater are the vapor pressures of the component elements Mn, Cr, Cu, Si, Fe, Ni, Co, Ti and the stronger the emission of gases and metallic vapors.

These vapors are entrained by the relaxing of the CO bubbles resulted from the metallic bath decarburization. Also, as a result of the bubbles action and of the oxygen jet impact with the slag-metal emulsion surface, an entrainment of the flux fine particles is achieved, especially during slag formation. At the level of the oxygen jet impact zone, the ascending gas flow has the pressure P_t corresponding to a temperature T_1 with which the gas-vapor mixture enters the recovery unit (approx. 1923 K):

$$P_t = P_{t_1} + P_{t_2} \ , \quad (1)$$

$$P_{t_1} = P_{Fe} + P_{Si} + P_{Mn} + P_{Al} + ... \quad (2)$$

$$P_{t_2} = P_{CO} + P_{CO_2} + P_{O_2} + P_{H_2O} + P_{H_2} \quad (3)$$

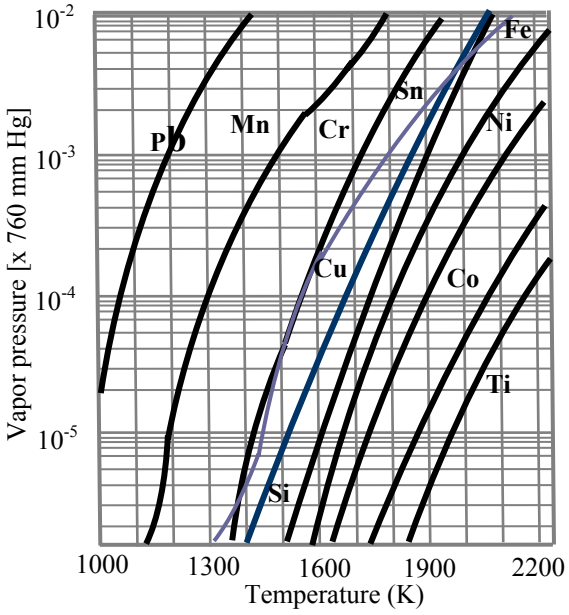

Fig. 1. *Variation of the vapor pressure with temperature*

Because of the oxidizing conditions in the recovery unit (false air excess) the elements vapors

are oxidized and condensed at the temperature T_2 corresponding to the dew point (Fig. 2), being recovered in a proportion of 98% in the resulted sludge from the wet cleaning unit. T_3 is the temperature of condensation of the Fe, Mn and Al vapors, which were cooled with the aid of cooling water in Venturi tubes. Of the evaporated elements, Fe has an important weight and influences the level of the steel taking out [4].

The iron vaporization is influenced by the converter atmosphere, the carbon content of the iron bath; the speed of the oxygen jet, the decarburizing rate.

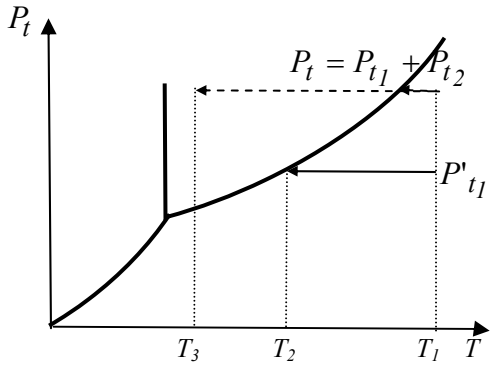

Fig. 2. *Diagram of the vapors condensation of a gaseous mixture*

2. The influence of the converter atmosphere upon the elements vaporization

For example it is considered the iron vaporization because Fe is quantitatively predominant in the heterogeneous system subjected to the process.

As a result of the oxygen blowing, a Fe vapors counter-flow appears and determines at a distance δ from the surface of the metallic bath the formation of a fog layer of FeO, the following reaction being produced:

$$\{Fe\}+\frac{1}{2}\{O_2\}\rightarrow\{FeO\}$$

resulting for the fluxes of the Fe vapors, F_{Fe}, and of oxygen, F_{O_2}:

$$F_{Fe} = -2F_{O_2} \qquad (4)$$

In conformity with Fick's law, the flux of the Fe vapors is given by the relation

$$F_{Fe} = -CD_{Fe}\frac{\partial X_{Fe}}{\partial y} + X_{Fe}(F_{Fe} + F_{O_2}) \qquad (5)$$

From the relations (4) and (5) it is obtained:

$$F_{Fe}(2 + X_{Fe}) = -2CD_{Fe}\frac{\partial X_{Fe}}{\partial y} \qquad (6)$$

$$\int_0^{\delta} F_{Fe}\,dy = -2CD_{Fe}\int_{X^0_{Fe}}^{X'_{Fe}}\frac{dX_{Fe}}{2 + X_{Fe}} \qquad (7)$$

$$F_{Fe} = -\frac{2CD_{Fe}}{\delta}\ln\frac{2 + X'_{Fe}}{2 + X^0_{Fe}} \qquad (8)$$

where: F_{Fe} the flux of the Fe vapors, in mol/m^2.s; D_{Fe} – the diffusion coefficient of Fe in oxygen, in m/s; X^0_{Fe} – the molar fraction of Fe at the distance *y=0*;

X'_{Fe} – the molar fraction of Fe at the distance $y=\delta$; *C* – the molar concentration of the Fe vapors, in mol/m^3,

$$C = \frac{n}{V_{Fe}} = \frac{P_{Fe}}{RT} \qquad (9)$$

n – the number of moles of Fe which vaporize; V_{Fe} – the molar volume of Fe;

P_{Fe} – the pressure of Fe vapors. In conclusion, the flux of the Fe vapors is twice the flux of oxygen and it is determined by the oxygen partial pressure P_{O_2} which characterizes the converter atmosphere.

3. The influence of the carbon content from the bath subjected to the vaporization

It is observed that during the decarburizing of a metallic bath with upper oxygen jet, the carbon content has a strong influence upon the decarburizing process. Thus, for a carbon content of less than 2% C (Fig. 3), the Fe vaporization becomes much weaker and tends to zero as the carbon content decreases. In industrial practice the medium decarburizing rate in LD converter is 10% C/h, at a bath depth of 100 mm. The disappearance of the flame at the converter mouth and the observation of the lance are realized at a carbon content of approximately 0.05% in the metallic bath, when the vaporization is minimum. It is important to determine the critical content of carbon from which the vaporization begins to decrease.

The Fick's first law is applied to the carbon transport through a thin diffusion layer at the metal-gas interface:

$$-\frac{d[C]}{dt} = \frac{1}{L}\frac{D_C}{g_0}(C_0 - C_{cr}) \qquad (10)$$

where: L – the depth along which the boiling of the metallic bath takes place (~ 100 mm); D_C – carbon diffusion coefficient in iron [3.10^{-8} m^2/s]; g_0 – the thickness of the limit diffusion layer [3.10^{-5} m]; C_0 – the carbon content at the interface (~ 0.03%); C_{cr} – the critical carbon content when the vaporization is reduced.

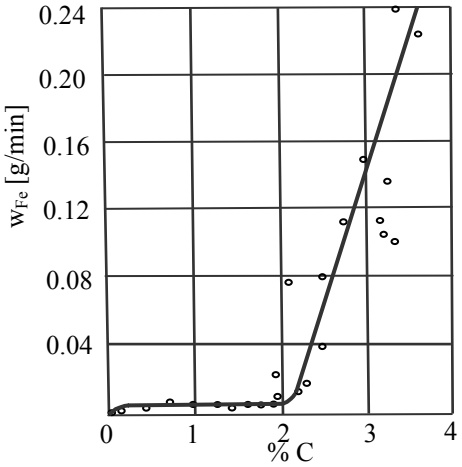

Fig.3. *Variation of Fe vaporization speed with the carbon content [C]*

From the relation (10) it results the value $C_{cr} = 0.31\,\%$ which corresponds to the practical values: 0.20-0.40 %C.

4. The influence of the oxygen jet speed upon the elements vaporization

In Fig. 4 is presented the variation of the oxygen jet speed as a function of the carbon content of the metallic bath.

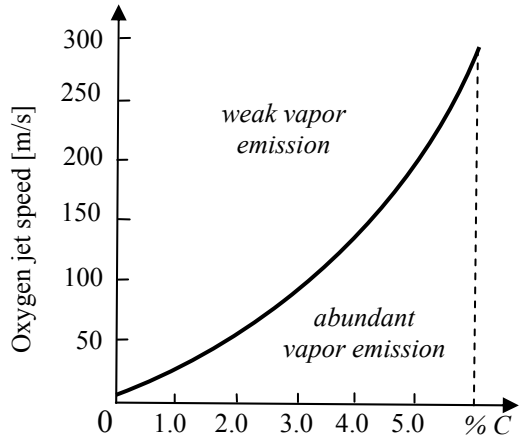

Fig. 4. *Variation of oxygen jet speed with [C]*

If the oxygen jet speed is bigger than the value given by this curve for all the carbon contents, the vapors emission is weak.

If the oxygen jet speed is smaller than the critical value, Fe is vaporized at a rate close to its maximum value: $w_{O_2} = K[C]^2$ (11)

where: w_{O_2} – the oxygen jet speed; *[C]* – the carbon concentration in the metallic bath; K – proportionality constant. The relation (11) is established on the basis of the relation:

$$2F_{O_2} = F_{CO_2} > F_C \qquad (12)$$

obtained when the vapors release ends, from the reaction:

$$\{CO\} + \frac{1}{2}\{O_2\} \rightarrow \{CO_2\} \qquad (13)$$

with F_{O_2}, F_{CO_2} and F_C – the oxygen, CO_2 and carbon fluxes. The domain upon the curve from the Fig. 4 corresponds to the case in which the steel making takes place with minimum emissions of red gases and the domain under the curve corresponds to the case in which the steel making takes place with maximum emissions.

It is concluded that during iron decarburization by oxygen blowing through the upper side, in order to obtain a reduced vaporization, the oxygen speed at the lance nozzle exit must be as great as possible in the case that the metallic bath has great carbon contents. As the decarburization advances, the iron oxidation must be maintained to a minimum value in order to suppress the smoke formation.

5. Experimental researches

The sludge samples were taken from the sludge funnel every two minutes of blowing from nine charges. The chemical composition of the converter dust (dry sludge) is presented in Tab. 1 from which some aspects concerning the vaporization process in the LD converter can be highlighted:

- the Fe content from the red smokes is a maximum in the minute 4 of blowing and corresponds to the maximum content of Fe_2O_3;
- the SiO_2 content is a maximum in the minutes 8-10 of blowing;
- the Al_2O_3 content variation is a maximum in the minute 4 of blowing, as the Fe content;
- the CaO content variation is a maximum in the minute 14 of blowing;
- the MgO content variation is a maximum in the first two minutes of blowing and a maxim in the last minutes;
- the Mn content variation presents a loop in the minute 20 of blowing;

- the calcination losses (PC) variation is a maximum in the minute 14 of blowing, as CaO;

Using a statistical program, from the data in Tab. 1 there were obtained the histograms of the main parameters of the vaporization process as well as the simple and multiple correlations between them [5]. Out of these, we have selected the Fe content histogram (Fig.5). From the histograms the following conclusions can be drawn:

- the Fe content in the red smokes varies in the range 20-60% and the maximum frequency of 40% is obtained for a 42-50% Fe content (fig. 5);
- the FeO content in the dry sludge varies in the range 6-27% and the maximum frequency of 28% is obtained for a 18-20% FeO content;
- the CaO content in the in the dry sludge varies in the range 10-30% and the maximum frequency of 43% is obtained for a 15-20% CaO content;
- the quantity of dry substance SU varies between 5 and 35 g/l and has a maximum frequency of 40% for a concentration of 17-23 g/l;
- the dry substance (SU) variation has a maximum concentration in the minute 12 of blowing.
- the calcinations losses PC vary in the range 5-28% and the maxim frequency of 28% is obtained for a 17-20% PC;
- the vaporized elements Ca, Si, Al, Mg pass as oxides CaO, SiO_2, Al_2O_3 and MgO, respectively;
- the SiO_2 content in the dry sludge varies in the range 0-2.4% and the maximum frequency of 37% is obtained for a 1.3-1.5% SiO_2 content;
- the Al_2O_3 content in the dry sludge varies in the range 0-3.8% and the maximum frequency of 42% is obtained for a 0.7-1.2% Al_2O_3 content;
- the MgO content in the dry sludge varies in the range 0-4.2% and the maximum frequency of 38% is obtained for a 0-0.8% MgO content;
- the Mn content in the dry sludge varies in the range 0.5-2.5% and the maximum frequency of 42% is obtained for a 1.3-1.5% Mn content.

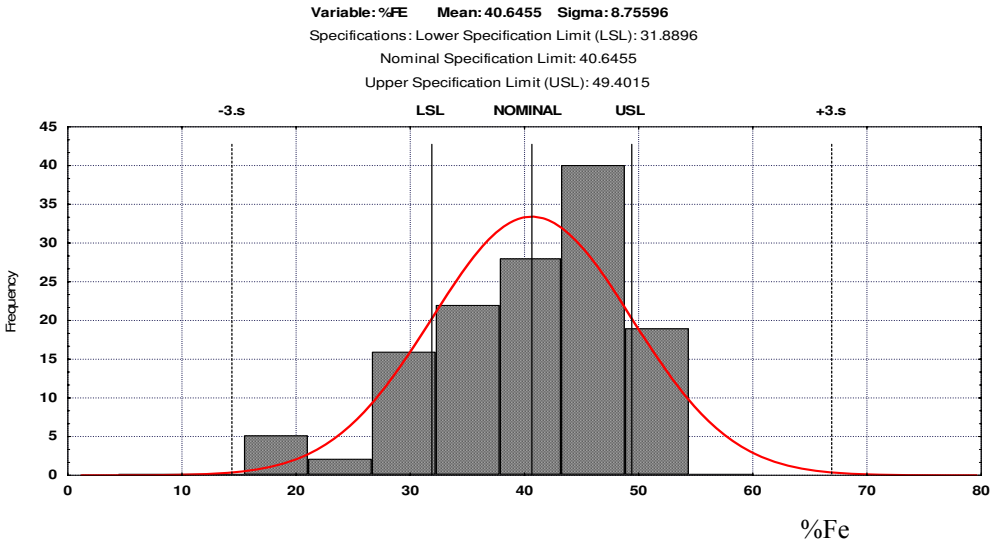

Fig. 5. *The histogram of the absolute frequencies of % Fe*

Table 1. *Chemical analyses of the sludge samples*

Minute of blow	Fe	FeO	Fe_2O_3	SiO_2,	Al_2O_3	CaO	MgO	Mn	PC	SU	Remarks
	[%]									[g/l]	
2	41.98	5.34	54.50	1.57	0.63	18.96	0.12	0.57	17.46	11.74	Charge 1 (923654)
4	53.60	11.04	65.05	1.39	0.91	13.02	1.07	1.28	9.32	28.94	
6	45.65	18.37	45.95	1.94	0.49	18.43	0.12	1.13	13.62	13.74	
8	53.19	26.02	49.72	1.61	0.77	12.33	0.75	1.31	5.42	14.74	
10	50.77	18.81	52.88	1.59	0.89	12.33	0.11	1.36	13.90	27.04	
12	47.03	16.16	50.34	1.33	0.49	18.82	0.13	1.51	15.05	29.94	
14	17.13	7.22	17.03	0.81	1.46	49.31	0.37	0.70	26.02	27.44	
16	32.73	22.01	24.30	1.25	0.34	27.25	0.16	1.42	22.31	11.04	
18	39.46	21.08	34.35	0.82	1.96	20.53	0.12	1.99	19.74	20.34	
20	35.40	17.89	31.91	0.63	1.33	14.93	1.87	2.35	21.18	9.74	
22	27.45	5.34	33.75	0.55	2.58	30.82	5.14	1.32	13.83	8.94	
2	42.79	5.43	55.63	1.70	0.69	19.06	0.20	0.64	18.33	12.71	Charge 2

4	54.41	11.13	66.18	1.52	0.97	13.12	1.15	1.35	10.19	29.91	(923655)
6	46.46	18.46	47.08	2.07	0.55	18.53	0.20	1.20	14.49	14.71	
8	54.00	26.11	50.85	1.74	0.83	12.43	0.83	1.38	6.29	15.71	
10	51.58	18.90	54.01	1.72	0.95	12.43	0.11	1.43	14.77	28.01	
12	47.84	16.25	51.47	1.46	0.55	18.92	0.13	1.58	15.92	30.91	
14	17.94	7.31	18.16	0.94	1.52	49.41	0.45	0.77	26.89	28.41	
16	33.54	22.10	25.43	1.38	0.40	27.35	0.16	1.49	23.18	12.01	
18	40.27	21.17	35.48	0.95	2.02	20.63	0.20	2.06	20.61	21.31	
20	36.21	17.98	33.04	0.76	1.39	15.03	1.95	2.42	22.05	10.71	
22	28.26	5.43	34.88	0.68	2.64	30.92	5.22	1.39	14.70	9.91	
2	42.24	5.09	54.86	1.47	0.67	18.97	0.18	0.52	17.77	12.05	Charge 3 (933944)
4	53.86	10.79	65.41	1.29	0.95	13.03	0.88	1.23	9.63	29.25	
6	45.91	18.12	46.31	1.84	0.53	18.44	0.18	1.08	13.93	14.05	
8	53.45	25.77	50.08	1.51	0.81	12.34	0.81	1.26	5.73	15.05	
10	51.03	18.56	53.24	1.49	0.93	12.34	0.11	1.31	14.21	27.35	
12	47.29	15.91	50.70	1.23	0.53	18.83	0.13	1.46	15.36	30.25	
14	17.39	6.97	17.39	0.71	1.50	49.32	0.43	0.65	26.33	27.75	
16	32.99	21.76	24.66	1.15	0.38	27.26	0.16	1.37	22.62	11.35	
18	39.72	20.83	34.71	0.72	2.00	20.54	0.18	1.94	20.05	20.65	
20	35.66	17.64	32.27	0.53	1.37	14.94	1.93	2.30	21.49	10.05	
22	27.71	5.09	34.11	0.45	2.62	30.83	5.20	1.27	14.14	9.25	
2	51.80	8.56	63.38	1.28	0.65	11.39	1.44	0.74	9.99	12.20	Charge 4 (923653)
4	50.75	12.79	57.52	1.28	0.52	13.76	0.70	0.85	11.24	14.71	
6	49.45	16.12	52.24	1.25	0.44	15.89	0.16	0.95	12.37	16.22	
8	47.90	18.53	47.54	1.19	0.43	17.78	0.00	1.04	13.38	16.70	
10	46.10	20.04	43.42	1.11	0.48	19.42	0.00	1.13	14.25	16.17	
12	44.06	20.63	39.88	1.00	0.59	20.81	0.00	1.21	15.00	14.62	
14	41.76	20.32	36.91	0.87	0.76	21.97	0.00	1.28	15.61	12.06	
16	39.22	19.10	34.53	0.71	1.00	22.87	0.44	1.35	16.10	8.47	
18	36.42	16.97	32.72	0.53	1.29	23.53	1.09	1.41	16.47	3.88	
20	33.38	13.93	31.50	0.32	1.65	23.95	1.94	1.46	16.70	19.20	
22	30.09	9.99	30.85	0.09	2.07	24.12	2.99	1.50	16.81	8.60	
2	48.53	7.73	61.16	1.46	0.76	13.21	1.54	0.75	9.86	13.29	Charge 5 (918798)
4	47.48	11.96	55.30	1.45	0.63	15.58	0.89	0.88	11.31	17.16	
6	46.18	15.29	50.02	1.42	0.55	17.71	0.44	0.99	12.62	20.01	
8	44.63	17.70	45.32	1.37	0.54	19.60	0.19	1.10	13.80	21.84	
10	42.83	19.21	41.19	1.29	0.59	21.24	0.14	1.21	14.85	22.66	
12	40.79	19.81	37.65	1.18	0.77	22.63	0.29	1.30	15.77	22.46	
14	38.49	19.49	34.69	1.05	0.87	23.78	0.63	1.39	16.55	21.24	
16	35.95	18.27	32.30	0.89	1.11	24.69	1.18	1.47	17.20	19.00	
18	33.15	16.14	30.50	0.71	1.40	25.35	1.93	1.54	17.71	15.75	
20	30.11	13.11	29.27	0.50	1.76	25.77	2.87	1.61	18.09	11.49	
22	26.82	9.16	28.63	0.26	2.18	25.94	4.02	1.67	18.34	6.20	
2	48.73	7.53	61.25	1.44	0.96	13.40	1.73	0.74	9.90	13.49	Charge 6 (923648)
4	47.88	11.56	55.39	1.41	1.03	15.97	1.28	0.85	11.40	17.56	
6	46.78	14.69	50.11	1.36	1.15	18.30	1.03	0.95	12.77	20.61	
8	45.43	16.90	45.41	1.29	1.34	20.39	0.98	1.04	14.00	22.64	
10	43.83	18.21	41.28	1.19	1.40	22.23	0.77	1.13	15.10	23.66	
12	41.99	18.61	37.74	1.06	1.45	23.82	0.90	1.21	16.07	23.66	
14	39.89	18.09	34.78	0.91	2.17	25.18	1.30	1.28	16.90	22.64	
16	37.55	16.67	32.39	0.73	2.32	26.28	1.40	1.35	17.59	20.60	
18	34.95	14.34	30.59	0.53	2.80	27.14	1.99	1.41	18.16	17.55	
20	32.11	11.11	29.36	0.30	2.95	27.76	2.60	1.46	18.59	13.49	
22	29.02	6.96	28.72	0.04	3.20	28.13	3.00	1.50	18.89	8.40	

From the ten simple correlations we have selected for presentation the regression curves of % FeO (Fig. 6a), and of SU (Fig. 6b), in g/l, as function of the

blowing time, *t*. From the regression curves the following conclusions can be drawn:
- the FeO content presents two maxims in the minutes 8 and 20 and between them a minimum corresponding to the minute 14 when the decarburization is advanced (Fig. 6a);
- the quantity of dry substance SU presents a parabolic variation, presenting a maximum of 25 g/l in the minute 12 of blowing (Fig. 6b);
- the MgO content in the dry sludge presents a parabolic variation, presenting a minimum of 0.2% in the minute 12 of blowing;
- the Fe content presents a linear variation, descending from a maximum value of approx. 55% in the minute 4 of blowing to a value of approx. 30% in the minute 22 of blowing;
- the SiO_2 content variation is linear, descending from a maximum value of 1.8% in the first two minutes of blowing to a value of 0.2% in the minute 22 of blowing;
- the Al_2O_3 content variation is linear, ascending from a 0.5% minimum value in the minute 2 of blowing to a maximum value of 2.5% in the minute 22.

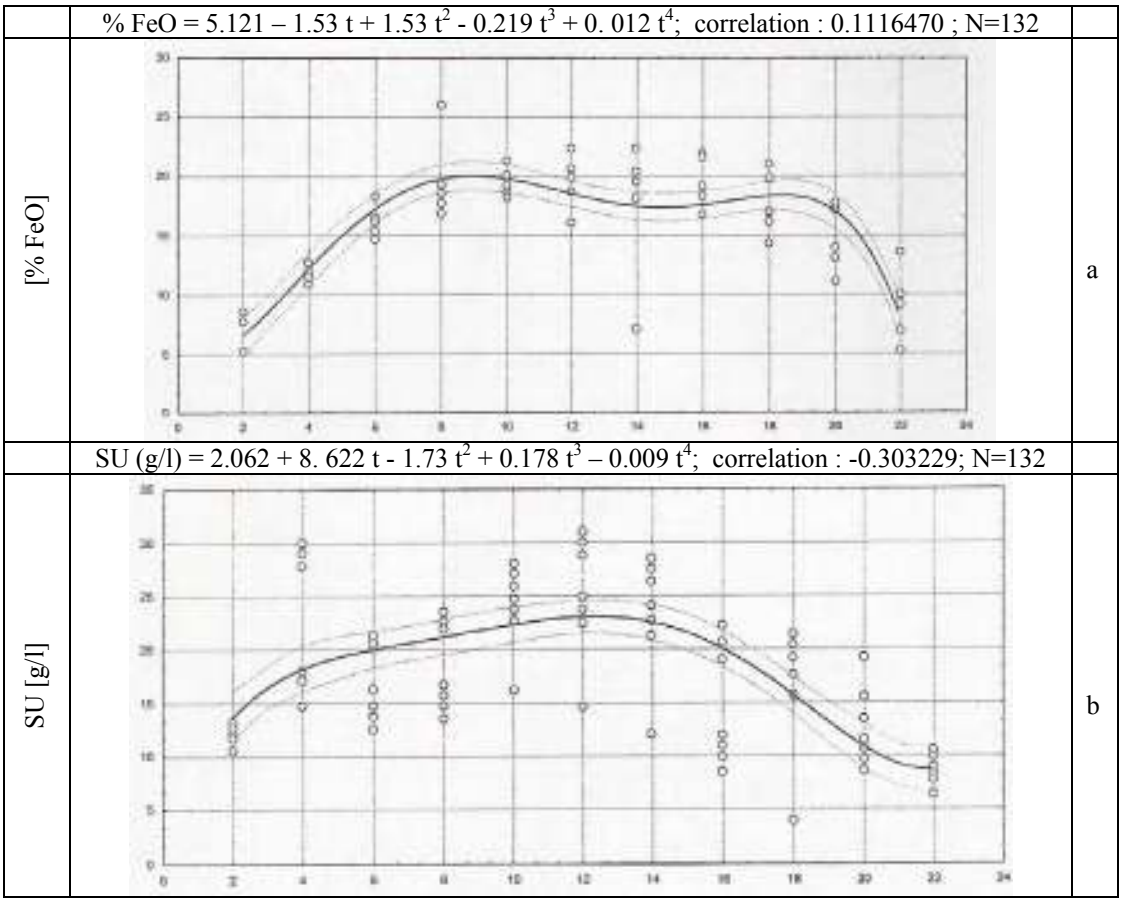

Fig. 6. *Regression curves for % FeO and dry substance SU [g/l]*

From the multiple correlations we have selected for presentation the regression surfaces of % Fe=f(%CaO, %SiO_2) (Fig. 7) and of SU=f(%Fe, %CaO) (Fig. 8) and the following technological aspects can be detached:

- the Fe content in the red smokes depends to a great extent on the CaO and SiO_2 contents from the sludge obtained by the vaporization of Ca and Si and by the lime dust training in the converter. A maxim of 54-55% Fe is registered for a 15% CaO and 2.2% SiO_2 content. The greater the CaO content in the sludge, the smaller the Fe content. This fact conducts to the conclusion that the iron vaporization can be diminished with a great CaO content in slag;
- the quantity of dry substance is determined by an intense Fe and Ca vaporization, obtaining a maximum of 35% SU for 55% Fe and 35% CaO and a minimum of 2% SU for 10% Fe and 6% CaO;
- the calcination losses are influenced by the Fe and Si vaporization, obtaining a maximum of 28% PC for 8% Fe and 2.2% SiO_2 and a minimum of 6% PC for 55% Fe and 0.2% SiO_2.

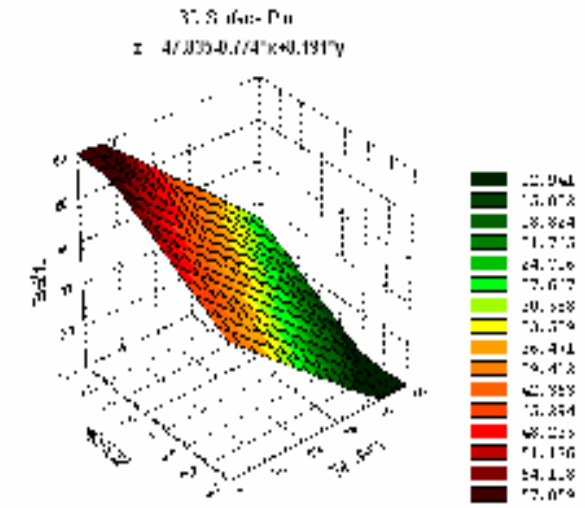

***Fig.7**. Correlation of %Fe as function of %CaO şi %SiO_2*

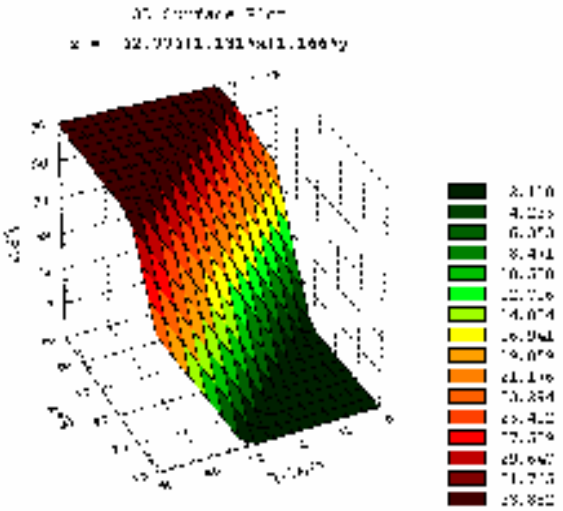

***Fig.8.** Correlation of %SU as function of %Fe şi %CaO*

6. Conclusions

The iron volatilization in the LD converters with oxygen blowing at top through lance is important because great iron quantities (0.6-1.2%) from the metallic charge are lost as fine particles having a size of approximately 1μm, mainly made of iron oxides. In order to diminish this loss it is necessary to achieve an intense oxygen blowing regime being able to ensure as greater oxygen jet speeds as the carbon content in the metallic bath is higher. The sludge obtained from the LD converter gases' purging represents an ore enriched in iron (approx. 50-55% Fe). The maintaining of a quantity of liquid slag from the previous charge determines, on one hand the faster formation of slag and, on the other hand, helps to obtain poorer emissions of vapors of Fe, Mn, Si, Mg, Al, Ca, etc at high carbon contents in the metallic bath. At small carbon contents (less than the critical one) the oxygen speed at the lance nozzle exit is the factor whose size influences the emission of metallic vapors: the greater the speed, the poorer emission of metallic vapors.

References

[1]. Alberny R, Birat P. - *"Iron volatilization"*, Circulaires d'Informations Techniques 11 (1962), p. 66-70.
[2]. Oprea F, Taloi D, Ivanescu A. -*"Theory of the metallurgical processes"*, Editura Didactica si Pedagogica, Bucharest (1984).
[3]. Ackermann W: *"Mass and energy transfer between the gaseous and liquid phase in oxygen converter"*, Stahl und Eisen 9 (1979), p. 36-41.
[4]. Ivanescu A, Ene A, Ivanescu L, Catana C. - *"Researches regarding the vaporization process of the existing elements in the metallic bath during steel making in LD converter"*, International Conference METAL 2005, Hradec nad Moravici, Czech Republic, paper A6P.
[5]. Mustata C, Munteanu V, Zorlescu D. - *"Mathematical modelling of the steel making in oxygen converter"*, Editura Tehnica, Bucharest, 2002.

THE ANNALS OF "DUNAREA DE JOS" UNIVERSITY OF GALATI.
FASCICLE IX. METALLURGY AND MATERIALS SCIENCE
N^0. 2 – 2009, ISSN 1453 – 083X

BEHAVIOR OF Ni/Al_2O_3 NANOCOMPOSITE THIN LAYERS IN CORRODING ENVIRONMENT

C. GHEORGHIEŞ, Livia GHEORGHIEŞ, V. O. ATANASIU
"Dunarea de Jos" University of Galati
email: cgheorg@ugal.ro

ABSTRACT

This paper investigates the effects of adding alumina nanoparticles in the electrolyte bath on surface topomorphologies and structure of electrodeposited nickel. The influence on the corrosion process in NaCl solutions having various concentration was investigated by using impedance spectroscopy. The experimental data indicates the beneficial roles of alumina nanoparticles on Ni/Al_2O_3 nanocomposite thin films. The structure of electrocodeposited nanocomposite thin films was investigated by XRD and SEM techniques

KEYWORDS: nanocomposite, structure, corrosion, XRD, SEM.

1. Introduction

This paper investigates the effects of adding alumina nanoparticles in the electrolyte bath on surface topomorphologies and structure of electrodeposited nickel. The influence on the corrosion process in NaCl solutions having various concentrations was investigated by using impedance spectroscopy.

The experimental data indicate the beneficial roles of alumina nanoparticles on Ni/Al_2O_3 nanocomposite thin films.

These results are essential in manufacturing thermal or corrosion barriers by covering of some metallic surfaces with protective layers.

The structure of electrocodeposited nanocomposite thin films was investigated by XRD and SEM techniques and allows doing a correlation with their corrosion behavior in various corroding environments such as: NaCl or Na_2SO_4 having different concentrations.

2. Experimental research

On 5 copper supports, nanocomposite thin layers were deposited consisting of a nickel matrix and Al2O3 particles (20 nm) in concentrations ranging between 3 g/l and 15 g/l.

On 5 copper supports thin layers were deposited consisting of only of nickel matrix in order to compare their behavior with the version with nanoparticles. The copper support specimens have been properly prepared for deposition, using specific solutions for degreasing and in presence of ultrasonic waves.

As nickel plating bath a Watt bath was used having the following features: NiSO4·6H2O-0.90M; NiCl2·6H2O-0.20M; H3BO3-0.28M; sodium dodecylsulphate [CH3(CH2)11OSO3Na]-0.4g/l [1].

The concentration of alumina nanoparticles varied from 3 g/l to 15 g/l, and they were kept in suspension by a magnetic stirrer having a stirring rate of 700 rpm. The pH value of the electroplating solution was maintained at 4.2 – 4.5 and the corrections were made using a typical acidic solution.

Electrocodeposition processes were made at an optimal temperature of 40^o C for 60 minutes and a current density of 2A/dm^2. The cathode consisted of the working specimen, namely copper, and the anode consisted of nickel having the same surface area as the copper specimen.

3. Structural analysis

The obtained electrocodeposited thin films of Ni/Al_2O_3 were studied by SEM at optimal magnifications on order to obtain the best images in which some agglomeration of alumina nanoparticles in the electrocodeposited thin films can be observed.

For this aim a Quanta 200, made of FEI Company instrument was used. In Fig. 1 SEM images of Ni/Al2O3 electrocodeposited for 0g/l and 10g/l alumina are displayed, respectively.

Ni/ Al2O3: 0 g/l Ni/ Al2O3 :10 g/l

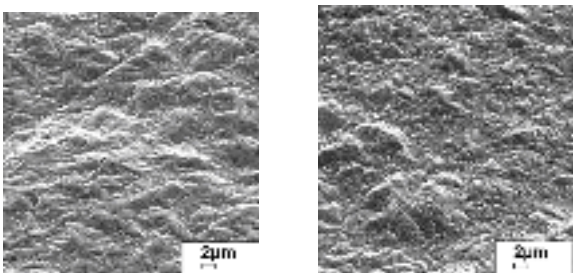

Fig 1. *SEM images of Ni surface without and with Al_2O_3 nanoparticles*

As alumina nanoparticles were added to the electrolyte in increasing concentrations, a general refinement in the grain structure on the surface was observed. With addition of 10 g/l of alumina, the average size of the pyramids on the surface is clearly reduced. These results show that the surface topomorphology is greatly refined by the presence of alumina nanoparticles. The chemical analysis of electrocodeposited thin films of nickel with alumina nanoparticles has been estimated by EDAX method. The typical spectrum showing the chemical construction is presented in Fig. 2.

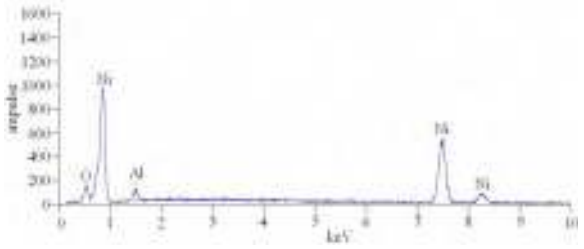

Fig. 2. *EDAX spectrum of electrodeposited film with 10% alumina*

X-ray pattern obtained on DRON-3 equipment from electrocodeposited thin films of nickel having a concentration of 10 % alumina nanoparticles is presented in Fig. 3 [2, 3]. Although EDAX spectra pointed out aluminum, only the characteristic peaks of nickel can be observed.

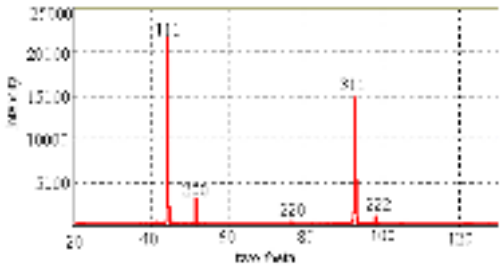

Fig.3. *XRD pattern of electrocodeposited nickel thin film with 10 % alumina*

4. Corrosion tests

Corrosion tests have been performed for nanocomposite thin films on specimens of Ni/Al_2O_3 in three different types of solvents: NaCl 3%, 5% and 7%. The results were compared with depositions of metallurgical nickel [4, 5]. Previously, the surface not subjected to electrochemical tests was isolated with polytetrafluoroethylene. Out of the eletrocodeposited thin films (Ni/Al_2O_3) of area of 4 cm^2, an area of 0.5–1cm^2 was kept for the electrochemical experiments consisting in drawing polarization curves [6-9]. The electrochemical tests were performed in an electrochemical cell consisted of a glass recipient with a lid having a series of apertures through which were inserted the corrosion solution, the working electrode [electrocodeposition thin films as specimen obtained on the copper support], the auxiliary electrode [helical platinum (Pt) wire] and the referential electrode [horn mercury electrode $Hg/HgCl_2$sat. (ε = 0.234 V)].

The solution was stirred by introducing a small magnet covered by glass layer, which was then moved by magnetic stirrer. Nickel specimens with aluminium oxide particles have been studied against pure nickel specimens. Initially, polarization curves were achieved in the electrolyte solutions of NaCl. The working circuit consisted of: referential electrode: horn mercury, auxiliary electrode: platinum and working electrode: deposition in nickel matrix.

This circuit was connected to a computer which recorded the experimental data. The polarization curves i = i (E) were obtained in the following conditions: voltage 1: - 500 mV**;** voltage 2: +500 mV**;** voltage 3: +1000 mV**;** sweeping rate v = 150 mV/min**;** number of cycles: 1**,** minimum current: -50 mA and maximum current: +50 mA. Figs. 4 and 5 contain the obtained polarization curves in NaCl 3% solution, while Figs. 6 and 7 display the polarization curves obtained in Na_2SO_4 having a concentration of 0.1 M.

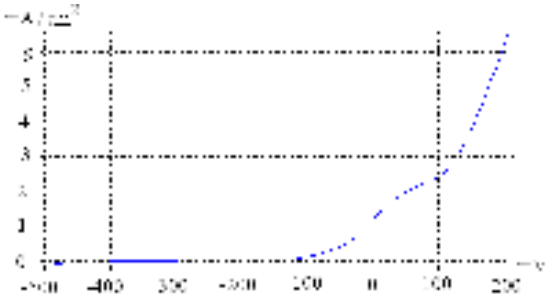

Fig.4. *Polarization curve of Ni in NaCl 3% solution*

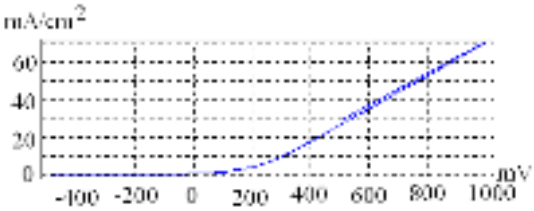

Fig.5. *Polarization curve of Ni/ Al_2O_3 in NaCl 3% solution*

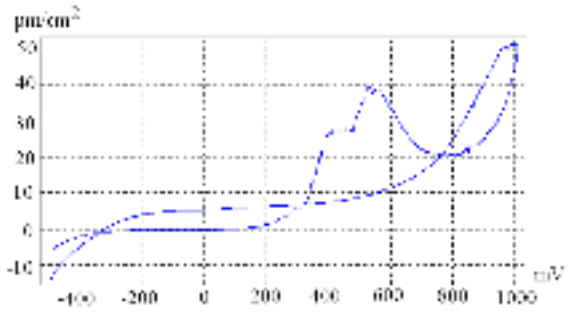

Fig.6. *Polarization curve of Ni in Na_2SO_4 having a concentration of 0.1 M.*

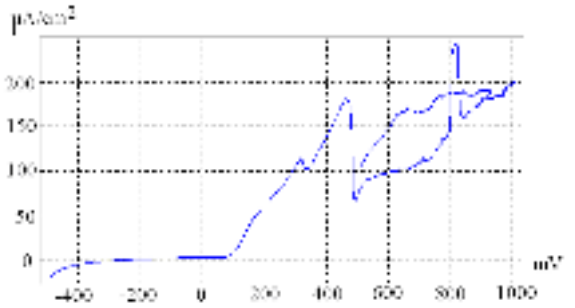

Fig.7. *Polarization curve of Ni/ Al_2O_3 in Na_2SO_4 having a concentration of 0.1 M.*

Analyzing the above polarization curves obtained for pure nickel and for nanocomposite of type Ni/Al_2O_3, it result a major difference in behavior of the two materials in corroding solutions of NaCl and Na_2SO_4. These results show the versatility of nanocomposite based on nickel matrix reported to various corroding solutions having certain compositions and/or concentrations [10].

The corrosion protection can be accredited to the presence of Al_2O_3 nanoparticles in nickel matrix, because their presence on the metal surface creates a barrier for oxygen reduction. In solutions, the composites are not stable. It is possible to selectively dissolve the metallic matrix or the disperse phase or both (matrix-disperse phase).

Corrosion process is essentially electrochemical; voltage and current parameters can be precisely measured with modern equipment. For the corrosion study, polarization resistances can be estimated from spectro-electrochemical impedance data (EIS) in a large frequency range (105 – 10-3 Hz). A voltage change indicates a corresponding change of intermediate species concentration.

Figures. 8 and 9 show the representation of impedance spectroscopy diagrams for the experimental system of Ni/ Al_2O_3 in Na_2SO_4 0.1 M solution at, 1h, and 46 h.

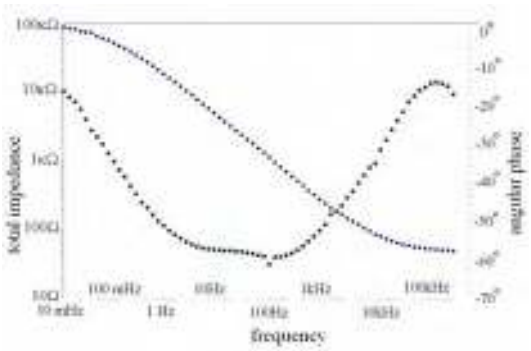

Fig. 8. *EIS diagram at 1h.*

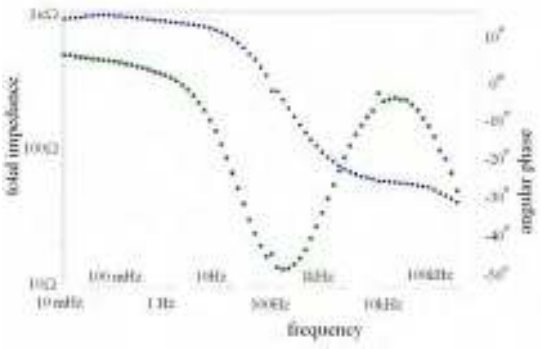

Fig. 9*. EIS diagram at 46 h*

5. Conclusions

This paper reveals some experimental data concerning the preparation by electrocodeposition of a nanocomposite of type Ni/Al_2O_3 on a copper substrate as well as its behavior in a corroding environment as NaCl.

It has been determined that the most relevant factors for the success of nanocomposite coatings with directed composition are the nature of constituents, and electrolyte and electrolysis conditions.

References

[1]. Viswanathan, V., Agarwal, A., Ocelik, V., Hossom, J T M De, Sobczak, N., Seal, S. - J. Nanosci Nanotech., 6 (2006) 651-660
[2]. Gheorghies, C. *Controlul structurii fine a materialelor cu radiatii X*, Ed. Tehnica, Bucuresti, 1990, p 272
[3]. Gheorghies, C., The Ann. of Dunarea de Jos Univ. of Galati, Fasc. VIII, Tribology, (2003) vol.I, pp.302-312.
[4]. Carac, G., Stoian, A., Iticescu C. - *Electrochimie- lucrari practice***,** Ed. Academica, Galati, (2004) 100.
[5]. Abdallah, M., El-Etre, A.Y. - Portugaliae Electrochimica Acta 21 (2003) 315-326
[6]. Gladkovs, M., Medeliene, V., Samuliciene, M., Juzeliunas, E. - Chemija (Vilnius) T13, no.1, (2002) 36-40
[7]. Liu, F.G., Du , M., Zhang, J., Qiu, M. - Corrosion Science 51 (2009) 102–109
[8]. Yoo, B-Y, Hendricks, R. K., Ozkan, M., Myung, N.V. - Electrochem. Acta, 51 (2006) 3543-3549.
[9]. Ciubotariu, A. C., Benea, L., Lakatos-Varsany - Revista de Corozune si Protectie Anticoroziva, vol. III, (2008), 1
[10]. *** http://nonferrous.keytometals.com

THE ANNALS OF "DUNAREA DE JOS" UNIVERSITY OF GALATI.
FASCICLE IX. METALLURGY AND MATERIALS SCIENCE
N^0. 2 – 2009, ISSN 1453 – 083X

MONITORING OF THE ROLLING MILL VIBRATION

Stefan DRAGOMIR, Georgeta DRAGOMIR, Marian BORDEI
"Dunărea de Jos" University of Galati
email: sdragomir@ugal.ro

ABSTRACT

These researches show the influence of mill vibration on the thickness profile of the stainless steel sheet. The alloy elements like Ni and Cr inside the stainless steel could amplify the rolling mill vibration and determine severe damages for rolling sheet. These damages consist in variation of thickness on the length of strip. We made recordings of vibrations during the rolling process and we propose an integrate system for vibration monitoring.

KEYWORDS: mill vibration, sheet thickness, monitoring, sheet damage

1. Introduction Vibration monitoring in rolling mills

During the rolling process, the oscillation of mill stands installation is produced for reasons of construction (coupling, gear box, gap into the back up rolls and coupled bars).

The process parameters (sheet tension, mill speed, deformation force and thickness percentage of reduce in every cage), can determine a major influence on the vibrations.

The bearings lubrication or hydraulic cylinders for damping the oscillations of mill machine cannot decrease to a sufficient degree the rolling mill vibration.

We must ensure that the rolling mill machine operates with roll speeds at which the oscillation level will not determine severe diminution of the product quality.

This can be achieved by using an integrate system online vibration monitoring.

The aims of online vibration monitoring systems in rolling mills are quality control and a predictive maintenance for equipment functionability.

We used acceleration sensors seated on the rolls backup. The signals of the acceleration sensors are amplified, passed through low-pass filter, transformed in a digital signal and transmitted to a computer.

The result of the quality diagnosis is displayed online in the control unit. Figure 1 shows schematically the construction of the integrate vibration measuring system.

The online and offline-display of all the recorded data in different display modes, allows the performance of standard signal processing, the comparing with the` standard mill signal and a simultaneous analysis.

2. Measurement of vibration in a rolling mill stand

Figure 2 presents the results of gage chatter on a 4th stand cold rolling mill in terms of roll stand vibrations. We see an intense increase of oscillations in the 4 stand and after the decrease trend.

The results of the analysis showed that stand number four initially caused the gage chatter. The stand vibrations are transmitted in the strip beginning from the stand three.

The vibration showed a level of frequency of about 125 Hz. The change of the level of upper screw down, determines a reduction of the vibrations.

The record, what we made, shows the necessity to install a permanent vibration monitoring system at the rolling mill.

During the experiments we could analyze how mill stand resonance is exited by speed in correlation with the tension strip.

The speed, correlated with tension strip excitations is generally due to mechanical defects within the rolling mill, bearing and gear box. A very important problem is represented by work roll shape which depends on rolls wear.

This wear appears in time and determines a particular pattern on the surface of work rolls which is printed on the strip surface.

The level of vibrations can alarm us when damage is produced inside of mill machine. Mechanical damages causes can represent interne excitations whose effects depend on many strip

parameters (material, width, thickness etc.), and thus do not appear during each pass in our research.

The cumulative frequency-speed has been developed to simplify the evaluation of vibration spectrum.

This cumulative frequency-speed has the greater time basis and can equilibrate the distribution in the cinematic of rolling mill.

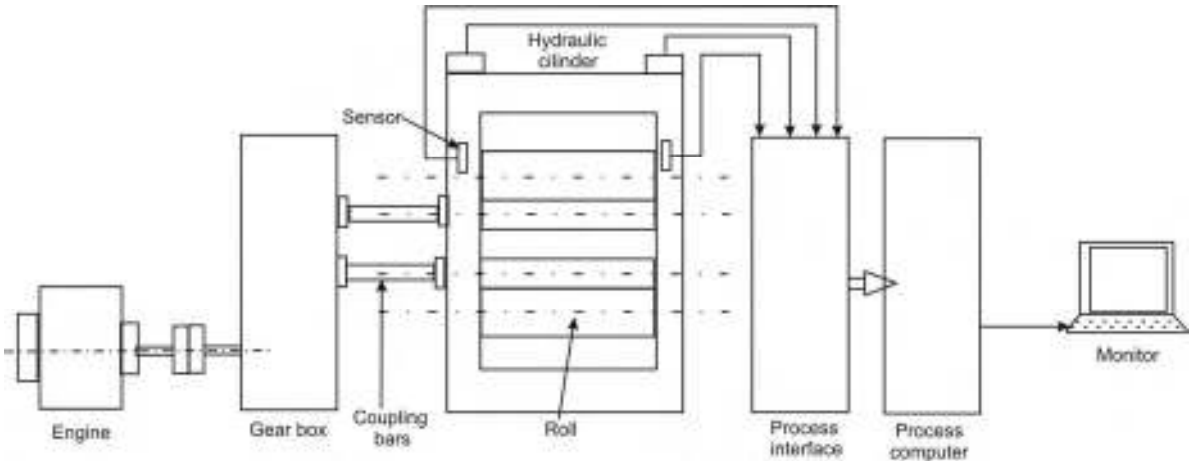

Fig.1. *The integrated on line for rolling mill monitoring system.*

3. Measurement of coupling torque

The measurement of coupling torque is necessary because a lot of dynamics effects are transmitted from the propulsion system. This dynamics effects are transmitted like oscillations from engine, through coupling, gear box, coupling bars, to work rolls to backup rolls inside the milling stand.

The torque monitoring systems for rolling mills can create predictive maintenance strategies and optimize the rolling process.

The measurement was made in three round and the results are shown in table no.1.

Table 1

Mill vibr. / **No. of frame**	**Vibration amplitude**			**Vibration frequency engine zone**			**Vibration frequency operator zone**		
	[mm]			[Hz]					
	I	II	III	I	II	III	I	II	III
3	0.128	0.120	0.119	127.9	128.1	128.4	126.3	125.6	127.2
4	0.198	0.193	0.211	127.4	127.9	126.8	125.8	124.9	126.8
5	0.118	0.115	0.113	127.8	127.3	127.6	123.7	125.1	124.7

A torque monitoring system has a torque sensor, mounted on the shafts of the main drive (engine zone) of the rolling mill an interface for data acquisition and a process computer. The system has the possibility to record, display and storage the data about the level of torque online and offline display of time signal. The two systems (vibration monitoring and torque monitoring) can give the level and limit for rolling mill normal functionary.

The torque sensors used in rolling mills must be very robust due to the rough ambient conditions. A strain gauge was used for torque measuring and a system protects the strain gauge and the electronics parts on the shaft against industrial fluids or mechanical damage.

Torque sensors are sensitive and must be protected on during operation.

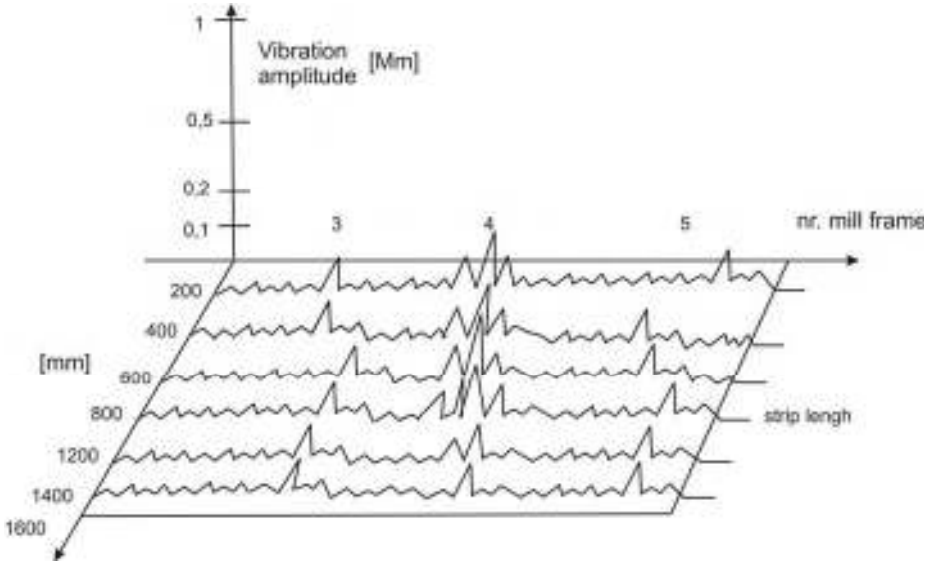

Fig. 2. *The spectrum of frequency-speed-cumulative of the vibrations measured at the last rolling on the three, four and five stands. The vibrations was measured during the rolling of 10 coils.*

4. Conclusions and results

The results of some examinations on different types of rolling mills illustrate the benefits of monitoring systems in rolling mills. The first example shows a machine-related pass schedule optimization.

This leads to longer lifetime expectations for the high loaded components of the main drive. The loss of production time is insignificant, but the lifetime expectation of the spindles increases dramatically. The use of integrate monitoring system means a constantly high level of product quality.

The heavy torsion chatter which occurs in the middle of the pass marks the surface of the block and causes severe damage to the drive.

A process optimization may be carried out if such events are recorded and analyzed. In this case, the lubrication system was improved in the last three years.

During the first pass the entering torque impact is very high. During the reversing pass a similar, but inverted characteristic was observed.

This research was developing in two directions: the first we analyze mill stand components during mill vibrations and the second, the actionnary system (engine, coupling, gear box, coupling bars).

This all, was doing to obtain a quality strip and a good maintenance for rolling mills systems. We analyze the vibration monitoring system to reduce the risk of gage or roll vibrations and than we measuring the torque inside of monitoring system, for process optimization and condition-based maintenance.

The diagram and the schedule presented here confirm the efficiency of the two systems to obtain a quality product.

References

[1]. Asch, A., Hohn, W. - *Monitoring System for Roll Stand Drives using Strain Gage Technology*. In: Proceedings of the 9th IF AC Symposium on Automation in Mining, Minaral and Metal Processing, S. 175 - 180, IF AC International Federation of Automatic Control, 1998

[2]. Farkas, T. - *Entwickung eines Verfahrens zur Identifikation von drehzahlpropor-tionalen und nicht-drehzahlproportionalen Storschwingungen an Walzanlagen*. Diplomarbeit an der RWTH-Aachen, 1999.

[3]. Hani, K. - *Untersuchung hochfrequenter Storschwingungen an schnell laufenden Kaltwalzanlagen*. Dissertation, RWTH Aachen, Umformtechnische Schriften Band 28, Verlag Stahleisen, 1991

[4]. Donkle HI, L. - *Fifth octave chatter problem solved using vibration analysis*. In: AISE Steel Technology, Volume 76 No. 11, 1999

[5]. Mackel, A., Cerv, H., KeBler, H.-W., Luckmann, F. - *Mill Diagnostic System (Mi-DaS) - a monitoring system with quality- and maintenance-related diagnostic functions.* In: Aluminium, Volume 74 (1998).

[6]. Mackel, J., Asch, A., Seeliger, A. - *Brummerschwingungen an Walzgeriisten vol-lkontinuierlicher Kaltwalzanlagen*: Detektierung, Verifikation, Vermeidung. VDI-Berichte Nummer 1220, 1995.

[7]. Mackel, J., Seeliger, A. - *Qualitatssicherung an schnell laufenden Walzanlagen.* In: Alma Mater Aquensis RWTH-Aachen (1995/96).

[8]. Mackel, J., Seeliger, A., Georges, D. - *Measurment and Diagnosis of Process-Disturbing Oscillations on Plants for Machine Condition Monitoring and Quality Control.* In: Proceedings of the XIV Imeko World Congress (1997).

[9]. Mackel, J. - *Maintenance and Quality Related Condition Monitoring in Rolling Mills.* Presented at the AISE Annual Convention in Chicago (2000).

[10]. Markworth, M. - *Querwellen auf kaltgewalztem Band*. In: Stahl und Eisen 114, Nr. 11(1994).

THE ANNALS OF "DUNAREA DE JOS" UNIVERSITY OF GALATI.
FASCICLE IX. METALLURGY AND MATERIALS SCIENCE
N^0. 2 – 2009, ISSN 1453 – 083X

INTERCRITICAL THERMOMECHANICAL TREATMENTS OF THE MICROALLOYED STEEL PRODUCTS FOR WELDED STRUCTURES

Elisabeta VASILESCU, Ana DONIGA, Marian NEACSU
"Dunărea de Jos" University of Galati
email: elisabeta.vasilescu@yahoo.com, uscaeni@yahoo.com

ABSTRACT

This paper shows the laboratory experiments made on several grade steels by applying some intercritical thermomechanical treatments; Two variants were used: "down-up" thermomechanical treatment with heating and rolling in the intercritical range and "up-down" thermomechanical treatment with preliminary complete austenitizing and rolling in the intercritic interval. Structural changes, as well as changes of properties revealed in the experimental variants of the intrercritical treatment, have been compared to those revealed by controlled rolling and normalization states of delivery that are recommended to flat products from these steel grades. High values of the strength characteristics and a good plasticity have been obtained.

The paper presents only a part of the results obtained when applying different regimes of thermal and thermomechanical treatment within experimental researches made at laboratory and industrial scale, on thick plates of different thicknesses and qualities of the weldable steels.

KEYWORDS: termomechanical treatments, microalloyed steel, intercritical interval

1. Introduction

The literature recommends that the intercritical heat treatments should be applied to hypoeutectoide alloyed steels, underlining their positive effect on the plasticity characteristics and mainly on ductility characteristics. Nowadays researches show that the intercritical heat treatments can be successfully used in normalizing shipbuilding plates, in quenching some of the steel grades used in construction and in regeneration of the thermally influenced zone (TIZ) at welded joints of Ni-Mo-V low carbon steels as well as biphase steels. [1]

The purpose of unconventional thermal processing is to find alternative technological solutions to classical thermal processing, in order to obtain comparable using characteristics, but with economical advantages, such as: the decrement of energetic consumption and of metal losses by oxidation (the case of thermal treatments at low temperatures, which suppose intercritical heating of the hypoeutectoid steels) or the elimination of final thermal treatments (the case of the thermomechanical treatments that suppose the combination between plastic deformation and thermal treatment, (fig1).[2]

The paper presents some results concerning the influence of the intercritical thermomechanical treatment on the structure and the mechanical characteristics of microalloyed heavy steel plates.

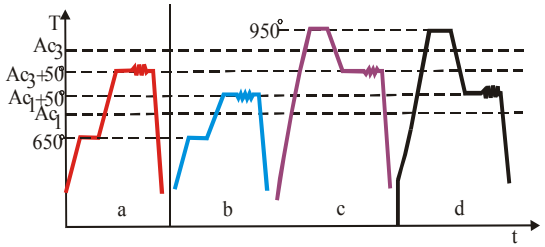

***Fig. 1** Technological variants for the intercritical thermomechanical treatment of the steel: a, b) "down-up" thermomechanical treatment; c,d) "up-down" thermomechanical treatment*

2. Experimental conditions

The research has been made on X60, X65 steels for welded pipes line.

The quality conditions in delivery state of the flat products are stipulated by European norms, Romanian standards.

In the title following tables are presented the chemical composition and mechanical characteristics imposed by the norms for the studied steels. (table no.1,2) [3]

Table 1. *Chemical composition of fine-grained, welded steels, for welded pipes (X60, X65)*

Steel Grade	C max	Mn max	P max	S max	Details
X 60	0,22	1,40	0,025	0,015	c, d
X 65	0,22	1,45	0,025	0,015	c, d

Note: (c) Nb,V,Ti or the combination between them is estabished by the producer.

(d) The Sum of the elements (Ni+V+Ti) must not exceed 0,15%

Table 2. *Mechanical properties according to API 5L/ 2004*

Grade steel	Rc, min [MPa]	Rm min [MPa]	A5 Min [%]
X 60	414	517	a
X 65	448	531	a

Note: (a) is determined through relations specified by the norm.

Table 3. *Chemical composition, [%]*

C	Mn	Si	P	S	Al	V	Nb
0,09-0,12	1,30-1,60	1,17-0,30	max. 0,025	max. 0,007	0,015-0,05	0,03-0,08	0,03-0,05

At Mittal Steel S.A. Galaţi, for the making of thick plates with the mentioned destination, the X65 steel qualities are elaborated, with the following chemical composition:

At Mittal Steel have been applied many classic thermal treatments regimes, that consisted in normalizations, hardenings and returns, and intercritical treatments consisting in normalizations and hardenings with returns in intercritical domains (fig.2).

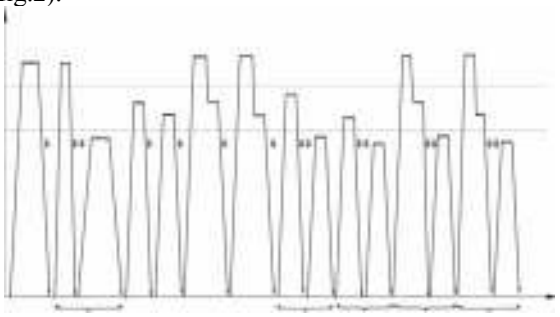

Fig. 2 *Experimental heating regimes*
** Air cooling ** Water cooling*

3. Experimental results

Furthermore, it is presented a part of the experimental results regarding the microstructural aspects and the values of physical and mechanical properties of the studied steels for certain experimental regimes of thermal treatments and intercritical thermomechanical treatments.

The following regimes have been applied:

A=normalizing

B= heating at 920^{o}C →cooling at 850^{o}C, rolling and cooling in water; ε =20% and 30%

C= heating at 920^{o}C →cooling at 850^{o}C, rolling→ air; ε =20% and 30%

D= heating at 920^{o}C→cooling at 800^{o}C+ rolling→ water

E= heating at 920^{o}C→cooling at 800 ^{o}C+ rolling→ air

F= heating at 850^{o}C→rolling→ water

G= heating at 850^{o}C→rolling→ air

H= heating at 800^{o}C→rolling→ water; ε =20% and 30%

I= heating at 800^{o}C→rolling→ air; ε =20% and 30% (ε - degree of rolling reduction)

In table 3 the mechanical properties obtained for the 13 regimes variants are presented:

Table 4. *Mechanical characteristics for the experimental regimes*

No.	Variants	Mechanical characteristics				
		ε [%]	Rm [N/mm^2]	Rp0,2 [N/mm^2]	A5 [%]	HB
1	A	-	546	368	29	278
2	B	30	804	764	22	292
3	C	30	637	579	29	191
4	D	30	803	753	20	285
5	E	30	577	412	26	174
6	F	20	834	685	32	292
7	G	20	686	566	26	202
8	H	30	1027	852	20	329
9	I	30	651	498	20	215
10	H	20	933	756	20	315
11	I	20	651	498	20	215
12	B	20	880	696	20	301
13	C	20	636	526	26	148

In figure 3 are presented the Rm and Rc values for the experimental regimes where the rolling deformation degree is ε =30%.

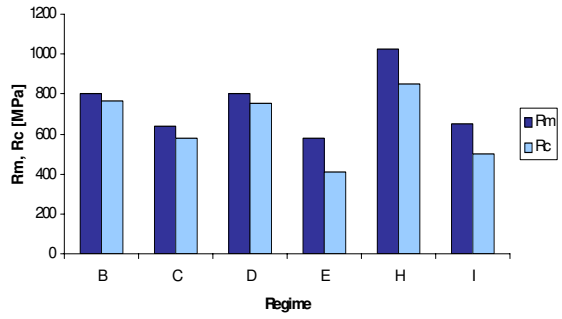

Fig.3 *Mechanical properties for some experimental regimes*

The following diagrams presents the laboratory experimental conditions at thermal and intercritical thermomechanical treatments.(fig.4)

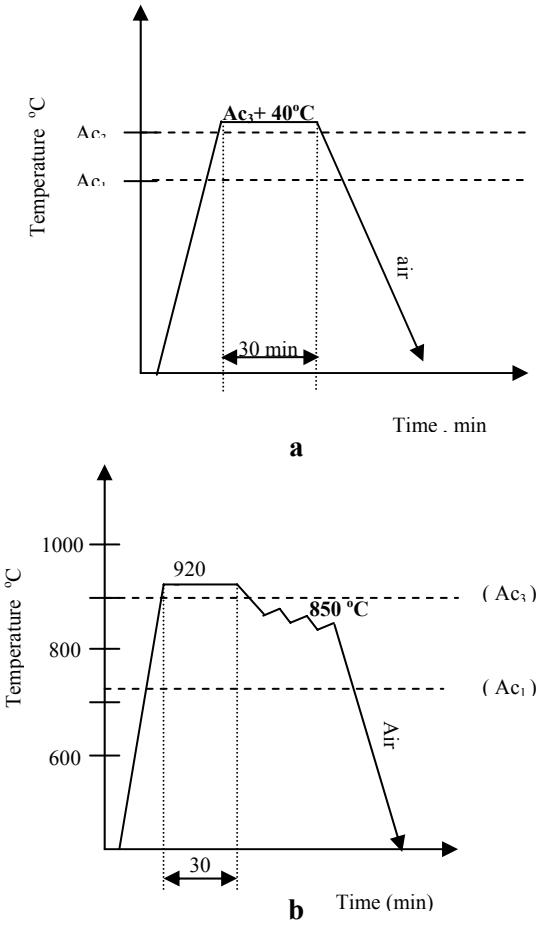

Fig.4 *Treatment cycles a – normalizing; b - intercritical thermomechanical treatment (C variant).*

The followig pictures shows the microstructures that resulted after the applying of thermal and thermomechanical treatment regimes on steel X65.

Fig. 5. *Diagram of normalization heat treatment - A variant (x500).*

Fig.6. *Intercritical thermomechanical treatment state - B variant (x500).*

Fig.7. *Intercritical thermomechanical treatment state - C variant (x500).*

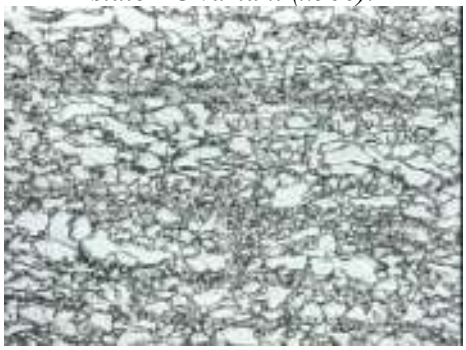

Fig. 8. *Intercritical thermomechanical treatment state - D variant (x500).*

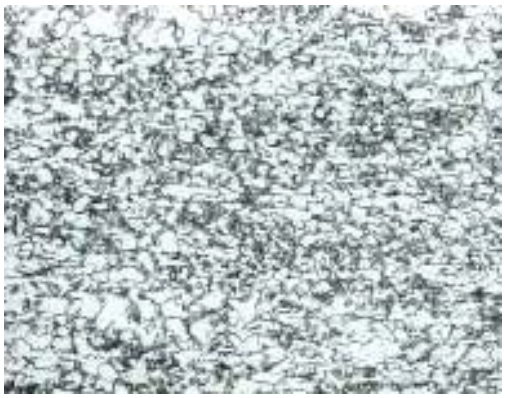

Fig.9. *Intercritical thermomechanical treatment state - G variant (x500).*

Fig.10. *Intercritical thermomechanical treatment state - I variant (x500).*

4. Conclusions

The laboratory experiments were made on several grade steels (X60, X65 for welded pipes) with same intercritical thermomechanical treatment application. According to present norms, the flat products made of the steel whose qualities have been characterized above, are delivered in normalized state or in equivalent state obtained by normalizing rolling (thermomechanical rolled steels).

Two variants were used: "down-up" thermomechanical treatment with heating and rolling in the intercritical range and "up-down" thermomechanical treatment with preliminary complete austenitizing and rolling in the intercritic interval. In this paper there are presented a part of the experimental results regarding the microstructural aspects and the mechanical properties values of the studied steels for certain experimental regimes of intercritical thermomechanical treatments.

Structural changes, as well as changes of properties revealed in the experimental variants of the intercritical treatment have been compared to those revealed by controlled rolling and normalization, states of delivery that are recommended to flat products from this steel grade.

For the X65 grade steel (with the chemical composition shown in table 3), for which the microstructural aspects for certain experimental regimes were presented in this paper, we can make up the following conclusions:

a) the air cooling, ("top to bottom" heating experimental variants) in opposition with water cooling, in all experimental variants, leads to the improvement of the plasticity properties, by maintaining their resistance mechanical properties, according to the norms;

b) the water cooling (all experimental variants) from intercritical interval, with 20 and 30% deformation stages, leads to very significant values of resistance properties (R_m= 636-1027 N/mm^2) while the plasticity properties drop (A_5= 20 –32%) the experimental variants with heating directly into intercritical interval ("bottom to top" variants, with no previous austenitizing), for deformation stages higher than 40%, independently from the cooling manner (air, water), lead to the achievement of an optimal complex of mechanical properties.

The analysis also reveals the fact that the main purpose of these experiments – namely to find a heat treatment variant able to efficiently replace the classical making process and of heat treating from the point of view of the energetic consumption, of the output costs and of the mechanical and properties – has been accomplished.

Thus, these mechanical characteristics of the flat rolled plates obtained by classical normalisation can be reached under optimal conditions by the intercritical thermomechanical treatments.

References

[1]. Leger, I. – ***Etude des traitements intercritique*** **(A1-A3) des** aciers hypoeutectoides- Mem. Scient. Met. LXVII. Nr.5/1971.
[2]. Popescu, N; Gheorghe, C; Popescu, O. - *Tratamente termice neconvenţionale*, Editura Tehnică Bucureşti, 1990.
[3]. SR EN 10113/2-1993 (STAS 9021/1-1989) - API Specification for Line Pipe 5L- forty second Edition, 2000; STAS 8324/86.

THE ANNALS OF "DUNAREA DE JOS" UNIVERSITY OF GALATI.
FASCICLE IX. METALLURGY AND MATERIALS SCIENCE
N^0. 2 – 2009, ISSN 1453 – 083X

GENERATION, MORPHOLOGY AND MINERALOGY OF THE DUST PARTICLES FROM OFF-GAS BLAST FURNACE

Anișoara CIOCAN, Florentina POTECAȘU, Liliana IVANCEA
"Dunărea de Jos" University of Galati
email: aciocan@ugal.ro

ABSTRACT

In order to elucidate the morphology and mineralogy of the dust from blast furnace, the fundamental aspects of its generation process were studied. A dust generated by the dry dedusting step of the cleaning process for the BF off-gas was analysed by microscopy and chemical analyses. The results indicated that the shape of particles is predominantly non-regular. We established with approximation the main mineralogical compounds: hematite, magnetite, calcium ferrites, glass and silicate phases. These are in accordance with mineralogy of the feed materials charged into blast furnace and in correlation with the complex processes that are developed into specifical zones where the dust particles were generated. The properties of BF dust and its structural phases are discused in respect to the blast furnace processes, the temperature zones and the gas composition.

KEYWORDS: integrated steelwork, BF dust, structural properties, mineralogy, shape of particles, valorisation, sintering process

1. Introduction

The knowledge of the mineralogical characteristics of the dust from blast furnace is necessary to create the fundamentals that can be utilized to design the dust recycling technology. Also, this is necessary for good knowledge of the waste in respect to making the forecast that is its behavior into a recycling flow, in this case in the sinter plant by feeding directly to the mixing beds.

The dust and sludge are generated from the off-gas of the blast furnaces. This is cleaned in 2 steps. In the first step, that is the dry dedusting step, the coarse particles are separated so that the BF dust is formed. After passing the first step of the cleaning process, the off-gas is cleaned in a wet process. The fine particles are separated in this way and the BF sludge is generated.

As result of the diverse phenomena that occur in the different zones of the blast furnace, the powder mixes are formed from a part of the varied materials charged into the blast furnace such as feed materials. These are collected in the hot ascendent gases that pass up the descendent charge materials. The dust quantity and its properties is in accordance with its generation process in respect to the blast furnace processes (the temperature zones and the gas composition, Figure 1).

Also, the caracteristics of the BF dust genered are influenced by the nature, the quantity and the properties (chemical composition, mechanical strengh) of the feed materials (sinter, iron ores, fluxes, coal injected).

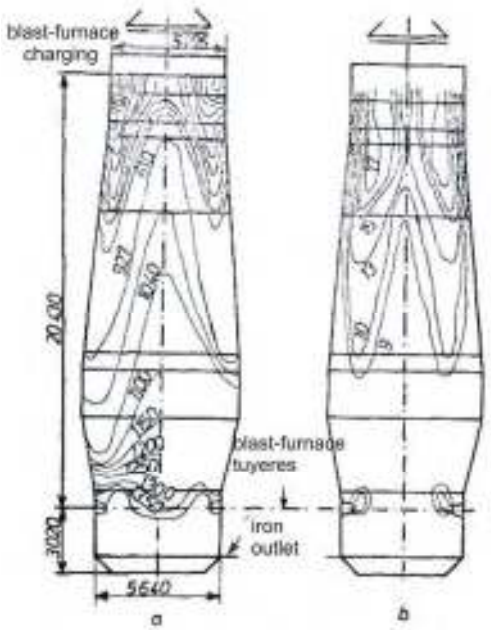

Fig.1. *Temperature (a) and the CO content (b) of the gas into a section of the blast furnace [1].*

The properties of the dust particles and the properties of the feed materials from the blast furnace, that is the generator for this dust, are likewise. Supplementary it is necessary to take into consideration the zones where the dust particles are generated and the zones which are passed by the dust particles until their collecting in the dust catcher. The temperatures and the composition of the gas are different and transformations are developed in the dust particles (for example the disintegration of the sinter and the iron ores, attributed to the volume change associated with the reduction of hematite to magnetite).

The descending of the charge materials is accompanied by physical changes and chemical reactions, Figure 2. A lot of mechanical processes occur: abrasion, crushing, cracking. Also, the softening of materials, the formation of the liquid phases and, interactions between the gases, liquids and solides can occur. The reduction processes and oxidation are produced and these are specific for each zone of the blast furnace, according to its temperature and its composition of the gases generated now by coke (the lower, middle and upperzone).

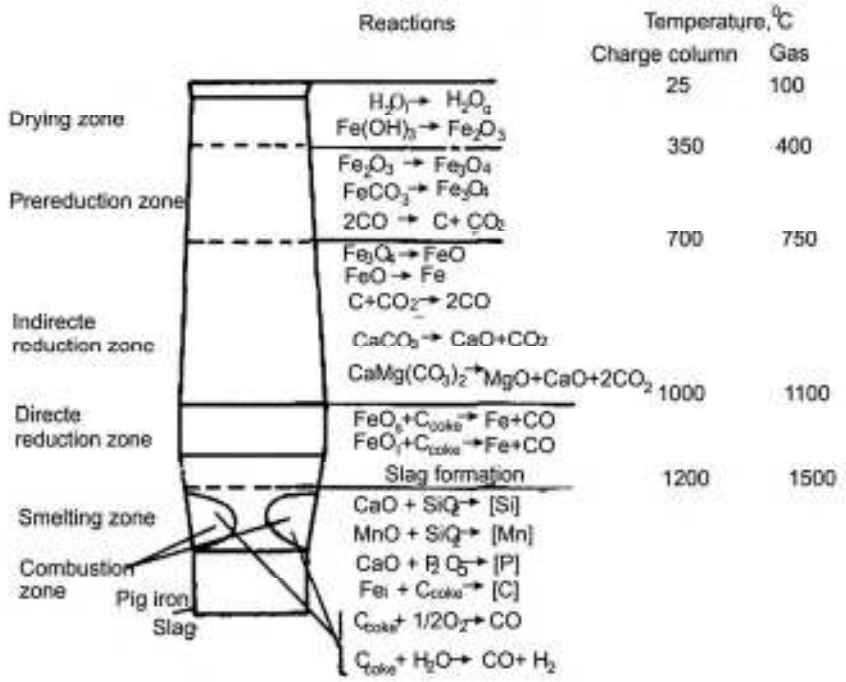

Fig.2. *Chemical reactions that are taking place in the zones of the blast furnace [1]*

The formation of the dust particle in the zone that have lower temperatures (so called upper zone or preparation zone where the ascending gas decreases in temperature to about 250^{0}C and the solids temperature rises from the ambient temperature to about 800^{0}C) is accompanied by the decomposition of carbonates other than calcium, vaporization of moisture and hydrated water of the burden, carbon deposition according $2CO = CO_2 + C$ and partial or complete reduction of hematite as well as magnetite into their lower oxides.

The most part of the coarse particles are formed from the particles of the feed materials (sinter particles, iron ore particles, flux particles, carbon and ash from coke or powder coal), the carbon black from the processes passed into upper zone of the charge column, the volatile mass of the powder coal (that is injected into tuyeres and condensed at the surface of the dust particles), hygroscopic water and residual capillary.

For an integrated steel plant with the sintering plant as upstream facility, the BF dust is internally valorized. The dust is generally recycled at the sinter making in more advanced countries. In this case, the BF dust together with other iron bearing materials are utilised into sinter feed. For good results, a special process of micro-pelletisation of the sinter feed into the mixing drum followed by sintering process must be considered [2, 3].

On other hand, the iron sinter and iron ores are introduced into BF furnace to produce molten iron. The most important factor that conditioned the good BF furnace function is the quality of each feed material component. The sinter quality is dependent on the properties of all components that formed the sinter mix. The chemistry of the iron-bearing materials and the variation in process parameters decide the sinter structure which, in turn, governs the sinter quality. Therefore, it is important to know which is the chemical composition and the

mineralogical structure for the iron-bearing components, and also for the BF dust. Their knowledge gives the possibility to forecast their behaviour durring the sintering process. In our case, this is very important in the evaluation of valorization solution for the dust of blast furnace in the sintering process. This paper presents the mineralogy of the dust from blast furnace in accordance with its morphology. The fundamental aspects of its generation process were studied.

2. Experimental method and materials

In the investigations, we used samples of BF dust taken from the discharge of the de-dusting unit. After homogenization by stirring and reduction of mass by quartering, the sample was reduced to a necessary size. The average chemical composition of BF dust samples, determined by classical quantitative methods is given in Table 1.

Table 1. *Average chemical composition of BF dust, % wt*

Fe	Mn	SiO_2	CaO	MgO	Al_2O_3	C	P	S	Oily mass
28.20	0.50	7.00	5.66	0.98	2.40	44.27	0.030	0.32	0.70

The powdery material was included into the synthetic resin and for obtaining a flattening surface, the samples were polished. The reflected-light micrographs of the dust samples were analyzed with optical microscope OLYMPUS and NEPHOT. Also, the dust samples were thermally treated and then were structurally analyzed.

The parameters of this treatment were: ~1100 ^oC for the heating temperature, 2 hours maintaining time, 20 minutes for cooling at the ambient temperature.

For correct approximation of the main mineralogic compounds, the results of the analyses that meet the requirements of international standard specifications for the magnetic fraction and CaO free content were used [4, 5].

3. Results and discussion

The macroscopic structure of dusts analyzed is non-uniform, with large pores and high permeability, Figure 3.

Fig.3. *Dust BF sample*

In respect to morphology and their different origin, the BF dust particles have varied shapes and dimensions. A lot of BF dust particles have polyhedral shapes and some of these have rounded shapes (a little proportion), Figure 4.

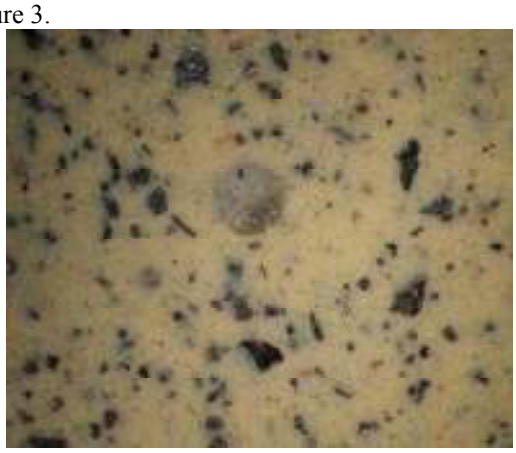

(x50)

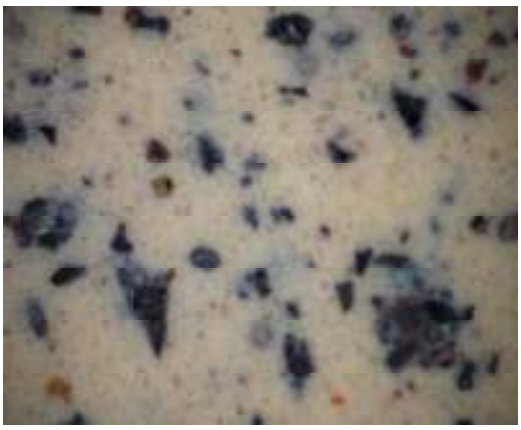

(x110)

Fig.4. *BF dust particles with varied shapes (polyhedral shapes and rounded)*

According to the researches reported by other references about the sintering process, the particles of the ferrous materials with irregular polyhedral shapes have the better adherence capacity on the bigger particles considered as nucleus for the process. This aspect is specific for the preparation

step of the sintering flow that is referred to the mixing operations by simultaneous balling and wetting of fine materials into mixing drum. These various materials formed by particles with various sizes and shapes are homogenized. As result of the wetting, the fine and small particles are covered with a water layer and then by adherence under superficial tension and balling acts, the micropellets are formed.

For BF dust samples, the particles with polyhedral shapes are prevalent. As a result, the following forecast is possible: the BF dust will have a good behavior during the preparation process of the feeding materials. Also the formation speed of the micropellets is favorably influenced by the presence of the polyhedral particles.

The generation process of the dust and the mineralogy of feed materials charged into blast furnace must be considered for establish the phase composition of the BF dust particles. The micrographs of the BF dust samples are given in Figure 5. Main phases include hematite, magnetite, ferrites, glass, and silicate phases.

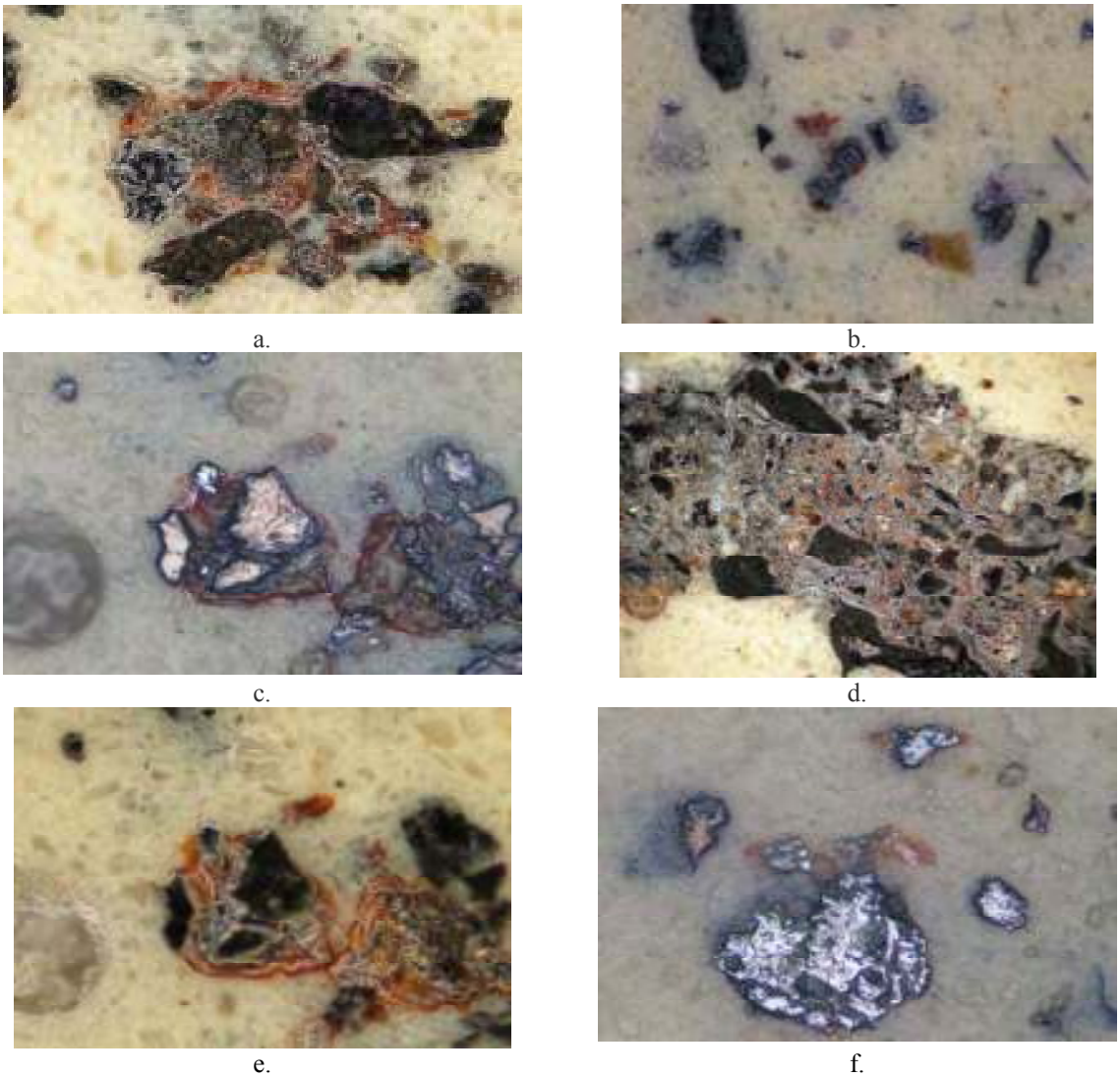

Fig.5. *Reflected-light micrographs of BF dust structure: a. magnetite, hematite set in partially devitrified glass, ghelenit, silicoferrite of calcium and aluminium (x400); b. magnetite, hematite, ghelenit, wallostonit (x200); c. magnetite, hematite, wallostonit (x400); d. magnetite, hematite, ghelenit, olivine, calcium ferrite crystals with interstitial calcium orthosilicate (x200); e. magnetite, hematite, wallostonit (x400); f. magnetite, hematite (x400)*

All feed materials components of the BF charge, namely the iron ores and sinter, transfer their mineralogy to the mineralogical structure of the BF dust particles. Also these are influenced by the presence of the lime, coke, and pulverized fine coal. The variations in compositions of the raw materials

and their heterogeneity also play a big role in the heterogeneity of the phase composition of the BF dust. Additionally this is influenced by the physical, thermal and chemical processes that take place in the zones of the blast furnace height.

Firstly the structural phases of the superior iron oxides are present, magnetite and secondary types of hematite are the prevalent phases. Wustite is absent because an oxidation process takes place into the cold zone of the off-gas cleaning system. Wustite formed in the first step at the exit of the gas is reoxidated, this process is positivelly influenced by the great surface of the BF dust particles. For summarysing, together with the iron prelevant phases (magnetite and hematite), there are present other phases such as ghelenit, wallostonit, olivine. Circumstantially, the fine coal particles that pass nonburned through the column of the feed materials can be present in the dust [5].

To estimate the phase composition, can be used the results of the magnetic fraction pattern and the free CaO content for the BF dust analyzed. The magnetic separation is possible for materials that have mineralogical components with different magnetic properties. This difference is in accordance with iron oxide types and its proportion into BF dust. According to the low value (11.15%) of the magnetic fraction for the material analyzed, the BF dust is a weak magnetic material like hematite ore, limonite and siderite. For BF dust, an important quantity of CaO forms chemical combinations (ferrite of calcium, wallostonit, and olivine). Other quantity of CaO is free (1.27 %wt or 24.44 % of total quantity) and for consequence the decreasing of the lime addition for self-fluxing sinter is possible.

The recycling of the BF dust in the sinter plant by feeding directly to the mixing beds involves structural transformations of its particles [6]. To establish the approximate morphological and mineralogical changes that are produced in the BF dust particles after the sintering process, the samples were heated at ~ 1100 ^{0}C, held at this temperature, and cooled down (the cooler time was 10 – 20 min). The oxygen from the atmosphere furnace and the high carbon of the BF dust leads to the structural modifications for the samples that are thermally treated. The transformations can be attributed to calcination losses associated with carbon oxidation, oily mass, other physical and chemical processes. The micrographs of the BF dust samples are given in Figure 6.

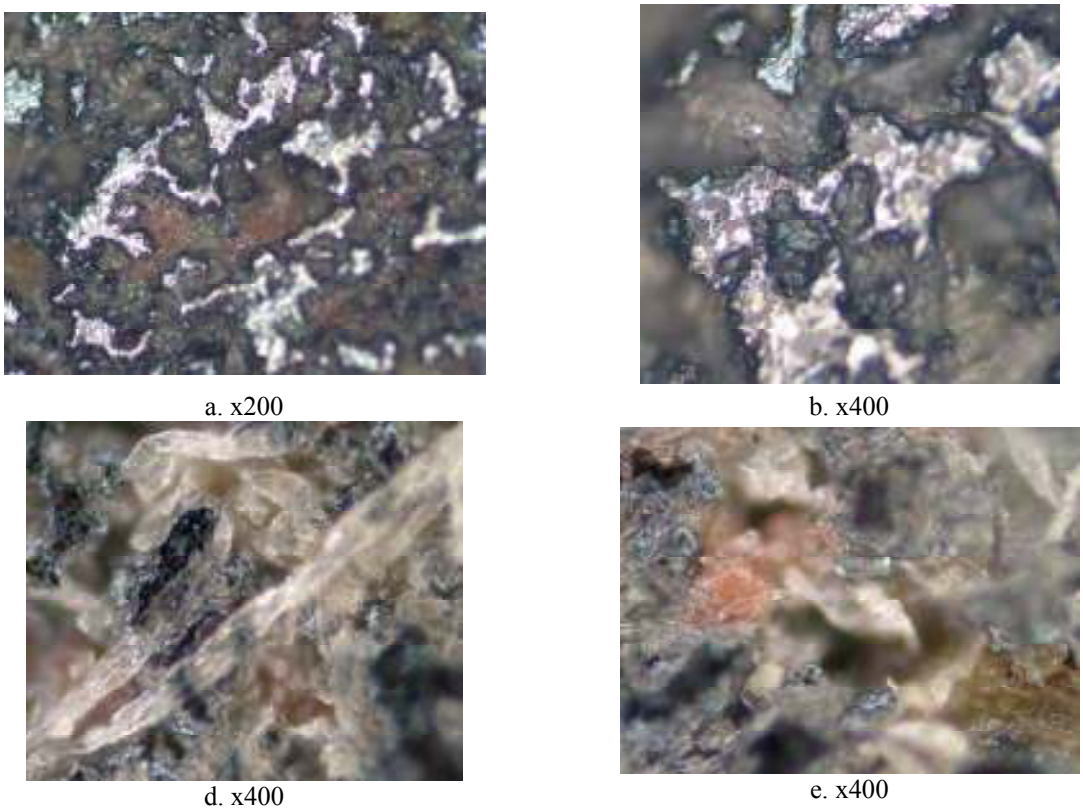

a. x200 b. x400

d. x400 e. x400

Fig.6. *Micrographs of BF dust samples thermally treated: a. magnetite with partially reoxidized zones of lamellar hematite; matrix of glass and crystallized phases of silicoferrite of calcium and aluminium-SFCA, olivine, wallostonit*

4. Conclusions

The sintering process can be the best solution for BF dust recycling for an integrated steel work. This is determined by properties of the dust (chemical composition, particles shape, morphology, and structure) because the sinter quality is dependent on the properties of all components that formed the sinter mix. The dust properties are influenced by its generation process: feed materials components of the blast furnace, the physical and chemical phenomena that occur in the different zones of the blast furnace and cleaning system etc.

For the samples analyzed the majority of the dust particles have irregular polyhedral shapes. This shape of iron components leads to a good behavior during the preparation process of the feeding materials for sintering process. The main mineralogic compounds of the BF dust particles are transformed hematite, magnetite, calcium ferrites, glass and silicate phases. These are similar to the mineralogical structure of the feed materials components of the blast furnace. The structural transformations that occur in the dust particles at the thermal treatment, oxygen presence and carbon are similar to those are passed into components that formed the sinter mix.

References

[1]. Kalenga, M. - *Investigation into the influence of magnesia content, alumina content, basicity and ignifugation temperature on the mineralogy and properties of iron sinter*, dissertation work, Universityof Pretoria, July 2007

[2]. Ciocan, A. - *Valorificarea deşeurilor mărunte şi pulverulente generate în siderurgie*, Grup editorial Naţional, Bucuresti, 2003

[3]. Ciocan, A. - *Valorificarea deşeurilor metalurgice. Procese şi tehnologii*", Galaţi University Press, 2008

[4]. Mitoşeriu, O. - *Cristalografie*, Ed. Porto Franco, Galaţi, 1993

[5]. Panaitescu, S. - *Studii şi cercetări privind îmbunătăţirea calităţii aglomeratului feros prin optimizarea reţetelor de şarjă şi a procesului de sinterizare pe maşinile de aglomerare cu bandă*, Teză de doctorat, Universitatea Dunărea de Jos din Galaţi, 2003

[6]. Heino J., Makkonen H. - *Recycling or Utilization of Dust, Scales and Sludge from Steel Industry,* www.ce.jyn.fi/helsie/pdf/heino.pdf.

THE ANNALS OF "DUNAREA DE JOS" UNIVERSITY OF GALATI.
FASCICLE IX. METALLURGY AND MATERIALS SCIENCE
N^0. 2 – 2009, ISSN 1453 – 083X

SOFTWARE USED AT CASTINGS PRODUCTION

Ioan MARGINEAN, Constantin BRATU,
Sorin–Adrian COCOLAS
Politehnica University of Bucuresti

ABSTRACT

The foundry industry has been developed worldwide, a number of software that can assist the design work and various processes in the production of castings. Current usage of such software by metallurgical engineers is possible after a few days training, advanced computer knowledge is not required. Also, the simplicity, performance that can ensure the sales prices and that does not require powerful software equipment is the main advantages of these programs.

KEYWORDS: foundry industry, software, casting

1. Software Foundry Industry

It should be noted that these programs and computer in general, do not replace the "man" factor. Technology is thinking how to do technology. The used computer program supports the designer by making calculations for sizing and optimization are much more accurate and are obtained in a much smaller, making it possible to decide whether a design is correct or not. Using the soft prevents the execution of design errors that lead mostly to attainment of the required technical performance.

These professional programs to simulate various phenomena occurring during flow and solidification of cast can be changed to simulate different methods of casting. Mathematical models of these programs differ in principle by introducing additional conditions that arise due to their use in the solidification simulation for the various processes of casting. Simulation programs are generally intended for simulation of thermal fields in solidification of cast.

Conditions to limit allowed by the software may be:

- *type Diriclet* when considered as input data to the surface temperature of ingots or castings;
- *Neumann type* when considering the input heat flux of the considered border segment, such as radiation or external sources of heat;
- *Cauchy type*, it is considered as input data as well as the outside temperature coefficient of heat exchange between the global environment and system analysis.

In general, the basic structure of the program, which was conceived and developed in a structure with multiple user options, distinguishes the following stages of work:

- automatic mesh (the graphical) of castings in volume elements;
- determining the type of coordinates used;
- enter the number of areas of different materials;
- introducing thermo-physical material characteristics for each area;
- placing temperature of the mixture of hardware and training;
- introduction of the surface temperature shrink head or mold;
- introducing of time step and total time simulated;
- the graphical representation of temperature and solidified areas.

General use of software provides a convenient way of operating through a menu system which can call their main functions as handling input and output files; mesh domain analysis; enter the material; introduction of casting temperature and initial temperature; placing conditions on the surface heat exchange system analysis; implementation of the program and other.

2. Software Process for Simulation and Optimization of Solidification of Castings with Different Procedures

2.1. NovaFlow & Solid CV Gravity

NovaFlow & Solid CV is a complete mould filling and solidification simulation package based on advanced fluid flow and heat transfer theories. NovaFlow & Solid CV utilizes Control Volume

Meshing technology (CVM). With this technology, the surface of the 3D model controls the shape of the mesh elements on the border of the casting. This creates cubic elements inside the casting and border cells on the boundary of the casting. This program simulates most of the casting methods on the market such as: gravity sand casting, gravity permanent mould, low pressure die casting, high pressure die casting, lost wax method, tilt pouring and lost foam process. All commercial alloys can be simulated such as: grey and ductile iron, steel, aluminum alloys, copper, zinc, magnesium-based alloys, super alloys and all types of mould and core materials that exist on the market and also exothermic materials as well as chills. Simulations visualize the consequences of a certain design of gating system and moulds. Casting defects such as oxide inclusions due to excessive turbulence, cold-shuts, shrinkage cavities and slag inclusions can be avoided by optimizing the design of the gating and venting system.

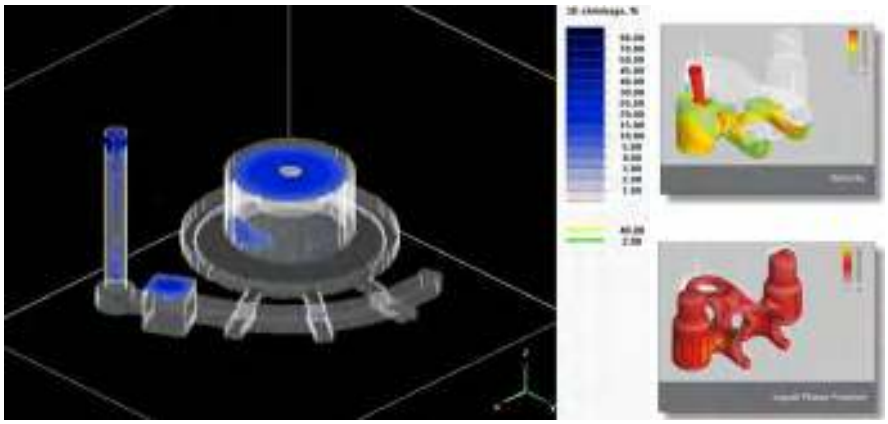

Fig. 1. *Print-screen of NovaFlow & Solid interface.*

2.2. SIMTEC/Wincast

The program was developed by the company RWP (Germany) and uses the finite difference method (mesh is done automatically). It proposes a complete offer, from filling up efforts to determine the mechanical and thermal model using an elastic or elasto-plastic. In addition to modeling the processes that occur in the gravitational field are dealing with other processes (die casting, low pressure casting, "squeeze casting", "loast foam").

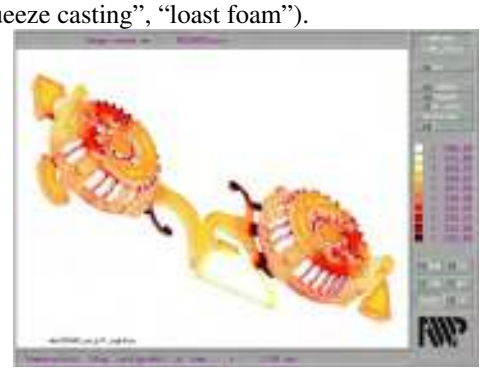

Fig. 2. *Screen capture of Simtec interface.*

2.3. Metal Master

This program is expected to optimize the composition of cast irons under the conditions obtaining in the development of a minimum cost price, the achievement of numerous tests with various melt compositions: it does not require high performance computers and is very easy to use.

2.4. ProCAST

This program is developed by UES, USA and has a wide range of possible uses, grouped by modules. ProCAST has a way to determine enthalpy and solid fraction depending on temperature and alloy composition. It features a high performance mesh mode. The program integrates: a database of material characteristics, thermal analysis models, the flow and the efforts of components and metallurgical and specific models.

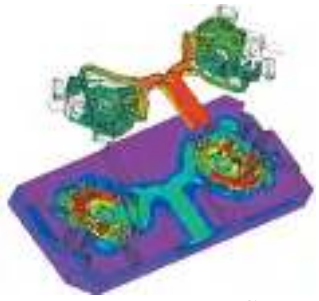

Fig. 3. *Low Pressure Casting.*

2.5. IronCAD 4.0

It is a package CAD / CAM product company Desing Visionary Systems Inc. - USA and distributed in Romania by Metal Progress Soft. It's designated geometric solids modeling and complex mechanical assemblies, molds, foundry molds, SDV's, electrical installations, and others.

Fig. 4. *IronCAD 4.0 program interface.*

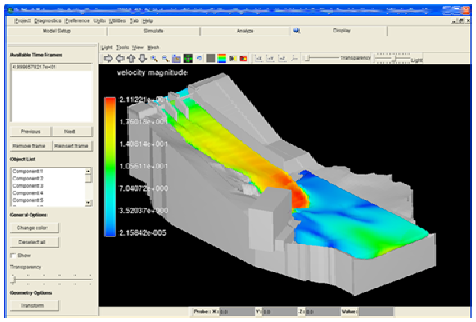

Fig. 5. *Simulation flow and filling forms.*

2.6. Flow-3D

The program was developed by Flow Science in the U.S. and specializes in the design flow. For application in the foundry to propose a list of models that allow even simulate hydraulic phenomena related to the development of special procedures such as filling the form for the process "lost foam", Thixocoulée ".

Resolution is made by the method of control volumes.

2.7. MAGMA

MAGMA is a German program, including flow and solidification, and modular design stays true to revolve around the control volume method. At the same time, the program includes the calculation efforts and deformations. It proposed a method of procedure "thixocoulée", which was developed in collaboration with the EFU. At the same time, models have been developed for determining segregation and mechanical characteristics, based on chemical composition and thermal evolution during solidification.

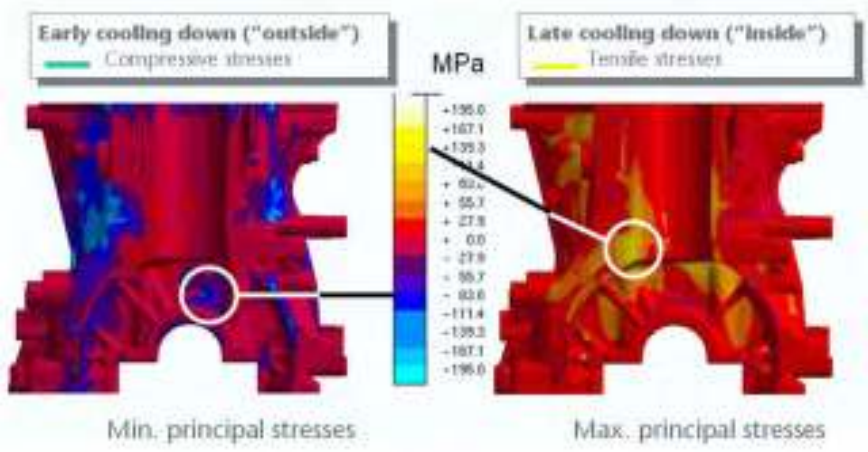

Fig. 6. *Magma casting design.*

2.8. ATAS^{TM} (Adaptive Thermal Analysis System)

It is composed of system control and optimization of design for gray cast iron, malleable and nodular cast iron. The method was developed by NovaCast AB in collaboration with the Swedish Foundry Association and is based on the first derivative of the cooling curve combined with artificial intelligence applied. The system is a fully automatic registration of cooling curve from the time the iron is poured into the sample cup. After registration, the system looks at the curve; it calculate the derivative I and about 40 thermodynamic properties. A test result is usually given in 3-5 min.

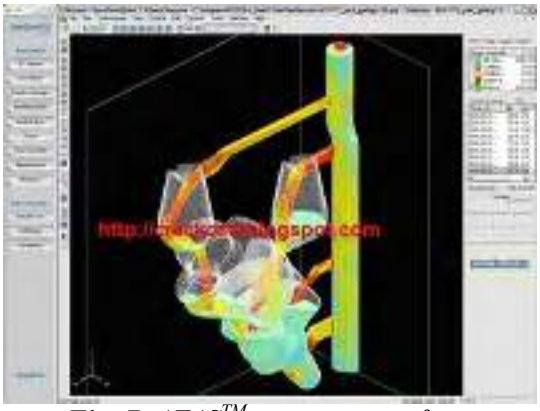

Fig. 7. *ATAS^{TM} program interface.*

2.9. NovaCast

NOVACAST Program (Sweden) presented at the GIFA 1989 Congress solidification of alloys in simulated three-dimensional (3D) has incorporated an interface for downloading directly from AutoCAD drawings cast. The program analyzes the heat transfer finite difference method and can cause iso-solidus curves, field temperature alloy-form system, the biphasic and the fraction of solidified alloy and place of occurrence and size of areas where appears micro-porosity. Currently, there are two modules: module solidification (NovaSolid) and module simulating cavity filling forms (NovaFlow).

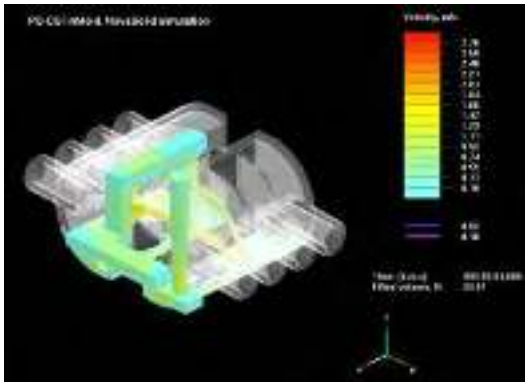

Fig. 8. *System Design with NovaCast.*

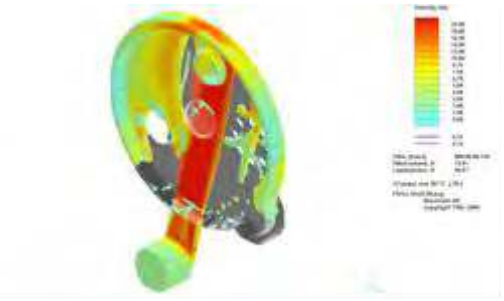

Fig. 9. *Modeling and simulation of high pressure die casting.*

2.10. CASTech

The program simulates the filling and solidification of castings. Filling in Injection molding, currently proposed to be included in a future version of the program. Program CastDESIGN associated CastCAE version is used to calculate shrink head, which is to determine their size and location. The choice is made from a database, based on simulation results of solidification processes.

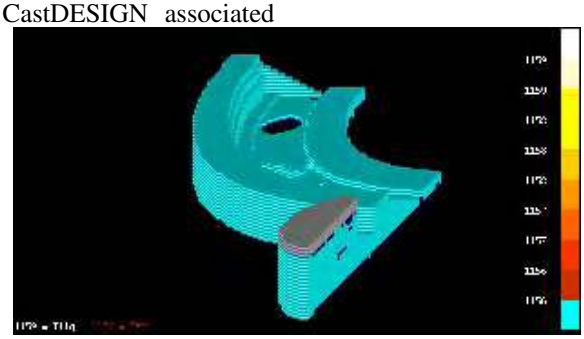

Fig. 10. *Porosity simulation with CASTTech*

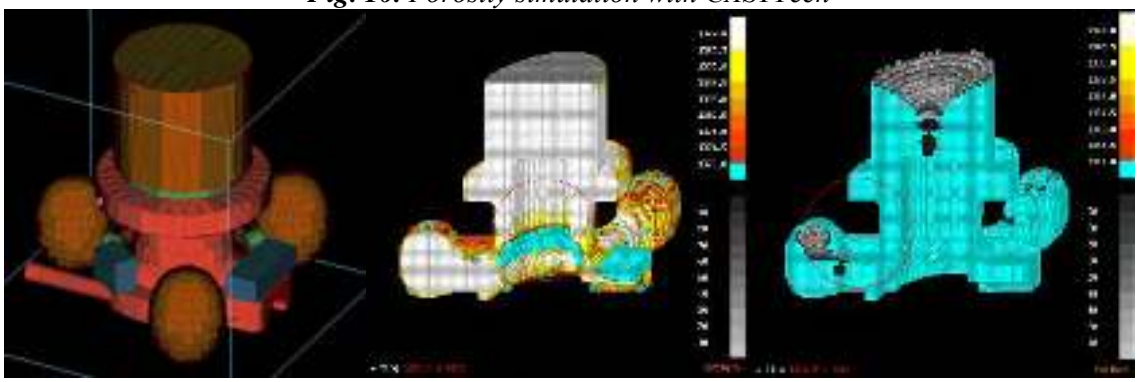

Fig. 11. *Modeling of a valve body casting.*

2.11. SIMULOR / PAM-CAST

Simulation program developed by Silicon Graphics can simulate flow and solidification of alloys and is based on finite volume method. The method of calculation used is that of the control volumes. The program offers the following

advantages: the program is modular, allowing computing desired choice; CAO interface programs are taken into account in the thermal model, densener indoor, outdoor and air strips which are formed at the interface alloy-form; it makes a physical database for several aluminum-based alloys.

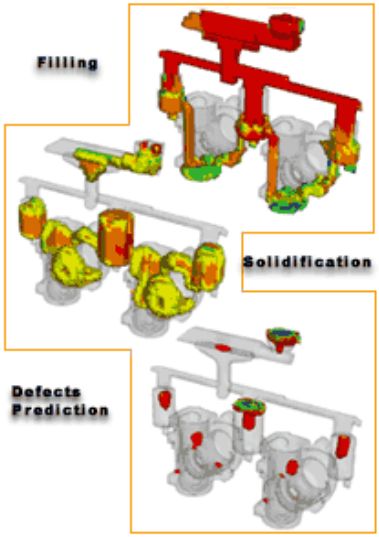

Fig. 12. *Specific solvers used at casting process.*

Fig. 13. *High pressure die casting.*

2.12. AFSolid3D

The program is conducted by the American Foundrymen Society and uses the finite difference method and can run on a PC. This program proposed by the foundry in 1986, claimed more than 300 licenses worldwide. It has its own system and enables simulation training CAO shrink hole that occurs during solidification. It is possible, while shaping and filling the cavity, where casting gravitational field.

2.13.SOLSTAR

SOLSTAR company FONSECO program can calculate and divide the piece into a million parts by volume. Thus, multimillion version 3 can be calculated and share a song in 64 million volume elements and multimillion variant 2 than 3 million items in volume. Increased volume elements improve simulation accuracy in case hardening.

The program presents facilities, such as easy to work with files, improved interface, an analysis of areas of developing micro-porosity. The program can be run only on powerful computers.

3. Conclusion

At current technical conditions such a design may be cast to ensure a controlled management of the process of solidification in industrial conditions. The usage of computer to study processes taking place during solidification leads to lower consumption of raw materials and energy, liquid alloy, labor, fluid technology and a significant decrease of time for approval of optimal technology. One of the major problems faced by designers of hardware technology is to achieve the possible removal of its thermal nodes inside castings. Simulation programs made offers to guide the process of solidification so that correctly dimensioning the designer and shrink head exterior or interior, thermal nodes castings should be completely eliminated. The emergence in recent times, the program flow and solidification simulation of composite materials make the new provisions to limit the matrix (metal) and particle or fiber. Phenomena that occur in these conditions are very difficult to simulate because of the multitude of factors that influence the solidification process of composite materials and make mathematical models that describe these processes to be cumbersome and error rising. Generally, the processes of solidification of alloys to be simulated in real conditions with very small errors; making the manufacture of castings has become much easier and it requires less time. This results in a saving of labor, materials and castings lower price, therefore more efficient foundry.

References

[1]. Godfroid, H. - *Simulation Processes: Computer Simulation and Modeling*, Workshop 50 th Int. Foundry Congress, Cairo, CIATF, 1983.
[2]. Soporan, V., Vamos, C., Pavai, C. - *Modelarea numerică a solidificării*, Editura Dacia, Cluj – Napoca, 2003.
[3]. Thomas, B.G. - *Stress and Advanced Solidification Processes VI*, Palm Coast, FL, March 21-26, 1993.
[4]. Bratu C, Soporan V. - CeEx 260/2006 - *Modelarea matematică a proceselor care au loc la turnarea pieselor metalice, in vederea reducerii consumurilor de materiale şi energie*, 2006
[5]. Cocolas Sorin-Adrian – Lucrare disertatie – *„Model experimental destinat modelarii matematica procesului de curgere la turnarea pieselor"*, 2008.
[6]. http://www.castech.fi/
[7]. http://www.ironcad.com/
[8]. http://tptc.iit.edu/Center/Resource/ApplicationOfSoftware/pamcast.html
[9]. http://www.esi-group.com/products/casting/procast
[10]. http://www.novacastfoundry.se/
[11]. http://www.afsinc.org/

THE ANNALS OF "DUNAREA DE JOS" UNIVERSITY OF GALATI.
FASCICLE IX. METALLURGY AND MATERIALS SCIENCE
N^0. 2 – 2009, ISSN 1453 – 083X

EXPERIMENTAL MODEL FOR POLLUTANTS MONITORING INTO THE COKE-CHEMICAL PLANT

Viorel MUNTEANU, Maria VLAD, Lucica BALINT
"Dunărea de Jos" University from Galaţi
e-mail: Viorel.Munteanu@ugal.ro, Maria.Vlad@ugal.ro, Lucica.Balint@ugal.ro

ABSTRACT

The Coke-Chemical plants contribute heavily to producing and emitting in the atmosphere a big amount of polluting agents.

Polluting emissions diminution and situating them within the international specific standards, can be realized by introducing a monitoring model with automate prominence of atmospheric noxa concentrations and with the possibility of connecting it to an open communication system. In the paper is conceived an experimental model for noxa and pollutants monitoring and in a frame of a polluting field existing in the coke-chemical sector from an integrated iron and steel complex.

KEYWORDS: coke-chemical plant, atmospheric pollutants, air samples, coke coking, suspension powders

1. Introduction

Worldwide there is a constant preoccupation among the environment agencies towards diminishing noxious emissions from the plants. The already existing programs permit a rigorous control of the polluting emissions level through which can be avoided the maximum acceptable concentrations provided by the international standards.

These result from the processes needed in coking, from the raw materials variety, from the adjustment of installations functional parameters etc., resulting in big amounts of polluting agents to be liberated in atmosphere, with major impact on environment and on health of the workers.

By estimating the polluting level and by comparing the specific noxa concentrations with the maximum admissible values regulated through norms, there can be dignified their deviation and can be established which atmospheric pollutants can be selected to be monitored.

2. The technological flux from a coke chemical plant

The technological flux from a coke-chemical plant contains:

a) *The coke preparation sector* with important role in feeding the coking ovens. They have the role of obtaining a quality coke and a coke gas abundant in coal by-products. The main operations from the coke packing flux are: reception, homogenization and coke storage, coke grinding, the coke packing burdening, coke packing moistening and mixing, preparation for loading the coking oven.

b) *Coking section*, in which is situated the coking oven, with an attribution in pyrogenated decomposition for coke obtaining. There are created two heating front-sides that are progressivelly advancing from the periphery to the center of the oven, the coal layers passing successively through drying, plastifing, mass hardening and degassing phases. The raw coke gas liberated from the oven due to the coal pyrogenetical decomposition is a complex mix of gas and steam, in which composition exists: tar vapor and water, ammonia, benzoic hydrocarbons, sulphuretted hydrogen, albocarbon, hydrocyanic acid, basic pyridine, organic compounds with sulfur (alkyl hydrosulphide, tiophene, carbon sulphide etc.), phenols, hydrochloric acid and chlorides, nitrogen oxides.

c) *The chemical section.* After exiting the oven, the raw coke gas is passed in the purification-treatment sections, respectively that of chemical products collecting. The raw coke gas, at the oven exit passes through circulation raise pipe towards the gas collector. In the circulation rise pipes elduite is made a first aspersion with raw ammonium water, the coke gas being cooled from ~700°C to ~90°C, hereby considering 50 ÷ 60 % from the contained tar. In the oven's loading-unloading periods, the cover of circulation rise pipe is opened, and the raw gas is evacuated in the atmosphere.

c_1) the cooling-condensing subsection. The cooled coke gas is sucked by the exhaust fans through un-tarring electrofilters. The tar content after the main coolers is about ~ 3g/Nm^3, and after the electrofilters about ~ 0,02 $g_{tar}/Nm^3_{coke\ gas}$. The insolubles in the resulted tars from the two coking sections are of different qualities. From the superior side of the mechanized settlers, the raw ammonia water, that represents the main component of the introduced liquid debit, is draining continuously into the water reservoirs. From here it is aspirated and pumped in the conducts that feed the cooling installation by sprinkling the gas collector of the batteries. This way is opened the so called barilet's circuit. Pursuant to partial vaporization of the water in the barilet, it is growing the concentration of un-volatile ammonia salts dissolved in the water, conducting to the impossibility of tar separation from water.

c_2) ammonia subsection. The raw coke gas after cooling and un-tarring in electrofilters gets to the ammonia subsection with a content of about ~ 5,0 ÷ 7,0 $g_{ammonia}/Nm^3_{gas}$. Regardless the ulterior use of the purified coke gas, the ammonia catching as completely as possible from the gas is obligatory, for environment pollution but also for avoiding the corrosion in the coke gas process installations and sub-products impurity. The ammonia is found fixed in two ways: 1) as free or volatile ammonia, dissolved in water or fixed in dissociable combinations that are decomposing simply by heating; 2) as tied ammonia (fixedly) in combinations from which no longer can be drawn out by the chemical action of NaOH. Besides the ammonia, the raw waters from the condensation area, contain CO_2, H_2S, phenols, tars, pyridine bases etc. The coke gas from the cooling-condensation subsection, after the un-tarring in the electrofilters and compression in exhaust fans, having the temperature of about 45÷50°C is conducted towards the saturation chambers. At the exit of the saturation chamber the gas is passing through drops captivator to retain the carried solution (lye) drops. The coke gas with a content of ~0,03 $g/Nm^3_{ammonia}$ is conducted towards the final coolers and the benzene washers. The main phases in the process of obtaining the ammonia sulphate are:

- the ammonia catching by coke gas barbotage in a solution of about 4-^8% H_2SO_4. By the reaction of the sulfuric acid with the ammonia from the gas, ammonia sulphate crystals are formed that are evacuated from the back side of the saturation chamber;
- the ammonia sulphate crystals separation from the acid solution by settling in the salt reservoir and by centrifuging in centrifuges with strainers;
- the ammonia sulphate drying by hot blow in a salt dryer;
- the ammonia sulphate transport and storage;
- the neutralization with concentrated ammonia water of acid tar separated from the separator.

To obtain the concentrated ammonia water, the raw ammonia water is taken over and passed through rubble filters to obtain the tar at a content of 30÷50 mg/l. After the filtration, the raw ammonia water is preheated with steam up to 80°C in pre-heaters, from which is conducted in the distillation columns. After the cooling in the dephegmator of the water – ammonia vapors at 35÷40°C mixing, concentrated ammonia water is obtained as finite product and waste water that is continuously sent to the stripping installation in order to reduce the contaminants (fixed ammonia). Due to cooling and water vapors condensation, the ammonia concentration from vapors is rising from 6 ÷ 8% to 18 ÷ 20%. The stripping installation has in endowment two columns that can take over the resulted waste ammonia waters from the process. By NaOH proportioning (sol. 8÷10%) and maintaining the pH=11, the fixed ammonia salts (NH_4SCN, NH_4Cl and $(NH_4)_2S_2O_3$) are transformed in the volatile ammonia salts: $(NH_4)_2SO_4$, $(NH_4)_2CO_3$, $(NH_4)_2S$, NH_4HCO_3, NH_4CN.

c_3) the Benzene subsection. After the ammonia catching in the settling chambers, the coke gas is passed in the Benzene subsection for benzene hydrocarbons to be collected. Because the gas leaves the settling chambers with a temperature of 50 ÷ 55°C, its cooling is necessary before entering the benzene washers. The gas cooling takes place in the final cooler where by re-circulated water sprinkling the gas is cooled down to 20 ÷ 30°C. In the final cooler, by cold water contact, from the gas is also separated the naphthalene which, together with the water is drained in the inferior part of the final cooler. For the naphthalene absorption the heavy tar is introduced, pumped from the cooling-condensation subsection. The tar in which the naphthalene was absorbed is draining through the superabundance regulator in the tar reservoirs from where is re-circulated in the cooling-condensing subsection. The cooling water, naphthalene purified are settling in the vertical settler and then are re-circulated at the water Household where are cooled in the cooling towers with forced ventilation. The coke gas cooled at ~25°C containing ~30 ÷ 34 $g_{benzene}/Nm_{gas}$, enters the washers mounted in range and provided with ceramic filling.

d) The tar processing section is formed of following installations: oils and tar storage, tar distillation, coal-tar thermal treatment, raw naphthalene obtaining, rectified naphthalene obtaining; biochemical purification. The tar is received from the chemical Section in the tar and oil storage where is heated, homogenized and dehydrated

for distillation purposes. For the tar heating at 80 ÷ 85°C there is introduced steam of 4,5÷6 atm in the reservoir's serpentines, where also is taking place its settling. By settling is separated the ammonia water that is sent in the Chemical Section. The main activities that are developed in the tar distillation installation are:

- the tar storage in reservoirs;
- the tar heating in the first heating step of the tubular oven;
- the tar heating in the evaporator – first step and its dehydration;
- the tar heating in the second step of the tubular oven;
- the tar heating in the evaporator – second step;
- vapors heating and separation in the tar distillation column;
- cooling of the obtained fractions.

The tar fractioned distillation consists in separation on the basis of inequalities between boiling temperatures of fractions: easy, phenolic, naphthalenic, absorption, anthracene I and II.

3. Experimentations

3.1. Settling the noxa testing areas

There were taken gas samples and powders from the next areas: The Coking Section, The Chemical Section and The Tar Preparation Section. During the experimentations period there were also registered the main meteorological parameters that counted for the analyses results interpretation. For choosing the points of sampling it was taken into consideration: knowing all the polluting sources and the main climate characteristics in the area. The three activity sectors specific polluting sources are determining the noxa accumulation that is emitted simultaneously. The diversity of emitted pollutants and of their concentrations, determines the liberation in the atmosphere of a mix noxa complex. The meteorological factors influence the auto-purifying processes through air temperature, humidity, precipitations, air currents and radiations. Regarding the air temperature, the density changes have neglecting influence, very important being the thermal gradient. Depending on the area where the pollutant is emitted and the temperature, there are situations where along with the temperature diminution a pollutants dilution takes place, because the ascendant currents that push them towards higher altitudes. The temperature inequalities are frequent in the periods with unstable weather (fall, the winter beginning, and the spring beginning). The air raised humidity blocks generally the noxa diffusion and so the dilution of pollutants in the air, and the suspensions constitutes condensing cores that favors the fog apparition.

The fog represents one of the meteorological conditions most averse to the air purifying, by reducing the diffusion capacity and by favoring the dissolution of the pollutants soluble in the water that can confer it toxic properties. The precipitations, favors the atmospheric pollutants deposition on the soil and plays an important purifier role. In exchange the water from precipitations can modify its natural properties due to some pollutants dissolution; a phenomenon meets also at appreciable distances from their emission place.

3.2. Sampling

For air sampling the apparatus and the reactives provided in the working methodology specific for the determination of each type of pollutant have been used. When the sampling period was established, it was pursued the obtaining of information on pollutants high concentrations on a short period of time (30 minutes). At gases determination, parallel with the sampling device was prepared an identical device, without sampling air through it that represented the blank test. To enssure the total retention of the gas that will be gathered there were used two gathering devices linked in succession. The results referred to the entire absorption liquid quantity. The gathered air volume was established based on the supposed concentration of the pollutant from the air and on the sensibility of the method. After air sampling, the devices were transported to the laboratory in appropriate conditions, so as the samples would not undergo changes during the transportation.

The experimentations took place in two stages: in spring – S_1 (15 April - 15 May) and in summer – S_2 (15 July - 15 August). For the three sections the determined pollutants by standardized methods were:

- At the Coking Section (CS): ammonia, sulfur dioxide, carbon monoxide, nitrogen dioxide, sulfured hydrogen, aromatic hydrocarbons (AH), aromatic poly-cyclic hydrocarbons (APH), sedimentary and in suspension powders.
- At the Chemical Section (ChS): ammonia, sulfur dioxide, carbon monoxide, nitrogen dioxide, AH;
- At the Tar Preparation Section (TPS): carbon monoxide, AH, APH.

In the spring season (S_1), wind medium speed was included between 1 and 8 m/s, the daily maximum temperature was included between 11 and 25 °C, and the wind blew preponderant from the SSW and ESE. In the summer season (S_2), the wind speed was included between 0 and 9 m/s, the maximum daily temperature of the air was included between 27,5 and 36,2 °C, and at the soil level, was included between 47.8 and 60,8°C. The medium daily humidity was included between 39 and 50 %, and the wind blew with maximum speed from the N and NNW direction.

***Table 1**. The results centralizing of medium analyses made during the experiments*

Sampling area	Period	Pollutant, [mg/m$^3_{air}$]								
		NH_3	SO_2	CO	NO_2	H_2S	AH	APH	Sedimentary powders	Suspended powders
CS	S_1	0,327	0,18	17,72	0,017	0,014	0,416	0,198	12,53**	1,098
	S_2	0,607	0,53	19,38	0,022	0,028	0,625	0,33 1,012*	15,16	1,167
ChS	S_1	0,924	0,221	11,59	0,0043	-	1,52	-	-	-
	S_2	1,664	0,274	14,47	0,0053	-	1,79	0,098	-	-
TPS	S_1	-	-	6,57	-	-	0,131	0,201 0,616*	-	-
	S_2	-	-	7,01	-	-	0,160	0,260 0,797*	-	-

The blank spaces indicate that those analyses were not made.
* 3,4 benzopyrene, in μg/m$^3_{air}$; ** in g/m$^2_{month}$

Because the air samplings were made in different temperature conditions, it was made the air volume correction for normal conditions with the next formula:

$V_0 = V \cdot 273 \cdot p/ (273 + t) \cdot 760$

where: V_0 – the air volume in liters, at the air standard temperature and pressure;

V - the air volume in liters, at the temperature and pressure at the sampling moment;

p – the atmospheric pressure at the sampling moment;

t – the air temperature at the sampling moment.

The results centralizing of medium analyses made during the experiments are presented in table 1.

3.3. Results interpretation

The results of analyses made on the air samples taken in the industrial experimentations, proved that in a coke-chemical plant is emitted considerable quantities of pollutants that can exceed the maximum

- acceptable concentrations (MAC).

These exceeds are on the one hand due to different meteorological conditions (wind speed and direction, the temperature, the humidity etc), and on the other hand due to the technological factors involved in the coking process (the coking batteries loading regularity reflected by the coking time and also by the chemical characteristics of the charge).

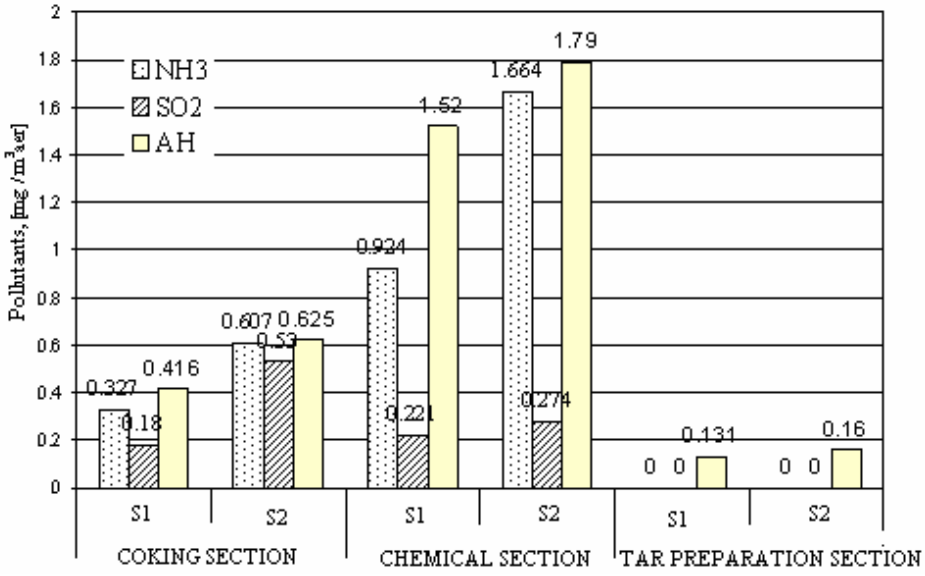

***Fig. 1.** The NH_3, SO_2 and AH noxa variation, in the spring and in the summer, respectively in the Coking Section, the Chemical Section and the Tar Preparation Section*

Generally, in all the plant's sections, were registered low concentrations of the pollutants in the spring season in comparison with the summer season:

- In the Coking Section were surpassed the MAC values for: ammonia (in both seasons), carbon monoxide (in both seasons), sulfured hydrogen (in the

summer season), and also for the suspended powders (in both seasons), figures 2 - 4;

- In the Chemical Section, the performed analyses indicated values that exceeded the MAC values, except for the concentrations of SO_2 and NO_2, figures 1 - 4;
- In the TPS, were registered medium values of CO concentrations, close to the maximum admissible concentrations, for the two seasons' samplings, figure 3.

Because the coke-chemical industry is classically associated with the exposure to aromatic poly-cyclic hydrocarbons (APH), starting from the coal coking and ending with tars and coal tars processing, the performed actions demonstrated their presence in the three sections.

There have been observed that the concentration level for APH from the Coking Section is higher than in the other sections due to high temperatures registered in the batteries zone, figure 2.

The settling and in suspension powders have visibly passed the maximum acceptable values in both sampling periods, figure 4.

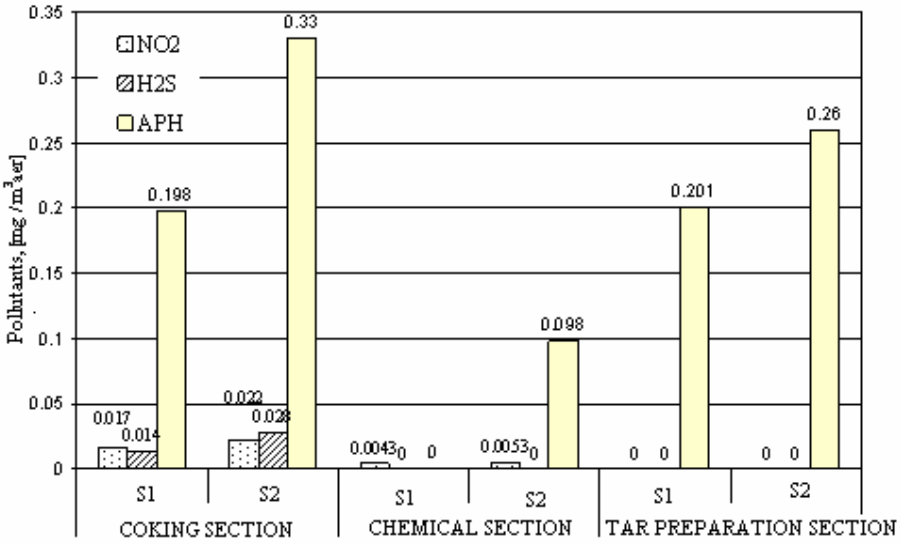

Fig. 2. *The NO_2, H_2S and APH noxa variation, in spring and in summer respectively in Coking Section, Chemical Section and Tar Preparation Section*

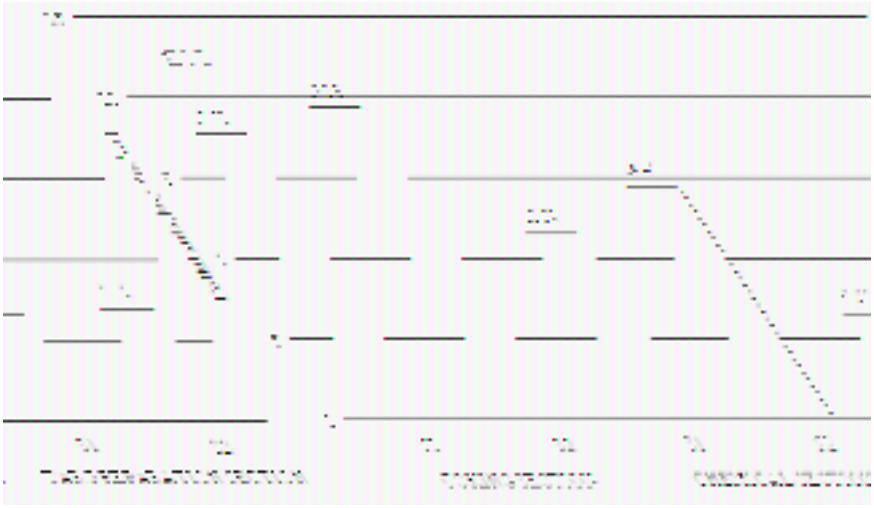

Fig. 3. *The CO variation, in spring and in summer, respectively in Coking Section, Chemical Section and Tar Preparation Section*

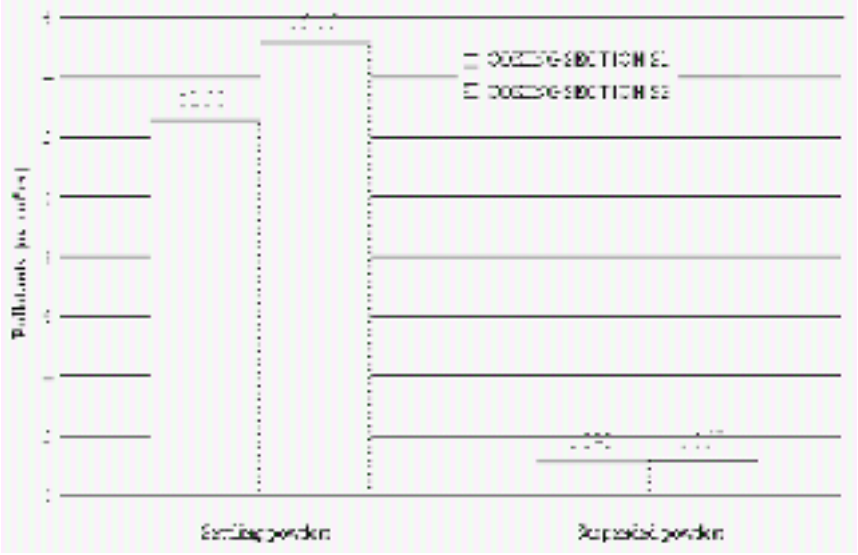

Fig. 4. *Quantity variation of settling powders, in the spring and in the summer in the Coking Section*

4. Conclusions

There have been established for each section, the specific pollutants taking into consideration the concentrations level and the representative noxa type.

According to the season, some particular pollutants were present in the air in different concentrations, contributing to this mostly the meteorological conditions but also the technological parameters of installations functioning.

Between the analyzed pollutants, the NH_3 determined in the Chemical Section atmosphere has averagely surpassed the maximum admitted value (0,3 mg/m), of about 5 times, CO has been the pollutant whose concentration has surpassed the maximum admitted limit (6mg/m) of about 3,5 times. The suspended powders determined in the no. 3 coking-battery area have surpassed the MAC (0,5 mg/m^3) about 2 times. Beside these, there have been pollutants of wose the concentrations have been with in the maximum limits (NO_2, SO_2, H_2S, settling powders), but through their cumulative effect the professional illness risk is increased.

References

[1]. *** **-** *Enciclopedia Ulman*, nr.6.
[2]. Edgar, W.D., Muller, J.M. - *The status of coke oven pollution control*, 1990.
[3]. *** - *Proceduri de fabricaţie ale proceselor din sectoarle cocso-chimice UZINSIDER ENGINEERING*, 1999.
[4]. Negulescu, M., Ianculescu, S. - *Protecţia mediului înconjurător*, Ed. Tehnică, Bucureşti, 1995.
[5]. Voicu, V. - *Agenda pentru combaterea noxelor în industrie,* Ed. Tehnică, Bucureşti, 1994.
[6]. Chiriac, N., Păscălin, G. - *Direcţii prioritare privind protecţia mediului în siderurgia românească,* Conferinţa Ştiinţifică Naţională Aniversară, Bucureşti, 2000.
[7]. Hriţac M., Bălănescu M. - *Siderurgia şi efectul de seră,* Conferinţa Ştiinţifică Naţională Aniversară, Bucureşti, 2000.
[8]. Antoine, J., Graillat, A., Pazdej, R. - *Exemple de reabilitation d'une fiche cokerie,* Seminaire, Hongrie, 1996.

THE ANNALS OF "DUNAREA DE JOS" UNIVERSITY OF GALATI.
FASCICLE IX. METALLURGY AND MATERIALS SCIENCE
N^0. 2 – 2009, ISSN 1453 – 083X

STUDY OF THE RV52 STEEL PLATES PROPERTIES AFTER THERMIC TREATMENT

Maria VLAD, Stela CONSTANTINESCU
Universitatea "Dunarea de Jos Galati"
email: mvlad@ugal.ro

ABSTRACT

The thermal treatment of RV52 steel plates determines high mechanical properties such as: strength, wear resistance and tenacity. The normalized plate samples were studied to determine the effect of the tension release heat treatment on the properties of steel plates used for metallic welded construction. From the relations expressing the link between the strength and tenacity relation on one hand and the structural characteristics, on the other it is obvious that the only factor which leads both to increasing strength properties and decreasing transition temperature is the finishing of the ferrite grains.

KEYWORD: ingot, properties, steel, treatment, structure

1. Introduction

During the processing and operation in the basic steel mass a number of phenomena can occur such as: lamellar spreading, fissures in the welded areas and easy breaking. Occurrence of these phenomena depends on the steel chemical composition and the semi blanks elaboration and processing conditions.

The normalised plates of RV52 steel feature a ferite-perlite structure, the obvious tendency being that of reaching an as low as possible content of perlite with the corresponding decrease in the carbon content. The heat normalising treatment of the thick plates took place in the roller continuing furnaces from the rolling mill of ARCELOR-MITTAL Galati observing the following parameters: heating up to temperatures A_{C3} + 20 ^{o} C ÷ 40^o C, air cooling [1]. The analysis of the relationship between strength and tenacity, on the one hand, and structure characteristics, on the other hand, shows that the heat tension-relieving treatment and especially, the normalising treatment considerably increase the tension strength and decrease the transition temperature due to the ferrite grain shrinking process.

Manufacturing plates of high chemical (table 1) and structure homogeneity leads to an isotropy corresponding to these properties, which attracted the researchers' interest [2].

2. Experimental researches and results

In order to carry out the researches on the correlation of microstructure with the properties of steel RV52, normalized and tension relieved, the following working variants have been established:
- steel making in a 50t electrical furnace by 15 t ingot casting of thick rolled plates, normalising treatment, and sampling for heat treatment tension relieving in laboratory;
- steel making in a 150t converter, by 25t ingot casting and continuing casting in slab, of thick rolled plates, normalising treatment, and sampling for heat treatment for tension relieving.

Table 1. *Chemical composition*

C	Mn	Si	P	S	V	Al	Ni	N
[%]								[ppm]
0.14	1.40	0.26	0.01	0.01	0.05	0.02	0.28	120

Sampling the steel RV52 plates before and after normalising has been carried out according to the following scheme:

- the samples of the plates made by ingot rolling have been taken from the edges and the axis corresponding to the head, middle and leg parts;

- the samples of the plates made by cast slabs rolling have been taken from the edge and axis. The samples have been taken from the central axis of the plate corresponding to: a) head, b) middle part; and c) leg.

The samples of normalized plate have been prepared in longitudinal section and non- metallic inclusion score are given in Table 2.

Table 2. *Non- metallic inclusions score*

Score	*Types of non- metallic inclusions*				*Total score over the same field*
	Sulphides S)	Oxides OL+OP	Silicates SF+SP(SN)	Nitrides NT+NA	
	Non- metallic inclusions score				
1	2	3	4	5	6
a	1.0 0.5 1.0	1.5 1.5 1.0	1.0 1.0 1.5	0.5 0.5 0.5	4.0 3.5 4.0
Max. score of inclusions	1.0	1.5	1.5	0.5	
b	0.5 0.5 1.0	1.5 1.5 0.5	1.5 1.5 1.5	0.5 0 0	4.0 3.5 3.0
Max. score	1.0	1.5	1.5	0.5	
c	1.0 1.0 1.0	0.5 1.5 1.0	1.0 1.0 1.5	0.5 0 0	3.0 3.5 3.5
Max. score	1.0	1.5	1.5	0.5	

The impure zones, irrespective of the sample position, are those corresponding to the head and middle side of the ingot. In the axis purity is lower as compared with the sample edge. When elaborated in the electrical furnace, a higher purity is reached than in a converter. The metallographic structure of the heat treated plates is given in Figure 1 which highlights a fine-granulation ferrite-perlite structure.

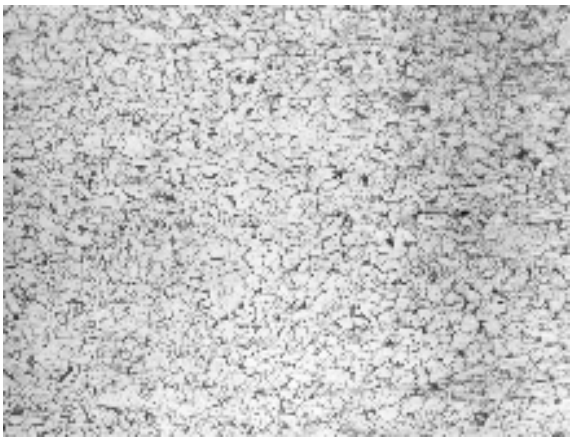

Fig. 1. *Microstructure of normalized RV52 steel plates Magnified x 100*

Variations and distributions of the mechanical properties: tensile strength (R_m), yield strength ($Rp_{0,2}$), elongation (A_5%), resilience on-v-grooved longitudinal samples, tested to - 20 ^{o}C and –50^{o}C, from head, middle and leg sides are graphically illustrated in Figures 2, 3, 4.

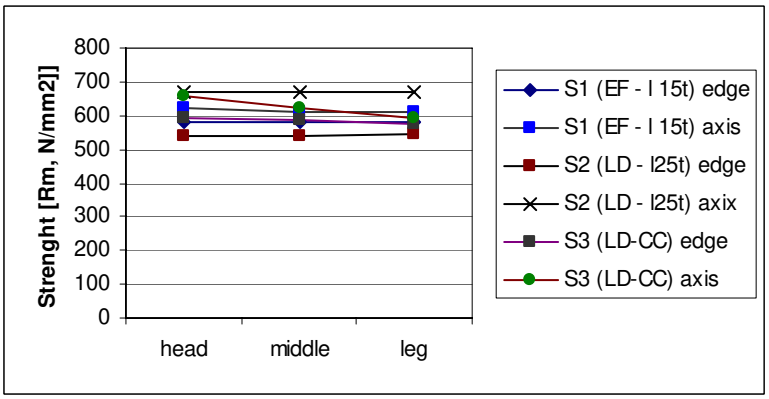

Fig. 2. *Tensil strength (Rm) values distribution of samples in various zone of the sheet*

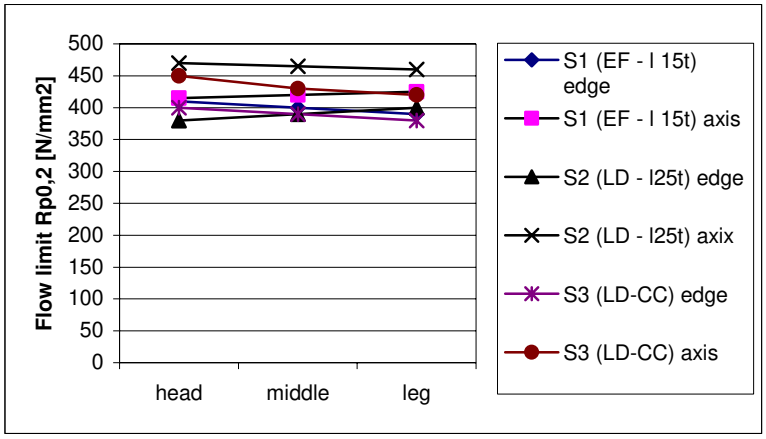

Sample position in comparison with the ingot

Fig. 3. *Yield strength (Rp $_{0.2}$) values distribution of samples in various zone of the sheet*

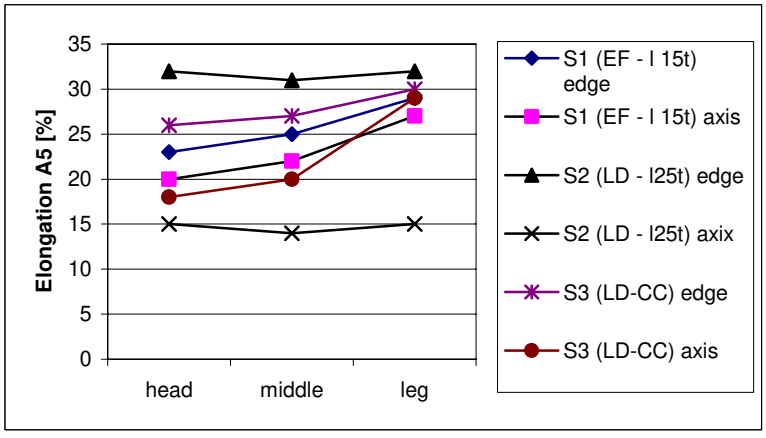

Sample position in comparison with the ingot

Fig. 4. *Elongation A_5 values distribution of samples in various zone of the sheet*

The resilience of the cold - deformed and heat-treated samples under the above mentioned conditions has been determined at temperatures of - 20^{o}C.

In order to establish the influence of the heating temperature subsequent to cold deformation of the samples subject to 4%,8% and 12% degree of deformation, these have been treated acc to the treatment cycle described below:

- heating: 250^{0}C; 500^{0}C; 650^{0}C;

- exposure: 160 min. as a result of 2 min/ mm exposure;
- air cooling.

From the analysis of the tension relieving treatment graphics, it has been found that:

- as a result of the tension relieving heat treatment at 250 ^{o}C, the break energy at shock KV at -20^{o}C and –50^{o}C decreases with respect to the values of the samples from plates of 4%,8% and 12% degree of deformations, and the values of the normalized samples, Figures 5, 6.

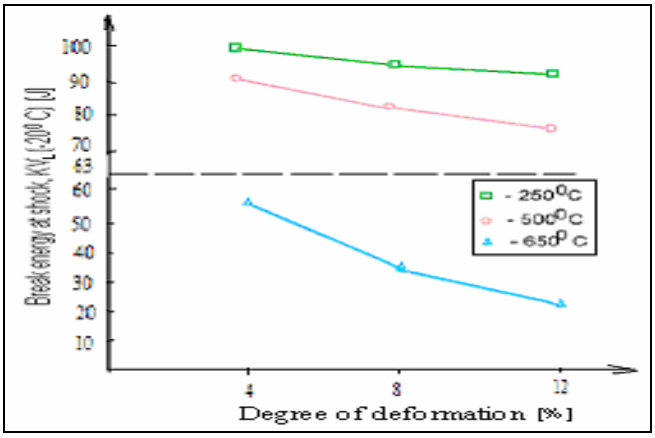

Fig. 5. *The degrees of deformation and heating influence for values of break energy at shock, KV_L (-20^{o}C)*

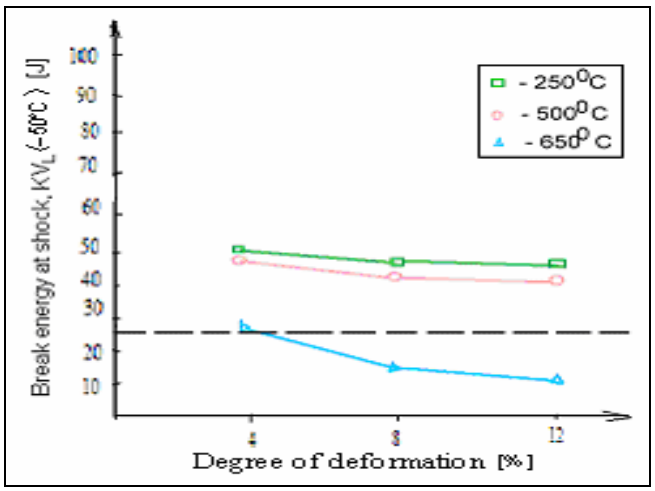

Fig.6. *The degrees of deformation and heating influence for values of break energy at shock, KV_L (-50^{o}C)*

Determining the shock behaviour is more obvious when the degree of deformation is higher.

With degrees of deformation of 12%, the shock ultimate strength at -20 ^{o}C and –50^{o}C takes lower values than that min admissible.

Heating at 650^{o}C results in recovery of the tenacity properties of RV52 steel, without having reached the level of normalization.

Heating at 250^{o}C has disastrous consequences, because tenacity is completely damaged both with respect to normalization and deformation states.

By heating at 500^{o}C, the values of the shock ultimate strength increase as compared with those obtained by cold deformation, while keeping however the influence of the cold deformation, i. e. lower values for higher degrees of deformation.

3. Conclusions

The researches were focused on determining the factors that cause properties variation in different zones of the RV52 steel plates manufactured by Arcelor- Mittal Galati.

In order to obtain highly improved properties a good correlation should be achieved between the conditions of elaboration, deformation and heat treatments highlighted by the chemical composition and structure.

The cold plastic deformation of low degrees of deformation: 4, 8, 12% results in poorer tenacity properties as compared with the normalised state values, which is more sensitive with higher degrees of deformation.

The best values of shock ultimate strength both at -20^{o}C and –50^{o}C have been obtained after a tension relieving treatment at 650 ^{o}C for 8 % degree of deformation.

References

[1]. Constantinescu S. - *Metals properties and physical control methods,* Didactica and Pedagogica, Publishing House, Bucharest Romania, 2004, p.128.

[2]. Sugiyama T. - *Kobe Seel,* Engineering Reports, 1995, Vol.25, nr.4, p.4.

THE ANNALS OF "DUNAREA DE JOS" UNIVERSITY OF GALATI.
FASCICLE IX. METALLURGY AND MATERIALS SCIENCE
N^0. 2 – 2009, ISSN 1453 – 083X

TRANSPARENT AND CONDUCTING TIN OXIDE THIN FILMS DEPOSITED BY SPRAY PYROLYSIS

Elvira FORTUNATO[1], Elamurugu ELANGOVAN[1], Anca-Ionela DANCIU[2], Alexandru TECARU[2], Viorica MUSAT[2]
[1]Faculty of Science and Technology, CENIMAT, New University of Lisbon
[2]Dunarea de Jos University of Galati
email: elvira.fortunato@fct.unl.pt

ABSTRACT

The chemical spray pyrolysis technique has been one of the major techniques to deposit a wide variety of materials in thin film form, for different applications. The most important control parameters for obtaining good quality thin film are the nature and temperature of the substrate, the composition of the precursor solution, the gas and solution flow rates and the deposition time.

The paper presents the morphology, the electrical and optical properties of tin oxide (SnO_2) thin films deposited by spray pyrolysis technique onto glass substrates at 400^{0}C using $SnCl_2$ as precursor and methanol as solvent. The change in the grain shapes and orientation is presented based on SEM data. The minimum sheet resistance of 21.4 Ω/sqr *was obtained, being the lowest value reported in the literature for these materials. Optical transmittance in the range of 58-85 % has been obtained for the prepared films.*

Keywords: spray pyrolysis, tin oxide thin films, transparent conductive oxide

1. Introduction

Thin films of tin oxide (SnO_2) that belong to the category of transparent and conducting oxides have been successfully used in various applications such as optical windows in solar cells [1], flat panel displays (FPD), low-emissivity (low-e) windows, electromagnetic shielding of CRTs in video display terminals, as electro-chromic (EC) materials in rear-view mirrors of automobiles, EC-windows for privacy (smart windows), oven windows, touch-sensitive control panels [2], light emitting diodes (LEDs) [3], and electrochromic displays (ECDs) [4], due to their outstanding properties. The versatility of SnO_2 thin films in the before mentioned various applications motivated us to deposit these films by the economical spray pyrolysis deposition technique.

2. Experimental details

2.1. Thin films preparation

An economic stannous chloride ($SnCl_2$) was used as precursor of tin oxide films. The amount of tin precursor was varied for achieving films with different thickness. Microscopic glass slides were used as substrates. The substrates were cleaned using distilled water and organic solvents such as acetone and isopropyl alcohol. Cleanliness of the substrate plays a vital role in deciding the quality of the deposited film. In the present work, the following substrate cleaning procedure was adopted. The microscopic glass slide substrates were cleaned initially with soap (to remove greasy material) and then with distilled water. The substrates were then kept in acetone and finally washed with isopropyl alcohol to remove any traces of dust particles or other contaminants.

The substrate was placed in contact with a hot plate and its temperature (T_s) was monitored by a temperature controller using a standard thermocouple system. The substrates were pre-heated to the required temperature. After deposition, the coated substrates were kept in the spray chamber itself and allowed to cool down naturally at room temperature.

The tin precursor ($SnCl_2$) was dissolved in hydrochloric acid and methanol to form the starting solution. The repeated experiments of each deposition showed that the films could be reproduced easily. An extensive care was taken in giving sufficient spray interval between successive sprays for the substrates to get back to deposition temperature after undergoing thermal decomposition. The substrate temperature (T_s) was between 350-400^{0}C. For each concentration

of the precursor solution, several sets of films were prepared and found to be reproducible.

2.2 Thin films characterization

The thickness of the films was measured using a surface profilometer (Dektak^3), with an accuracy of 20nm. Optical transmittance was measured using a double-beam spectrophotometer (Shimadzu UV-3100) with a bare substrate in the reference path of the beam. The surface morphology was analyzed using Scanning Electron Microscopy (Hitachi, SU-70).

The electrical parameters were estimated using a Hall measurements setup (Bio Rad HC5500 Hall system) with a permanent magnet of 5 KG in van der Pauw configuration).

3. Results and Discussion

3.1 Thin films thickness and morphology

The initial estimation of film thickness was obtained through the conventional weight-gain (gravimetric) method. This method is earlier applied to calculate the thickness of the films deposited by spray pyrolysis technique [5-8]. The standard density value of tin oxide (6.99 g/cm^3) was used for the calculations [9]. This preliminary estimation of thickness was found in good agreement with the values obtained by thickness profilometer.

It is known that the step required by the thickness profilometer measurement cannot be made on the spray deposited samples during film deposition, due to diffusion effect below the mask. Hence, the step was formed after deposition by selective etching on different place of sample surface. The solution used for the etching is ETCH-Cr (A). With the step formed by this etching procedure, the film thickness was estimated at 4 corners of the sample with dimension of 50 mm × 50 mm.

The estimated values suggested that the film is uniform through the entire substrate area.

Average value is taken for the calculations such as resistivity and absorption coefficient. The films thickness ranges from about 144 nm to about 850 nm, depending on the concentration of the $SnCl_2$ precursor solution. It increased with the increasing amount of precursor to reach a maximum of ~ 850 nm. The Fig. 1 shows the SEM images on the films surface.

This data indicates that the grain growth follows the increase in the concentration of the precursor solution.

The grains seem to be agglomerated together to appear as big as ~350 nm in size (Fig 1a). Apart from this agglomeration, grains with size as small as ~70 nm are observed.

The agglomerated grains transform in bigger grain size with the increasing film thickness, following the increase in amount of precursor, as seen in Fig. 1b.

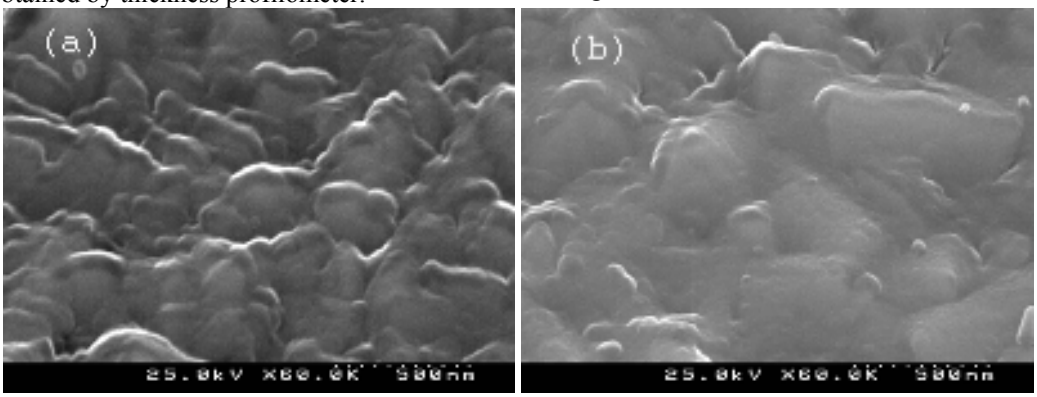

Fig.1. *SEM morphology on the surface of the films deposited on glass substrate using precursor solution of 0.3 mol/l (a) and 0.75 mol/l (b).*

3.2 Electrical properties

The electrical measurements were carried out using Hall measurement in van der Pauw configuration.

The negative sign of Hall coefficient confirmed that the films are n-type conducting.

A maximum sheet resistance (R_{sh}) of ~ 486 Ω/sqr was obtained for the films with a thickness of 144 nm. The R_{sh} is found to decrease with the increase in the thickness of the film until ~23 Ω/ sqr for the films of 850 nm thick.

The electrical parameters obtained from the Hall measurements are presented in Table 1. It can be noticed that the resistivity (ρ) decreases when the film thickness increases. Minimum value of ~1.4 × 10^{-3} Ωcm was obtained for the film of about 720 nm thick. On the other hand, the carrier mobility (μ) is found to increase with the increasing of the film thickness. The minimum value of ~2.2 cm^2 V^{-1} s^{-1} increased at 18.5 V^{-1}s^{-1} when the film thickness decreases from 850 nm to 144 nm. The variation trend of ρ and μ is also comparative, as shown in Table 1.

Table 1. *Electrical properties of the films, obtained from the Hall measurements*

Film thickness	Sheet resistance	Resistivity	Mobility	Carrier concentration
[nm]	[Ω/sqr]	[Ω cm]	[$cm^2 V^{-1} s^{-1}$]	[cm^3]
144	486	7.0×10^{-3}	2.2	4.0×10^{20}
565	46	2.6×10^{-3}	14.9	1.6×10^{20}
850	21	1.4×10^{-3}	18.5	2.5×10^{20}

In Table 2 are presented the sheet resistance and resistivity values reported in literature up-to-now, comparing with our best result.

One can notice that the resistivity of film reported in this paper is lower than the one mentioned in the literature.

Table 2. *Comparison of sheet resistance of SnO_2 films in previous reports and this paper*

Substrate temperature	Film thickness	Sheet resistance	Resistivity	Reference
[°C]	[nm]	[Ω/sqr]	[$\times 10^{-3}$ Ω cm]	
400	638	23	1.4	This work
400	480 ± 50	66 ± 19	3.2 ± 1.2	[10]
400	720	51	1.5	[11]
400	441	1320	58.2	[12]
350	300	12.4	20.3	[13]
400	850	21.4	1.4	[This paper]

3.3 Optical properties

Fig. 2 shows the transmittance spectra obtained at the wavelength between 300-2500 nm. The optical transmission depends on the film thickness. The increase of the film thickness leads to higher absorption and thus reducing the transmittance. The average visible transmittance (*AVT*) calculated in the wavelength ranging 400-700 nm varied between ~58 and 85 %.

A maximum *AVT* of 85 % obtained for 144 nm thick films is decreased to a minimum of ~58 % when the thickness of the film increased to 850 nm.

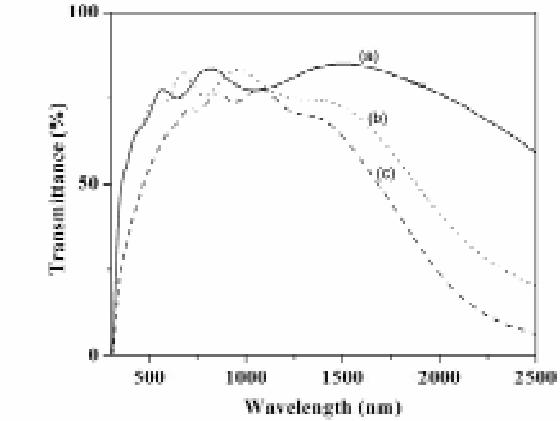

Fig. 2. *Variation in the optical transmittance of SnO_2 films as a function of the film thickness: 144 nm (a), 565 nm (b) and 850 nm (c).*

The fundamental absorption refers to band-to-band transitions, i.e. to the excitation of an electron from the valence band to the conduction band. The fundamental absorption, which manifests itself by a rapid rise in absorption, can be used to determine the band gap of materials.

The absorption coefficient (α) can be calculated from the transmittance values at the absorption edge in the transmittance spectra. The variation of absorption coefficient against photon energy (hν) for direct band-to-band transition has the form of $\alpha = A (h\nu E_g)^x$.

Where hν is the photon energy, E_g the band gap and A the edge parameter. The SnO_2 films are proven to possess direct allowed transition and thus the value of x is ½. Hence plots have been made by taking hν along x-axis and $(\alpha h\nu)^2$ along y-axis.

The values of direct band gap were estimated from the extrapolation of the linear portion of the curve to zero absorption and found to be in the range 3.88 - 3.90 eV for SnO_2 films with different thickness. Theoretically, a gap of at least 3.5 eV is needed for a TCO in most anticipated applications [10] and the obtained values confirm that the produced films meet this requirement.

4. Conclusions

Thin films of tin oxide (SnO_2) was successfully prepared by spray pyrolysis technique. The experimental results showed that the growth rate and subsequently the films thickness can by controlled by solution concentration, substrate temperature and the deposition time. SEM images showed that the

agglomerated grains transform in bigger grain size with the increasing film thickness.

The minimum value of ~ 2.2 cm^2 $V^{-1}s^{-1}$ increased at 18.5 $V^{-1}s^{-1}$ when the film thickness decreases from 850 nm to 144 nm.

The variation trend of ρ and μ is also comparative.

A maximum *AVT* of 85 % for 144 nm thick films decreases to a minimum value of ~58 % when the thickness of the film increases to 850 nm.

References

[1]. J. Xu - *Solid State Communications* 149 (2009) 527.
[2]. J. Wang, B. Xu, Z. Shen, X. Ni, J. Lu - *Applied Surface Science* 254 (2008) 7178.
[3]. J. Ouerfelli - *Materials Chemistry and Physics* 112 (2008) 198.
[4]. K. K. Purushothaman - *Surface Review and Letters* 14 (2007) 1149.
[5]. A.E. Rakhshani - *J. Appl. Phys*. 81 (1997) 7988.
[6]. A.E. Rakhshani, Y. Makdisi, H. A. Ramazaniyan - *J. Appl. Phys.* 83 (1997) 1049.
[7]. D.R. Lide (Ed.) - *Handbook of Chemistry and Physics*, CRC Press, London (1993) pp. 4–136.
[8]. T.J. Coutts, D.L. Young, X. Li - *MRS Bull.* 25 (2000) 58.
[9]. R.R Kasar., N.G. Deshpande, Y.G. Gudage, J.C. Vyas - Ramphal Sharma - *Physica B: Physics of Condensed Matter*, 403 (2008) 3724.
[10]. C.D. Canestraro - *Applied Surface Science* 255 (2008) 1874.
[11]. D. Perednis, L.J. Gauckler - *Journal of Electroceramics* 14 (2005) 103.
[12]. S Chacko, Ninan Sajeeth Philip, and V. K. Vaidyan - Phys. stat. sol. (a) 204, No. 10, 3305– 3315 (2007)
[13]. K. S. Shamala and L. C. S. Murthy - *Surface Review and Letters*, Vol. 13, No. 4 (2006) 357–364

THE ANNALS OF "DUNAREA DE JOS" UNIVERSITY OF GALATI.
FASCICLE IX. METALLURGY AND MATERIALS SCIENCE
N^0. 2 – 2009, ISSN 1453 – 083X

EFFECTS OF PLASTIC DEFORMATION AND TEMPERATURE ON MICROSTRUCTURAL AND MECHANICAL PROPERTIES OF A CuAlNi SHAPE MEMORY ALLOY

Carmela GURAU, Gheorghe GURAU
"Dunărea de Jos" University of Galaţi
carmela.gurau@ugal.ro

ABSTARCT

In Cu 12.88% wt.Al4 %wt. Ni shape memory alloy the influence of plastic deformation and thermal treatments on the microstructures and hardness were studied by optical microscopy, scanning electron microscopy (SEM), Vickers Hardness. The plastic deformation on the austenite (b) was studied at temperatures T>Md when transformation can occur with no stress or strain induced condition. Lattice defects were introduced into stable austenite of a Cu Al Ni alloy by a hot rolling, in one pass, and subsequent quenching after leaving the rolling cylinders. From microstructural observations it has been seen that two b_1' (18R) and g_1' (2H) martensite phases coexists at different fractions in the undeformed and deformed states. Plastic deformation causes change in the relative amounts of b_1' and g_1' martensites with a new morphology. The finest martensite structure has been obtained by thermo-mechanical treatment. The hardness test highlights the influence of treatments tightly correlated with the structures obtained.

KEYWORDS: shape memory alloy (SMA), martensite transformation, Cu Al Ni alloy, thermo mechanical treatment

1. Introduction

The reason for studying the thermo-mechanical treatments of Cu Al Ni shape memory alloys comes from engineering demanding for low cost, higher working temperatures than brass and *nitinol* in the same time good classical properties (i.e. hardness) and shape memory.

Thermo-mechanical treatments represent a set of operations of plastic deformation, heating and cooling – made in a certain sequence – and as a result of the final structure of the metallic material, they take place in a high density of lattice defects, associated with plastic deformation.

In the case of SMA thermo-mechanical treatment involves plastic deformation of austenite (β) at a temperature above the temperature where stress induced martensite can not appear.

Through this plastic deformation at heating is introduced certain defects which will cause the change of the martensitic transformation parameters and the martensitic structure [1-2].

Also the researches are following the increases of the mechanical properties of the alloys.

The establishment of the thermo-mechanical treatment temperatures depends on the initial phase (β): ordered, unordered, which undergoes massive transformation or which precipitates in a solid phase. Copper based alloys have an unordered structure.

Beside the importance of the M_s and M_f points at cooling and A_s and A_f points at heating, of high importance is also the M_d point placement. This point is situated above the martensitic transformation interval up to where can be obtained no stress or stress induced martensite [1]. Above this temperature the martensitic state can not be induced. It is obvious that an important role in the reversible martensitic transformation development is played by the quantity of lattice defects mainly the density of the preexistent dislocations in the austenite phase (β) and which have to interact with the moving interfaces during the martensitic transformation. A large quantity of defects introduced in the high temperature phase can favor germination of the grains or it can make sliding more difficult. Thus the A→M or M→A transformation occurs easily and through this the memories properties are improved. Also the hardness and plasticity properties will be affected.

2. Experimental research

The research program has used extruded wires 4 mm in diameter Cu Al Ni shape memory alloy prepared by classical methods at *Dunarea de Jos University of Galati.* The extruded samples of 4 mm diameter have been heated in a vertical furnace type Nabertherm for 30 min. at 850^{0}C. The samples have been introduced into the furnace at the solubilization temperature. After heating they have been rapidly immersed into ice water. Part of the extruded samples has been hot rolled on a double reversible rolling mill.

Those samples have been hot rolled in three successive passes up to 2.6 mm thickness. Some of them have been annealed to 850 C^0 and quenched in ice water. The specimens of 2.6mm thickness had been thermo-mechanically treated at high temperature respective by 1000 C^0, 950 C^0 and 850 C^0 with 20% deformation degree and cooled in ice water ride after being taken out from the rolling mill. The specimen plastically deformed at 950 C^0 have been deformed with 10%, 20% and 30% deformation degree and cooled in the same conditions.

The plastic deformations were done on a duo reversible rolling mill, home made, in one pass. The heating furnace was placed in front of the rolling mill.

The sample route has been protected by the ceramic tube. The loss of heat through radiation is limited, aspect that posed more problems as the rolled sample thickness decreased. The rolling cylinders were preheated with methane gas burner.

The high thermo-mechanical treatment domain limits for the Cu Al Ni alloy were fixed according to the melting temperature and the minimum temperature was chosen to have no cracks in the sample.

$850^0C \leq T < T_{melting}$

After rolling, the subsequent quenching is essential. It can be considered that the alloy leaves the rolling mill at about the same temperature at which it entered do to adiabatic heating.[1]

The samples were analyzed by optical and electronic microscopy and hardness test. Prior to investigate the specimen was metallographically prepared.

2.1. Analysis of the crystalline structure by optical microscopy

The microstructural study has been carried out with an optical microscope Olympus type equipped with a digital camera and connected to a computer at *Dunarea de Jos University of Galati*. The sample surfaces have been metallographically prepared and attacked by Klemm's III.

2.2. Analysis of the crystalline structure by scanning electron microscopy (SEM)

The microstructural study has been carried out with an optical microscope Philips type at *Dunarea de Jos University of Galati*. Also the sample surfaces have been metallographically prepared and attacked by $FeCl_3$ in water solution.

2.3. Hardness test

The hardness tests have been performed with a hardness meter Vickers at *Dunarea de Jos* University of Galati. The sample surfaces have been metalographically prepared.

3. Results and discussions

The Cu Al Ni SMA alloy that undergoes this type of thermo-mechanical treatment has a critical point for transformation, M_f above the room temperature. The introduction of a volume of defects in the initial phase has been done by hot rolling. The applied thermo-mechanical treatment consists in heating in the stable domain of the initial phase then plastic deformation at high temperature followed by quenching.

The procedure allows the variation of temperature also the application of range of deformation degrees. There are 3 intervals:

a) *High temperature interval up to the temperature where the stress induced martensite can appear ($T > M_d$).*

In this temperature interval, the austenite is thermodynamically stable. Above the critical temperature A_f, inside the alloy the stable solid solution is type B_2 unordered. In the austenitic transformation domain takes place the arrangement of this solid solution into a type DO3 long ordered solution. Under the critical temperature A_s inside the ordered solid solution, the martensite b_1' incipient crystal germs appear. Also it can appear metastable compounds.

b) *The interval between the temperature up to which stress induced martensite appears and the finish martensitic temperature ($M_d \leq T \geq M_f$).*

In this temperature interval the thermodynamic stable austenite has been converted to martensite. Through application of the plastic deformation on the austenitic phase alloy, the initial transformation into stress induced martensite has been slowed. Also we will have transformations and reorientations in the partially transformed martensite:

$\beta + M^{+/-} \rightarrow (\beta \rightarrow M^{+}) + (M^{+/-} \rightarrow M) \rightarrow M$ [1]

c) *Low temperature interval under the finish martensite critical point ($T > Mf$).*

In this temperature interval the martensite is thermodynamically stable. This interval corresponds to the last part of the thermo-mechanical treatment, rapid quenching occurs. There are only reorientations of the martensite: $M^{+/-} \rightarrow M^{+} \rightarrow M$ [4].

In order the study has been focused in the first temperature domain because most of reports refers only to the third domain.

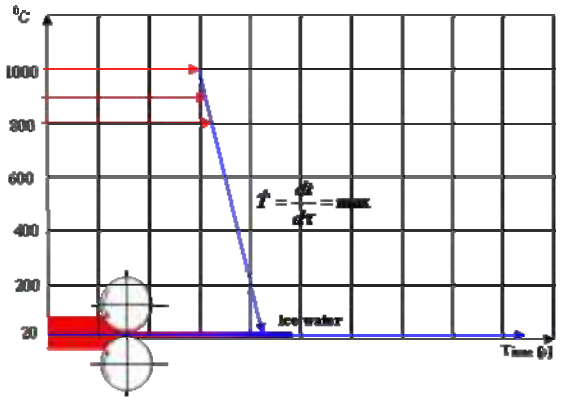

Fig. 1. *The thermo-mechanical treatment scheme*

Thus the increase in the deformation degree and the decrease deformation temperature favors the random distribution of the dislocation in the material volume.

We assume that all the induced dislocation in the initial phase will be found in the martensite which will be strengthen. During the reversible transformation $b \leftrightarrow M$ the Burgers vectors must undergo the $b(b) \leftrightarrow b(M)$ transformation. In both phases the dislocations must be connected to the limits of antiphase domains. That is necessary for a reversible and thermoelastic process, mandatory for the shape memory alloys [1].

The austenite dislocations favor martensite at cooling moving the Ms point towards higher values.

$$Ms = Ms_0 + M_{sr}$$

3.1. Optical microscopy

The specimens rolled at 1000^{0}C, 950^{0}C, 850 ^{0}C were subjected to metallographic study, in order to investigate the influence of thermal treatment on the grain size responsible for mechanical properties and memory properties of the alloy.

From all microstructural observations, it is seen that b_1'*(18R)* and g_1' *(2H)* martensite phases coexist at different fractions also in deformed states. In the figure 2a, these is preponderantly a typical martensite morphology b_1'*(monoclinic),* zig-zag structures [3]. The originate grains have a polygonal shape, linear smooth faces and coarse needles. In the figure 2b and 2c predominantly are variants of the g_1' *(orthorhombic)* martensite, along with smaller amounts of b_1' martensite.

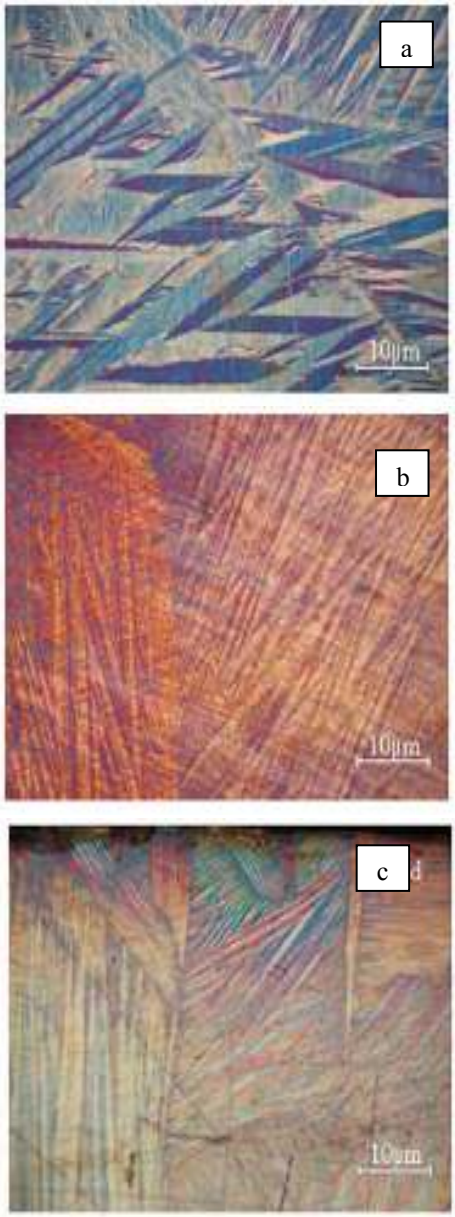

Fig.2. *Microstructures of hot rolled alloy at 20% deformation degree*
a- 1000^{0}C,b- 950^{0}C, c- 850^{0}C

These results show that the decrease of temperature induces changes in the relative amounts of the b_1' *and* g_1' martensites. There are structures with more fine needles. The g_1' *(2H)* martensites have been germinated on b_1'. Plastically deformed specimens at 850^{0}C have curved martensite perpendicular to rolling direction. The grains boundaries become rugged. In each analyzed sample the grains have generally large sizes. The average

grain sizes do not present large differences among the samples thermo-mechanically treated at the same strain but in three different plastic deformation temperatures.

The influence of strain is seen in figure 3. It can be observed that structures are obviously inhomogeneous.

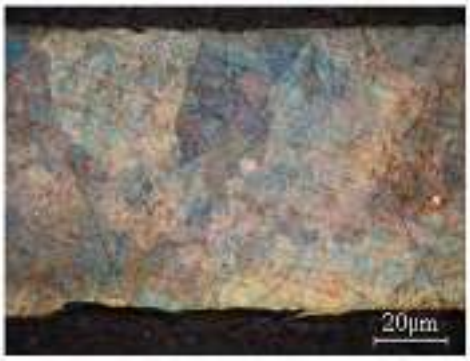

Fig3. *Microstructures of hot rolled alloy at 30% deformation degree and* 950^{0}C

There are large grains beside small grains elongated in the rolling direction. The average of grain size presents significant difference at different deformation degree. The high refinement can be observed at 30% deformed.

3.2 Scanning electron microscopy

In figure 4are presented SEM observations for the samples rolled at different temperatures but at the same deformation degree.

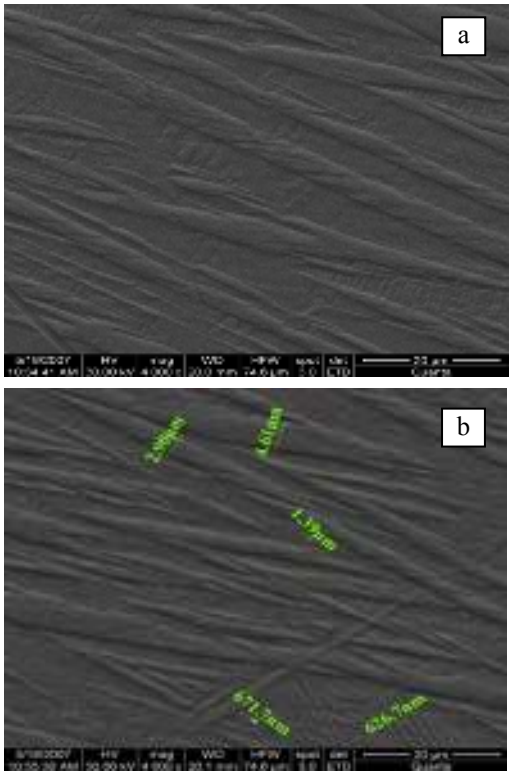

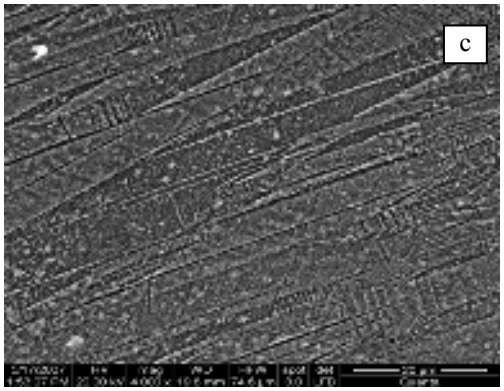

Fig.4. *SEM microstructures of hot rolled alloy, at 20% deformation degree and*
a- 1000^{0}C,b- 950^{0}C, c-850^{0}C

The pictures highlight two typical martensites morphologies that coexist in the relative amounts alloy for different plastic deformation temperatures. In conditions of decreasing temperatures it can be observed a refinement of needles. In figure 4b the needles for the specimen deformed at 950^{0}C have sizes ranging from 4.61 μm to 626.7nm. It can be also observed that those specimens contain mechanical twins especially the sample from picture 4c thermo-mechanically treated at 850^{0}C and 20% deformation degree [4].

3.3. Hardness test

Figure 5 gives the hardness test results for the sample Cu Al Ni thermo mechanically processed at different temperatures (1000^{0}C, 950^{0}C, 850^{0}C), 20% deformation degree.

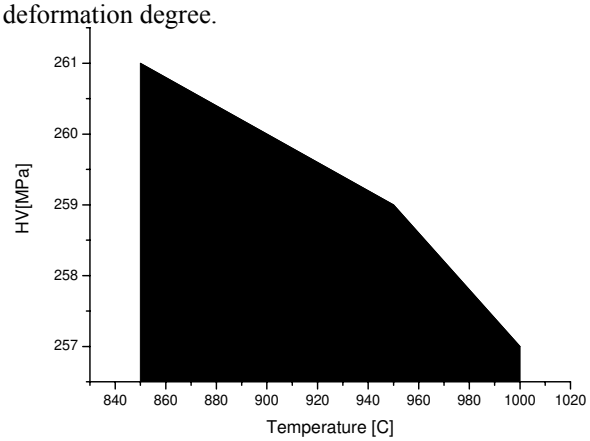

Fig.5. *Hardness versus deformation temperature*

Figure 6 gives the hardness test results for the sample Cu Al Ni thermo mechanically processed at

950^0C, in range of 10%, 20%, 30% deformation degree.

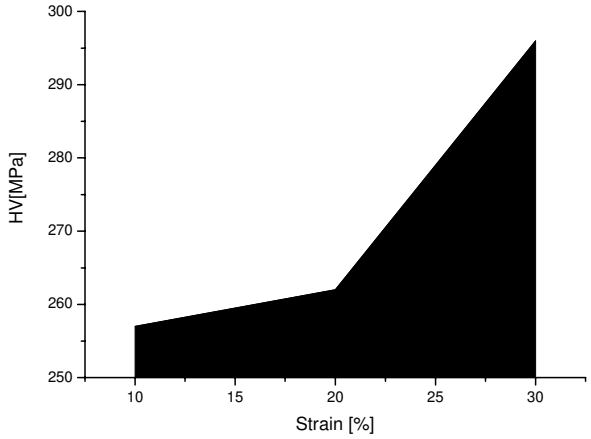

Fig.6. *Hardness versus strain*

It can be observed that the influence of strain is more important in increasing hardness values then the influence of plastic deformation temperatures.

The lowest hardness was obtained for the material subjected to quench after extrusion (250MPa). The specimen with higher hardness was obtained by thermo mechanical treatment from 950^0C with 30 deformation degree (296 MPa). Those values are tightly correlated with obtained structures.

4. Conclusions

1. The thermo-mechanical treatment applied in initial phase of shape memory alloy (b) can change the general properties of the alloy having a positive impact on the shape memory applications.

2. High dislocation density in the initial phase improves the martensitic transformation.

3. The martensitic transformation points are established through the introduction of preferential dislocation distributions for certain martensitic variants.

4. The optical microscopy highlights the coexistence within the alloy of two types of martensite b_1'*(18R)* and g_1' *(2H)*. The heat treatments applied affect the structure and properties of the alloy and implicitly its memory features. The finest martensitic structure has been obtained by thermo-mechanical treatment (T=950^0C, ε=30%);

5. There was a grains refinement accompanied by the elongation phenomenon of the initial austenitic grains. The g_1' martensites have been germinated on b_1' martensites as a results of increasing deformation degree and decreasing plastic deformation temperature.

6. The hardness test highlights the influence of the thermal treatments tightly correlated with the structure obtained.

References

[1]. M. Franz, E. Hornbogen - *Martensitic transformation of a CuZnAl-shape memory alloy strengthened by hot-rolling,* Materials Science and Engineering A252 (1998) 157–165

[2]. Erhard Hornbogen - A *comparative study of ausforming of shape memory alloys with A2 and B2 structures,* Materials Science and Engineering A273–275 (1999) 630–633

[3]. Z.C. Lin, W. Yu, R.H. Zee, B.A. Chin - *CuAlPdalloys for sensor and actuator applications, Intermetallics 8 (2000) 605±611*

[4]. U. Sari, T. Kirindi - *Effects of deformation on microstructure and mechanical properties of a Cu Al Ni shape memory alloy,* Material Characterization 59 (2008), 920-929.

THE ANNALS OF "DUNAREA DE JOS" UNIVERSITY OF GALATI.
FASCICLE IX. METALLURGY AND MATERIALS SCIENCE
N^0. 2 – 2009, ISSN 1453 – 083X

TIME SCALES OF PHYSICO-CHEMICALY DRIVEN PROCESSES IN DESULPHURIZATION $CaO-Al_2O_3$ SLAG

Petre Stelian NITA
"Dunărea de Jos" University of Galaţi
email: pnita@ugal.ro

ABSTRACT

The paper is dealing with the expression of times scales associated to different physically and physico-chemically driven processes taking place on the slag side of the interface $CaO-Al_2O_3$ slags-steel, specific to the steel refining process. The driving process is that presenting the shortest time scale in comparable conditions with others. The time scale of the main physico-chemically driven process at interface steel-slag, on the slag side serves to evaluate the local interfacial flow. In this paper the conditions to evaluate the time scales are connected to the characteristic length scale of solutocapillarity effect in the form of Marangoni convection which results to be the faster process at the specified length scale taken into account, over the critical values of the solutal parameters, called threshold values.

KEYWORDS: physico-chemically driven process, time scale, solutocapillarity, characteristic length, Marangoni effect.

1. General aspects

Flow phenomena are present and they are of outmost importance in many individual and unitary metallurgical processes. Interfacial flow contributes to the adequate evolution of many refining processes such as non-metallic inclusions removal from metallic melts, gaseous bubbles formation and floating, mass transfer at interfaces between metallic melts and slag (or fluxes). In accordance with the advanced trends in science and technology, aspects concerning the occurrence, evolution, efficiency and mastering of the flow phenomena to achieve a high quality melts must be better analyzed at micrometers and even at nanometers scales. It is also broadly recognized the effect of temperature and of the surface active solutes on the surface and interfacial tensions in both fluids at interface and the adjacent flow phenomena, mainly on occurrence of the Marangoni effects [1] consisting in flow and convection. In order to state the problem of a certain type of interfacial flow an adequate set of dimensionless criteria and the specific time scale must be used. In metallurgical refining systems solutal effects, further called also as solutocapillary effect or solutocapillarity, are predominant compared to other aspects of capillarity. Even the electrocapillarity, which is supposed (considered) to be stronger than the solutocapillarity, originates in the presence and concentration of surface active ionic species. The high values of the thermal conductive coefficient in liquid metals contribute to this particularity, making the thermocapillarity without significance in liquid metal and slag layers even at high values of their depths. The Marangoni solutal effect acts at macroscale, by imposing gradients of concentration through external actions, or at microscale when local gradients of concentration appear due to local inhomogeneities of different origins, along the interface or across it. The actions of different physical and physico-chemical factors as gravity, diffusion/viscosity (called also viscous diffusion), surface tension and solutocapillarity are competing according to their time scales. If the thermal equilibrium in the system steel-slag is considered and the electrical phenomena at interface are neglected, the instability/stability at the interface on the slag side is determined by the competition between the actions of different physical and physico-chemical factors as gravity, diffusion/viscosity surface tension and capillarity. The solutocapillarity is the driving process among different actions affecting the stability in interfacial flow when there are accomplished its conditions of prevalence.

2. Time scale significance

An adequate time scale reflects the dynamics of physical process taken into account and serves to a

correct establishing of the time–step size for a numerical simulation of the dynamics.

The representative physical time scales must be adequate to the specificity of the considered problem, evaluated by the typical physical or physico-chemical phenomena such as are gravity, viscosity, diffusion and capillarity, this last the most broad sense. Excepting gravity, these phenomena originate in the complex manifestation of the properties of matter mainly influenced by temperature and chemical composition and these last contribute to them in the form of the thermodynamic and transport properties of the liquid phases. Certain solutes like oxygen and sulphur act simultaneously in systems steel-slag on viscosity, diffusion and capillarity of both mentioned fluid phases. This influence must be evaluated in the complex situation consisting in the simultaneous presence of the above mentioned situation which practically consists in a competition between them to exert the main influence.

If the length scale of the analyzed problem is generically noted L, there will be several ways to define it.

Firstly, the length scale is linked to the space extend where the analyzed phenomenon acts and where the phenomenological and quantitative analysis of flow is performed. Then, there are cases where the length scale results from conditions of prevalence of a certain phenomenon compared to another, or of many several phenomena, acting simultaneously.

A phenomenon is characterized by a characteristic time scale resulting from the condition that all physical and physico-chemical effects, reflected by their relevant quantities, counterbalance between them. In this case an adequate selected dimensionless group will have the value equal to unity.

In principle, the time scale associated with the considered driven physical process must be understood as an interval of time of a specific order of magnitude, where the respectively considered phenomenon or effect is the relevant physical phenomenon, presenting the maximal probability to take place, compared with another or several present phenomenon also.

From this point of view there is a certain similitude to the constructal theory and perhaps it may be a way to approach and explore new facets of the behavior of flow phenomena at interface.The point of view of the author of the present paper is that there is a strong similitude with other observed situations at different scales. Until an evaluation is performed on these aspects, it appears as being of outmost importance the establishing of smallest scale of the system, including the time scale, because the competition between the competing processes takes place locally, in determined intervals of time where different variable conditions appear.

3. Characteristic time scales associated to various kinds of physically and physico-chemically driven processes

3.1. Characteristic time scale of gravity driven physical process, (τ_g)

On Earth gravity acts unidirectionally upon the normal direction to the Earth surface and directed to center of the Earth core. Therefore gravity–driven physical process is analyzed always as 1-D problem. The dimensionless Froude number[2] is adequate to characterize the gravity phenomenon:

$$Fr=\frac{inertial\,force}{gravitational\,force}=V_{(g)}^{2}\cdot(g\cdot L)^{-1}$$

where: g - is the magnitude of the gravity acceleration; $V_{(g)}$ - is the characteristic scale of velocity; L - is the length scale of the considered problem or the characteristic length of the system were the gravity is considered.

The time scale associated with the gravity driven physical process is noted τ_g and it must be understood as an interval of time of a specific order of magnitude, where the gravity is the relevant physical phenomenon. The characteristic scale of velocity $V_{(g)}$, acting on the length scale L of the analyzed problem is:

$V_{(g)}= L/\tau_g$

Imposing the Froude dimensionless number to be of unity order:

$Fr= V_{(g)}^{2}\cdot(g\cdot L)^{-1} \approx 1$

and replacing the relation giving the characteristic scale of velocity given by the relation

( ), the time scale of the gravity driven process is given by the following relation:

$\tau_g \approx (L/g)^{1/2}$

3.2. Characteristic time scale of viscous-diffusion driven physical process

There are specific situations including cases in liquid steel refining processes when only viscosity-driven physical process is the relevant process in fluid flow. As an example, the case of steel flow around a solid and non-reactive, non-metallic inclusion which is very stable from chemical point of view, could be considered. Also, cases referring to the rising in steel of gas bubbles of different origins or produced using different devices are considered.

In the cases of pure viscous flow, an adequate dimensionless number is the Roshko number [3] which is the product of dimensionless Strouhal number (St) [4] [5] and dimensionless Reynolds

number (*Re*) [5]. *St* number is used in the study of periodic or quasiperiodic variations in the wake of objects immersed in a fluid stream. The Strouhal Number can be important when analyzing unsteady, oscillating flow problems. The Strouhal number represents a measure of the ratio of inertial forces due to the unsteadiness of the flow or local acceleration to the inertial forces due to changes in velocity from one point to another in the flow field. It is a dimensionless number describing oscillating flow mechanisms.

The *St* number is often given as:

$St= \omega \cdot L \cdot V^{-1}$

Ro number is given by the relation:

$Ro=St \cdot Re= \cdot \omega \cdot L^2 \cdot v= \omega \cdot L^2 \cdot \rho \cdot v^{-1}$

In both numbers: ω - is the frequency of vortex shedding; L - is the characteristic length; V - is the velocity of the fluid; ρ - density of the fluid; v - kinematic viscosity of the fluid.

The use of the *Ro* number instead of the *St* number allows to avoid the main uncertainty due to the determination of the velocity V.

In specified conditions these dimensionless numbers make possible to evaluate the development of turbulent wakes from vortex streets. At *Re*=40-150, called stable range, regular vortex streets are formed and no turbulent motion at macroscale is developed. In the stable range the vortices decay by viscous diffusion. At *Re*=150-300 it follows a transition of flow to a regime called irregular range in which turbulent velocity fluctuations accompany the periodic formation of vortices. Further, at higher values of *Re* number it follows the fully turbulent flow.

Therefore the time scaling must be performed in different ways. Of a special interest are the stable regime, including the region of very low Reynolds numbers and the transition regime.

3.2.1. Characteristic time scale in the macroscopic stable regime (viscous diffusion)

3.2.1.1. Characteristic time scale at low values of Reynolds number

At enough low values of the *Re* number (<40), the diffusive-viscosity time scale (τ^2_{diff}) results from combining the simultaneous effects of diffusion and of viscosity and it results from the following relation:

$\tau^2_{diff}=\tau_{diff} \cdot \tau_{visc}=(L^2/D)(L^2/v)=L^4/v \cdot D$

where: L - is the characteristic length; D - mass diffusion coefficient of the chemical element able to influence the properties of the interface of the system and thus to act on flow; v - kinematic viscosity of the fluid.

Many times it is considered that what happens at a macroscopic scale it happens also at a microscopic scale and in consequence also at a local scale. Therefore also this regime must be taken into consideration as a competing one against the others.

The relation between the effects of mass diffusion and of the momentum diffusivity is given by the dimensionless Schmidt number *Sc*, expressing the ratio between mass diffusion relaxation time and the viscous time:

$Sc= \tau_{diff} / \tau_{visc}= v/D$

3.2.1.2 Characteristic time scale at values 40<Re<150

In this range, of values vortex street patterns appear [6], frequently called stable von Kármán streets; they are classically regular, stable and well defined for long distances downstream. This aspect of flow also appears at higher values of Reynolds number, up to Re≈10^5 and higher, but the free vortices moving downstream are dumped by the turbulent diffusion and the flow aspect turns into turbulent wakes.

3.2.1.3. Characteristic time scale in the transition regime (Re=150-300)

The value of Ro dimensionless number is correlated with the values of the Re dimensionless number [6]:

$R_o= -3.6 \cdot 10^{-4}$ Re^2 +0.391 Re -48.2 established for Re=260-350 and R_o=34-44.

Another relation, established for Re=50-180 is the following:

R_o=0.212 (Re - 21.2)

The condition R_o>0 obtained by extrapolation of the first relation gives the value Re> 142. At Re=150 the value R_o=2.35 is obtained, which seems to be consistent with the minimal experimental pair data Re=260; R_o=34. Replacing $f= 1/\tau_{Ro}$ in Roshko number and making R_o=1 the following relation is obtained:

$R_o=L^2 \cdot \rho \cdot v^{-1} \cdot \tau^{-1}_{Ro}=1$

$\tau_{Ro}= L^2 \cdot \rho \cdot v^{-1}$

3.3.Characteristic time scale of surface tension-driven physical process (τ_{Ca})

In viscous flow the surface tension phenomenon is characterized by the capillary number *Ca* [1], frequently called the crispation number *Cr*:

$Ca=\mu \cdot D \cdot \sigma^{-1} \cdot L^{-1}=\mu \cdot V_{(Ca)} \cdot \sigma^{-1}$

where: μ - is the dynamic viscosity; D - mass diffusion coefficient of the chemical element; σ – is the surface tension of the slag; L - is the characteristic length; $V_{(Ca)}$ - is the characteristic scale of velocity in surface driven physical process.

If τ_{Ca} is the typical time scale of the surface driven process then:

$V_{(ca)}=D/L= L/ \tau_{Ca}$

Imposing the capillary dimensionless number to be of unity order:

$Ca=\mu \cdot V_{(Ca)} \cdot \sigma^{-1} \approx 1$

and replacing the relation giving the characteristic scale of velocity $V_{(ca)}$, the time scale of the surface tension-driven process is given by the following relation:

$\tau_{Ca} \approx L \cdot \mu \cdot \sigma^{-1}$

3.4. Characteristic time scale of solutocapillarity

The variations of the chemical compositions of the slag and steel at interface, due to the mass transfer of the surface active elements as sulphur and oxygen, locally affect the interfacial tension.

In the most frequent situations, due to the actions of many factors the surface tension of liquid phases and in a larger sense the interfacial tension liquid-liquid is not a constant one, mainly due to the specific chemical reactions. It is case of interfaces liquid-liquid (steel-slag, steel-liquid inclusion), liquid-solid (steel-solid inclusion), liquid-gaze (steel-bubble of gaze). In such cases the surface tension presents important variations on local small scale for a certain interval of time, because the re-equilibration of the interface is not an instantaneous one. In the system of two immiscible fluids, separated on the vertical direction according to the difference of density, there are several kinds of gradients of the superficial tension upon the factors affecting this quantity and this is expressed in the global relation (1) for the 1-D case:

$$\tau_S = \frac{d\gamma(c,T,\psi)}{dx} = \frac{\partial \gamma}{\partial c}\frac{dc}{dx} + \frac{\partial \gamma}{\partial T}\frac{dT}{dx} + \frac{\partial \gamma}{\partial \psi}\frac{d\psi}{dx}$$

where: γ is superficial tension of the fluid taken into consideration, or interfacial tension; c – concentration of the superficial active element; T – temperature; Ψ – electric potential, existing or applied; x – direction on which the respective gradient of the superficial tension (or the surface tension) gradient acts, being estimated or computed.

The contribution of the temperature gradient could be considered closed to zero because of the high values of the thermal coefficient in liquid steel which affects also the slag layer in the neighboring zone at interface.

When the dynamic effects induced by solutocapillary effects is analyzed, mainly at a local scale, it is necessary to evaluate first the conditions when the shortest time scale is that of solutocapillarity, when many competing actions are present. If these conditions are accomplished the overcoming of the neutral stability conditions takes place.

In this case, overcoming of a threshold value of the surface active solute concentration leads to the appearance of hydrodynamic instability of the interface, on short scale and on long-scale, caused by the surface tension gradients (the Marangoni effect) of solutal origin. The solutocapillarity is a factor of instability while the viscosity/diffusion and gravity act as stabilizing factors by damping the effects of this instability. Diffusion acts to dampen the concentration fluctuations and the associate fluid flow either along surface or across it, because the directionality of diffusion depends only on the concentration gradient which is a vector. Viscosity acts to dissipate in bulk the kinetic energy of flow.

The gravity acts physically to flatten the interface and thus to stabilize the deformational perturbations. All these actions are competing and the dominating action in this competition is the one having the shortest time scale. This instability presents different convective patterns as regular convective structures (rolls, hexagons), interfacial waves and chaotic convective motions in the vicinity of the interface, called also interfacial turbulence.

It is remarked that the short scale of solutal capillary effects, in the form of local Marangoni flow and adjacent convection contribute to accelerating the interfacial mass transfer which interests in different steel refining processes.

The dimensionless Marangoni number for the solutal case represents the ratio between the destabilizing driving force F_m due to the surface tension gradient and the resistive force F_f due to viscosity/diffusion which is opposed to the first; for the solutal case the following relation for the dimensionless number Marangoni was adapted [1]:

$$Ma_{sol} = \frac{F_m}{F_f} = \frac{\frac{\partial \sigma}{\partial C} \cdot \Delta C \cdot L}{\mu \cdot D}$$

where: $\frac{\partial \sigma}{\partial c}$ – the surface tension coefficient, related to the concentration of the considered surface active element, usually in $N \cdot m^{-1} \cdot (mass\%)^{-1}$; Δc – the surface concentration difference of the considered surface active element, in mole, molar fraction (X) or mass percentage(%mass) between two points separated by the distance L; L – the characteristic length of the Marangoni effect, in meter (m); μ – the dynamic viscosity of the considered fluid,

in $kg \cdot m^{-1} \cdot s^1$; D – the diffusion coefficient of the surface active element in the considered liquid, in $m^2 \cdot s$.

The flow is destabilized when $F_d > F_f$,i.e when Ma>1. Experimentally, the critical value of the dimensionless Marangoni number is $Ma_c = 80$. Taken into consideration that $\mu = \rho \cdot \nu$, the Marangoni time scale results in the form:

$$\tau_{Ma}=\left(\frac{\rho\cdot L^2}{\frac{\partial\sigma}{\partial c}\cdot\frac{\Delta c}{L}}\right)^{1/2}=\left(\rho\cdot L^3/\left(\frac{\partial\sigma}{\partial c}\right)\cdot\Delta c\right)^{1/2}$$

The solutocapillary effects are physically present in a sensitive manner when the conditions are accomplished, i.e. when $Ma>Ma_c$, and in this conditions the equivalent time scale is designed by

$\tau_{solutocap}$, where $\frac{\partial\sigma}{\partial c}\cdot\Delta c>\left(\frac{\partial\sigma}{\partial c}\cdot\Delta c\right)_{crit.}$.

For the critical value of the dimensionless number Marangoni for the solutal case, a critical value of the time scale is obtained [1]:

$$(\tau_{Ma})_{crit.}=\left(\frac{\tau_{diff}\cdot\tau_{visc}}{Ma_c}\right)^{1/2}$$

4. Comparison between time scales of different physico-chemical actions in liquid steel and slags

A major interest for these aspects is in the field of steel refining under slags.

The case of low carbon aluminium killed steel (LCAK) and desulphurization slags in the CaO-Al_2O_3system at the temperature of 1873K will be considered, because it influences in many ways the purity of the steel, due to the dynamics of the interface. The data taken into consideration are shown in the table1.

Table 1. *Physico-chemical data and time scale of several physico-chemical driven process in CaO-Al_2O_3 slags at temperature of 1873K*

Quantity, symbol, units	Values, references	
	Slag 50% CaO+50% Al_2O_3	Slag 60% CaO+40% Al_2O_3
Density, ρ, kg·m^{-3}	2710 [10]	2685 [7]
Dynamic viscosity, μ, Pa·s	0.23 [9]	0.1184 [9]
Diffusion coefficient of sulphur, D_S, m^2·s^{-1}	$2.48\cdot10^{-10}$ [10]	
Surface tension upon the sulphur content (S, mass%), σ, 10^{-3}N·m^{-1}	$1.4781(\%S)^2-22.159(\%S)+546$	$2.1217(\%S)^2-22.922(\%S)+563$
Time scale of the gravity driven process, τ_g, s	$\sim0.32L^{1/2}$	
Time scale of the mass diffusion driven process, τ_{diff}, s	$\sim4.03\cdot10^9\,L^2$	
Time scale of the viscosity driven process, τ_{visc}, s;*Sc* value	$1.178\cdot10^4L^2$; $Sc=3.42\cdot10^5$	$2.26\cdot10^4\,L^2$; $Sc=1.78\cdot10^5$
Time scale of the viscous diffusion driven process (*Re*<40), $\tau_{visc.diff}$, s	$\sim8.47\cdot10^6\,L^2$	$\sim9.54\cdot10^6\,L^2$
Time scale in the transition regime (stable vortex streets) (*Re*=150-300), τ_{Ro}, s	$\sim3.193\cdot10^7L^2$	$\sim6.889\cdot10^7L^2$
Time scale of the surface tension driven process, τ_{Ca}, s	$0.23\cdot L\cdot\sigma^{-1}$	$0.1184\cdot L\cdot\sigma^{-1}$
Time scale of solutocapillarity, $\tau_{solutocap}$, s Time scale for Ma_c, $(\tau_{Ma})_{crit}$, s	$2710\cdot L^3\cdot\left(\frac{\partial\sigma}{\partial c}\cdot\Delta c\right)^{1/2}$ $8.613\cdot10^2\cdot L^2$	$2685\cdot L^3\cdot\left(\frac{\partial\sigma}{\partial c}\cdot\Delta c\right)^{1/2}$ $1.067\cdot10^2\cdot L^2$

5. Commentaries and conclusions

The analysis of the relations giving the time scales of different physico-chemically driven processes are dependent upon the reference length scale. As it is known the physico-chemical processes take place simultaneously but according to their time scale and at different lengths. Like the time scales, the length scales presents specific values called characteristic scales. The importance of the length scale results from the value of its power in the established expressions. The greater the exponent value, the greater the effect at small values of considered length L, in minimizing the time scale of the respective physico-chemical action. This length scale L cannot be however too much. For example a limit for the surface tension physically-driven process could be the characteristic length L_c, given by the relation:

$L_c=(\sigma/\rho\cdot g)^{1/2}$

In the considered cases in slags, values of L_c are around 4.5 mm but this is less significance for the solutocapillary effect where the characteristic length scale is about 50-300μm in CaO-Al_2O_3 slags. At these values of the length scales the shorter time scale results for the solutocapillarity action because of the factor L^3. At the same value of the length scale L, lets say 100μm, the following order relation results

between the time scales of the considered physico-chemical –driven actions:

$$\tau_{diff} > \tau_{visc.diff} > \tau_g > \tau_{visc} > \tau_{Ro} > (\tau_{Ma})_{crit} \approx \tau_{ca}$$

In the mentioned conditions it is expected that solutocapillarity should play a major role in the local interfacial dynamics at micrometric scale. At values of the product

$$\left(\frac{\partial\sigma}{\partial c}\cdot\Delta c\right)^{1/2} > \left(\frac{\partial\sigma}{\partial c}\cdot\Delta c\right)^{1/2}_{crit}$$

the value of the time scale τ_{Ma} decreases below the critical value $(\tau_{Ma})_{crit}$ and in consequence the solutocapillary–driven processes (the direct effects and the connected processes) are faster.

The problems of stability around and over these values, called threshold values of parameters, need a separate and special treatment, in specific conditions.

References

[1]. **Colinet, P., Legos, J.C., Velarde, M.G.** - *"Nonlinear Dynamics of Surface –Tension-Driven Instabilities"* Wiley-VCH, Berlin, 2001, 54-57.

[2]. **Vaughan, C. L., O'Malley, M. J.** - *"Froude and the contribution of naval architecture to our understanding of bipedal locomotion",* Gait & Posture 21 (3) (2005), 350–362.

[3]. **Ormières, D., Provansal, M.** - *Transition to Turbulence in the Wake of a Sphere* PHYSICAL REVIEW LETTERS 83, 1 (1999), 80-83.

[4]. **Sakamoto, H. and Haniu, H**. - "*A study on vortex shedding from spheres in uniform flow,"* Journal of Fluids Engineering, 112, (1990), 386-392.

[5]. **Holman, J.P.** - *Heat transfer*, McGraw-Hill, 2002

[6]. **Roshko, A.** - *"On the development of turbulent wakes from vortex streets, "*Ph.D. thesis, California Institute of Technology, Pasadena, Ca.USA, 1952.

[7]. **A.S. Panov, I.S. Kulikov, L.M. Selev** - Isv.Akad.Nauk SSSR, otdel Teckn.nauk, Metallurgiya i toplivo, 3 (1961), 25

[8]. **G.I. Zhmoidin, L.N.Sokolov, G.V.Podgornov, G.S. Smirnov** - Teoriya Metallurgicheskih Protsesov, 3 (1975), 150

[9]. **Elyutin, V.P., Kostikov, V.I.,Mitin, B.S., Nagibin, Yu.A.** - Russian Journal of Physical Chemistry, 43 (1969), 316.

[10]. **L. Jonsson, Du Sichen, P. Jonsson** - ISIJ Int., 38 (1998), 260

THE ANNALS OF "DUNAREA DE JOS" UNIVERSITY OF GALATI.
FASCICLE IX. METALLURGY AND MATERIALS SCIENCE
N^0. 2 – 2009, ISSN 1453 – 083X

THE STEAM- SECONDARY SOURCE OF ENERGY IN METALLURGY

Lilica IVANESCU
"Dunărea de Jos" University of Galati

ABSTRACT

The paper is focused on a study of how to use the steam from recovery boilers of LD converters to produce electricity in turbine generators and heat in a heat network.

KEYWORDS: steam, converter gas, recovered energy

1. Introduction

The paper presents how to obtain and efficiently use the steam from recovery boilers of LD converters on the Steel Factory-Galati, Romania.

Each LD steel section contains three LD converters out of which two operates concomitantly. Each converter is fitted with steam recovery boilers. The thermal dynamic parameters of the steam are:

P=8-13 at

T=265 ^{0}C

Flow rate=34t/h

The steam obtained from the recovery boilers in the LD factories was further used in the coke plant to heat the tar and radiators.

Now coke-plant is stopped so that excess steam is vented to the atmosphere.

The paper is focused on a study of how to use this steam, from boilers, to produce electricity in turbine generators and heat in a heat network.

2. Obtaining the converter gas

When preparing the steel in the oxygen converters, in the impact zone of the oxygen jet with the metal bath a local temperature of 3000 ^{0}C is created. As a result of these high temperatures, 0.6 – 1.2% of the metal load is volatilized, as a reddish color smoke called converter gas.

Figure 1 illustrates the temperature dependence of the vapors pressure of Pb, Mn, Si, Fe, Ni.

The converter gas contains:

- metals vapors;
- gases: CO, H_2, CO_2;
- powder.

It is worth mentioning that there is quite an amount of furnace gas in CO, about 75% per charge and therefore its caloric power reaches 8500 kJ/Nm^3.

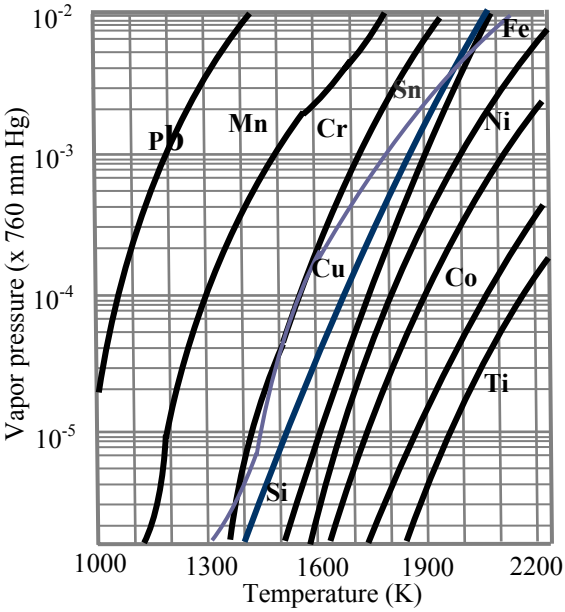

***Fig 1.** Temperature dependence of vapor pressure for some metals*

3. The heat recovered in the boilers from the LD converters section

At the converter outlet, the gas exhausted has a temperature of 1700 ºC.

In addition, in the annular space, between the converter outlet and hood, goals the air from the hall which helps burn CO in the converter gas.

This leads to an increase in temperature to 2750 ºC and an increase in the volume of burned gas about three times its volume before burning (Fig 2).

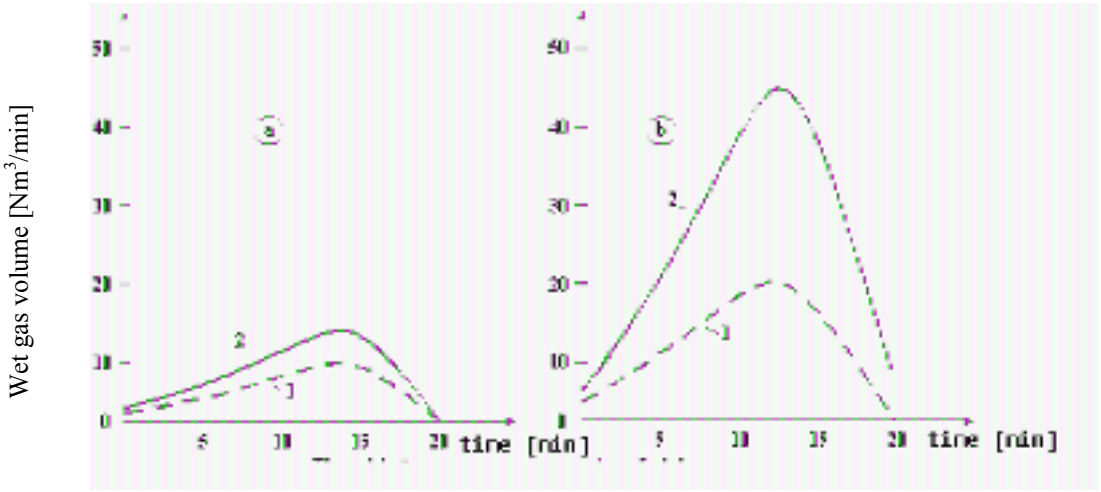

Fig 2. *Variation of the converter gas volume*
a. no gas in burnt in the hood: b. gas is burnt; 1.dry gas volume; 2.wet gas volume

In the recovery boiler, fitted above the converter, the gas physical heat of 1700 ºC is recovered and, in the same time, the chemical heat of the fuel elements (CO and H_2). In the Figure 3 the scheme of the converter gas caption system is shown in the case of the gas burning in the radiation tower. The gases are cooled down to 1000 ºC in the radiation tower, and then are cooled down to 300 ºC in the converting part of the cooling tower.

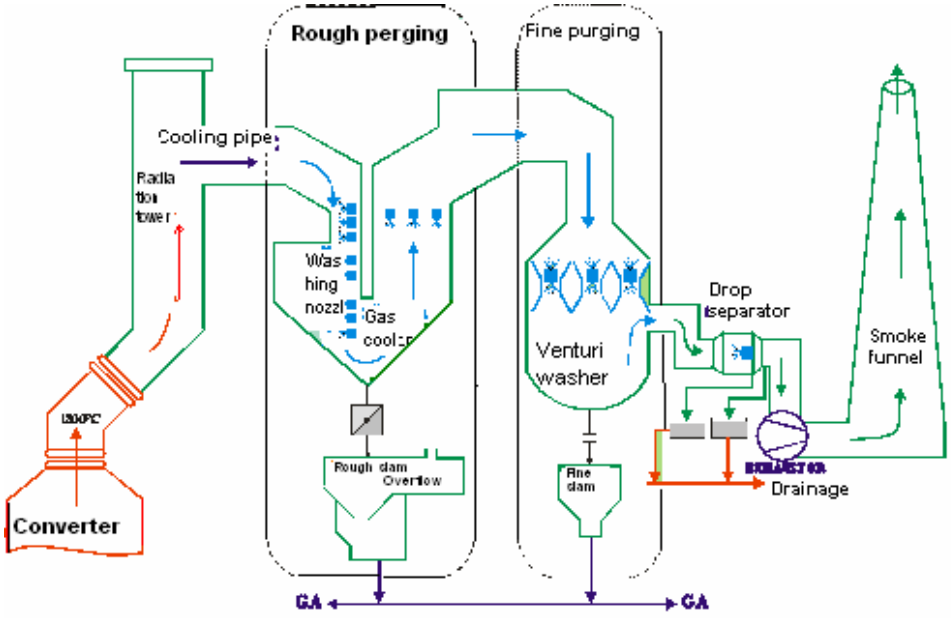

Fig 3. *Scheme of the furnace gas capture system when the gas is burning in the radiator, where gases are cooled down to 1000 ^0C , and then the converting part gases are cooled down to 300^0C*

4. Efficient use of the steam produced in the recovery boilers in LD plants

Because the process inside the LD converter is non stationary, the steam debit inside the recovery boiler is fluctuating. For this reason each LD converter plant has available a steam accumulator serving the three converters.

In figure 4 in shown the cooling system of the radiation tower, in the case of using the steam accumulator. In figure 5 is shown the functional scheme for a thermo-electrical plant, which uses steam from the recovery boilers of the siderurgical factory.

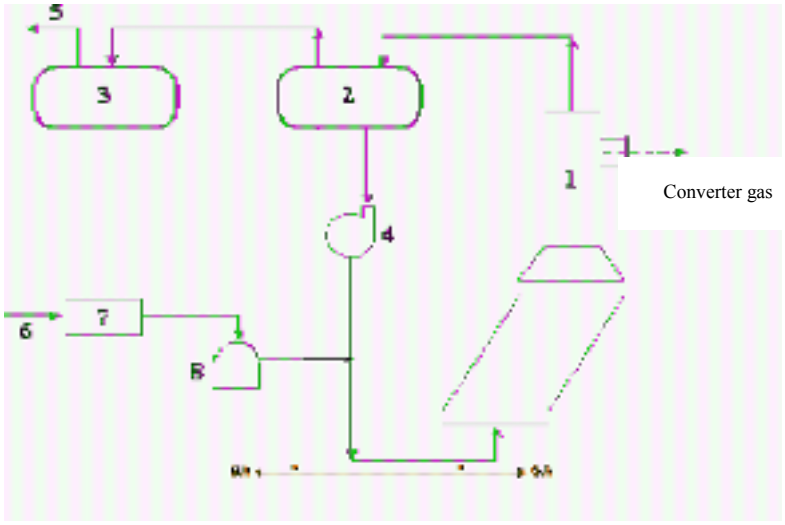

Fig.4. *The hood cooling system when the steam accumulator is used:*
1-hood; 2 – drum; 3 - steam accumulator; 4- recirculation pump, 5- steam for customers;
6- water supply; 7 - reservoir; 8 – boiler feed pump

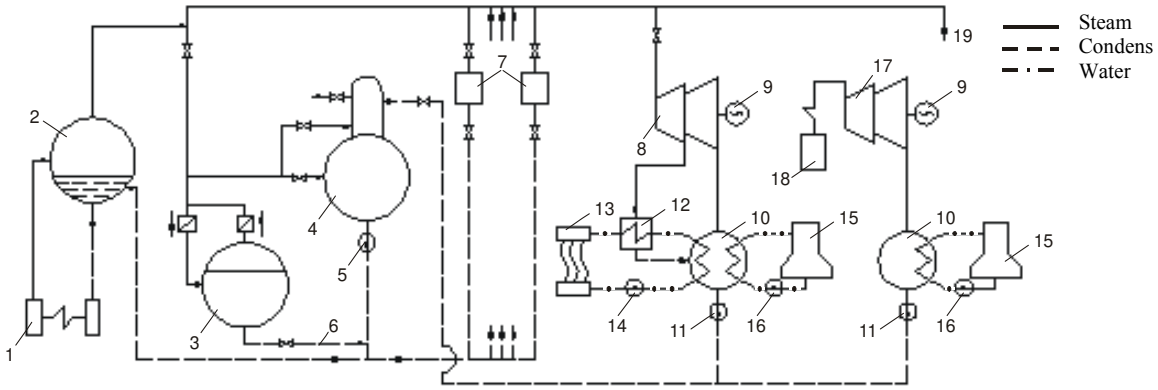

Fig.5. *Scheme of a termo-electrical plant with steam from syderugical factory*
1- recovery boilers; 2- drum, 3 - accumulator; 4- degassing; 5 – water pump,
6 – recovery condens;7 – steam boilers; 8,9 – turbogenerator, 10-condenser;
11 - condense pump, 12-water preheater; 13- radiators.

5.Conclusions

The use of steam form recovery boilers of the LD steel plants in the production of electricity is very effective because the thermodynamic parameters of steam correspond, at the obtaining of a power of approx. 25 MW, to one turbo-generator. The investment required can be covered in about 3 years. The cost of electricity obtained by recovering the converter gas heat, in the recovery boilers, can be as low as 4 EURO/MWh, in comparison with the cost of 60 EURO/MWh in the national electric system.

References

[1]. F. Oprea, D. Taloi, A. Ivanescu - *"Theory of the metallurgical processes"*, Editura Didactica si Pedagogica, Bucharest (1984).
[2]. W. Ackermann: *"Mass and energy transfer between the gaseous and liquid phase in oxygen converter"*, Stahl und Eisen 9 (1979), p. 36-41.
[3]. A. Ivanescu, A. Ene, L. Ivanescu, C. Catana - *"Researches regarding the vaporization process of the existing elements in the metallic bath during steel making in LD converter"*, International Conference METAL 2005, Hradec nad Moravici, Czech Republic, paper A6P.
[4]. C. Mustata, V. Munteanu, D. Zorlescu - *"Mathematical modelling of the steel making in oxygen converter"*, Editura Tehnica, Bucharest (2000).

THE ANNALS OF "DUNAREA DE JOS" UNIVERSITY OF GALATI.
FASCICLE IX. METALLURGY AND MATERIALS SCIENCE
N^0. 2 – 2009, ISSN 1453 – 083X

MODELLING, OPERATION AND CONTROL OF MULTITERMINAL DC CONNECTION FOR OFFSHORE WIND FARMS

Mircea Viorel DRAGAN, Cristina Madalina DRAGAN, Crina Violeta DRAGAN, Doru HANGANU
"Dunărea de Jos" University of Galati
email: vdragan@ugal.ro

ABSTRACT

Renewable energy systems are tending to become more and more present in the energy market and wind power has already proven its potential. Wind parks of thousands of MW are planned to be place into sea faraway from the mainland. Appropriate transmission systems should be designed in order to be able to handle a significant amount of power with high efficiency and to be economically competitive. This paper discusses a Multiterminal DC connection, based on VSC technology, between one offshore wind farm and two different grids. The main focus was on developing the control strategy for connecting these three systems via DC connection. The modelling and designing of the WF components, of the power converters, of the DC system components and of all the controllers played a major role in developing a simulation platform for future studies. The proposed concept may enable integration of large offshore wind farms at considerable distances. Experimental verifications follow the theoretical investigations in order to prove the reability of the modelled system for different test scenarios.

KEYWORDS: multiterminal DC power wind farm, modelling, simulation, Power Factory DIgSILENT

1. Introduction

Offshore wind energy is one of the key component in helping the EU to fulfil the agreement to achieve the 20% of renewable energy from the total energy by 2020.

Although the offshore market is currently smaller then the onshore one, it is of high interest for the energy policies because of its important capacity of producing energy.

The offshore wind market is characterized by projects that are significantly larger and more difficult to implement than most of the onshore projects [1]. Currently limitations are encountered in connecting the large scale offshore wind energy.

Also the current onshore transmission networks can not be able to integrate the energy that can be available in most of the large scale offshore projects.

To correct these deficiencies a redesign of the grid infrastructure, system management, grid regulation and grid codes are needed.

The large scale offshore wind farms have to be treated as conventional power plants, thus the necessity for both national and cross border network upgrades is increasing.

2. Transmission features for offshore Wind farms

One of the challenges is to find a suitable type of connection for offshore wind farms, having different power ratings and different distances from the onshore connection point. This selection should be done by taking into consideration power efficiency and economical aspects. Until now for the already build WFs, like Horns Rev I, Nysted, Middelgrunden, in Denmark, the only connection used was the AC connection. The reasons for choosing this type are: lower station costs, no power converters needed, a simple layout for the offshore park. By choosing the AC transmission for the offshore WF several disadvantages are encountered, such as: the need of reactive power compensators, such as SVCs or STATCOMs, AC cable cost becomes higher as the distance grows, the decrease of the transmission capability of AC system decreases together with distance because of the dielectric losses and the reactive power that is produced along the cable.

The solution could be the HVDC transmission. Some benefits of using HVDC transmission instead of AC transmission are: less power losses for long

distances, lower cost for cables above certain distances, connection of asynchronous AC networks and offshore WFs can operate at variable speeds.

When it comes to decide which is the best transmission system option, two parameters which have a great impact on transmission efficiency and costs are considered. These are the transmitted power and the distance. Figure 1 reveals what is the suitable connection type for electrical systems.

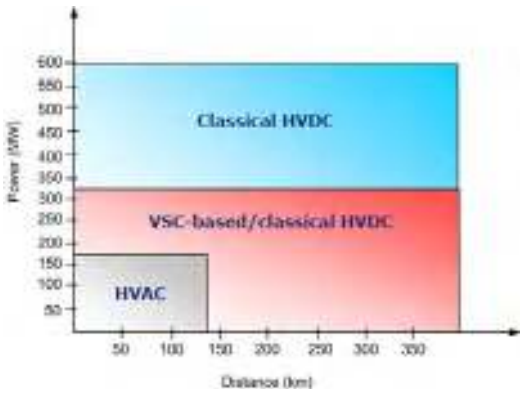

Fig 1.*Transmission type depending on power and distance [2]*

It can be seen that the HVAC is the best solution for small power systems and short distances. One of the reason is the increased price for installations and cables when it comes to transmit high levels of power on long distances. As the power and distances increase the HVDC connection should be considered. The VSC-HVDC technology is preferable to transmit medium amount of power on long distances, but when it comes to transmit on large distances a significant amount of power, the solution is classic HVDC.

The HVDC-VSC transmission is a relatively new technology that uses the latest power semiconductor, the IGBTs.

These power semiconductors have self-commuted turn-on and turn-off capability, thus allow generating reactive power to supply wind turbines in the offshore station while active power injected to the transmission system can be control. With the development of this semiconductor and control equipment, the voltage source converter became viable systems. The HVDCVSC technology is used by several manufacturers, two of them can be mentioned: Siemens which developed HVDC Plus (12 pulses) and ABB which HVDC Light (6 pulses).

The advantages provided by using HVDC-VSC in an wind farm are:

- Smaller transformer substations;
- Low weight DC cables making the process easier to transport, install and more economical;
- Ensures reactive power compensation;
- It can be easily expanded;
- Fault ride-through and black start capability.

Currently one of the concerns is the limited power exchange between the EU country members due to the lack of physical interconnection capacity and the capacity allocation mechanisms.

The development of the offshore wind farms is one of the factors that leads to the demand of increased interconnections and improve the possibility of power exchange.

Taking into consideration the advantages of the HVDC-VSC technology, the suitable solution that can provide the offshore WFs connection and also that can facilitate the trans-national exchange with a high cost efficiency, is the multiterminal DC transmission system (MTDC).

3. Modelling

A number of three identical wind turbines connected in parallel are modelled for the wind farm configuration. The generating side of each WT is connected with the AC/DC side of a full scale power converter, through a phase reactor in parallel with an AC filter. Each wind turbine was designed to have its own rectifier. The output power of the wind farm is linked in a common point offshore, followed by a step up DC/DC booster. Next two DC links will connect each grid. An inverter is placed on both of the grid sides. The main function of the VSC-HVDC is to transmit constant DC power from the rectifiers to the inverters. The connection to the grids is made through a set of phase reactors and AC filters. A transformer is also used for AC voltage boosting and galvanic isolation.

The modelling includes a wind turbine system, a wind turbine full scale power converters control, and a grid side converters control.

3.1. Wind Turbine Model

The wind turbine's rotor extracts the kinetic power from the wind and transforms it into mechanical power. Then the mechanical power is converted into electrical energy by the generator and fed into the grids through converters. A simplified block diagram of the wind turbine components is presented in Figure 2. As shown in the scheme, the elements of wind turbine are the wind model, the aerodynamic model, the mechanical model, the generator model, the rectifier and the pitch control block model.

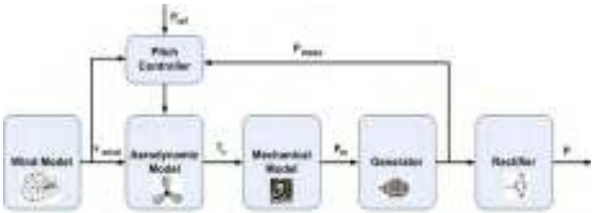

Fig. 2. *Layout of the Wind Turbine Model*

The input of the system is the wind and the output is the electrical power. The wind model provides a realistic characteristic of the wind which is modelled based on an average wind speed profile. This wind is further on applied to the rotor blades. The aerodynamic model computes the rotor torque (T_r) which is the input for the mechanical model that makes the conversion of the mechanical torque of rotor into a torque proper for the high speed shaft. For the generator model a squirrel cage induction generator is used. This performs the conversion of the mechanical power outputted by the mechanical model (P_m) into the electrical power (P_{meas}), followed by the transformation from an AC to DC transmission system made by the rectifier.

The aim of the pitch controller is to ensure that the wind turbine, depending on the available wind is producing the desired power imposed by the TSO. Based on the measured power of the system and the reference value for power, the pitch control has to adjust the angle of the blades in order

to maintain a constant reference power when higher winds are applied to the WT. The power reference can be set to be the rated power of the WT but depending on the demands of electricity. The grid operator can change this reference in order to maintain the stability of the grid. The offshore wind farm represents the third terminal in the MTDC system.

3.2. Generator Side Converter

The main issue regarding the control of the full power scale converter (sending end station) for the wind turbine is to ensure system stability and maximum operating point of the generators by providing suitable voltage and frequency set-points on to the grid. For optimizing the power output of the SCIGs, the constant voltage/frequency control has been implemented for the generator side converters.

Each wind turbine is equipped with a 2,3 MW squirrel cage induction generator. Figure 3 shows the generator's power output having the pitch angle set to its optimal value and having a wind speed that varies from the cut-in wind speed (4m/s) to the rated wind speed (11.9m/s). Even if the pitch angle is equal to the optimal value, the operating points of the active power are not optimal due to low wind speeds. Figure 3 indicates that the rated active power is achieved for the rated synchronous speed that corresponds to the frequency of 50 Hz. Therefore, for wind speeds below the rated values, the optimum operational points of the WT must be found. This is done by varying the generator's synchronous speed. The interval of variation for the synchronous speed is considered between 500 and 1500 rpm. The black line drawn in Figure 3 shows these points. The range of speed operation is obtained for a maximum output of the WT for all the considered wind speeds [3]. Considering Figure 3 the optimal frequency for the stator side of the SCIG for different wind speed is computed.

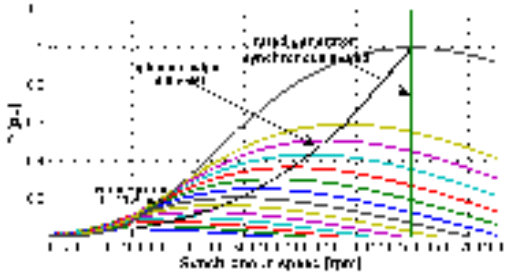

Fig. 3. *Power output of the generators for different wind speeds*

The control scheme of the rectifiers implemented in Power Factory is based on the dependence of frequency on active power and voltage on reactive power from Figure 4.

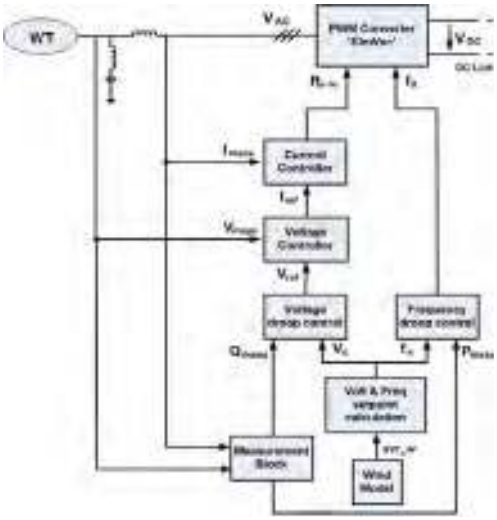

Fig. 4. *Control structure of the rectifiers*

As depicted Figure 4 the control of the rectifier is composed of voltage-frequency control, frequency droop control block, voltage droop control block and PI regulators for voltage and current. Using the Pulse Width Modulation (PWM) technique in the VSC converter, it is possible to obtain the desired voltage waveform at the AC terminals. Limitations apply due to the power ratings of the converter, the DC voltage and the maximum switching frequency. The inputs of the PWM model are $P_{min\text{-}in}$ and f_0 and they can be adjusted independently by the VSC converter to give any combination of voltage magnitude and phase shift in relation to the fundamental frequency-voltage in the WT side. A measurement block is used to obtain information about the AC current and voltage on the AC side. These signals are used for the current and

voltage loops in order to minimize the errors. I_{meas} and V_{meas} are also used to calculate the active and reactive power on the AC side. So, according to the V/f constant principle the optimal output voltage can be calculate according to (1):

$$\frac{Vrated}{frated} = ct \qquad (1)$$

Therefore by keeping the ratio between voltage and frequency constant, the voltage set-point Vs is obtained. :

$$\frac{Vs}{fs} = \frac{Vrated}{frated} \qquad (2)$$

The setpoints for frequency and voltage provided by the Voltage and Frequency setpoint calculation block are optimized by the *Voltage droop* control and *Frequency droop* control blocks.

The voltage control loop should ensure that the reactive currents, which circulate inside the wind farm, are within limits. A droop characteristic for the voltage controller will minimize the stationary error in this case. Since the induction generator will always draw reactive power from the PWM converter, the voltage reference should be increased when the generator's demand for reactive power increases [4]. Voltage reference for the voltage controller is calculated using Eq. 4.

In order to optimize the transfer of the entire available power from the wind farm to the main power grid, a frequency droop characteristic is used. The set-point frequency provided by the V/f block is optimized as a function of the produced power as shown in Eq. 3.

$$V_{ref} = V_s + K_v \cdot Q_{meas} \qquad (3)$$

$$f_0 = f_s - K_f(1 - P_{meas}) \qquad (4)$$

where: K_f - frequency droop coefficient, $K_f = \frac{\Delta f}{\Delta p}$; K_v - voltage droop coefficient; V_s - voltage setpoint fed by the V/f control system.

3.3. Grid Side Converter

While the converters connected to each wind turbine control the active power flow and the AC voltage, the receiving end stations are designed to control the DC link voltage and the reactive power. For the grid connected applications, the typical control strategy of the VSC-HVDC receiving end station is the voltage oriented control.

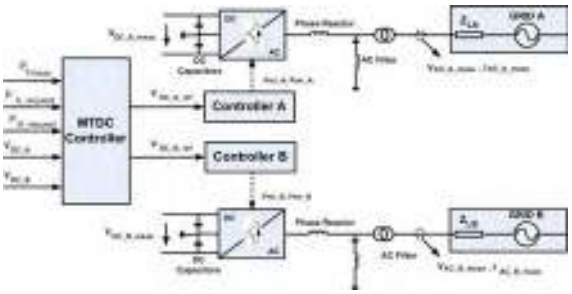

Fig. 5. *Overall control structure of the receiving end stations implied in MTDC [3]*

The overall control structure of the receiving end stations of System A and System B is presented in Figure 5. It is based on the linear dependence of the DC voltage on the active power. The control block implemented in DIgSILENT Power Factory contains the MTDC Controller that handles with the active power sharing between the two grids, function of the measured output of the wind farm PTmeas, the power demands of each grid (P1 for GRID A and P2 for GRID B) and the DC voltage levels from each inverter. Communication lines are needed between the three terminals for real time acquisition of the terminals parameters. The MTDC Controller takes into consideration also the losses from the transmission system that is represented by intern parameters. For a more accurate computation, the losses have to be monitored in real time.

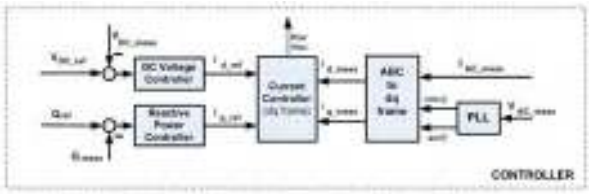

Fig. 6. *Detailed control structure of receiving end converter [3]*

Based on these parameters, the MTDC Controller block supplies the DC voltage setpoints for both of the controllers for GRID A and GRID B. The control blocks for each inverter are identical and a detailed structure is shown in Figure 6. The main control blocks contain a fast current controller that outputs the real and imaginary part of the modulation index. The references values for the current controller block are provided by additional controllers for the DC voltage and reactive power.

The reference for the 'Reactive Power Controller' are given by each TSO of GRID A and GRID B. The setpoints for the DC voltage controller are sent by the MTDC controller for each inverter. The measuring points of DC voltage, AC voltage and AC current are placed in each of the system as indicated in Figure 5. A PLL block is used in order to

synchronize the phase of the dq references with the AC source voltage.

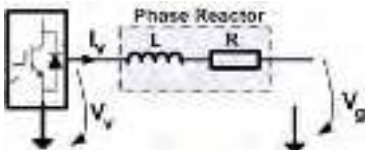

***Fig. 7**. Equivalent circuit of the receiving end station*

The equivalent circuit of a single phase receiving end converter is shown in Figure 7 where the converter and the grid can be considered as voltage sources V_v and V_g. It is considered that the circuit is functioning at the nominal frequency 50 Hz, thus the AC filter can be neglected [4].

Looking at the circuit from Figure 7, the voltage on the phase reactor can be derived as:

$$V_v - V_g = L\frac{div}{dt} + Ri_v, \quad (5)$$

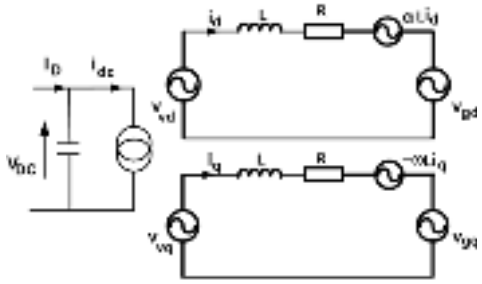

***Fig. 8.** VSC equivalent circuit in dq reference frame*

In order to decouple the DC voltage and the reactive power controllers, the synchronous rotation dq reference frame is used.

First (5) is translated from the abc stationary frame in the αβ orthogonal coordinates using the Clarke Transform.

The voltage droop on the line reactor in αβ coordinates is [5]:

$$\begin{cases} V_{v\alpha} - V_{g\beta} = L\dfrac{di_{v\alpha}}{dt} + Ri_{v\alpha} \\ V_{v\beta} - V_{g\beta} = L\dfrac{di_{v\beta}}{dt} + Ri_{v\beta} \end{cases} \quad (6)$$

where the voltages Vv and Vg have the following expression in αβ stationary frame function of the abc coordinates:

$$V_\alpha = \sqrt{3}\cdot V_{ab} + \frac{\sqrt{3}}{2}V_{bc} \quad (7)$$

$$V_\beta = \frac{3}{2}V_{bc} \quad (8)$$

Furthermore, using the Park transformation Eq. (6) are expressed in the dq coordinates:

$$\begin{cases} V_{vd} - V_{gd} = L\dfrac{di_{vd}}{dt} + j\omega Li_{vq} + Ri_{vd} \\ V_{vq} - V_{gq} = L\dfrac{di_{vq}}{dt} + j\omega Li_{vd} + Ri_{vq} \end{cases} \quad (9)$$

The relation between the dq and αβ quantities is [6]:

$$\begin{cases} V_d = \dfrac{2}{3\sqrt{2}}(V_\alpha \cos\theta - V_\beta \sin\theta) \\ V_q = \dfrac{2}{3\sqrt{2}}(V_\beta \cos\theta + V_\alpha \sin\theta) \end{cases} \quad (10)$$

where: θ – the angle between the α and β axes:

$$\theta = \arctan\frac{V_\beta}{V_\alpha};$$

ω - the angular frequency: $\omega = \dfrac{d\theta}{dt}$;

Based on (9) the VSC equivalent circuit is obtained in the dq axes representation as shown in Figure 8.

By assuming that the d-axis is aligned with the axis of one phase voltage V_v from stationary abc reference frame, it results that $V_{vq} = 0$ and $V_{vd} = Vv$ [6]. From Figure 8, the apparent power injected by the converter in the AC grid can be written as [7]:

$$S = 3(V_{vd} + j0)(i_d - ji_q) \quad (11)$$

Therefore, the active and reactive powers are:

$$P_{DC} = P_{AC} = 3V_{vd}i_d \quad (12)$$

$$Q = -3V_{vd}i_q \quad (13)$$

It can be observed that the active power is related to the current id and the reactive power to iq. Relation (12) must be satisfied in order to ensure the stability of the system. Any unbalance in the active power flow transferred through the converter will cause DC voltage fluctuations. Therefore, to provide reference values for the currents id and I which are responsible for controlling the DC voltage and reactive power control loops must be used.

Equation (12) can be written as:

$$V_{DC}i_{dc} = 3V_{vd}i_d \quad (14)$$

The real part of the modulation index of the inverter corresponding to the d axis is [9]:

$$P_{mr} = \frac{v_{gd} 2\sqrt{2}}{V_{DC}} \qquad (15)$$

From (14) and (15) the relation between the current of the d axes and the DC current is:

$$i_{dc} = \frac{3}{2\sqrt{2}} P_m i_d \qquad (16)$$

The variation of the DC voltage is given by the voltage droop VD on the capacitor from the DC side of the converter:

$$\frac{dV_{DC}}{dt} = \frac{1}{C}(I_D - i_{dc}) \qquad (17)$$

If it is assumed that the DC voltage is constant, the voltage on the capacitor is zero and $I_D = i_{dc}$.

By using this assumption in (16) and (17) the DC voltage can be written as:

$$V_{DC} = \frac{1}{C}\int (I_D - \frac{3P_m i_d}{2\sqrt{2}})dt \qquad (18)$$

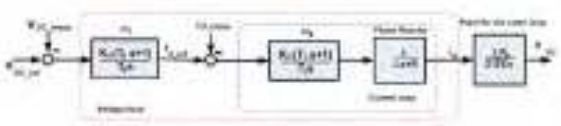

Fig. 9. *Outer loop and inner loop controllers of the receiving end station*

The fast current controllers used for obtaining the id and iq currents are complemented with additionally controllers that output the reference values needed for the voltage controller and reactive power. Therefore the current controllers represent the inner controller and the outer controllers are the DC voltage and reactive power controllers. The control scheme for the DC voltage is described in Figure 9. The control loops for d and q axes are the same, resulting in design of identical PIs for each loop.

4. Simulation results

Different study cases were performed in order to verify and illustrate the performance of the control system for the entire structure of a small offshore wind farm connected to a HVDC line transmission system.

4.1. Study Case 1 - Voltage/Hertz Controller

The purpose of this simulation is to test the efficiency of the voltage/frequency controller implemented for the generator side converters.

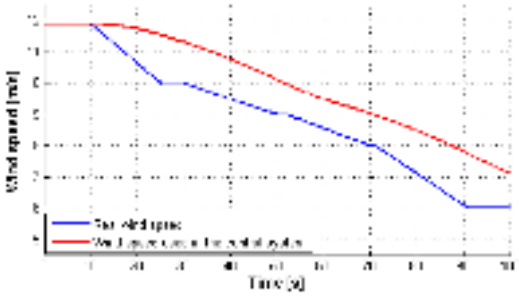

Fig. 10*. Wind profile for V/F controller*

The wind profile applied for this study case may be seen in Figure 10. For testing the controller, the averaged wind speed is computed by a moving average filter (green signal).

The moving average function is used to smooth out short term fluctuations. Having set the wind speed, two tests are made for analyzing the power generation: with and without V/f control

When the wind speed starts to have values below 11,9m/s, the frequency is adjusted in order to maximize the WT's power output.

Figure 11 presents the active power production of the induction generator. In blue is presented the power outputted by the WT without enabling the V/f control algorithm on the generator side converter. By activating the controller, the generation of active power (in red) is maximized by modifying the voltage and frequency setpoints.

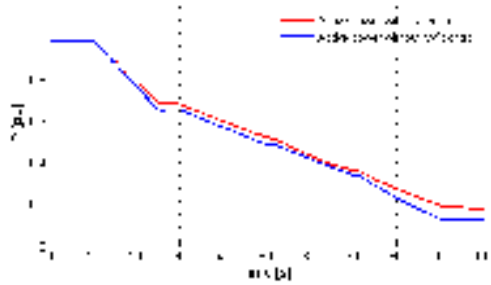

Fig.11. *Generator's active power with and without V/F control*

Comparing the results shown in Figure 11 it can be concluded that the power production with V/f control is higher than without it.

From Figure 11 the gain in active power can be obtained.

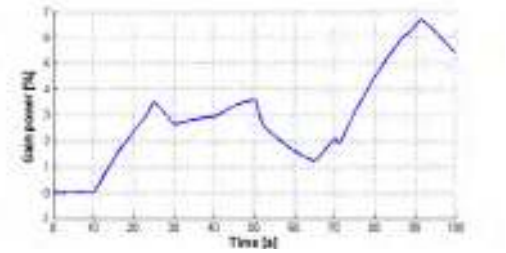

Fig. 12*. Active power gain*

In the first time interval when the wind is kept constant to the rated value, the gain is zero because no control is active. When the wind speed drops the V/f controller starts actuating. Figure 12 highlights the gain in the power production by activating the voltage/frequency control for wind speeds within the interval [$v_{cut\text{-}in}$; v_{rated}].

The generator side converter proved its use in operation control for different wind speeds situations.

4.2. Study Case 2 - Pitch Controller

To test that the wind farm operates correctly, the power production of the WTs is analyzed. After designing the parameters of the PI for the pitch controller loop, the WF must be able to limit the power output as the wind speed increases over the rated value. The testing will be made using the real wind profile provided by the wind model of each WT. The simulations are run for 100 seconds.

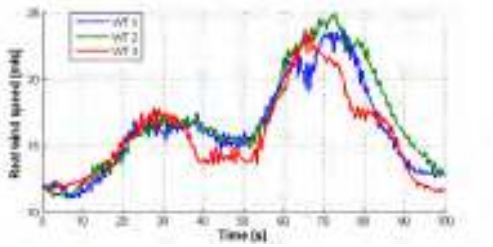

***Fig 13**. Wind speed profile*

The average wind speeds vary from the rated value 11,9m/s until they reach 23m/s. Based on the average wind, the wind profiles outputted by the wind model are obtained. They are depicted in Figure 13. It can be seen that the three winds start

to rise until they reach 23m/s and then drop to the rated value.

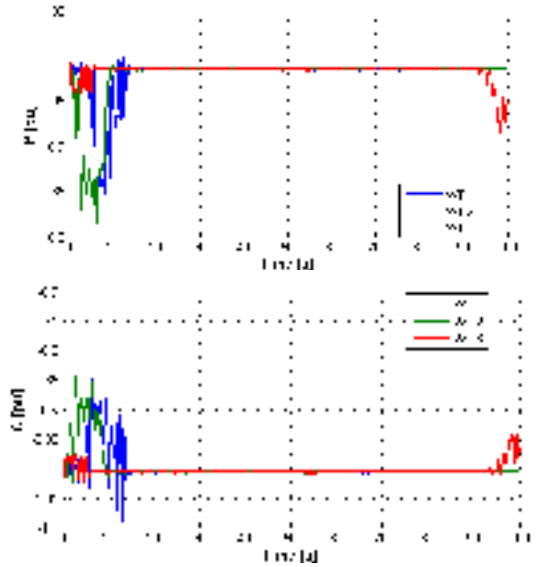

***Fig. 14.** Active and reactive power regulation*

By activating the pitch control, the blades start to be pitched in and out of the wind in order to keep constant the power.

The pitch angle variations should be directly proportional with the wind.

In the first time interval the wind speed is at the rated value, the pitch controller is inactive - thus, the pitch angle is maintained to zero in order to obtain the rated power value.

When the wind becomes greater than v_{rated}, the blade control angle is varying in such a way that it holds the powers to the nominal value (see Figure 14).

As it can be observed the active and reactive power limitation is achieved.

4.3. Study Case 3-Active Power Sharing

This study case deals with the analysis of the power sharing between the two grids. The simulations are based on the control algorithm investigated in [3]. The simulation conditions are:

- One WF and two grids situated at different distances are connected through the MTDC (GRID A 10 km from the offshore WF and GRID B 30 km from the offshore WF);

- The wind farm is functioning at the rated parameters.

Some simulations are performed with constant output power from the wind farm in order to analyze the DC voltage level fluctuations of the inverters of each of the grids depending on their power demands. Another set of simulations are made with a variable output power from the WF, to present a realistic behaviour of the MTDC system where the power generated by the WF is varying function of the wind speed.

- For all the simulations is considered that GRID A TSO settles the active power request. GRID B is adjusting its power consumption function of GRID A, meaning that is taking the excess of power from the WF or it is generating extra power for the GRID A in order for the active power demand to be accomplished. Figure 15 shows the active power request of GRID A that was considered. In all the simulation time the active power request varies from 100% to 10% from the total active power generated by the WF.

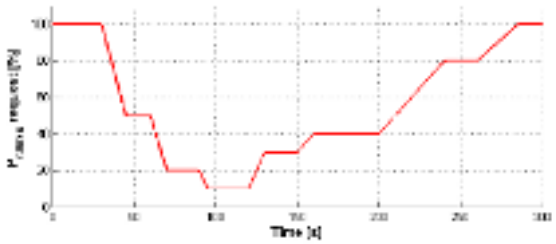

***Fig. 15**. Active power request from GRID A TSO*

First it is considered the functioning of the wind turbines at nominal parameters and at constant wind speed conditions.

Thus the WF output active power is kept constant to its rated value of 0.8 pu.

Two cases were taking into account function of the two grids:

1. GRID A and GRID B are identical;

2. GRID B is stronger than GRID A having the short circuit power ten times greater;

By sending the power demand of GRID A shown in Figure 15 to the MTDC controller, the DC voltage reference points VDCA and VDCB of the grid side inverters are set. Both DC voltage levels follow an inverse proportionality dependence according to the active power consumptions as presented in Figure 16. Also the variation in DC voltage is proportional with the distance between the WF and the receiving end.

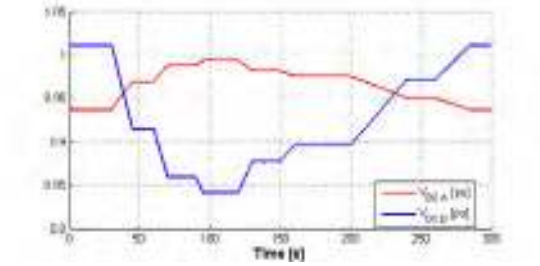

Fig. 16. *DC voltage set points for Converter$_{GRIDA}$ and Converter$_{GRIDB}$*

Converter$_{GRIDA}$ which is closer to the WF's PCC has smaller variations comparing to Converter$_{GRIDB}$. The DC voltage level has to be maintained in _5% limits of the rated value [10]. The maximum deviation of the DC voltage from the acceptable limit is recorded when GRID A demands only 10% of the total power. MTDC controller is sending to Converter$_{GRIDB}$ a reference value for the DC voltage that is lower than the the allowed limit, in order to fulfil the power sharing.

Therefore an additional control method has to be implemented in order to maintain the variations of the DC voltages in the allowed limits. One of the solution would be for the MTDC controller to be able to vary the DC voltage in the PCC of the WF in order to obtain smaller variations at the inverters terminals.

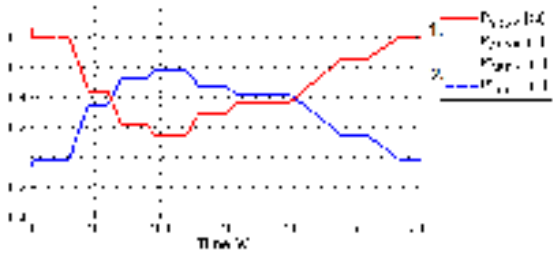

Fig.17*. Active power sharing between GRID A and GRID B in Case 1 and Case 2*

By knowing the DC voltage setpoints according to the power request of GRID A, the power sharing that was obtained between the two grids is shown in Figure 17. The power injected into the networks has the same variation in both cases.

Also no notifiable change exist between the two cases when the short circuit power of the grids is different.

The power sharing for GRID A follows the active power request from Figure 15. A small error exists between the imposed value for requested power and the one that is obtained as shown in 18 for GRID A. The maximum error is 6.5% and it occurs for the smallest power demand 10%. By looking at the error for all the MTDC system in Figure (b), the error is 11% for the same 10% value of power request from GRID A.

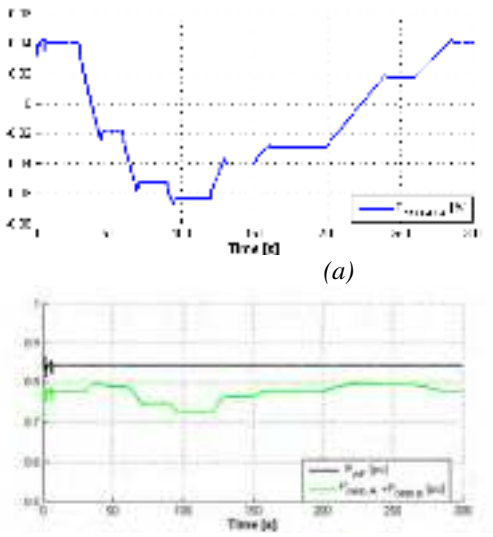

(a)

(b)

Fig. 18*. Power sharing error for (a) GRID A and (b) MTDC system*

These errors can be justified by the losses that exist in the system besides the losses from the DC cables. This difference in power is due to the power losses on the phase reactors and converters. For the power sharing algorithm based on steady state analysis only the losses of the DC cables were taken into consideration.

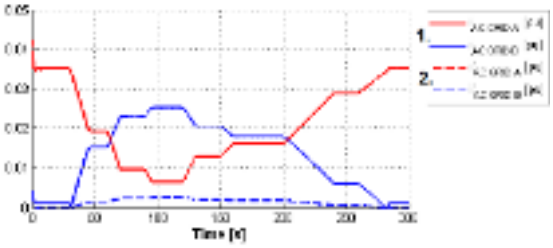

Fig. 19. *Current injected in GRID A and GRID B*

The different values of short circuit power influence the current injected into to grid and also the voltage and frequency in the PCC. Figure 19 presents the variation of currents injected in GRID A and GRID B for both cases, when the grids have the same short circuit power and when they don't

have the same short circuit power. The currents curves have the same shape as the active power flowing into the grids. It can be also observed that for GRID B, the current variation is smaller in the case of greater short circuit power.

Figure 20 describes the variations in voltage and frequency on the PCC of the two grids. It is shown that the stronger grid has less significant variations in both voltage and frequency in the PCC. The voltage and frequency have the same variation according to the power changing in each grid.

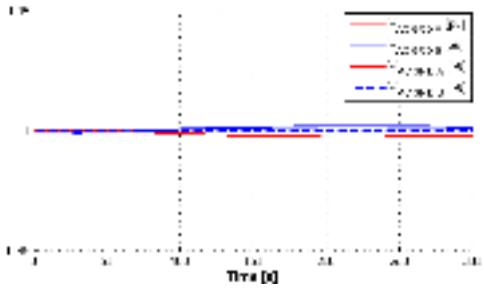

(a)

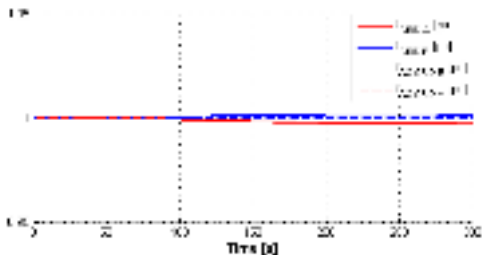

(b)

***Fig. 20**. Voltage (a) and frequency (b) on the busbar of GRID A and GRID B*

4.4. Study Case 4 - Reactive Power Control at the Receiving End Stations

The TSO of each grid is responsible for the control of the reactive power. This control is made independently from one converter to another and also from the WF controller.

Limitations are applied to the operating conditions in reactive power regulation due to the VSC operation parameters. Based on [5] the limits of the reactive power consumption and generators are considered to be between -0.5 and 0.5 pu, where the base value is the active power. Simulation conditions: the output power of the wind farm is constant and the active power regulation for GRID A and GRID B follows the curves from Figure 21.

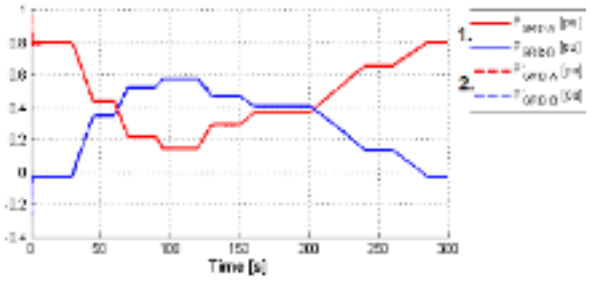

***Fig. 21.** Active power sharing between GRID A and GRID B in Case 1 and Case 2*

During the simulation time different values for reactive power demand were chosen, as shown in Figure 22. Q_{TSOA} and Q_{TSOB} represent the TSO's references for reactive power. A positive value of reactive power indicates reactive power generation into the PCC while a negative value corresponds to reactive power consumption from the grid. Figure 22 demonstrates that the reactive power obtained in the PCC of each grid follows the TSO requirements and that is limited by the operation points of the converters. The TSO has to demand reactive power in the interval [-0:5; +0:5]. In the simulation it was supposed that the grid operator of the GRID B sends the command for 0.7 pu. It can be seen that the inverter manage to limit the reactive power to the minimum limit of -0.5 pu.

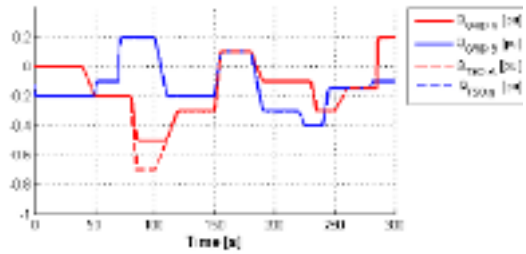

***Fig. 22.**Reactive power regulation in the GRID A and GRID B PCC*

The reactive power flow is the result of changing the voltage amplitude by means of the phase reactors. If the voltage on the grid side is greater than the voltage on the converter side it will result reactive power consumption mode, otherwise the converter will generate reactive power. The next two figures illustrate the relation between the reactive power and the voltage levels in the PCC and at the AC terminal of the converters.

The AC voltage from the converters follows the variations of the reactive power in Figure 23. The simulation results of the voltages in the PCCs of the grids are presented in Figure 24 and show small variations comparing to the converters AC voltages.

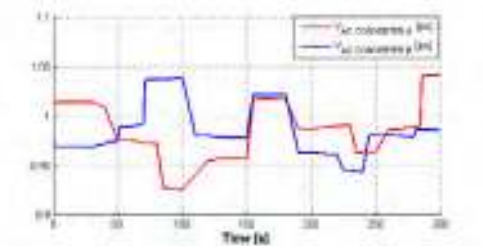

Fig. 23. *AC voltage fluctuations at CONVERTER A and CONVERTER B*

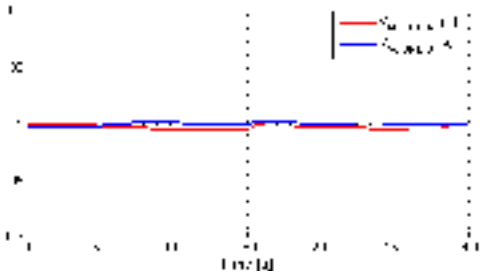

Fig. 24. *Voltage variations in the GRID A and GRID B PCC*

The simulation results conclude that the objectives of the reactive power controller have been accomplished. The main goal was to control independently the reactive power for each grid. The reactive power regulation was performed in real time according to the TSOs request and it complies with the nominal operation of the converter. For a more precise control, the active power through the converter has to be considered and the reactive power control should follow the typical PQ diagram for VSC.

5. Conclusions

The perspective of DC power interchange between three or more terminals has been under active consideration for the last years. This paper presents a proposed three terminal VSC-HVDC model linking two onshore grids and one offshore wind farm. The main focus was on developing the control strategy for connecting these three systems via DC connection. A significant interest was shown not only for the modelling and implementation of the transmission system, the converters and their control, but also on the development of the WF components and their control. All the models have been designed and build in DIgSILENT Power Factory. The major achievement is the assessment of the control method for the 'Multiterminal DC Connection'. This proved to be a feasible solution and could be the solution for futures projects regarding the algorithm, extending it to 'n' number of systems, this might be the answer for the 'Supergrid' project connection of large offshore wind farms with far distances from the land. By improving the control

References

[1]. European Wind Energy Association. *Wind Energy - The Facts.* [cited 5 March 2009]. Available from:ww.ewea.org/leadmin/ewea_documents/documents/publications/WETF/1565_ExSum_ENG.pdf

[2]. Ervin Spahić and Gerd Balzer. *Offshore Wind Farms* - VSC-based HVDC Connection. Power Tech, 2005 IEEE Russia. ISBN: 978-5-93208-034-4

[3]. Adelina Agap and Cristina Madalina Dragan - *Multiterminal DC Connection for Offshore Wind Farm.* Master thesis, Institute of Energy Technology, Aalborg University. Aalborg 2009.

[4]. Florin Iov - *VSC based DC Transmission System for connecting Active Stall Wind Farms to Grid* . Risø Library. Aalborg University 2004.

[5]. Adelina Agap, Adrian Constantin, Cristina Madalina Dragan and Borja Imanol Markinez Iurre - Modelling, *Operation and Control of HVDC* Connected Oshore Wind Farms. Third semester project at Institute of Energy Technology. AAU, 2008.

[6]. S. Douangsyla, P. Indarack, A. Kanthee, M. Kando, S. Kittiratsatcha and V. Kinnares - *Modelling for PWM Voltage Source Converter Controlled Power Transfer*, 2004. International Symposium on Communications and Information Technologies. Sapporo, Japan.

[7]. Temesgen M. Haileselassie, Marta Molinas - *Tore Undeland. Multiterminal VSC-HVDC* System for Integration of Oshore Wind Farms and Green Electrication of Platforms in the North Sea. NORPIE/2008, Nordic Workshop on Power and Industrial Electronics, June 9-11, 2008.

[8]. ABB - *It's time to Connect.* Technical description of HVDC Light® technology. ABB - Grid Systems - HVDC. SE-771 80 Ludvika, Sweden.

[9]. Power Factory - *DIgSILENT G*mbh. PWM Converter - Technical Reference.Power Factory v. 3.2 - Help Manual.

[10]. B. Burger, A. Engel - Fast Signal Conditioning in Single Phase Systems. Institut fürSolare Energieversorgungstechnik (ISET) e. V. EPE 2001.

THE ANNALS OF "DUNAREA DE JOS" UNIVERSITY OF GALATI.
FASCICLE IX. METALLURGY AND MATERIALS SCIENCE
N^0. 2 – 2009, ISSN 1453 – 083X

WASTE MINIMIZATION BY REUSE AND RECYCLING

Daniela L. NEGOITA[1], Ion V. ION[2],
[1]Faculty of Metallurgy and Materials Science
[2]Faculty of Mechanical Engineering
"Dunărea de Jos" University of Galati
email: dana.negoita@gmail.com

ABSTRACT

Recently, pollution prevention directs attention towards the elimination or reduction of undesired by- products within the production process itself before treatment. On the long term, pollution prevention through waste minimization and cleaner production is more cost-effective and environmentally sound than traditional pollution control methods.

The objective of this work was to carry out a feasibility study to define and implement an integrated pollution prevention and control measure in order to minimize waste and therefore to achieve compliance with the Romanian Environmental law.

KEYWORDS: pollution prevention, waste minimization

1. Introduction. Solid wastes

Waste is defined as any losses produced by activities that generate direct or indirect costs but do not add any value to the product from the point of view of the client (Formoso et al., 1999). Symonds Group Ltd, ARGUS, COWI and PRC Bouwcentrum (1999) define waste as any substance or object which the holder intends or is required to discard.

According to the Directive 2008/98/EC of the European Parliament and of the Council of 19 November 2008 on waste and repealing certain Directives:

1. „waste" means any substance or object which the holder discards or intends or is required to discard;

2. „hazardous waste" means waste which displays one or more of the hazardous properties listed in Annex III;

3. „waste oils" means any mineral or synthetic lubrication or industrial oils which have become unfit for the use for which they were originally intended, such as used combustion engine oils and gearbox oils, lubricating oils, oils for turbines and hydraulic oils;

4. „bio-waste" means biodegradable garden and park waste, food and kitchen waste from households, restaurants, caterers and retail premises and comparable waste from food processing plants;

5. „waste producer" means anyone whose activities produce waste (original waste producer) or anyone who carries out pre-processing, mixing or other operations resulting in a change in the nature or composition of this waste;

6. „waste holder" means the waste producer or the natural or legal person who is in possession of the waste;

7. „dealer" means any undertaking which acts in the role of principal to purchase and subsequently sell waste, including such dealers who do not take physical possession of the waste;

8. „broker" means any undertaking arranging the recovery or disposal of waste on behalf of others, including such brokers who do not take physical possession of the waste;

9. „waste management" means the collection, transport, recovery and disposal of waste, including the supervision of such operations and the after-care of disposal sites, and including actions taken as a dealer or broker;

10. „collection" means the gathering of waste, including the preliminary sorting and preliminary storage of waste for the purposes of transport to a waste treatment facility;

11. „separate collection" means the collection where a waste stream is kept separately by type and nature so as to facilitate a specific treatment;

12. „prevention" means measures taken before a substance, material or product has become waste, that reduce:

(a) the quantity of waste, including through the re-use of products or the extension of the life span of products;

(b) the adverse impacts of the generated waste on the environment and human health; or

(c) the content of harmful substances in materials and products;

13. „re-use" means any operation by which products or components that are not waste are used again for the same purpose for which they were conceived;

14. „treatment" means recovery or disposal operations, including preparation prior to recovery or disposal;

15. „recovery" means any operation the principal result of which is waste serving a useful purpose by replacing other materials which would otherwise have been used to fulfill a particular function, or waste being prepared to fulfill that function, in the plant or in the wider economy. Annex II sets out a non-exhaustive list of recovery operations;

16. „preparing for re-use" means checking, cleaning or repairing recovery operations, by which products or components of products that have become waste are prepared so that they can be re-used without any other pre-processing;

17. „recycling" means any recovery operation by which waste materials are reprocessed into products, materials or substances whether for the original or other purposes. It includes the reprocessing of organic material but does not include energy recovery and the reprocessing into materials that are to be used as fuels or for backfilling operations;

18. „regeneration of waste oils" means any recycling operation whereby base oils can be produced by refining waste oils, in particular by removing the contaminants, the oxidation products and the additives contained in such oils;

19. „disposal" means any operation which is not recovery even where the operation has as a secondary consequence the reclamation of substances or energy. Annex I sets out a non-exhaustive list of disposal operations;

20. „best available techniques" means best available techniques as defined in Article 2(11) of Directive 96/61/EC.

2. The waste management hierarchy

Presently, waste management represents one of the most important issues for the sustainable development of all Countries in the world, in particular for the most industrialized ones. UE directed a considerable effort to steer a management strategy which could allow all States to consider waste as a resource, whose recovery can save much raw materials and energy.

A comprehensive knowledge, in a life cycle perspective, of waste management, not only municipal but also deriving from agricultural and industrial activities, is required at all levels, since the problem is closely related to all three dimensions of sustainable development: economical, social, environmental.

There are different ways of waste management in order to minimize risk to public health and the environment. For a long time, waste management was conducted in a divided and relatively unplanned way. Experience has shown that a more sustainable resource use and waste management is required. The step towards the integrated approach to waste management was done in 1962, when this approach has been described as treating the problem as a whole interconnected system operations and functions. Recognizing the complexity of management practices and the acceptance of waste that mathematical modeling and analysis systems are needed to optimize operations management was the fundamental step towards the concept of integrated waste management.

Recognizing that the implementation of integrated management systems must be different from case to case occurred in 1978 when the Environmental Protection Agency in the U.S. stated that "methods of waste management equipment and practices should not be the same throughout the country as long as conditions vary and it is vital that procedures vary to meet". This was the transition from a hierarchical approach to waste management approach which is more flexible in application.

In 1991, a working group of the European Economic Community has published a draft regional strategy for integrated waste management that defines the integrated waste management as a process of changes, where the concept of waste management is gradually expanded to include the possible need to control the flow of gas, liquid and solid materials from the human environment. Thus, the concept of integrated waste management includes all types of waste, the option of using a range of treatment technologies depending on the situation. Also in the same period has developed the concept of sustainable development as "development which aims to present needs without compromising the ability of future generations to meet their needs". The Brundtland Report of the World Commission for Environment and Development (WCED) entitled "Our Common Future" clearly emphasizes that sustainable development can only be achieved if society in general and industry in particular have learned to produce "more from less", more goods and services with fewer resources (including energy) and less pollution and wastes.

The integrated waste management systems combine waste streams, waste collection, methods of treatment and disposal in a waste management system that aims at sustainable development, economic and

social efforts acceptable to any specific region. This is achieved through a combination of options for waste management including waste reduction, reuse, recycling, composting, anaerobic fermentation (biogazification), thermal treatment and landfill (Figure 1). It is vital neither how many options for waste management are used, nor if they are used at the same time but how they are combined in an optimal way as part of an integrated approach. The integrated waste management considers the entire system and finds the best combination of methods to minimize costs and maximize environmental and social benefit.

Fig. 1. *The elements of integrated waste.*

The principles of the integrated waste management are:

• integrated waste management makes it possible that the decisions to be based on the best practices and transparent costs. The lower amount of waste produced the incumbent generators costs of waste are lower. This provides incentives for the users to reduce the amount of waste they generate;

• integrated waste management takes into consideration all options (collection, recycling, composting, anaerobic fermentation, thermal treatment with heat recovery and landfill) for the whole flow of the solid waste;

• dividing responsibilities. Manufacturers, distributors, merchants and consumers have the responsibility to support integrated management of waste. Each group is responsible for properly managing the waste they produce;

• are considered three criteria: the action on the environment, economic efficiency and social acceptability;

• flexible application to different communities and regions;

• transparent costs for waste management;

• recovery and recycling-oriented market;

• continuous evaluation for accommodation to changes in quantity and quality of the waste stream.

Integrated waste management is a concept that has different local applications and which depends on many variables such as composition of the waste flow, infrastructure, markets for recyclable materials, budget, legislation and local availability of land for storage. Integrated Waste Management is seeking the best options for waste management with emphasis on evaluation of all available strategies to provide more sustainable systems.

3. European policies for waste management

Every year, some 2 billion tones of waste - including particularly hazardous waste - are produced in the Member States, and this figure is rising steadily.

Stockpiling waste is not a viable solution and destroying it is unsatisfactory due to the resulting emissions and highly concentrated, polluting residues.

The best solution is, as always, to prevent the production of such waste, reintroducing it into the product cycle by recycling its components where there are ecologically and economically viable methods of doing so.

The EU has a framework for coordinating waste management in the Member States in order to limit the generation of waste and to optimise the organisation of waste treatment and disposal.

The main European legislative instruments are:

• Council Directive 75/439/EEC of 16 June 1975 on the disposal of waste oils;

• Council Directive 78/176/EEC of 20 February 1978 on waste from the titanium dioxide industry;

• Council Directive 82/883/EEC of 3 December 1982 on procedures for the surveillance and monitoring of environments concerned by waste from the titanium dioxide industry;

• Council Directive 86/278/EEC of 12 June 1986 on the protection of the environment, and in particular of the soil, when sewage sludge is used in agriculture;

• Council Directive 91/689/EEC of 12 December 1991 on hazardous waste;

• Council Directive 92/112/EEC of 15 December 1992 on procedures for harmonizing the programmes for the reduction and eventual elimination of pollution caused by waste from the titanium dioxide industry;

• European Parliament and Council Directive 94/62/EC of 20 December 1994 on packaging and packaging waste;

• Council Directive 96/59/EC of 16 September 1996 on the disposal of polychlorinated biphenyls and polychlorinated terphenyls (PCB/PCT);

• Council Directive 1999/31/EC of 26 April 1999 on the landfill of waste;

• 2000/532/EC: Commission Decision of 3 May 2000 replacing Decision 94/3/EC establishing a list of wastes pursuant to Article 1(a) of Council Directive 75/442/EEC on waste and Council Decision 94/904/EC establishing a list of hazardous waste pursuant to Article 1(4) of Council Directive 91/689/EEC on hazardous waste (notified under document number C(2000) 1147) (Text with EEA relevance);

• Directive 2000/53/EC of the European Parliament and of the Council of 18 September 2000 on end-of life vehicles - Commission Statements;

• Directive 2000/59/EC of the European Parliament and of the Council of 27 November 2000 on port reception facilities for ship-generated waste and cargo residues - Commission declaration;

• Directive 2000/76/EC of the European Parliament and of the Council of 4 December 2000 on the incineration of waste;

• Directive 2002/95/EC of the European Parliament and of the Council of 27 January 2003 on the restriction of the use of certain hazardous substances in electrical and electronic equipment;

• Directive 2002/96/EC of the European Parliament and of the Council of 27 January 2003 on waste electrical and electronic equipment (WEEE) - Joint declaration of the European Parliament, the Council and the Commission relating to Article 9;

• Regulation (EC) No 2150/2002 of the European Parliament and of the Council of 25 November 2002 on waste statistics (Text with EEA relevance);

• 2003/33/EC: Council Decision of 19 December 2002 establishing criteria and procedures for the acceptance of waste at landfills pursuant to Article 16 of and Annex II to Directive 1999/31/EC;

• 2005/270/EC: Commission Decision of 22 March 2005 establishing the formats relating to the database system pursuant to Directive 94/62/EC of the European Parliament and of the Council on packaging and packaging waste (notified under document number C(2005) 854) (Text with EEA relevance);

• Commission Regulation (EC) No 1418/2007 of 29 November 2007 concerning the export for recovery of certain waste listed in Annex III or IIIA to Regulation (EC) No 1013/2006 of the European Parliament and of the Council to certain countries to which the OECD Decision on the control of transboundary movements of wastes does not apply (Text with EEA relevance);

• 2008/312/Euratom: Commission Decision of 5 March 2008 establishing the standard document for the supervision and control of shipments of radioactive waste and spent fuel referred to in Council Directive 2006/117/Euratom (notified under document number C(2008) 793);

• Directive 2008/1/EC of the European Parliament and of the Council of 15 January 2008 concerning integrated pollution prevention and control (Codified version) (Text with EEA relevance);

• Commission Regulation (EC) No 669/2008 of 15 July 2008 on completing Annex IC of Regulation (EC) No 1013/2006 of the European Parliament and of the Council on shipments of waste (Text with EEA relevance).

4. Minimization and use of grit waste from surface cleaning operations - Case study

In Romania, as in other countries, the impact of waste on the environment has increased alarmingly in recent years, its inadequate management generating soil and groundwater contamination, as well as emissions of methane, carbon dioxide and toxic gases, with direct effects on health population. Facilities for landfill have reached saturation and finding new ones has become a big problem.

The industrial waste management consists of recovery, storage, landfill or incineration. In Romania the share of these options is approximately the same each year, namely: storage, 81%, 15% recovery, temporary storage 3.3% and incineration 0.7%. Since over 80% of the generated waste is stored, in the years has accumulated a large amount of smaller and powdery wastes. Also, total deposits of industrial waste, at least 50% do not have any arrangement for environmental protection; very few deposits have specific arrangements, but do not meet all the European conditions necessary for the environment protection.

For Romania, waste recycling is a priority strategy for sustainable development for the following reasons:

- natural resources for some raw materials are insufficient or poor. The industrial working of poor

resources are uncompetitive, the import of raw materials can not be done but within the limit allowed by current account balance;

- to complement the resources through waste recycling can be achieved with lower costs as a result of significant saving in energy, water, other materials, labour and significant reductions in pollution and mining waste, compared with extracting useful substances from ore [14].

In Table 1 are presented some benefits of recycling ferrous, nonferrous and non-metallic materials reported to energy consumption and water reduction, pollution and amount of waste reduction.

Table 1. *Advantages of the materials recycling*

Recycled material	Consumption reduction [%]		Pollution reduction [%]		mining waste reduction
	energy	water	air pollution	water pollution	
Steel	47-74	40	85	76	97
Aluminium	90-97	8-10	95	97	10-12
Paper	23-74	58	74	35	-
Glass	4-32	50	20	-	80

Considering that a healthy environment is essential to ensure the prosperity and quality of life and the reality that the costs and damages caused by pollution and climate change are considerable, policies that are promoted in Romania follow the implementation of concept for economical growth by promoting *eco-efficiency* (which also includes waste capitalization by reintroducing them into the economic circuit), by interpretation of high standards for environmental protection and by creating new markets and business opportunities.

Stephan Schmidheiny with the Business Council for Sustainable Development (BCSD) have written the book "*Changing Course"* with the aim to change the perception of industry as being part of the problem of environmental degradation to the reality of its becoming part – a key part – of the solution for sustainability and global development [20].

The book sought to develop a concept that, by marrying environmental and economic improvements, would make a business out of the challenge of sustainability. That concept was *eco-efficiency*. "*Changing Course"* defined eco-efficient companies as those which create ever more useful products and services – in other words, which add more value – while continuously reducing their consumption of resources and their pollution [20].

Eco-efficiency is a management philosophy which encourages business to search for environmental improvements that yield parallel economic benefits. It focuses on business opportunities and allows companies to become more environmentally responsible and more profitable. It fosters innovation and therefore growth and competitiveness.

As defined by the WBCSD: *Eco-efficiency* is achieved by the delivery of competitively-priced goods and services that satisfy human needs and bring quality of life, while progressively reducing ecological impacts and resource intensity throughout the life-cycle to a level at least in line with the earth's estimated carrying capacity. In short, it is concerned with creating more value with less impact [20].

The eco-efficiency is not limited simply to making incremental efficiency improvements in existing practices and habits. It should stimulate creativity and innovation in the search for new ways of doing things.

Eco-efficiency calls for businesses to achieve more value from lower inputs of materials and energy and with reduced emissions. It applies throughout a company – to marketing and product development as much as to manufacturing or distribution. It is concerned with three broad objectives:

- **Reducing the consumption of resources:** This includes minimizing the use of energy, materials, water and land, enhancing recyclability and product durability, and closing material loops;

- **Reducing the impact on nature:** This includes minimizing air emissions, water discharges, waste disposal and the dispersion of toxic substances, as well as fostering the sustainable use of renewable resources;

- **Increasing product or service value:** This means providing more benefits to customers through product functionality, flexibility and modularity, providing additional services and focusing on selling the functional needs that customers actually want. This raises the possibility of the customer receiving the same functional need with fewer materials and less resources.

Eco-efficiency calls for businesses to achieve more value from lower inputs of materials and energy and with reduced emissions. It applies throughout a company, to marketing and product development as much as to manufacturing or distribution.

4.1. Case study

Currently, the naval and metallurgical industry in Romania give considerable amounts of waste resulting from the technological operations of cleaning metal surfaces with various abrasive materials. After several cycles of use in blasting operations, the material used consisting of mixtures of metal shot, grit made of iron or steel and sand loses its abrasive properties, entering into the category of waste. Grit fractions of waste material can be recycled and used in other applications. The grit with spherical form is produced from steel wire cold drawn with average carbon content, or from stainless steel, with several degrees of roundness, according to standards.

These wastes are stored on the ground creating environmental problems. Since there is still not a technology, the recovery of fractions separated from waste material is insignificant. It is therefore necessary to improve the efficiency of separation of metal components, and non-metallic fraction of paint that enriches the material used in the process of cleaning the metal surface. This required a detailed analysis of chemical, physical and granular characteristics of the material separated from the waste so that it can find the fulfilment of specific technical conditions imposed by the applications for materials capitalization.

Compared with the practice and trends manifested in the world, naval and metallurgical industry recorded deficiencies both in the collection, transport and storage of all categories of waste, as well as the technology of recovery by recycling and/or reutilization.

The „Dunarea de Jos" University of Galati conducted in collaboration with university centres with prestigious activity in the field of waste recovery and materials study (Pannon University from Hungary, University of Bologna from Italy) analyses on waste samples. In the cleaning operations of metal surfaces of new or repaired ships are used mixtures of metal shot, grit (made of iron or steel) and natural sand (derived from natural or artificial crushing of rocks).

The researches undertaken by „Dunarea de Jos" University of Galati aim at finding solutions to obtain new products, partial replacement of cement or fine aggregate in concrete or mortar. In looking for ways to use the waste resulting from cleaning process, the proposed solution could be to implement the technology of stabilized mixtures (granular aggregate with binders using treated waste asserted), following the example of Europe. In the study were compared the analysis of chemical composition of analyzed wastes with standard bulletins of classical materials used in the manufacture of cement and of building materials.

This required study of the waste materials with advanced methods of analysis to identify the chemical composition, mineralogical and phase composition at the micro and macrostructure.

Determining the elements of waste material composition was performed using Energy dispersive x-ray spectrometry technique. The energy dispersive X-ray spectroscopy (EDS, EDX or EDXRF) is an analytical technique used for the elemental analysis or chemical characterization of a sample. It relies on the investigation of a sample through interactions between electromagnetic radiation and matter, analyzing x-rays emitted by the matter in response to being hit with charged particles. Its characterization capabilities are due in large part to the fundamental principle that each element has a unique atomic structure allowing x-rays that are characteristic of an element's atomic structure to be identified uniquely from each other.

It is the only characterization technique with simultaneously access in the direct space (through image) and reciprocally (by electron diffraction), able to provide at the same time complementary information on morphology, structure and chemistry both at micrometric scale and localized at atomic or nanometric scale (Figures 2-4).

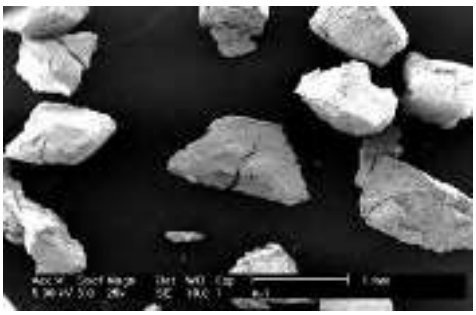

Fig 2. *Overview of unused grit; (Magnification x 25) [13]*

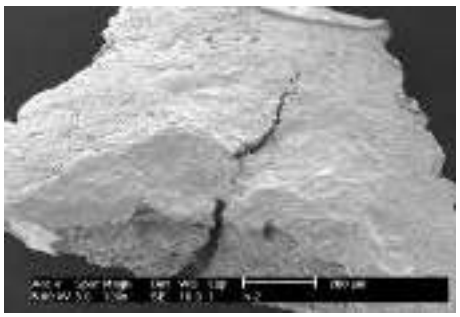

Fig 3. *Single grit particle image (original sample) (Magnification x 100) [13]*

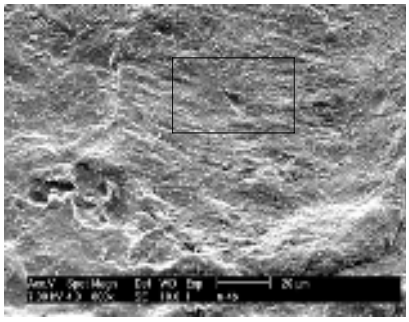

Fig. 4. *The grit particle with the place for chemical analysis (Magnification x 800) [13]*

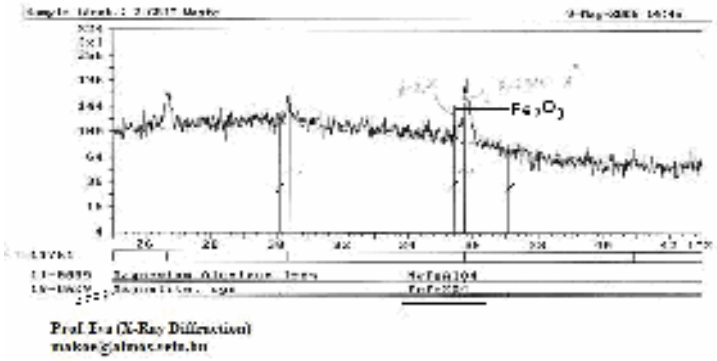

Fig. 5*. X-ray diffraction analysis [13].*

Table 2. *Chemical composition of the waste of Grit and chemical binders for theoretical puzzolanic.*

Material	Element, [%]								
	Mn	**SiO_2**	**S**	**CaO**	**MgO**	**Cr_2O_3**	**Al_2O_3**	**Fe_2O_3**	**P.C.**
Waste grit	0.28	42.78	0.70	6.72	6.36	1.20	7.10	31.17	0.09
Puzzolanic binder	0.39	39.28	-	6.7	6.57	1.20	7.56	38.28	-

The advantage of this method of analysis is that samples are not destroyed in the analysis, X rays fall on the sample surface with the characterization of chemical elements. Samples for quantitative analysis should have polished surfaces and are in the form of pills with a diameter of 40 mm and thickness of 2 mm.

The study put in evidence that the grit composition does not suffer significant deviations from its original one. The composition of analyzed waste is based on Si and iron oxides. Composition is similar to that which is formed to strengthen the hydraulic material. A rough texture, characteristic to aggregates, ensures larger adhesion forces between the granules of aggregate and cement, which is extremely important for concrete roads.

Thermogravimetry (TG) can be defined as the study of weight change function of temperature and time in a given environment. The method is useful in determining the purity of the sample, concentration of water, the carbonates, in general for study of any thermal decomposition reactions. By heating or cooling with constant speed of the material, it can suffer a series of both physical and chemical transformations that can be emphasized by measuring simultaneously the sample mass and temperature thereof. The registered changes in mass lead in some graphical representations called thermograme (Figure 3).

The thermogravimetry studies (TG) were carried out under air current and the isothermal absorption/desorbtion of N_2 were registered with the Micromeritics ASAP 2000.

To study the formed oxides was determined the particle surface area by obtaining the size pores using a surface area and pore size analyzer by gas adsorption (BET) (Figure 5).

By X-ray diffraction were determined the inorganic and organic compounds with crystalline structure, such as the determination of $Si0_2$

concentration in powders and other silicates (zeolite), of various metal oxides, carbonates, sulphates, and some metals.

5. Conclusions and Results

Results interpretation shows that the waste grit has physical and chemical properties similar to the sand used in the composition of road asphalt:

1. an angular grain, less round (influencing the strength of concrete);

2. a silico-alumina composition (compounds are similar to those that formed on the strengthening of building materials, puzzolanic cement, formed mainly from reactive silica and aluminium oxide).

Among the materials used in road construction, waste of grit can be placed on hydraulic/puzzolanic binders, along with sand and furnace slag.

In Table 2 are compared the chemical composition of the proposed recycling grit obtained with the PCA (Principal Components Analysis) with the chemical composition of puzzolanic binders.

References

[1]. Abbas Ghassemi - *Handbook of Pollution Control and Waste Minimization*, Marcel Dekker, Inc., New York, Basel, 2002.

[2]. Cheremisinoff N.P. - *Handbook of solid waste management and waste minimization technologies,* Butterworth-Heinemann, 2003.

[3]. Ebnesajjad S. - *Surface Treatment of Materials for Adhesion Bonding*, William Andrew Publishing, 2006.

[4]. Morselli L., Passarini F., Vassura I. - *Innovation Techologies and Environmental Impacts in Waste Management*, Lectures of the Summer School Rimini, Italy, 12-17 June, 2006.

[5]. Negoiţă D.L. - *Contribuţii la reducerea poluării provocate prin funcţionarea unui şantier naval (Studies on reduction of pollution caused by operation of a shipyard)*, PhD thesis, "Dunărea de Jos" University of Galaţi, 2007.

[6]. Nicolae M., et al. - *Dezvoltare durabilă în siderurgie prin valorificarea materialelor secundare (Sustainable development in ferrous metallurgy by capitalization of secondary materials)*, Printech, Bucuresti, 2004.

[7]. Woodard F. - *Industrial Waste Treatment Handbook,* Butterworth–Heinemann, 2001.

[8]. **** Best pollution prevention practices for abrasive blast media waste from shipyard repair activities,* in Best Management Practices Manual for the Shipbuilding and Repair industry, The Commonwealth of Virginia State Water Control Board.

[9]. **** Road and paving management technologies*, ASTM., vol.04.03.

[10]. **** Eco-efficiency- creating more value with less impact,* World Business Council for Sustainable Development, http://www.wbcsd.org.

THE ANNALS OF "DUNAREA DE JOS" UNIVERSITY OF GALATI.
FASCICLE IX. METALLURGY AND MATERIALS SCIENCE
N^0. 2 – 2009, ISSN 1453 – 083X

INFLUENCE OF pH GALVANIC BATHS ON THE NICKEL DEPOSITS

Maria POROCH – SERIŢAN, Gheorghe GUTT, Traian SEVERIN, Maria BOBU
"Ştefan cel Mare" University of Suceava,
email: mariap@usv.ro, g.gutt@usv.ro

ABSTRACT

The influence of pH on cathodic and anodic current efficiency, surface quality and morphology of nickel deposit in the electrolyte solutions of the Watts bath type was investigated. Cathodic current efficiency of nickel deposit is maximum for electrolytic bath whose pH value is about 4 and decreases for an electrolytic bath with a higher pH. The deposited thickness is a significant parameter because the thickness determining may establish if the deposition corresponds to the destination application deposition or not; and the measurements were made by non-destructive physical methods. The properties of nickel deposits, brightness and hardness are influenced by the pH of the bath electrolyte. The surface morphology of nickel deposit was analyzed by scanning electronic microscopy (SEM). The results showed that the structure of nickel deposits is influenced by pH of the bath. The pH increasing causes structural changes on the deposits in fine to coarse, while the electrodeposited nickel at pH 6.21 has a compact morphology with many cracks.

KEYWORDS: nickel electrodeposition, Watts bath, pH, qualitative and quantitative parameters

1. Introduction

Galvanic deposition of nickel improves a range of surface properties and size characteristics of metal or alloy support such as: corrosion and wear resistance, mechanical strength, magnetic permeability, appearance and other properties [1].

Deposits Properties and quantitative aspects of galvanic process is influenced by technological parameters such as: current density, temperature, pH, cathode or solution agitation for application, deposition time, s.a. [2].

The paper presents the effect of bath pH over the cathodic and anodic current efficiency, quality surface and morphology of nickel deposit in electrolyte solutions from bath Watts type.

2. Experimental details

2.1. Apparatus and materials

Nickel electrodeposition was carried out in a rectangular cell of size 13.9 cm x 12.5 cm x 10 cm made from Plexiglas, which corresponds to a volume of 1.75 l. The cathode [made by 99.98% purity copper, having the following dimensions (h x L x l): 8.0 cm x 9.8 cm x 0.1 cm] and the anode [made by 99.7% purity nickel, having the following dimensions (h x L x l): 10.0 cm x 4.0 cm x 0.3 cm] which fitted cell electrolysis was fixed so that cathode surface immersed in the electrolyte must be 0.6 dm^2, and the anode 0.25 dm^2, thus resulting a rate of cathode-anode rate by 2.4.

The cathode surface was prepared in advance for each electrodeposition experiment, according to the literature procedure [3].

2.2. Reagents

The nickel electrolyte of Watts bath type [4], with composition shown in Table 1 was prepared from following reagents (nickel sulphate, nickel chloride and boric acid) (INDUSTRIALCHIM, Bucharest). All solutions were prepared with bidistilate water. To adjust the pH of the electrolyte to the following study values (3.78, 5.00, 6.21) a solution of sodium hydroxide (NaOH) 0.1 N was used.

2.3. Electrolysis

All the electrodeposition experiments were carried out at a current density of 3.333 A dm^{-2} by applying current from a from a regulated power supplier (0 - 18 V, 0 - 10 A, d.c. power supply

GWINSTEK GPR-1810HD), for 20 minutes at a temperature of 30°C. A thermostatic water bath (Lauda E100) was used for maintaining invariable of electrolyte temperature. The pH of the electrolytes, before starting each experiment with a digital pH meter (Cole Parmer) was measured. After electrolysis, the cathode and anode were removed from the cells and thoroughly washed with water and dried. The cathodic and anodic respectively current efficiency were calculated from mass differences of the probes, before and after deposition ($\eta = m_p / m_t$). Where m_p is the obtained mass of the practical deposit and m_t is the theoretical mass of the deposit, what is determined by Faraday's law.

Table 1. *The chemical composition of Watts electrolytic bath for nickel electroplating*

Chemical composition	Quantity (g/L)
Nickel chloride, $NiCl_2 \cdot 6H_2O$	40.5
Nickel sulfate, $NiSO_4 \cdot 6H_2O$	292.5
Boric acid, H_3BO_3	31.5

2.4. Deposit examination

The average thickness of metallic layer, [μm], was calculated taking into consideration 7 local values of cathode thickness after electrodeposition, as against the standard comparison thickness. The measurements of the above mentioned thickness were carried out using a PosiTector 6000 - DeFesko Analyzer, based on non-destructive physical method.

The brightness of metallic cover, [%], was carried out using the HR 4000 CG-UV-NIR, Ocean Optics Inc., Dunedin, FL, a miniature spectrometer, based on reflection property of the electrodeposed metallic layer. A tungsten halogen light source (UV-VIS-NIR Light Source DH-2000, Mikropack) was used for this study. The light from Light Source DH-2000 was conveyed to the sample through an optical fibre (QP400-0.25-SR/BX, Ocean Optics Inc., Dunedin, FL) and an array of 7 optical fibres (QR400-7-SR-BX, Ocean Optics Inc., Dunedin, FL).

The hardness of metallic cover, [HV], was carried out using a Shimadzu, HMV – 2T, micro-hardness analyzer, having the loading weight F = 490.3 mN (HV - 0.05) and load duration of 15 s respectively.

The deposit surface morphology was examined by scanning electronic microscopy (SEM) using a Tescan microscope.

3. Results and discussion

The hydrogen ions concentration (pH) in the electrolyte has an important role over the metal ions deposit and formation of deposits; and it is closely related to the position, in the potential series, of the metal which is deposited [3].

The more negative the standard electrode potential, the more difficult it is to deposit the indicated metal. Reactions that have a more negative standard electrode potential than hydrogen $\left(2H^+ + 2e^- \rightarrow H_2\right)$ deposit with evolution of hydrogen as a side reaction. Electrodeposition of most of the non-noble metals such as Ni, Fe, Co and Zn are accompanied by hydrogen evolution and often their electrodepositions not achieved with a current efficiency of 100%. Normally a percentage of total current is used to evolution hydrogen [5], [6], [7].

Typical reactions which may take place during the deposition of metals having a negative standard electrode potential are as follows:

$M^{+n} + ne^- \Leftrightarrow M$ Metal deposition (1)

$2H^+ + 2e^- \Leftrightarrow H_2$ Hydrogen evolution (2)

$2H_2O + 2e^- \Leftrightarrow H_2 + 2OH^-$ Water decomposition (3)

$xM^{+n} + yH_2O \Leftrightarrow M_x(OH)_y^{(xn-y)+} + yH^+$

Hydrolysis of metal ion (4)

$xM_x(OH)_y^{(xn-y)+} + (xn-y)H_2O \Leftrightarrow xM(OH)_n + (xn-y)H^+$

Precipitation of hydroxide (5)

Electrochemical reactions (2) and (3) tend to consume H^+ or generate OH^-. Hence, when they take place at the cathode, the pH of the cathode will increase. Reactions (4) and (5) tend to produce H^+ and will counteract the pH rise at the cathode produced by reactions (2) and (3). When the pH near the surface becomes such that hydrolysis and precipitation reactions occur, any further pH rise will be slowed by reactions (4) and (5). If the hydrolysis reaction (4) is not able to slow the pH rise, the deposit may contain hydroxide inclusions because of reaction (5).

3.1. Cathodic and anodic current efficiency

In Figure 1 the cathodic and anodic current efficiency at different pH values of nickel plating baths are shown. It is clearly observed that the cathodic current efficiency of nickel deposit is maximum for electrolytic bath whose pH value is 3.78 and for electrolytic bath pH of 5 and 6.21 it decreases.

The anodic current efficiency of nickel dissolution in electrolytic bath presenting chloride ion concentration, c_{Cl^-} = 12.0972 g/l, is 100% at pH 3.78. The anodic current efficiency of nickel dissolution at higher pH (5.00; 6.21) and at the same concentration of chloride ions, c_{Cl^-} = 12.0972 g/l decreases.

This finding means that the reactions of discharge hydroxyl ions, (OH^-), and the oxygen evolution are preferable to the dissolution process of nickel, when the solution pH is too high and / or the chloride ion concentration too [4]. Nickel anode becomes passive and the efficiency of dissolution of the anode decreases to reach near zero.

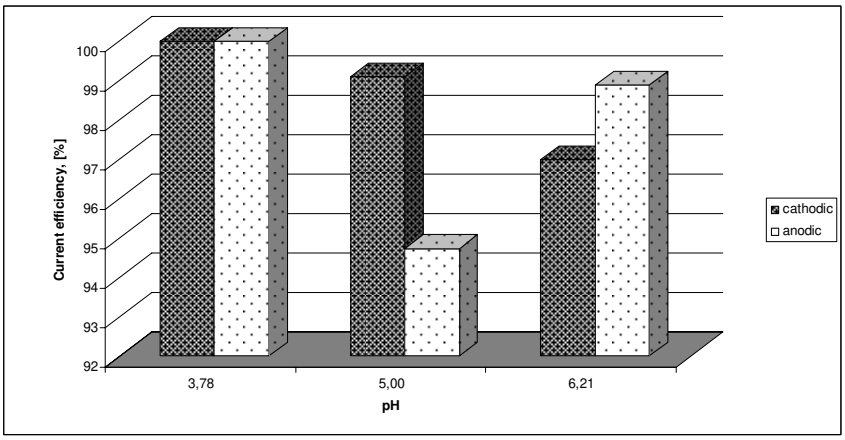

Fig. 1. *Influence of pH over cathodic and anodic current efficiency for nickel deposit on copper substrate*

3.2. Thickness of nickel electrodeposited

The measurement of the thickness of layers may determine whether the submission meets the destination application submission or not, since thickness deposit is a crucial parameter for assessing the quality of electrodeposition in order to ensure resistance galvanic coatings in different environments and climates [8], [9]. According to the values represented in Figure 2, the thickness of nickel electrodeposited in galvanic baths at pH 3.78 and 5.00 respectively are comparable.

The largest thickness was obtained for nickel plating bath pH of 6.21; but it should be noted that this layer is pulverous, brittle, with low adhesion to the substrate.

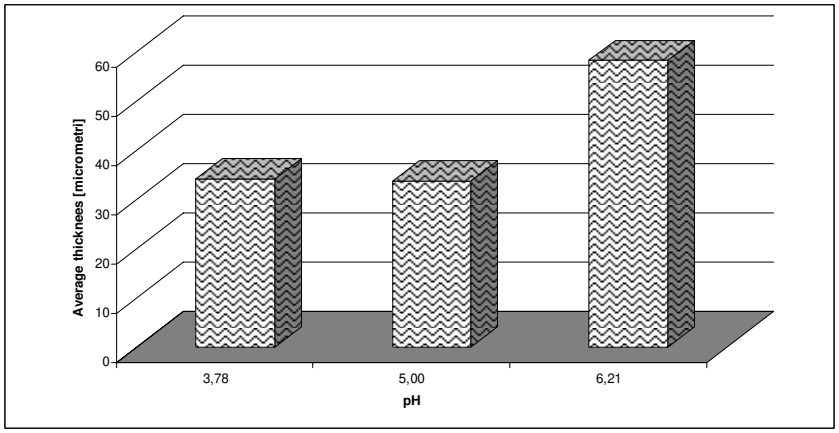

Fig. 2. *The pH influence over thickness of nickel deposit on copper substrate*

3.3. The brightness nickel coatings

The reflecting properties of the deposit is determines the degree of brightness, which defines quality decorative coatings. The reflection was done as a relative percent ($\%R_\lambda$) from the reflection of standard reference substance STAN-SSH (STAN-SSH High-reflectivity Specular Reflectance Standard, Ocean Optics Inc.), according to the equation (6):

$$\%R_\lambda = \frac{S_\lambda - D_\lambda}{R_\lambda - D_\lambda} \cdot 100\% \quad (6)$$

Where:

- S_λ - the intensity of sample at λ wavelength,
- D_λ - the black intensity of sample at λ wavelength,
- R_λ - the intensity of standard reference substance at λ wavelength.

The reflections measurements were carried out at the wavelengths, where the visual sensibility is maximum: 420 nm (blue), 534 nm (green) and 564 nm (red) [10], taking into consideration 3 points from the electrode surface.

The brightness value of metallic cover corresponding to the graphic representation is the average of these 9 reflection values (Figure 3).

The highest value of reflecting property of the nickel deposit was obtained at bath pH 3.78; and the lowest (matt deposition) have a deposit obtained from bath pH 5.00. Nickel deposit in electrolyte with pH of 6.21 was a higher brightness than the deposit from bath pH of 5.00, but because the nickel deposit obtained from electrolyte with pH 6.21 is pulverous with many cracks (Figure 5), we can say that the value of the reflecting property contributes and brightness substrate.

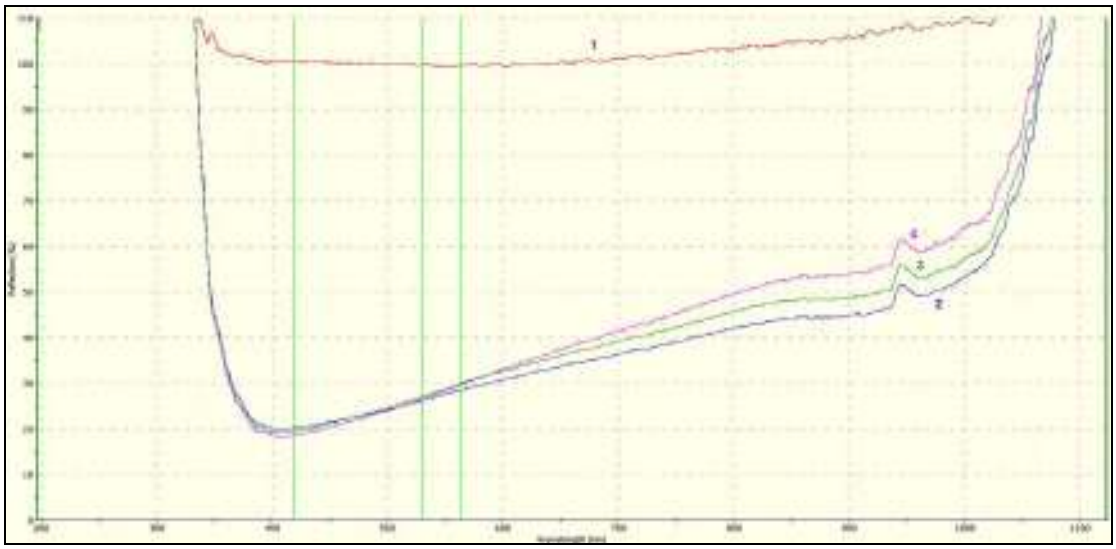

Fig. 3. *The reflection as function of wavelengths for: 1 - standard reference substance STAN-SSH, 2, 3, 4 - nickel deposit from pH 3.78 on copper substrate in 3 points of the electrode surface*

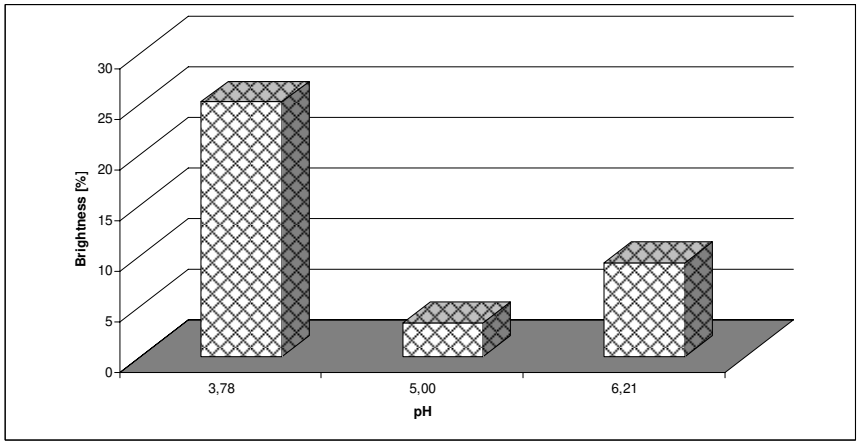

Fig. 4. *The pH influence over brightness of nickel deposit on copper substrate*

3.4. Electrodepositions hardness of nickel

The study results on the effect of electrolytes pH over the hardness of nickel deposits from Watts type bath is presented in Figure 4. the hardness obtained for layers deposited in an electrolytic baths pH of 3.78 and 5.00 respectively are comparable; while the layer of nickel electrodeposited in bath pH of 6.21 has a hardness around 500 HV [11], [12]. The nickel coating is about twice as hard, and this high hardness,

were assigned according to some authors, the formation of basic compounds in the cathode film [3] or by others, increases the amount of hydrogen included in the deposit [13].

Indentation hardness in electrodeposited Ni films obtained from electrolyte with pH 6.21 is shown in Figure 5, and also can be observed many cracks in the layer.

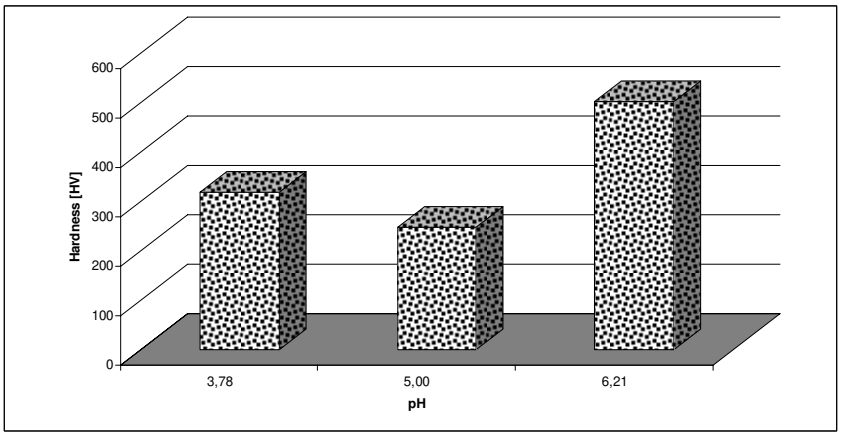

Fig. 4. *The pH influence over hardness of nickel deposit on copper substrate*

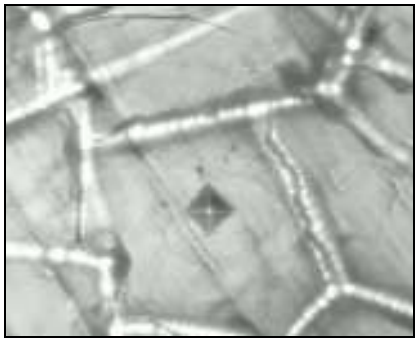

Fig. 5. *Indentation hardness in electrodeposited Ni films on Cu substrate at i = 3.333 (A/dm^2), T = 30 ºC and pH = 6.21*

3.5. Surface morphology

The deposits obtained from electrolyte baths whit pH of 3.78 and 5.00 respectively are adherent to the substrate, smooth, compact and coherent at examination with the naked eye; while nickel layer electrodeposition in bath pH of 6.21 is not compact, it has numerous cracks and gently exfoliating. In Figure 6a are present the morphology surface of nickel deposits obtained by scanning electron microscopy. The surface morphology of the deposit showed a smooth surface like the accumulation of fine spherical deposits (Figure 6 a) in case a bath pH value of 3.78. If can be seen, the entire surface of the deposit, growing crystals surrounded by smaller crystals uniformly distributed [14]. The deposit obtained at pH 6.21 has a compact morphology with many cracks (Figure 6 b).

4. Conclusions

1. The cathodic current efficiency is maximum for electrolytic bath whose pH value is about 4 and decreases for an electrolytic bath with a higher pH.

2. Properties of nickel deposits, brightness and hardness are influenced by the pH of the bath electrolyte.

3. Surface morphology of nickel deposit was analyzed by scanning electronic microscopy (SEM). Results showed that the structure of nickel deposits is dependent on bath pH. The increasing pH causes deposits structural changes from fine to coarse; while nickel electrodeposited at pH 6.21 has a compact morphology with many cracks.

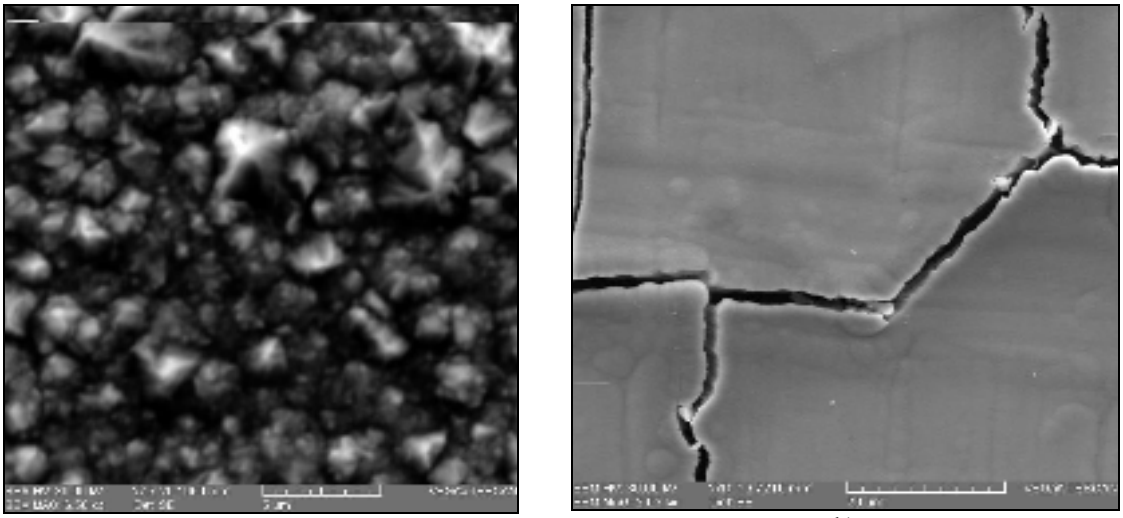

a) b)

Fig. 6. *Surface morphology of nickel deposit obtained from electrolytic baths with pH: a) 3,78; b) 6.21*

References

[1]. Oriňáková R, Turoňová A., Kladeková D., Gálová M., Smith R. M. - *Recent developments in the electrodeposition of nickel and some nickel-based alloys,* Journal of Applied Electrochemistry, (2006) **36**:957–972

[2]. Marinescu A., Andonianţ Gh., Bay E. - *Tehnologii electrochimice şi chimice de protecţie a materialelor metalice,* Editura Tehnică, Bucureşti, 1984;

[3]. Oniciu, L., Grűnwald, E. - *Galvanotehnica*, Editura Ştiinţifică şi Enciclopedică, Bucureşti, 1980

[4]. di Bari G. - *Modern Electroplating*, Fourth Edition, Edited by Mordechay Schlesinger and Milan Paunovic © 2000 John Wiley & Sons. Inc, New York, 2000

[5]. Deligianni H., L. Romankiw T. - I*n situ surface pH measurement during electrolysis using a rotating pH electrode, IBM* J. Res. Develop., 37, 2, 1993

[6]. Ji J., Cooper W.C., Dreisinger D.B., Peters E. - *Surface pH measurements during nickel electrodeposition*. Journal of Applied Electrochemistry (1995), **25** (7), 642–650.

[7]. Vasilache V., M Poroch – Seriţan M., Gutt Gh. - *Contributions on elaboration of a material balance, an energetic balance and an optimization way for nickel cover process*, Conferinţa Ştiinţifică UgalMat 2007, vol. II, 383 - 388

[8]. di Bari G. A. - *International Nickel Inc.,* Saddle Brook, N.J.; www.inco.com, electroplating solutions, Nickel Plating, Metal Finishing, Volume 98, Issue 1, Ianuary 2000, p. 270 - 288, wwwscience direct.com

[9]. Rose I., Whittington C. - *Nickel Plating Handbook,* OMG Finland Oy, 2002, nickel.sales@omgi.com, www.omgi.com;

[10]. http://ro.wikipedia.org/wiki/Culoare

[11]. Doi T., MizumotoK., Tanaka S., Yamashita T. - *Bright Nickel Plating from Nickel Citrate Electroplating Baths*, Metal Finishing, 2004, 26 - 35

[12]. Doi T., MizumotoK., Tanaka S., Yamashita T. - *Effect of Bath pH on Nickel Citrate Electroplating Bath*, Metal Finishing, 2004, 104 – 111

[13]. Firoiu C. - *Tehnologia proceselor electrochimice*, Editura Didactică şi Pedagogică, Bucureşti, 1983

[14]. LI Chao-qun, LI Xin-hai, WANG Zhi-xin, GUO Hua-jun - *Nickel electrodeposition from novel citrate bath*, Trans. Nonferrous Met. SOC. China, **17** (2007) 1300-1 306, www.csu.edu.cnlysxb.

THE ANNALS OF "DUNAREA DE JOS" UNIVERSITY OF GALATI.
FASCICLE IX. METALLURGY AND MATERIALS SCIENCE
N^0. 2 – 2009, ISSN 1453 – 083X

CORROSION BEHAVIOUR OF TOMBAC USED IN CULT OBJECTS MANUFACTURING

P. HAGIOGLU[1], C. GHEORGHIES[3], A.M. CANTARAGIU[1], R. BOICIUC[2], N. TIGAU[3]

[1]Faculty of Mechanics, "Dunarea de Jos" University of Galati
[2]Arcelor Mittal Company of Galati
[3]Department of Physics, Faculty of Science, "Dunarea de Jos" University of Galati
email: petricah@yahoo.com

Corrosion of metals and metallic alloys is due to their thermodynamic instability in relation to their oxidation form. Corrosion tests performed in this work simulate the exposure conditions in different environments of yellow tombac (brass containing 10-20% Zn). The aim of corrosion test in humid heat is to determine the behaviour of surface samples compared to their durability at high relative humidity conditions. Following the accelerated corrosion test in salt fog chamber, higher rates corrosion for tombac comparative with the corrosion test in continue humid heat are distinguished. Tombac samples show a good corrosion resistance as against aggressive environmental conditions which are tested. Surface morphology of treated samples in both corrosion tests was examined using the scanning electron microscopy. Again, the crystalline structure of metallic samples was analysed using the X-ray diffractometer. Also, the optical properties of tombac were analysed studying the reflectance spectra.

KEYWORDS: Tombac, Accelerated Corrosion, Structure

1. Introduction

Corrosion process represents the partial or total destruction of metallic materials due to chemical and electrochemical reactions occurred through interaction with environmental factors [1-3].

The nature and structure of metallic phase, the chemical composition of the aggressive environment and the conditions for carrying out a certain technological process have a decisive influence on the corrosion form and deterioration capacity of metallic materials [2-4].

The metals and metallic alloys corrosion is due to their thermodynamic instability as a function of their oxidation form [5-7].

2. Materials and methods

2.1. Preparation of tombac

The accelerated corrosion tests (in continue humid heat and salt fog chamber), performed in this work, simulate the exposure conditions of tombac in the presence of various corrosion environmental factors [7].

The corrosion chamber (Fig. 1) is provided with an automated system for the temperature measurement and adjustment, for the waste solution or condense exhaustion resulted during the experiment. The chamber, made of plastic material and stainless steel, has a capacity of 0.35 m^3. The upper side of the chamber was conceived so that the accumulated drops of solution which flow to the surface do not fall down on the tested objects.

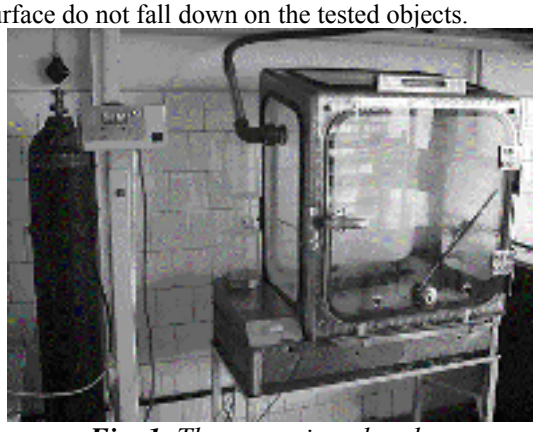

Fig. 1. *The corrosion chamber*

The aim of corrosion test in continuous humid heat is to determine the corrosion behaviour of samples subjected to high relative humidity conditions. In the corrosion chamber the temperature was kept at 40±2 °C and the relative humidity was

kept at 93±3%. The corrosion test was performed during a 96 h period of time. Initially, the samples were degreased with acetone, weighed using an analytical balance with an accuracy of 0.01 mg. At the end of the test, the samples were subjected to the normal atmospheric conditions for a period return of 1-2 h by quickly transferring of them in another room (maximum 5 min). Then the samples were washed with distilled water and acetone, dried and again weighed using the analytical balance. Finally, the mass loss and the corrosion rate were calculated on the basis of the relationship (1):

$$V_c = S \cdot t \cdot \rho \cdot \Delta m \cdot 10^7 \quad (1)$$

where: V_c is the corrosion rate [nm/h];

Δm is the mass difference between initial and final weight of the sample [g];

S is the sample area [cm^2];

ρ is the specific density [g/cm^2]; ρ = 8.2 (tombac);

t is the working time [h].

The specific results are presented in Table 1.

To carry out the accelerated corrosion test in the salt fog chamber, a NaCl solution was prepared. An amount of NaCl was dissolved in distilled water, whose conductivity is less than equal to 20 μScm^{-2}, at 25±2 °C temperature to obtain a final solution with 50±5 g/l concentration. The relative density of the obtained solution ranged between 1.00255 and 1.0400. The amount of NaCl used contains less than 0001% Cu and 0.001% Ni. Also, the content of NaI must not exceed 0.1% and the total content of impurities must be maximum 0.5%. The pH of saline solution was established so that the collected solution inside the spraying chamber has the pH ranged between 6.5 and 7.2. This pH was measured by means of a pH meter model HI 991001, made by Hanna Instruments provided with a temperature indicator. For this test a similar corrosion chamber to that of corrosion test in humid heat was used. The accelerated corrosion test in the salt fog chamber was performed during a 144 h period of time, at 35 °C temperature. Initially, the samples were degreased with acetone, weighed using an analytical balance with an accuracy of 0.01 mg. Finally, the mass loss and the corrosion rate were calculated on the basis of the relationship (1). The results are presented in Table 2.

2.2. Microscopical and structural characterization of tombac

The morphological characteristics of the surface of metallic samples were examined by means of scanning electron microscopy (SEM). The micrographs were recorded by means of Quanta 200 Philips FEI device. The crystallographic characteristics of specimens were analysed through X-ray diffraction method (XRD), by means of DRON-3M diffractometer. This diffractometer uses the CuK$_\alpha$ radiation, at 40 kV voltages and 30 mA current intensity. The XRD patterns were recorded at 2θ angular range between 30 si 80°, with a scanning speed of 0.02° min^{-1} and acquisition time of 0.1 s/step. The behaviour of tombac by interaction with a polychromatic beam was examined by reflectance measurements recorded by means of Perkin Elmer (type Lambda) Spectrophotometer with double beam in the spectral range of 190÷1100 nm.

3. Results and discussion

3.1. The accelerated corrosion test in continue humid heat

The accelerated corrosion test in continuous humid heat was performed according to the SREN ISO 9227/2007 standard [7].

The change of the visual appearance of sample surfaces 96 h later to maintain in the corrosion chamber in continuous humid heat can be observed. The sample colour is changed due to oxidation process without affecting the corrosion resistance.

To determine the effects produced by the accelerated corrosion in continuous humid heat the corrosion rate, V_c, was chosen as an indicator. The corrosion rate was calculated based on the measurements between the initial and treated sample weight during a 96 h period of time, according to the relationship (1).

Fig. 2 indicates the mass variation of three tombac samples subjected to the corrosion test in continue humid heat as a function of time. This study exhibits the specimen's behaviour during the accelerated corrosion tests in continuous humid heat.

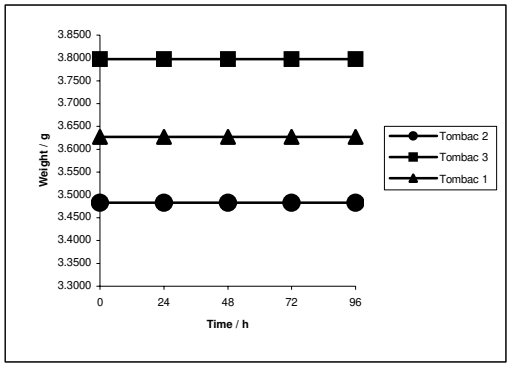

Fig. 2. *The behaviour of tombac samples subjected to accelerated corrosion test in continuous humid heat*

The results indicate the constant maintaining of mass loss over time for each sample. Therefore, the samples present a high corrosion resistance.

Table 1. *The corrosion rates of tombac samples subjected to the accelerated corrosion test in humid heat*

Sample	Corrosion rate (nm/h)
Tombac 1	0.32
Tombac 2	0.39
Tombac 3	0.32

The data presented in Table 1 and the graph of Fig. 2 show that the second sample with V_c = 0.39 nm/h corrodes the fastest because of the higher corrosion rate compared to the other two tombac samples.

3.2. The accelerated corrosion test in salt fog chamber

The change of the appearance of metallic surfaces 144 h later to maintain them in salt fog chamber to test the corrosion can be observed.

Fig. 3 indicates the mass variation of tombac subjected to the corrosion test in salt fog chamber as a function of time. Like in the case of corrosion in humid heat, the tombac specimens are very resistant to corrosion in the salt fog. This fact means that the mass variation of the samples is constant during the corrosion process.

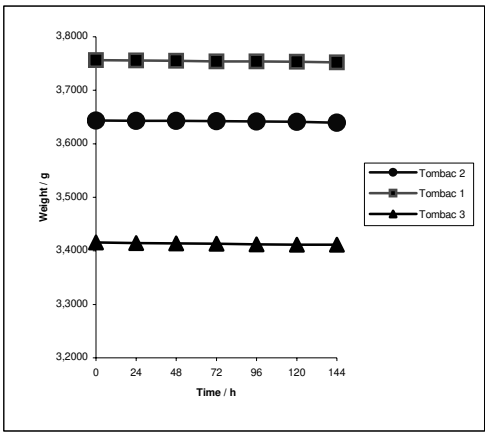

Fig. 3.*The behaviour of tombac samples subjected to accelerated corrosion test in salt fog chamber*

The data presented in Table 2 and the graph of Fig. 3 show that the first sample corrodes the fastest because of the higher corrosion rate compared to the other two tombac samples.

Therefore all results indicate that the specimens subjected to the salt fog test have higher corrosion rates compared with those recorded during the humid heat test. This increase of the corrosion rates is explained by the increase of aggressive conditions of the environment inside the salt fog chamber.

Table 2. *The corrosion rates of tombac samples subjected to the accelerated corrosion test in salt fog chamber*

Sample	Corrosion rate (nm/h)
Tombac 1	4.70
Tombac 2	4.66
Tombac 3	4.13

According to the obtained results, the metallic samples present high corrosion resistance by the formation of an oxide layer meant to protect than against the aggressive conditions of the environment.

3.3. Morphological study of tombac

The surfaces morphology of tombac 1 subjected to both tests in humid heat and salt fog at different magnifications is indicated in Fig. 4.

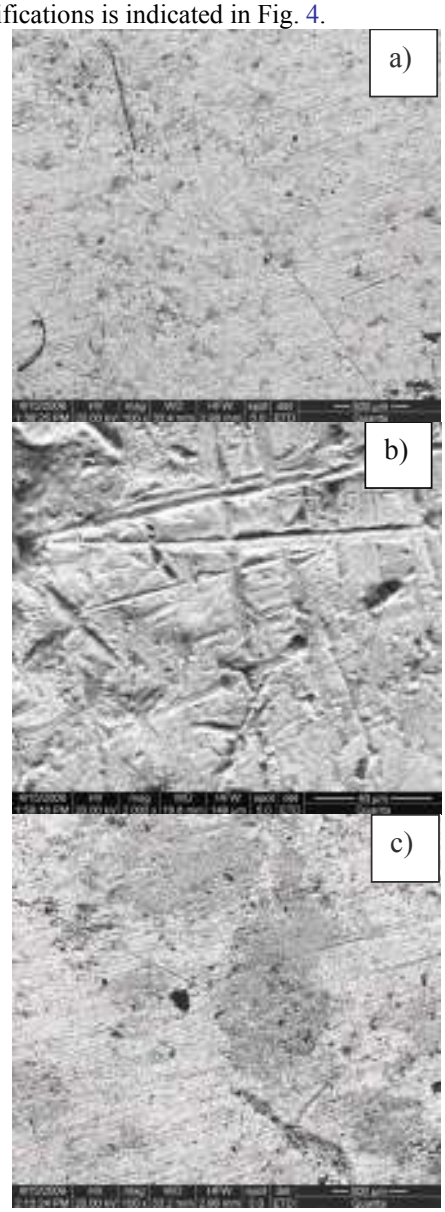

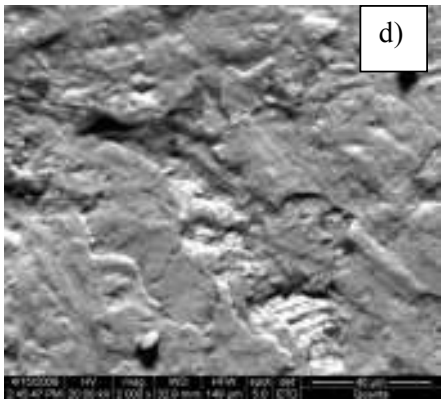

Fig. 4. *SEM micrographs at different magnifications of tombac 1 subjected to humid heat (a,b) and salt fog (c,d) tests*

SEM images of tombac 1 subjected to humid heat test emphasize the specific structure of tombac with a clean and shiny surface, which presents a few small scratches like material defects (Fig. 4a and b). A colour difference of the samples can be observed (Fig. 4c and d). By taking out the samples from the salt fog chamber, some corrosion marks appear due to the pitting phenomenon. Also, the cavities formation on the surface by loss of a small amount of substrate can be observed due to the corrosion effect of depth. The scratches existing on the sample surface subjected to humid heat test amplify the pitting process. Both environmental factors are more aggressive, the corrosion rate increases and the pinches are developed. On the other hand, the growing of an oxide layer on tombac surface subjected to salt fog having a dark colour can be shown.

3.4 Characterization of optical properties of tombac

Optical properties of reflectance of metallic samples are determined through interaction between a polychromatic beam and material surface. The incident radiation has the wavelength ranged between 190 nm and 1100 nm. The tombac 1 surface subjected to humid heat indicates higher values of reflectance than those of tombac 1 subjected to salt fog. For a certain value of wavelength, for example λ = 880 nm, the subjected sample to humid heat presents a reflectance of R = 5.86% and the subjected sample to salt fog presents a low value of reflectance of R = 2.16%. Therefore, tombac subjected to more aggressive corrosion conditions (salt fog) exhibits more opaque and darker (low reflectance capacity) due to the oxide compounds formed on the material surface.

The curve from Fig. 5, corresponding to tombac 1 subjected to humid heat, indicates the formation of an inverse pick more evident than in case of tombac 1 subjected to salt fog. It means that a minimum value of reflectance (R ≈ 6%) appears at a maximum value of absorbance.

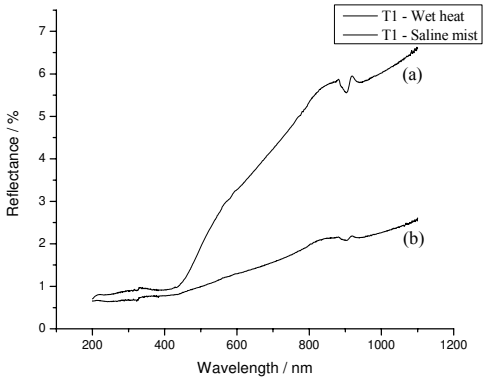

Fig. 5. *UV-VIS-IR spectra of tombac 1 subjected to humid heat (a) and salt fog (b)*

The reflectance plot follows almost exponentially the increase of the reflectance values with the increase of wavelength at the beginning in the visible region. The variation of reflectance decreases at higher wavelengths. By means of relationship (2) the reflexive index (n) can be calculated.

The reflexive index characterizes the type of dispersion specific to treated sample to a certain corrosion environment [8]:

$$R = \frac{(n-1)^2}{(n+1)^2} \Rightarrow n = \frac{1+R}{1-R} \qquad (2)$$

where: R is the reflectance [%]; $R < 1$;
n is the reflexive index.

The variation of optical constants (reflexive index) depending on wavelength for tombac 1 subjected to both corrosion tests are shown in Fig. 6. Both curves corresponding to two tests indicate a quick increasing to positive followed by a rapid decreasing to negative values when passing through zero value of reflexive index.

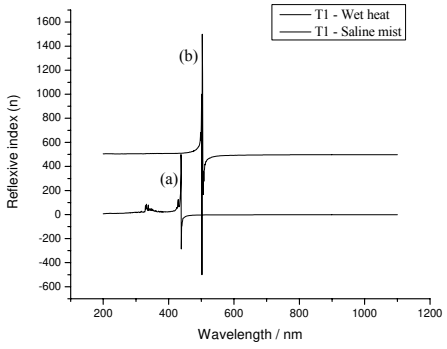

Fig. 6. *The plot of reflexive index depending on wavelength for tombac 1 subjected to humid heat (a) and salt fog (b)*

The first curve (Fig. 6a) shows a jump at $\lambda \approx$ 440 nm and the second curve (Fig. 6b) at $\lambda \approx$ 500 nm in visible range. The formation of an inverse pick is more evidently than it from the case of tombac 1 subjected to salt fog. At the beginning, the first plot of reflexive index (Fig. 6a) follows almost exponential to decrease with increasing the wavelength (330÷400) nm. The second plot (Fig. 6b) indicates a simple increasing of curve due to the inorganic compounds formed on the surface.

3.5. Structural characterization of tombac

By treatment in salt fog corrosion medium the tombac 1 presents a XRD pattern which is in agreement with that of tombac subjected to humid heat, except for some picks with low intensity. The specific lines of tombac are shown in Fig. 7. The most intensive diffraction line of tombac is (111) [9, 10].

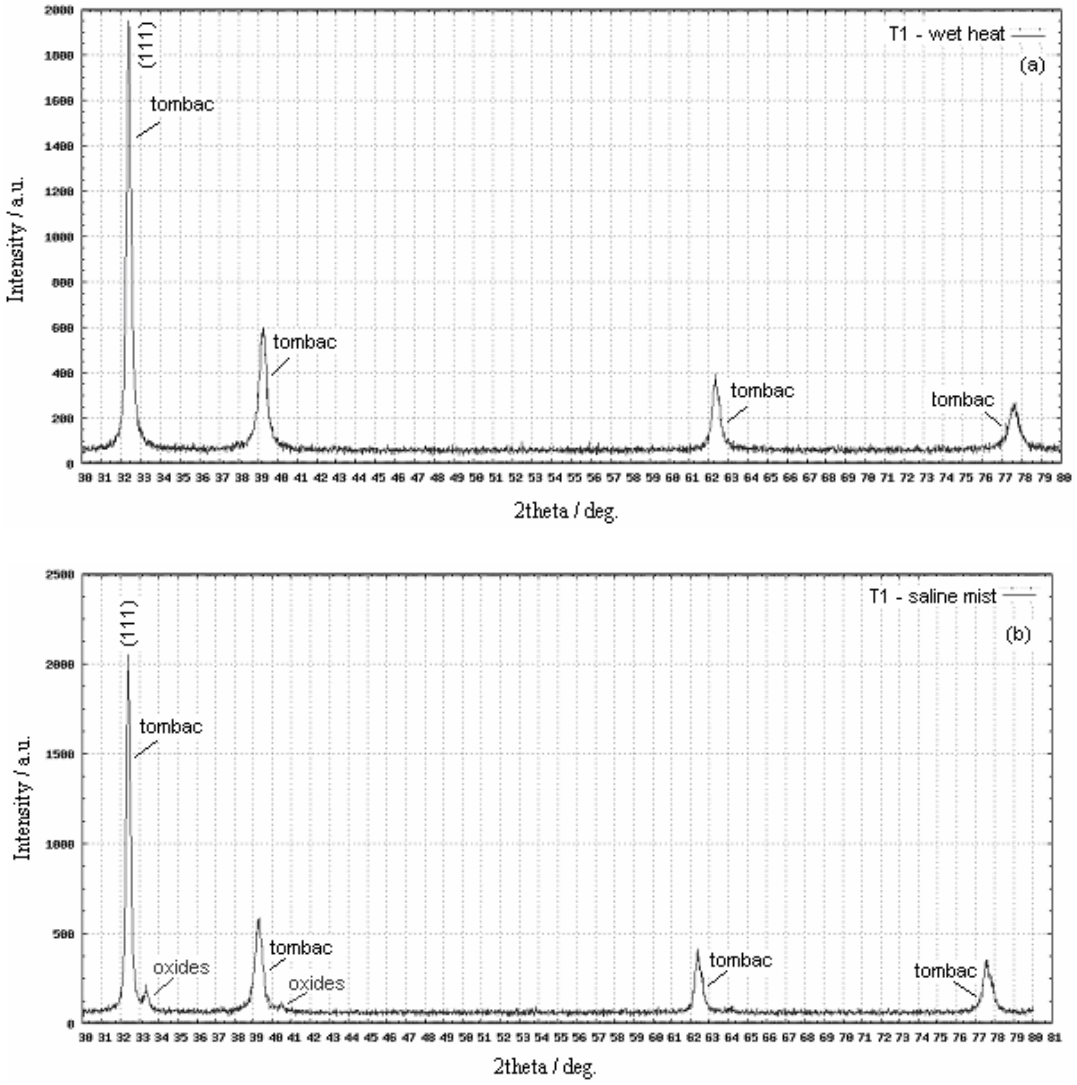

Fig. 7. *XRD patterns of tombac 1 subjected to humid heat (a) and salt fog (b)*

Furthermore, well noticeable are diffraction lines of oxide compounds formed during corrosion tests (Fig. 7a and b).

Therefore, the crystalline network is rearranged; the internal stresses are reduced by testing the sample in salt fog conditions. Also, the intensity picks of tombac decrease.

4. Conclusions

Based on experimental results regarding the corrosion of metallic samples, subjected to accelerated corrosion tests in continuous humid heat and salt fog chamber the corrosion rates and the mass variation of samples depending on the time of corrosion were calculated.

THE ANNALS OF "DUNAREA DE JOS" UNIVERSITY OF GALATI.
FASCICLE IX. METALLURGY AND MATERIALS SCIENCE
N^0. 2 – 2009, ISSN 1453 – 083X

EXPERIMENTAL RESEARCH REGARDING THE OBTAINING OF FRICTION ELEMENTS

Ionel PETREA, Vasile BASLIU
"Dunărea de Jos" University of Galati
email: ionel.petrea@ugal.ro

ABSTRACT

Friction materials are used as bimetallic friction elements, consisting of a friction material layer sintered on a steel backing. Using the electron microscopy techniques (microprobe analyzer) some of the diffusion processes were investigated, at the interface friction material-steel backing, showing the important role of intermediate layers-electrodeposited copper and sintered Fe-Cu.

KEYWORDS: friction materials, copper X-ray scan, intermediate layer, microcomposition

1. Introduction

Sintered friction materials represent one of the typical applications of powder metallurgy.

The requirements imposed on friction materials are:

- high friction coefficient, with values which do not vary too much with the temperature,
- low abrasive wear and long friction period,
- good thermal conductivity resistance at the high temperatures,
- corrosion resistance,
- good running and continuous friction properties.

In order to realize all these properties, the modern friction materials have complex composite composition, containing metallic constituents which form the metallic resistance mass (copper, iron, steel, cast iron), the friction modifies (elements used in the friction surface cleaning) and lubricants. Iron-based friction materials are used in heavy-duty friction applications, which implies high temperatures of 500-700 C (frequently over 1000 C at the friction surface; e.g. airplane brakes).

It has to be mentioned that not the friction materials are produced, but the friction elements. A friction element can be represented by a friction disk or a friction plate, every one of them representing an assembly composed of a metallic backing and the friction material.

The metallic backing attends, without exception, all the sintered friction materials. Its presence is determined by the reduced mechanical resistance of the friction material.

The sintered friction material is composed by two-layer parts: a layer of a complex composition and an intermediate layer, for improving the contact between the friction material and the steel backing.

The role of the intermediate layer is that of facilitating the diffusion processes that occur during the sintering, in order to enssure a high quality brazing; for the same goal, the steel backing can be copper plated or electrolytic nickel-plated.

2. Experimental procedure

The used iron-based friction material has the following composition: 80% Fe, 5% Al_2O_3, 5% SiC, 5% graphite, 5% Pb. First the backing from low allowed steel has been plated with electrolytic copper.

The intermediate layer is a powder mixture: 50% Fe-50% Cu.

After the powder mixture homogenization, the mixture was deposited on the backing and compacted with a pressure of 500 MPa.

The sintering has been realized in hydrogen atmosphere, 1h at 1100 C.

The investigation of diffusion processes taking place at the interface friction material-steel backing, by the intermediate layers of sintered Fe-Cu and electrodeposited Cu on steel, as well as in the friction material itself. It was realized using the microstructure analysis in a cross-entry test section (fig.1).

The microstructure and microcomposition of a cross section were analysed, investigating in a first stage the diffusion of Fe, Cu, Pb by using a Phillips, SEM 515.

Fig.1. *BEI of the cross section (x 35)*

3. Results

The structure of the cross section through the analysed material is shown in figure 1. Only three of the initial layers can be observed (from the left side): steel backing, the intermediate Fe-Cu layer and the friction material.

The copper layer cannot be observed, owing to its complete diffusion, as results from Cu X-ray scan on figure 2, that shows the interface steel backing-intermediate layer.

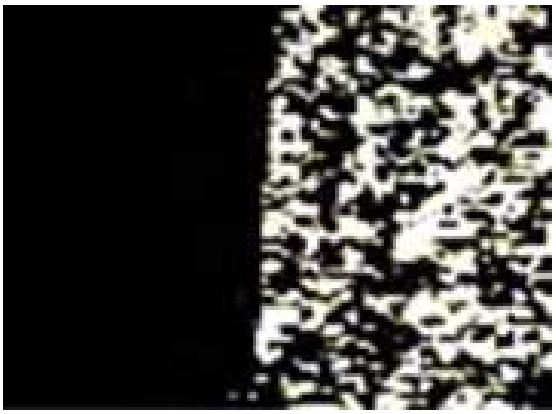

Fig.2. *X–ray scan, Cu K*

Three constituents of different composition and contrast level were identified in the intermediate layer material structure (Figure 3 and Table 1). Lead segregation in bright contrast phase (2) can be observed, as well as copper diffusion in Fe-Cu compounds (1 and 3).

Iron-based composite friction material structure is shown by Figure 4.

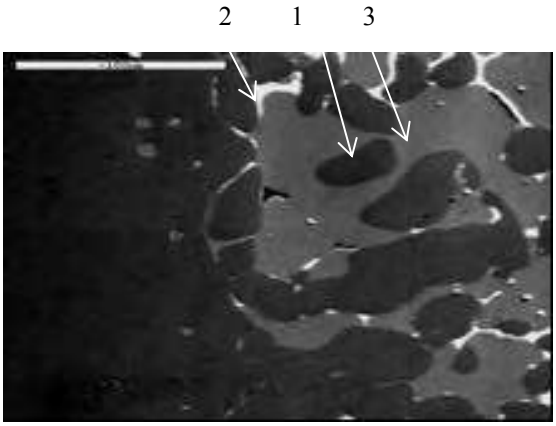

Fig.3. *BEI – Intermediate layer (x 500)*

Copper X-ray scan shows the intensive and uniform diffusion of this element, coming from the intermediate layer in the friction material.

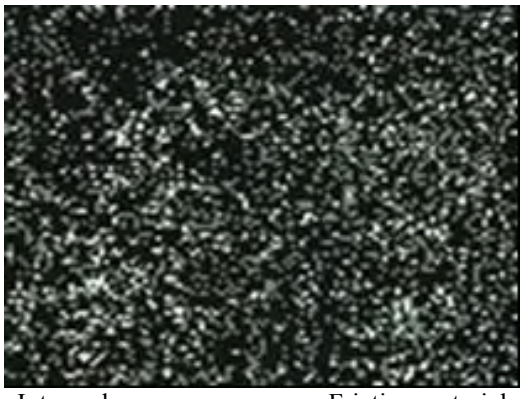

Fig.4. *X–ray scan, Cu K*

Table 1. *EDS analyses results for intermediate layer*

Phase	**Phase contrast**	**Chemical microanalyses,** [wt. %]				
		Fe	Cu	Pb	Al	Si
1	Medium-grey	90.45	9.22	-	-	0.65
2	Bright	4.07	7.02	61.82	-	0.68
3	Bright-grey	5.31	92.70	-	-	0.36

4. Conclusions

The strong and continuous bond between the iron-based friction material and the steel backing is enssured owing to some diffusion processes, identified by microstructural analysis: electrodeposited Cu into intermediate Fe-Cu layer; Cu from the intermediate layer into friction material; Pb-liquid at the sintering temperature - from the friction material into the intermediate layer.

From the technological point of view, the two bonding layers-electrodeposited Cu and sintered Fe-Cu, are in a high degree necessary for a good quality adherence between the steel backing and the sintered friction material.

References

[1]. Storin, A., et al. - *"Metallurgy and New Materials Researches"*, 1994, Vol. II, p.126-130.
[2]. Hausner, H.H, et al. -*"Friction and Antifriction Materials",* Plenum Press, N.Y.**,** 1970
[3]. Petrea, I. - *"Cercetari privind obtinerea si proprietatile trobologice ale materialelor compozite poroase in matrice de fier"*, Ph.D. Thesis, University of Galaţi, 2003
[4]. Tudor, A. - *"Frecarea şi uzarea materialelor"*, Ed. Bren, Bucureşti. 2002
[5]. Williams, J. A. - *"Engineering Tribology"*, Oxford University Press, Oxford, 1994.

MANUSCRISELE, CĂRŢILE ŞI REVISTELE PENTRU SCHIMB, PRECUM ŞI ORICE CORESPONDENŢE SE VOR TRIMITE PE ADRESA:

MANUSCRIPTS, REVIEWS AND BOOKS FOR EXCHANGE COOPERATION, AS WELL AS ANY CORRESPONDANCE WILL BE MAILED TO:

LES MANUSCRIPTS, LES REVUES ET LES LIVRES POUR L'ECHANGE, TOUT AUSSI QUE LA CORRESPONDANCE SERONT ENVOYES A L'ADRESSE:

MANUSCKRIPTEN, ZIETSCHRITFTEN UND BUCHER FUR AUSTAUCH SOWIE DIE KORRESPONDENZ SID AN FOLGENDE ANSCHRIFT ZU SEDEN:

UNIVERSITATEA "DUNĂREA DE JOS" DIN GALAŢI
REDACŢIA ANALELOR
Str. Domnească nr. 47 – 800036 Galaţi, ROMÂNIA
E-mail: mbordei@ugal.ro

AFFILIATED WITH:

- *ROMANIAN SOCIETY FOR METALLURGY*
- *ROMANIAN SOCIETY FOR CHEMISTRY*
- *ROMANIAN SOCIETY FOR BIOMATERIALS*
- *ROMANIAN TECHNICAL FOUNDRY SOCIETY*
- *THE MATERIALS INFORMATION SOCIETY (ASM INTERNATIONAL)*

Annual subscription (2 issues per year)

Edited under the care of
Faculty of
METALLURGY AND MATERIALS SCIENCE
and Research Center
QUALITY OF MATERIALS AND ENVIRONMENT

Edited date: 15.11.2009
Issues number: 200
Printed by
Galati University Press
accredited CNCSIS
47 Domneasca Street, 800036 Galati,
Romania